Numerical Simulation of a Film Cooled Turbine Blade Leading Edge Including Heat Transfer Effects

by

Laurene D. Dobrowolski, B.S.M.E

Thesis

Presented to the Faculty of the Graduate School of
The University of Texas at Austin
in Partial Fulfillment
of the Requirements
for the Degree of

Master of Science in Engineering

The University of Texas at Austin
May 2009

Numerical Simulation of a Film Cooled Turbine Blade Leading Edge Including Heat Transfer Effects

Approved by
Supervising Committee:

____

____

Dedication

To Bon Papa, my parents and Greg Popowski

Merci pour votre soutien

Acknowledgements

I would like to thank the Office of Naval Research for funding this study. I am very grateful to Dr. Bogard for his constant help and support. He took the time to share his knowledge and brilliant ideas with me. He also taught me to always analyze my results critically. This thesis would not have been completed without him. Thanks. I would also like to thank Dr. Da Silva for reviewing these 200 pages and giving me throughout comments.

Furthermore, I would also like to thank all the TTCRL students. Special thanks to the “Jasons”, Jason Albert and Jason Dees. Jason Albert was always willing to help me with his great source of knowledge. My American friend Jason Dees deserves special thanks. Not only did he help me with “Science”, but he also corrected my English with remarks “such as this”. I would also like to thank Tom Dyson, who spent so much time helping me. I enjoyed our parties at 9 pm in the lab. Thanks to Katie Harrison who helped me so much with FLUENT. Also, I do not forget Todd Davidson, Josh Blace Bruck, Aimie Faucett and Emily Pfautsch for having made this lab a great environment to work. I would also like to thank my good friend Ross Johnson, who I enjoyed working with.

Thanks to my friend Carlos Rios and Beto for their continuous support. I am also very grateful to Colin’s ebook, which allowed him to stay patient while waiting for me. Finally, I would like to thank my Frenchie friend Laure/a, without who these two years would not have been the same.

August 14, 2009

Numerical Simulation of a Film Cooled Turbine Blade Leading Edge Including Heat Transfer Effects

Laurene D. Dobrowolski, M.S.E

The University of Texas at Austin, 2009

Supervisor: David G. Bogard

Computations and experiments were run to study heat transfer and overall effectiveness for a simulated turbine blade leading edge. Computational predictions were run for a film cooled leading edge model using a conjugate numerical method to predict the normalized “metal” temperatures for the model. This computational study was done in conjunction with a parallel effort to experimentally determine normalized metal temperatures, i.e. overall effectiveness, using a specially designed high conductivity model. Predictions of overall effectiveness were higher than experimentally measured values in the stagnation region, but lower along the downstream section of the leading edge. Reasons for the differences between computational predictions and experimental measurements were examined. Also of interest was the validity of T_{aw} as the driving temperature for heat transfer into the blade, and this was examined via computations. Overall, this assumption gave reasonable results except near the stagnation line. Experiments were also conducted on a leading edge with no film cooling to gain a better understanding of the additional cooling provided by film cooling. Heat flux was also measured and external and internal heat transfer coefficients were determined. The results showed roughly constant overall effectiveness on the external surface.

Table of Contents

List of Tables

List of Figures

Nomenclature

A	Area of the hole
Bi	Biot Number = ht/k
c	Specific heat capacity
DR	Density ratio = ρ_c/ρ_∞
D	Leading edge diameter
d	Hole diameter
Fr	Frossling number = Nu/Re
h_f	Heat transfer coefficient with film cooling = $q''/(T_{aw}-T_{w,ext})$
h_0	Heat transfer coefficient without film cooling = $q''/(T_\infty-T_{w,ext})$
h_f/h_0	Heat transfer augmentation
k	Thermal conductivity
l	Thickness of airfoil
M	Blowing ratio = $\rho_c U_c/\rho_\infty U_\infty$
$\dot{m}$	Mass flow rate
Nu	Nusselt number = $hl/\,k(T)$
p	Hole-to-hole pitch
q''	Heat flux
q	Heat Transfer
Re	Reynolds number
T	Temperature
Tu	Turbulence intensity level
u	Velocity
x	Streamwise coordinate
$y+$	Non-dimensional distance from wall = $\rho\, u_\tau y/\mu$
z	Spanwise coordinate
α	Hole angle
δ_1	Displacement thickness
δ	Edge of the boundary layer
η	Adiabatic effectiveness = $(T_{aw}-T_\infty)/(T_{c,out}-T_\infty)$
ϕ	Overall Effectiveness = $(T_\infty-T_w)/(T_\infty-T_{c,in})$
ϕ'	Normalized temperature = $(T_\infty-T_{w,ext})/(\,T_\infty-T_{c,impingement})$
Λ	Integral length scale
μ_t	Turbulence viscosity
θ	Normalized temperature = $(T-T_\infty)/(T_{c,out}-T_\infty)$
ρ	Density

Subscripts and Superscripts

aw	Adiabatic wall
c	Coolant
cond	Conducting
ext	Property evaluated on the external surface
f	With film cooling
in	At the entry of the hole
int	Property evaluated on the internal surface
off-stag	Off Stagnation
out	At the exit of the hole
pred	Predicted
stag	Stagnation
w	Property evaluated at the wall
0	No film cooling injection
0,r	No film cooling injection for real engine
∞	Mainstream
—	Lateral average

Chapter 1: Introduction and Literature review

This first chapter will briefly explain the fundamental principles behind gas turbine engines. Film cooling design will be mainly described, as well as the nomenclature used. This chapter will also review film cooling studies done in the past.

1.1 INTRODUCTION

Gas turbine engines are critical to the transport industry (airplanes, ship), and also the energy world with the presence of gas turbine engines in power plants. The gas turbine consists of a compressor, combustor, turbine and exhaust nozzle, as shown in Figure 1.1.

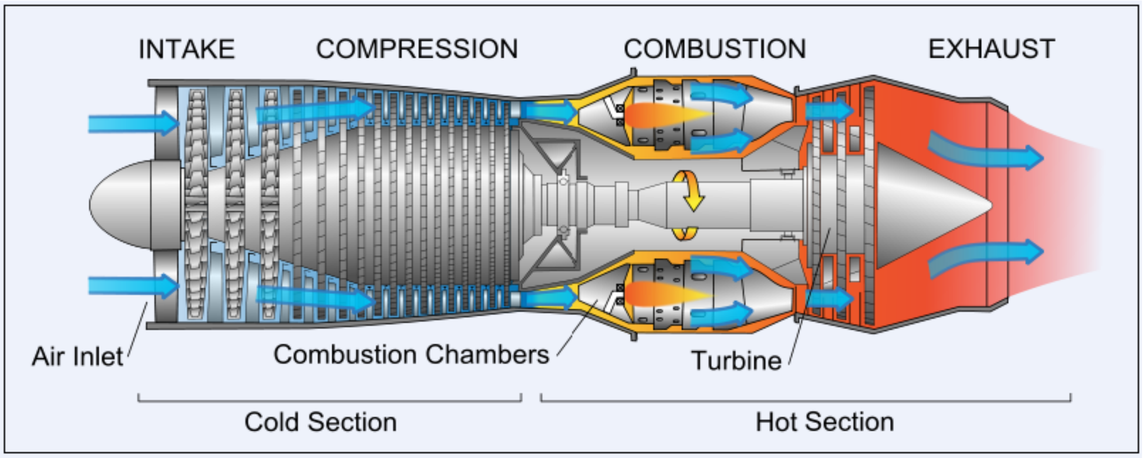

Figure 1.1: Diagram of a Gas Turbine Jet Engine http://en.wikipedia.org/wiki/File:Jet_engine.svg

The increasing demand on energy performance naturally leads to an effort to increase efficiency of gas turbines. This can be achieved by increasing inlet temperature.

Consequently, over the past fifty years, much research and development for gas turbines has focused increasing the operating temperature of the turbine section.

1.1.1 Efficiency of Gas Turbines Engines

A simplified model of the gas turbine can be expressed as a Brayton cycle, as shown in Figure 1.2 Four steps are involved in this process. The gas at an initial temperature T_1 is first compressed adiabatically and leaves the compressor with an exit temperature T_2. Then, heat is added into the combustor at a constant pressure until the gas reaches the temperature T_3. Then, the gas expands in the turbine and releases work adiabatically. At the exit of the turbine, the gas has a temperature T_4. Finally, in a closed system, the fluid is cooled to the initial temperature T_1. The ideal efficiency is defined by the following equation:

$$\eta_{eff} = \frac{Net \cdot work \cdot output}{Net \cdot work \cdot input} \tag{1.1.1.1}$$

The net work output is obtained by the subtraction of the work extracted from the turbine by the work required to compress the gas. The net heat input is the heat added in the combustor. The net work output per unit mass flow rate becomes $(h_3 - h_4) - (h_2 - h_1)$ since the process is adiabatic (1st law of thermodynamic) and the net heat input is $(h_3 - h_2)$ since the process is isobar ($q''_{2\text{-}3} = h_2 - h_3$). The efficiency can finally be expressed with Equation 1.1.1.2:

$$\eta_{eff} = \frac{(h_3 - h_4) - (h_2 - h_1)}{h_3 - h_2} \tag{1.1.1.2}$$

Assuming constant heat capacity, the ideal efficiency is given by the following equation:

$$\eta_{eff} = \frac{c_p(T_3 - T_4) - c_p(T_2 - T_1)}{c_p(T_3 - T_2)} = 1 - \frac{T_4 - T_1}{T_3 - T_2} \tag{1.1.1.3}$$

This equation shows the primary interest in increasing turbine inlet temperature, T_3 which leads to an increase in efficiency. It should be recalled that Equation 1.1.1.3 gives the ideal efficiency. In reality, the process is not reversible and the constant heat capacity c_p depends on the temperature. However, Moran and Shapiro (2000) indicates that the Brayton cycle gives a reasonable insight to the thermal efficiency.

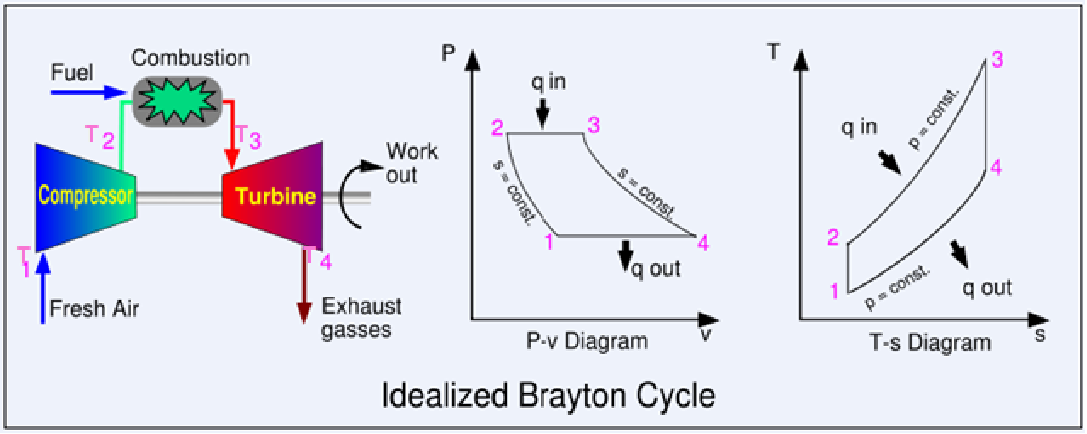

Figure 1.2: Brayton cycle for gas Turbine http://en.wikipedia.org/wiki/Brayton_cycle

With higher combustor exit temperatures, the efficiency can be improved and fuel consumption can also be reduced. Moreover, in aircraft application, the higher temperatures lead to increase thrust. Unfortunately, modern turbine stage inlet temperatures exceed the melting point temperatures of turbine blade materials, which results in irreversible damage. To allow the increase in inlet temperature and preserve the life of the blade materials, engineers have developed several cooling strategies. Film cooling is one of these techniques and of primary interest in this thesis.

1.1.2 Film Cooling Design

Two different methods have been employed to protect the metal from the hot freestream gas. The first one, named Thermal Barrier Coating (TBC), consists in the application of a thin layer of a low conductivity material, generally ceramic, on the external surface of the blade to insulate it from the hot mainstream. The low conductivity material reduces the amount of heat entering the solid. However, the TBC might reduce the gas turbine efficiency due to additional weigh on the rotating blades. A balance should be found between the thermal protection and the additional weight. (Bose et al., 1997)

Cooling is the second method employed to increase the gas turbine durability. Two strategies are employed: either internal cooling, or internal cooling and film cooling.

Internal cooling employs cooled air from the compressor stage and ducts it to the internal chambers of the turbine blades, where the coolant flows through serpentine passages with pins and turbulence generators. This aims to increase the internal heat transfer coefficient to drain as much heat as possible inside the plenum. Rib turbulators are often located in the middle of the blade, whereas an impingement plate is commonly used in the leading edge. An impingement plate is a perforated plate, whose primary goal is to increase heat transfer coefficients through high velocity jets. Internal walls experienced high heat transfer coefficients, where the jet impacts.

When film cooling is also used, the cooled air is discharged through small holes in the blade walls. The cooled air, also named coolant, extracts heat from the blade metal through the coolant holes. The coolant exiting from the hole provides a thin, cool, insulating layer of air along the external surface of the turbine blade. The process of ejecting coolant on the external surface to protect the metal from the mainstream gas is called film cooling. Turbine airfoil temperatures are a result of internal cooling, convective cooling, as well as film cooling. Cooling and TBC processes allow gas turbines to operate at much higher temperatures than the melting temperature dictated by the material. Figure 1.3 illustrates the process of internal cooling and film cooling.

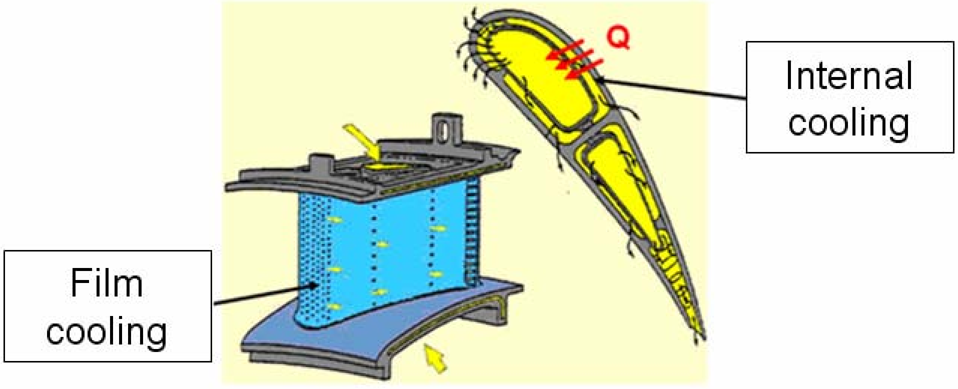

Figure 1.3: Illustration of film cooling process http://lttwww.epfl.ch/research/htprojects/filmcool.htm

Several criteria should be addressed when manufacturing the cooling design. The first one consists of the amount of cooling used to protect the temperature. Indeed, extracting air from the compressor results in a loss in the thermal efficiency. A balance needs to be found between an acceptable durability and high performance efficiency. The location of film cooling holes is also critical. Protecting the most exposed area such as the leading edge or the trailing edge will increase the durability of the gas turbine. Most of the time, blades must be thrown away because only part of it is damaged whereas the main body remains intact. Film cooling design is a complex process, which needs to be carefully studied.

1.1.3 Background Review

The schematic presented in Figure 1.4 summarizes the different variables influencing the external surface temperature. The temperature of the coolant exiting the impingement plate is referred as T_c where as the freestream temperature is T_∞. The coolant at the exit of the impingement plate warms up due to heat going into the plenum, rising the coolant temperature at the exit of the impingement plate T_c to $T_{c,in}$, the temperature at the entry of the coolant hole. Convective film cooling has also a strong effect in cooling down the metal temperature. As a result, the temperature of the coolant at the exit of the hole, $T_{c,out}$ is higher than the one at the entry $T_{c,in}$ due to convective heat gain as the coolant flows through the coolant holes. However, the exit coolant temperature is sufficiently low to protect the external surface temperature as the coolant spreads out externally. As the coolant spreads out on the external surface, it warms up due to heat transfer occurring from the solid to the coolant and also due to the mixing of the coolant and the freestream gas. The mixing results in an increase in external heat transfer coefficients right at a short distance downstream of the holes.

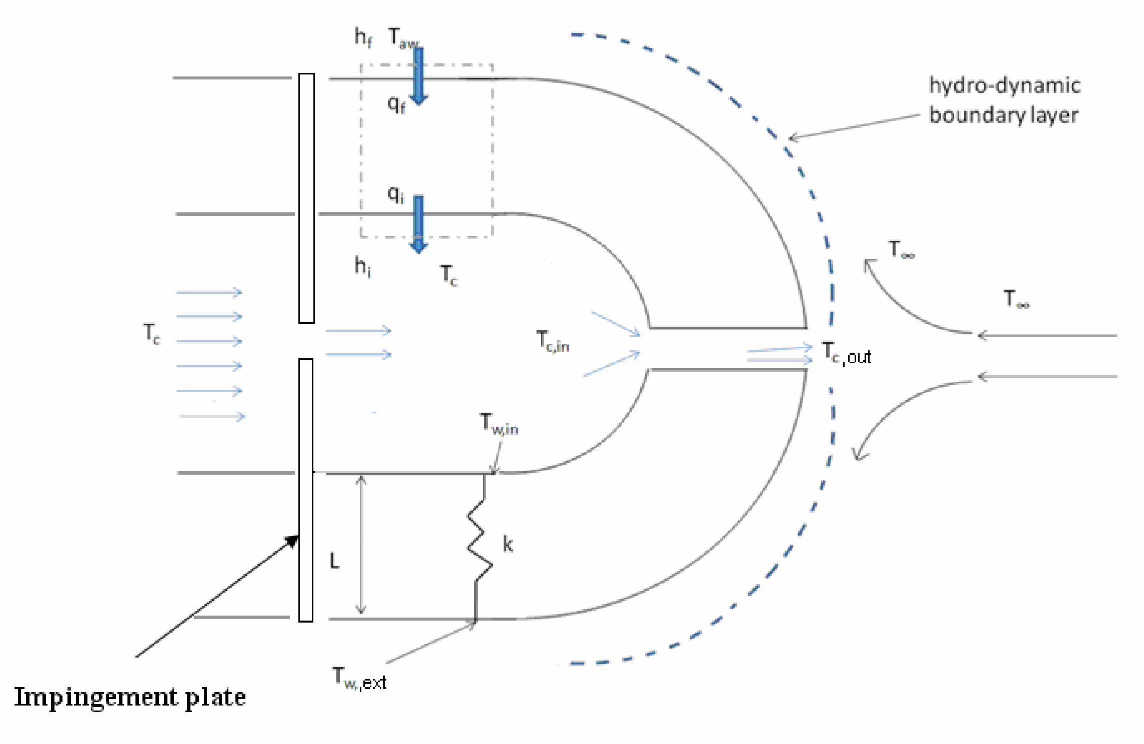

Figure 1.4: Internal, convective and film cooling for a conducting model

The heat transfer coefficient with film cooling is defined by the following equation:

$$q'' = h_f (T_{aw} - T_{w,ext}) \tag{1.1.3.1}$$

where T_{aw} is the temperature of the adiabatic wall and $T_{w,ext}$ is the metal temperature of the conducting model. Since, the coolant temperature right above the wall results from the mixing of the coolant at the inlet of the hole and the mainstream flow, neither the freestream temperature nor the internal coolant temperature is appropriate for the driving temperature. The adiabatic wall temperature T_{aw} is assumed to be the driving temperature for heat transfer into a conducting wall. This assumption turns out to be reasonable (except for some locations, generally along the centerline) on a flat plate according to the study of Harrison (2006), however it is still questionable for a leading edge since no study of the validity exits to date.

Most experiments have been carried out with near adiabatic models. Indeed, the knowledge of the adiabatic wall temperature T_{aw} and the heat transfer coefficients h_f are sufficient to predict the metal temperature, under the assumption that T_{aw} is the driving temperature. The adiabatic wall temperature is usually presented under a non-dimensional parameter η, the adiabatic effectiveness, defined as follows:

$$\eta = \frac{T_\infty - T_{aw}}{T_\infty - T_{c,out}} \tag{1.1.3.2}$$

The unity value corresponds to perfect film coverage and a zero value indicates no cooling. The adiabatic film effectiveness can be seen as a direct measurement of the mixing between the coolant and the freestream, since the gas temperature is proportional of the initial temperature and the amount of mixing with the freestream temperature.

The external heat transfer coefficient h_f is normalized by the external heat transfer coefficient with no film cooling, h_0. The ratio $\frac{h_f}{h_0}$ is called the heat transfer augmentation.

Experiments are conducted on large size models, which are properly dimensioned to match the engine operational conditions. Several parameters are taken into account. The adiabatic effectiveness is dependant on a number of variables such as the blowing ratio, M, the turbulence intensity, Tu, the density ratio, DR, the external Reynolds number, Re, and the model geometry. The blowing ratio, M, is the coolant jet-to-mainstream ratios of mass flux defined by the equation 1.1.3.3:

$$M = \frac{\rho_c U_c}{\rho_\infty U_\infty} \tag{1.1.3.3}$$

where ρ_c and ρ_∞ are respectively the coolant and freestream density and U_c and U_∞ are the coolant and freestream velocity, respectively.

The density ratio, DR, is the ratio of the coolant density to the freestream density:

$$DR = \frac{\rho_c}{\rho_\infty} \tag{1.1.3.4}$$

Real turbine engines operate at $DR = 2$ (Bogard and Thole (2006)). However, $DR = 2$ is difficult to achieve experimentally, so a density ratio of 1.5 was used. As the computational study matches the experimental conditions, a density ratio of 1.5 was also employed.

The simulation conducted was based on experiments, which include conduction through the solid. In this case, the blowing ratio is all the more important because it dictates not only the mixing at the exit of the hole but also the internal heat transfer coefficient and convective cooling in the holes. Indeed, heat transfer coefficients are highly dependant on the fluid motion close to the wall. The Nusselt number $Nu = hD/k$ is then matched if the blowing ratio M and Reynolds number Re are similar to the operating engines conditions and the geometry is similar to the real engine geometry.

The simulation includes the conduction through the solid. If the model is scaled correctly, the non-dimensional external temperature for a conducting model, ϕ should be exactly the same than the one for real engines. ϕ is called the overall cooling effectiveness and is defined as follows:

$$\phi = \frac{T_\infty - T_{w,ext}}{T_\infty - T_c} \tag{1.1.3.5}$$

(Albert 2003) demonstrates with a simple 1-D analysis that matching the Biot number, in addition to all the non-dimensional parameters quoted before, is sufficient to predict the overall effectiveness.

Indeed, the heat flux occurring on the external surface is:

$$q''_f = h_f (T_{aw} - T_{w,ext}) \tag{1.1.3.6}$$

The heat flux from the solid to the plenum is given by Equation 1.1.3.7

$$q''_{\text{int}} = h_{\text{int}} (T_{w,\text{int}} - T_c) \tag{1.1.3.7}$$

The heat flux from the conduction through the solid can be expressed as follows:

$$q''_{cond} = \frac{k}{l}(T_{w,ext} - T_{w,\text{int}}) \tag{1.1.3.8}$$

It should be recalled that the heat flux through the holes is not taken into account since this simplified model is a 1-D analysis. The 1-D analysis will not hold anymore with the insertion of the convective heat flux. However, a useful insight can be gained from this analysis.

Right at the wall, the energy balance requires the following under 1-D analysis:

$$q''_{f} = q''_{cond} \text{ and } q''_{\text{int}} = q''_{cond} \tag{1.1.3.9}$$

Equation 1.1.3.9 can be rewritten, which leads to the following expression for the heat flux on the external surface:

$$q'' = h_f(T_{aw} - T_{w,ext}) = h_i(T_{w,\text{int}} - T_c) = \frac{k}{l}(T_{w,ext} - T_{w,\text{int}}) \tag{1.1.3.10}$$

Rearranging the previous equation leads to the following equations:

$$q''_{f} = (T_{aw} - T_c)\frac{(T_{aw} - T_c)}{(\frac{1}{h_f} + \frac{l}{k} + \frac{1}{h_{\text{int}}})} \tag{1.1.3.11}$$

or

$$\frac{T_{aw} - T_{w,ext}}{T_{aw} - T_c} = \frac{1}{1 + \frac{h_f}{h_{\text{int}}} + Bi} \tag{1.1.3.12}$$

where $Bi = \frac{h_f l}{k}$, which is known as the Biot number, *Bi*, a non-dimensional number, which measures the influence of the conduction effect relative to the convection effect.

This interesting analysis indicates that the Biot number is the only extra parameter (in comparison with the adiabatic model) to be scaled if the conduction is taken into account. The length scale and the heat transfer coefficient being imposed respectively by the geometry and the fluid motion, the thermal conductivity is the only parameter, which can be set up.

The injection of the coolant through the coolant holes might increase the heat transfer coefficients, due to the turbulence generated by the mixing. If the heat transfer augmentation due to the mixing is too high, the beneficial effects of the film cooling are lost. It is important to measure the total benefit of film cooling over heat transferred into the solid. The net heat flux reduction is determined from the heat flux occurring with film cooling, q_f'' and the heat flux occurring without film cooling, q_0'', as expressed in the following equation developed by Sen et al. (1996):

$$\Delta q_r = 1 - \frac{q_f}{q_0} = 1 - \frac{h_f}{h_0}\left(\frac{T_{aw} - T_{w,ext}}{T_\infty - T_{w,ext}}\right) = 1 - \frac{h_f}{h_0}\left(1 - \frac{\eta}{\phi}\right) \qquad (1.1.3.13)$$

If $\Delta q''_r < 0$, the heat flux is increased due to the presence of the film cooling. This is a negative effect. If $\Delta q''_r > 0$, the heat flux into the solid is decreased, and film cooling decreases the metal temperature. An average value of ϕ = 0.6 is commonly used to represent the engine condition, according to Mick and Mayle's (1998) study.

1.1.4 Experimental Method of Heat Transfer Measurement

Many studies have been done on measurement of heat transfer coefficient for film cooling. Three different methods, described below, are commonly used.

The first method uses a constant heat flux applied on an external surface using “coolant” with density ratio of unity. The experiments are conducted at *DR* = 1 to reduce the uncertainty. At this density ratio, the mainstream temperature is the driving temperature, which is easily measurable. At a higher density ratio, the adiabatic wall temperature is the driving temperature. The uncertainty on the measurement of the mainstream temperature is much lower than the uncertainty on the measurement of the adiabatic wall temperature. Therefore, most experiments to determine heat transfer coefficients with a constant heat flux have been conducted at *DR* = 1.0. Moreover, the density ratio has a small influence on the external surface, according to Baldauf et al. (2002). They experimentally studied the influence of the density ratio on a flat plate. For $M < 1.0$, the augmentation of heat transfer coefficients was similar for *DR* = 1.2 and *DR* = 1.8. A slight difference was observed at higher blowing ratio.

For the second method, a constant wall temperature is set up. This is achieved by using a constant temperature bath. Kastell et al. (1992) used this technique to measure the development of the thermal boundary layer on a vertical plate.

The third method uses a transient liquid crystal thermography technique, described by Ekkad and Han (2000). The liquid crystals on the surface reflect different colors based on the temperature of the surface. The surface temperature depends on the local heat transfer coefficients, which can be obtained by measuring the time history of the surface temperature and assuming a 1-D semi-infinite solid. The 1-D assumption is achieved with a low thermal conductivity and low thermal diffusivity material.

1.1.5 Determination of the Metal Temperature in Industry

In industry, the adiabatic wall temperature, T_{aw}, and the laterally averaged heat transfer augmentation, h_f/h_0, are the two external parameters used to determine the metal temperature. A finite element code is run where internal and external boundary conditions are obtained from experimental data. The external boundary conditions are represented by η and h_f/h_0 found experimentally in laboratory. The external heat flux is then imposed to be governed by:

$$q'' = \frac{h_f}{h_0} h_{0,r} (T_{aw} - T_{w,ext}) \tag{1.1.5.1}$$

where $h_{0,r}$ represents the heat transfer coefficient with no film cooling for engine conditions. The adiabatic wall temperature, T_{aw}, is chosen to be the driving temperature, as seen previously with Equation 1.1.3.1. The boundary conditions are the internal heat transfer coefficient h_i determined experimentally and the coolant temperature $T_{c.}$

1.2 LITERATURE REVIEW

This literature review is focused on the conjugate heat transfer method on leading edge and turbine vane, computational overall effectiveness, adiabatic film effectiveness and heat transfer augmentation predictions on leading edges, as well as turbulence modeling. Also, in this thesis, experimental heat transfer augmentation was studied, as well as the influence of the thermal boundary layer on the heat transfer coefficient.

1.2.1 Computational Turbulence Model

The choice of the turbulence model is critical to obtaining accurate results. It is difficult to determine the best turbulence model for film cooling case, since many studies have different recommendations based on limited and varying criteria. While most of the computational studies focused on the adiabatic effectiveness prediction, only a few focused on heat transfer predictions. Also, none of the studies agreed on one turbulence models to predict accurately the adiabatic film effectiveness and the heat transfer coefficient predictions. The correct prediction of the external heat transfer coefficient is critical to obtain the correct surface temperature. As the primary interest of this study was the accurate prediction of heat transfer coefficient, only the ability of the turbulence model to correctly predict heat transfer coefficients was investigated.

Harrison and Bogard (2008) sought the most accurate turbulence model to predict adiabatic effectiveness and heat transfer coefficients on a flat plate with film cooling. The realizable k-ε model, standard k-ω and Reynolds's stress model (RSM) from FLUENT were compared. All three models agreed with less than 10% difference with the experimental results of the heat transfer coefficient prediction. They found that the realizable k-ε model best predicted h_0 and laterally averaged h_f/h_0. Centerline h_f/h_0 and spanwise h_f/h_0 predictions with the realizable k-ε model were respectively 5% lower and 30% higher than measured values at M = 1.0. However, the realizable k-ε model gave better results than the standard k-ω and RSM.

Laskowski et al. (2008) also studied different turbulence models using a wall function or an enhanced wall treatment function on the internally cooled 1983 C3X vane. Consistently, the enhanced wall treatment function delivered better agreement than the standard wall function, especially for heat transfer coefficient prediction. Three RANS model were used: k-ω, Shear Stress Transport (SST) and Omega Reynolds Stress (ORS). All three models gave results within the experimental uncertainty along the majority of the surface. However, none of the three models were able to predict the transition occurring on the suction side, which resulted in higher prediction of the temperature and heat transfer coefficient for the no film cooling case.

Luo and Razinsky (2007) investigated the performance of the V2F turbulence model developed by Medic and Durbin (2002) on the internally cooled turbine C-3X vane. This model used an elliptic relaxation methodology to model the near-wall turbulence behavior. It was compared to the standard k-ε model and the quadratic k-ε model. Whereas the standard k-ε model and quadratic k-ε model considerably predicted higher heat transfer coefficient up to 50%-100% on the pressure and suction sides, the V2F turbulence models gave reasonable values with 15% discrepancies on the pressure side and 35% on the suction side compared to experimental data. Medic and Durbin (2002) also studied the V2F turbulence model on the suction side of an internally and film cooled turbine blade (described in section 1.2.1). They found that the V2F turbulent model gave adequate results for the heat transfer coefficients on the suction side with a maximum discrepancy of 20% contrary to the pressure side which gave lower simulated results with a maximum 50% difference Also, the V2F code was unable to predict the heat transfer coefficient in the vicinity of the holes, since the simulated data were 75% lower than the experimental one.

Leylek and York (2002) studied the realizable k-ε and standard k-ε models to simulate an internally cooled gas turbine vane. The standard k-ε did not perform as well as the realizable k-ε model to predict the overall effectiveness. The standard k-ε results were consistently 10% higher than the experiments while the realizable k-ε agreed within 5%. It worth mentioning that a 10% discrepancy is equivalent to an error of 150K for a moderate turbine inlet temperature of 1500K, which exceeds the desirable temperature. There is a strong need for improved turbulence models (Luo and Razinki, 2007).

Other studies have been conducted on full turbine vanes with the concern of the adiabatic film effectiveness prediction.

Lakehal et al. (2001) studied different versions of the k-ε turbulence model to simulate η on a film cooled turbine blade model. Lakehal et al. (2001) run the standard k-ε model, the k-ε model with enhanced wall treatment, and the Bergeles et al. (1978) k-ε model, which includes an anisotropy correction to develop the lateral spreading of the coolant. The standard wall function gave the worst prediction of the adiabatic effectiveness due to under-estimation of the lateral spreading. The enhanced wall treatment gave slightly better results but the Bergeles anisotropy correction showed the closest results to experiments. Lakehal et al. (2002) presented a year later a new model taking into account the anisotropy of turbulence across the boundary layer. With this model, most of the mechanisms associated with jets in cross-flow were well predicted, especially the spanwise spreading of the coolant, resulting in a better prediction of the adiabatic effectiveness.

They have been no studies of the influence of the turbulence model on heat transfer coefficient prediction and the film-cooled leading edge location. Two of the primary requirements of the turbulence model herein are the ability of the computational code to deal with strong pressure gradients and to solve the flow conditions near the wall. The realizable k-ε was found to better meet these requirements compared to all the available turbulence models. Although the author is aware that the realizable k-ε model predicted lower lateral spreading due to the isotropic eddy viscosity, which could affect the accuracy of the heat transfer coefficient prediction. Although anisotropic models might provide improved predictions, FLUENT code, used in this study, does not offer anisotropic models.

1.2.2 Computational Prediction of Adiabatic Effectiveness

Numerous authors published papers on the computational prediction of the adiabatic effectiveness. Several discrepancies have been found in the past between the simulated and experimental contours of η.

York and Leylek (2002) predicted adiabatic film effectiveness on the same leading edge model used by Cruse (1997). Four different blowing ratio were investigated with the realizable k-ε turbulence model (M = 1, 1.5, 2, 2.5). Contours of η and plots of laterally averaged adiabatic effectiveness were used to validate the simulated data. Overall, the simulations did a good job to accurately match the experimental trends at the surface. However, the numerical predictions gave consistently higher values of η than the experiment at the exit of the stagnation and off-stagnation holes. At the stagnation line, the simulation predicted a wider region of high effectiveness. At $M = 2.0$, the numerical simulation gave $\eta > 0.8$, compared to $\eta > 0.6$ for the experiment. Downstream of the off-stagnation holes, the location and trajectory of the jets were almost perfectly predicted, matching the experiments within the uncertainty, although there was less lateral spreading and higher peak values. The laterally averaged effectiveness was always 50% higher then the experimental values between the two rows of holes at M = 2.0 and 2.5. This was seen in the contours of η, where the experimental jets did not spread as much as the simulation predicted. At M = 1.5 and M = 2, the laterally averaged film effectiveness was predicted within the experimental uncertainty downstream of the off stagnation rows, whereas at M = 1.0, the predicted η does not decay as fast as the experimental data.

United Technologies, Pratt & Whitney organized a blind test to simulate film cooling on a cylindrical leading edge model based on the experiments of Cruse (1997). The geometry studied consisted of two rows of staggered film-cooling holes located at the stagnation line and at ± 25°. Thakur et al. (1997), Lin et al. (1997), Martin and Thole (1997), all simulated this case at a blowing ratio of M = 2.0 using different approaches with FLUENT. Thakur et al. (1997) and Martin and Thole (1997) used the standard k-ε model with wall functions but different meshes. Martin and Thole (1997) used tetrahedral cells whereas Thakur et al. (1997) developed hexahedral cells to reach low skewness. Lin et al. (1997) used the k-ω turbulent model. Surprisingly, Thakur et al. (1997) gave the worst results in terms of laterally average film effectiveness. Martin and Thole (1997) and Lin et al. (1997) achieved the closest results to Cruse's experimental data with less than 10% of discrepancy, except at the stagnation line. Lin et al. (1997) tended to predict lower laterally average film effectiveness, whereas Martin and Thole (1997) gave higher values. Unlike Martin and Lin, Thakur did not match the low averaged film effectiveness at injection for the off stagnation line, observed by the experiments. Martin and Thole (1997) claimed that the higher simulated averaged film effectiveness was due to the fact that the jet stayed attached on the stagnation line, whereas the experiment clearly showed jet separation. Also, the simulated lateral spreading was not well caught by the code, resulting in a higher adiabatic effectiveness at the stagnation line and a lower adiabatic effectiveness between the holes. Chernobrovkin and Lakshminarayana (1998) also simulated the same leading edge model with the k-ε turbulence model a year later. Special care was exercised in the quality of the grid and the accuracy of the boundary conditions. They obtained better results than Martin and Thole (1997) with the prediction of the jet separation on the stagnation line. However, more intensive mixing and diffusion downstream of the holes were observed compared to the experimental data.

The numerical investigation can be used to predict reasonable values of adiabatic effectiveness, which implied that the overall effectiveness could also be correctly predicted with the Conjugate Heat Transfer (CHT) analysis, which is defined in the next section. However, all papers reported the deficit of lateral spreading when using the k-ε turbulence model. Moreover, the adiabatic effectiveness simulation revealed that the numerical simulations did not predict well jet separation, resulting in higher computational η values than the actual experimental values at the exit of the holes. This issue inherent to the computational code should also be taken into account when the conducting model is simulated.

1.2.3 Conjugate Heat Transfer Simulation

Conjugate heat transfer (CHT) analysis is a coupled method which takes into account the interaction of internal flows, external flows and conduction within the solid without the prescription of heat transfer coefficients. To validate the CHT analysis, computational studies simulate experiments already conducted in the past. However, papers on CHT analysis are limited due to the lack of experimental studies that the simulation can be compared with, and also the lack of information provided about these experiments. As a result, in most simulations, part of the boundary conditions has been assumed. None of the CHT analyses were able to predict accurately the experimental results, within experimental uncertainty, for heat transfer coefficients on a film cooled configuration. (Laskowski et al (2008), Luo et al (2007), Leylek et al (2003)…) However, these discrepancies were attributed to the difficulty of the computational codes to predict the transition location and/or the inaccurate assumptions used for the missing boundary conditions, which were issues associated with the CHT analysis.

However, the coupled technique of CHT is preferable over the uncoupled methods used in industry according to Starke et al. (2008). Three different uncoupled analyses were investigated by Starke et al. (2008) on a solid blade with film cooling holes to show how far off an uncoupled method could be compared to a coupled analysis. However, the film cooling holes were only at the tip and therefore the blade had almost no coolant holes. Before performing any uncoupled simulations, the heat transfer coefficient was predicted by applying a constant heat flux on the external surface. For the first uncoupled study, the averaged heat transfer coefficient, obtained from the constant heat flux simulation, was imposed on the external surface and the mainstream temperature was the driving temperature. The second analysis was similar to the first one with the use of the local heat transfer coefficient. The last uncoupled analysis also used the local heat transfer coefficient but considered the adiabatic wall temperature as the driving temperature. Out of the three uncoupled methods, only the last one was relevant. Starke et al (2008) claimed that the conjugate heat transfer method gave more physical acceptable results than the uncoupled methods, since the CHT analysis takes into account the interaction between the flow field and the conduction effect. However, there was an inconsistency in the paper because the CHT method showed an average mean temperature on the pressure side, which was 25% lower than the last uncoupled method, while the contours of the temperature were very similar for both simulations. These issues, which were not correctly addressed by the authors, raise some doubts concerning the accuracy of their paper.

Terrell et al. (2004) is the only paper known by the author to use CHT analysis on a film-cooled leading edge. The turbulence model chosen was the realizable k-ε turbulence model, introduced by Shi et al. (1995), and the standard wall function was selected. The standard wall function does not solve the flow near the wall. A semi-empirical function is employed up to $y+ = 30$, where $y+$ is a non-dimensional wall distance. However, accurate heat transfer coefficients require resolution in the viscous sub-layer. Thus, the standard wall function is not recommended for computations with an emphasis on heat transfer. Terrel compared his results to experimental data from Mouzon et al. (2005). The computational domain was a half-cylinder leading edge with a row of shaped holes at the stagnation line (0º) and at 25º. Flow inlet boundaries conditions were specified for the mainstream and coolant inflows, with blowing ratios and density ratio matching the experimental conditions. Of primary interest was the convective heat transfer taking place through the coolant holes. The coolant hole heat transfer was found to account for 50% to 80% of the total cooling. Temperature profiles and overall effectiveness gave adequate results, compared to Mouzon's data. The simulated overall effectiveness prediction was lower than the experimental value with a maximum deviation of $\Delta\phi = 0.1$. At $M = 2.0$, the prediction of the temperature rise through the holes turned out 30% lower than experimental results for the stagnation hole, and 45% lower for the off-stagnation hole. The ratio of total coolant hole heat transfer to external heat transfer was considerably lower than the experimental values at $M = 2.0$ with a 40% difference with experiments.

Although only one paper described the CHT analysis on a film cooled leading edge, several papers have analyzed conjugate simulations for internal and film cooled turbine blades. However, the lack of appropriate experimental data and the high computational cost result in a small number of papers.

The main experimental reference is Hylton et al. (1983, 1988), who conducted experiments on the C3X vane. Hylton et al. (1983) focused on an internally cooled vane, whereas Hylton et al. (1988) also included film cooling on the C3X NASA vane, but the film cooling did not include a showerhead configuration around the leading edge. Morerover, comparisons with experiments were limited to downstream locations since Hylton et al. (1983; 1988) did not provide any data upstream of the coolant holes. Coolant supply conditions for the 1988 C3X vane were not available in open literature and limited the accuracy for comparison. The experimental data did only refer to centerline data. Several computational studies have conducted a conjugate heat transfer analysis on the C3X NASA vane, and these are reviewed below.

Laskowski et al. (2008) predicted the metal temperature on the internally cooled vane and film cooled vane with the k-ω turbulence model. The interest of this study was to include the entire blade flow domain with the plenum and the coolant holes. The metal temperature for the no film cooling case was in good agreement with the experimental data. The pressure side was well matched, whereas the suction side presented a 10% discrepancy where the transition occurred, with higher values from the numerical simulation than for the experiments. The simulated heat transfer coefficients on the suction side for the internally cooled 1983 C3X vane were higher than the experimental measurements with a maximum discrepancy of 100% at the boundary layer transition. The pressure side was well predicted within 15%. For the film and internally cooled 1988 C3X vane, only the metal temperature was predicted. The cooling mass flow boundary conditions, which were missing in the recorded experimental data, were obtained by an inverse procedure. The cooling mass flow boundaries were varied until the simulation predicted the correct external surface temperature, starting with the conditions from the internally cooled 1983 C3X vane as a starting point. The simulated metal temperature was predicted within the experimental uncertainty except some points just downstream of the thermal barrier on the pressure side. Laskowski et al. (2007) also simulated the augmentation heat transfer coefficient h_f/h_0 on the internally and film cooled NASA C3X vane. The wall heat transfer coefficient was defined in agreement with the experiment.

The freestream temperature was the driving temperature, whereas in this thesis, the adiabatic wall temperature was chosen for the driving temperature. The external metal temperature was specified to match the experimental data and plenum walls were assumed isothermals. It was found that the predictions of the external heat transfer coefficient were generally 30-50% lower than measured values just downstream of the film cooling holes locations for both the pressure side and the suction side. Farther downstream from the hole location, the simulated heat transfer coefficients were accurately predicted on the suction side, whereas a 50% discrepancy was still observed on the pressure side.

Luo and Razinski (2007) employed the V2F turbulence model with conjugate heat transfer to predict the metal temperature and heat transfer coefficients of the internally cooled vane of Hylton et al. (1983). The V2F turbulent model differs from the two-equation models by solving an additional transport equation for $\overline{v}^2$.Three different Reynolds number were investigated. A primary analysis compared the V2F code with the k-ε turbulence model and quadratic k-ε turbulence model. These two last models predicted the heat transfer coefficient on the pressure side within 10% but showed 50-100% higher external heat transfer coefficient than measured values on the suction side. The authors believed that anomalous generation of turbulent kinetic energy were generated near the stagnation line due to the existence of large rates of strain. The V2F was able to predict accurately heat transfer coefficients on the pressure side. Furthermore, the V2F model gave better heat transfer coefficient results on the suction side than the two other turbulence models studied, with 35% higher values than the measured values.

Leylek and York (2003) used the conjugate numerical methodology to predict the metal temperature of the C-3X vane with no external film cooling. The standard k-ε model and the realizable k-ε model were compared. This was a simulation of Hylton et al. (1983) experimental test. The simulation was validated comparing the aerodynamic loading curves and the midspan temperature distribution on the vane external surface. The realizable model agreed well with experiment with less than 10% difference in overall effectiveness with the experimental data for midspan temperature distribution on the vane external surface. No predictions of external heat transfer coefficients were presented.

Kusterer et al. (2004) conducted CHT simulations of a turbine vane with internal serpentine circuit and film cooling holes at different hot gas conditions. Experiments were performed at KHI Gas Turbine R&D Center to provide data for external surface temperature for comparison to results for the CHT analysis. Surface temperatures measurements were obtained with thermal index paint. Due to the complexity of the configuration, two different conjugate calculations were run, one focusing only on the leading edge model and another one deleting the leading edge supply channel. The authors claimed good agreements with the experimental data for the surface temperature, especially in the region with high thermal load at the blade tip. However, only thermal profiles with a very coarse colorbar were used for comparison. According to Kusterer et al. (2004), the lack of precise inlet boundary conditions for the real flow was responsible for discrepancies between experimental and computational results. The authors also stressed that results were extremely sensitive to the leading edge cooling configuration.

Medic and Durbin (2002) developed a CHT analysis for a film-cooled blade geometry that was compared to experimental data of Camci and Arts (1985). The geometry consisted of an entire blade with coolant holes and plenum. Two rows of shaped holes were located on the suction side. The holes were inclined at 37º and 43º. The pressure side had only one row of shaped holes inclined at 35º. The k-ω, the standard k-ε model, the modified k-ε with a bound on turbulent time scale (T-bound), and the V2F turbulence models were investigated. This study focused on the prediction of the external heat transfer coefficients. Unlike this thesis, the heat transfer coefficient, h, was based on the freestream temperature; therefore the heat transfer coefficient was actually a measure of the heta flux. Several blowing ratios were run. Numerical results showed that the T-bound k-ε and V2F turbulence models gave reasonable results for the heat transfer coefficients except close to the holes, whereas the standard k-ε model predicted heat transfer coefficients 100% higher than Camci's test. On the pressure side, the T-bound k-ε model gave similar results than the experiments with less than 5% of discrepancies with experimental data at M = 1.75. The suction side was correctly predicted within 15% except close to the stagnation line at M = 1.0. The predictions of heat transfer coefficient for the V2F model on the pressure side were 50% lower than experimental values, which were attributed to a stronger lateral spreading than the T-bound k-ε turbulence model.

Stronger spreading caused lower heat transfer coefficients since the jet protected the surface from the hot ambient air.

Other conjugate analyses were conducted (Mazur et al., 2006, Heidmann et al., 2000) but no experimental data were available in open literature to validate their simulated results.

CHT analysis gave reasonable predictions of the metal temperature within 15% (Terrell et al, 2004, Laskowski et al, 2008). However, the predictions of heat transfer coefficient using CHT were consistently 30%-50% lower than measured values for film cooling configuration, especially in the vicinity of the holes. Also, none of these studies was concerned by the heat transfer predictions on the specific location of the leading edge. It should be recalled that none of the experimental studies recorded all the data required for the simulation, which might explain disparities between simulation and experiment. In this thesis, the key point is that all the experimental conditions required to predict accurate heat transfer coefficients were provided, since the experiments and the simulations were conducted in the same laboratory, the Turbine and Turbulence Cooling Research laboratory.

1.2.4 Computational Heat Transfer Coefficient without Film Cooling

Numerous experimental of heat transfer over a stationary circular cylinder have been conducted. However, a few simulations were run to validate these experiments.

Contrary to the film cooling case, good agreement was found between computation and experimentation on the heat transfer coefficient without film cooling h_0.

Zhang et al. (2008) studied an immersed boundary method to predict the Nusselt number on the surface of a cylindrical cylinder in cross-flow at a low Reynolds number. Their simulated data were compared to experimental data of Eckert et al. (1952) and also numerical results of Momose and Kimoto (1999) and Bharti et al. (2007). Momose and Kimoto (1999) used a Fredholm type boundary integral and Bharti et al. (2007) implemented a finite volume method on a Cartesian grid system. All results were conducted at low Reynolds number in the range as $10 < Re < 250$. Although these Reynolds numbers were much lower than used for turbine airfoil, this study was still interesting since it showed that the disparities between the constant heat flux and isothermal conditions could be accurately simulated. Zhang et al. (2008) were able to reproduce Bharti's results for the isothermal and iso-heat-flux conditions. These results were achieved at low Reynolds number, where the vortex structure in the wake was steady. At larger Reynolds number ($Re > 50$), simulated data of Zhan et al. (2008) predicted well the experimental data of Eckert at $Re = 120$, contrary to the higher Reynolds number of 218, for which the prediction was within 10% at the stagnation line. However, Momose and Kimoto (2007) predicted well Eckert's experimental results close to the stagnation line within 1% on error but predicted 15% higher Nusselt number after the separation region. This was attributed to the difficulty to predict the vortex shedding created at high Reynolds number.

Also, several studies have been conducted with RANS simulations. Szczepanik et al. (2004) ran the standard k-ω model, as well as a modified k-ω model with the integration of a limited criterion to limit the turbulence viscosity μ_t close to the stagnation point. Results were compared to Scholten and Murray (1998). Steady state results for the Nusselt number distribution were also compared to unsteady simulations which were time averaged over a single vortex shedding period. Unsteady simulations were conducted to a high Reynolds number of 21,580. A constant wall temperature was imposed. The standard k-ω turbulence model was found to consistently predict higher Nusselt number than the experiment due to abnormal high levels of turbulence kinetic energy k at the stagnation line. At the stagnation line, the Nusselt number was over-predicted by 100% by the standard k-ω turbulence model. The modified k-ω turbulence model agreed well with experimental data within 5% of uncertainty. The unsteady simulation gave slightly better results than the steady one in the stagnation region (< 5% improvement).

Surprisingly, only York and Leylek (2002) studied the simulation of heat transfer for a leading edge model with no film cooling. The same conditions as the film cooling leading edge, described earlier, were used. Results were given in the form of the Frossling number $Fr = Nu/Re^{0.5}$. The computation predicted a higher lever of Frossling number. On the stagnation line, the simulated Fr was 1.05 compared to the experimental number of $Fr = 0.83$ for Yuki. Leylek and York (2002) believed that the laminar boundary layer was not caught by the turbulence model. The discrepancy is now attributed to the data of Yuki, who used a quarter-cylinder instead of the half-cylinder simulated by Leylek and York (2002). Indeed, Mouzon (2005) conducted a similar heat transfer experiment with a half-cylinder and found $Fr = 1$ at the stagnation line. Contrary to the cylinder, leading edge simulations do not show the typical drop close to the rear region, which results in much higher heat transfer coefficient values after 90 º.

In summary, except for the standard k-ω turbulence model, computations conducted on the heat transfer coefficients on either a cylinder or a leading edge without film cooling gave accurate results with a maximum of 5% discrepancy.

Other results for the heat transfer coefficients were found on the complete blade model. In the absence of film cooling, the realizable k-ε turbulence models tend to predict higher heat transfer coefficient on the suction side (Laskowski et al. (2008), Luo and Razinski (2007)). According to Medic and Durbin (2002), this was due to anomalous production of turbulent energy at the stagnation line inherent to the model. Laskowski et al. (2008) attributed the discrepancies to the transition, not well predicted by the code. The use of SST turbulence model including a one equation transition model improved significantly the simulated results.

1.2.5 Computational Predictions of Heat Transfer Augmentation

Few simulations predicting heat transfer augmentation h_f/h_0 have been conducted on the film-cooled leading edge. Although Terrell et al. (2004) ran a CHT simulation; they did not investigate heat transfer coefficients. No CHT analysis with a focus on heat transfer coefficients has been published for a film-cooled leading edge. The only open literature studies on film cooled leading edges used adiabatic models.

York and Leylek (2002) conducted heat transfer analysis on a turbine airfoil leading edge model with experimental data of Yuki (1998). The leading edge model matched Yuki's geometry. One row of holes was centered on the stagnation line and two off-stagnation rows were at ± 25º. Four blowing ratio were run (M = 0.75, 1.0, 1.5 and 1.9) at a density ratio of DR = 1.8. The realizable k-ε turbulence model from FLUENT was selected with the enhanced wall function to accurately predict the heat transfer coefficients. The enhanced wall function solves the flow conditions close to the wall. The authors imposed a constant heat flux of $q'' = 1250$ W/m^2, because it resulted in approximately the same averaged surface temperature as the experiment. Computational predictions of the contours of h_f/h_0 were significantly different than the experimental data. At $M = 1.5$, the code predicted a large region of high h_f/h_0 ($h_f/h_0 = 3$) directly after the off-stagnation hole, whereas the experimental data showed $h_f/h_0 = 2$. Moreover, the area between two stagnation holes showed computed valued of $h_f/h_0 = 1.0$ whereas the experimental h_f/h_0 reached 1.6 at the same location. Also, the computation predicted, regardless of the blowing ratio used, a region of very high h_f/h_0 values at the leading edge of the off-stagnation hole, which was not observed in the experimental measurements of Yuki (1998). Although significant discrepancies were observed for the contours of heat transfer augmentation, the simulated laterally averaged heat transfer augmentation $\frac{\overline{h_f}}{h_0}$

gave reasonable results, predicting the right trend except at the stagnation line. The laterally averaged heat transfer augmentation $\frac{\overline{h_f}}{h_0}$ was significantly lower at the stagnation line, and higher at $x/d = 4$, compared to the experimental data. The simulation predicted that the higher values of the heat transfer augmentation was located at $x/d = 4$ at any blowing ratio, whereas the experimental data suggested that the highest value was on the stagnation line, except at $M = 0.75$. The simulation predicted values up to $h_f/h_0 = 1.8$ for the higher blowing ratio. Simulated and experimental values were between $h_f/h_0 = 1$ and $h_f/h_0 = 1.8$. As the blowing ratio increased, the discrepancies grew. Several solutions might explain the discrepancy between computation and experiment: a lower lateral spreading of the jet and an inability to predict jet separation for the k-ε turbulence model, which was mostly used for heat transfer coefficient prediction. However, the issues were never clearly resolved.

Rozati and Tafti (2008) employed the Large Eddy Simulation (LES) technique to predict external heat transfer coefficients. LES is a time dependent model, much more complicated than FLEUNT. The computational domain was adopted from an experimental study of Ekkad et al. (1998). The geometry consisted of a cylindrical leading edge with a 30 ° angle of injection. Two rows of holes were located at ± 15 °. A constant heat flux was imposed. The study quantified the heat transfer coefficients; adiabatic effectiveness and coolant-mainstream interaction at three different blowing ratios Rozati and Tafti (1998) presented their results using the non-dimensional Frossling number $Fr = Nu/Re^{0.5}$. Contours of Fr were not compared to experimental data. However, the abnormal very high region on the leading edge of the off-stagnation hole observed in the RANS model was not observed with the LES model. The laterally averaged Fr was presented from 20 º to 70 º at a blowing ratio of M = 0.4, 0.8 and 1.2. Simulated $\overline{Fr}$ was found within the uncertainty of Ekkad's experimental results at low blowing ratios, M = 0.4 and M = 0.8. The blowing ratio of M = 1.2 still gave acceptable results compared to experimental data with a maximum difference of 10% about 1.5 d downstream of the coolant hole.

LES simulation proved to be better than RANS simulations. Indeed, contours of heat transfer augmentation showed two regions of high h_f/h_0 values at the leading edge of the off-stagnation hole, whereas the experimental data presented only one region of high h_f/h_0 values. LES simulations agreed better with the experimental data, since they also showed one region of high Fr values. However, due to the complexity of the LES model, the RANS model was selected.

1.2.6 Experimental Measurement of the Influence of the Thermal Boundary Layer

No papers were found on heat transfer experiments using a conducting leading edge with no blowing. Most experiments on heat transfer coefficient measurements are conducted by applying a constant heat flux at a density ratio of unity or with the transient liquid crystal method. If the thermal boundary layer has a negligible effect compared to the hydrodymanic boundary layer, the heating process should not influence the heat transfer coefficient measurement. Studies of heat transfer from cylinders in cross flow have been widely reported, which gave a thorough insight to the heat transfer analysis on leading edge due to the similarity of their shapes.

Eckert et al. (1952), Papell (1981), Scholten and Murray (1997) analyzed heat transfer coefficient and thermal boundary conditions influence on cylinders. Data and results were presented in terms of the Frossling number or the Nusselt number. In all cases, the heat transfer maximized at the front stagnation line and decreased to a minimum value at an angular distance around the cylinder, corresponding to the laminar separation region. After the separation region, an increase in heat transfer coefficient was observed due to the high turbulence intensity of the flow in the wake of the cylinder. The Reynolds number did not affect the Frossling number until the separation region. The higher the Reynolds number was, the sooner the separation region occurred and the higher the heat transfer coefficient was in the rear region. Mills (1999) studied the variation of the local heat transfer coefficient around an isothermal cylinder in a cross-flow. A drop of the Frossling number up to 0.2° at 90° was observed at $Re = 5320$, and this drop reached 0.4° at 70° at the much higher Reynolds number of 70,800. Also, Papell (1981) revealed different results for the iso-heat-flux and isthermal conditions. The two curves showed that the Nusselt number was similar at the stagnation line but around 60 °, the iso-heat-flux showed a higher Nusselt number, which indicated a better convective-heat-transfer with iso-heat-flux boundary conditions.

Authors who conducted heat transfer experiments on leading edge with film cooling, also studied the experimental heat transfer augmentation with no blowing. Yuki (1998), Mouzon (2005), Ou and Rivir (2001) are some of these studies. Yuki used a quarter cylinder with a suction slot to adjust the approach flow and place the stagnation line at the desired location. Yuki (1998) did not find the well accepted Frossling number of unity at the stagnation line. The use of a quarter cylinder did not simulate the real geometry, and considerably affected the boundary layer at the stagnation line. Indeed, Mouzon (2005) conducted the same experiment with a half cylinder and found the Frossling number of unity, characteristic of the cylinder data at the stagnation line. Mouzon (2005) found that the distribution of *h* was similar to a cylinder up to 60 º away from the stagnation line. Beyond 60 º, the flat after-body part of the model considerably affected the heat transfer coefficient. The heat transfer coefficient was augmented by 100% with the flat-part body adjustment. These results were consistent with that found by Ou and Rivir (2001). Also, the Reynolds number did not influence the Frossling number. Less than 5% of difference were involved in a range of Reynolds number from 30, 000 to 100,000. However, turbulence intensity considerably affected the heat transfer coefficient. Mouzon (2005) indicated an increase of 25% of the Frossling number factor when the turbulence intensity of the approach flow was 10% instead of 0.5%.

In summary, papers on heat transfer coefficient around a cylinder or a leading edge have been widely reported. All studies found the same trend for the Frossling number with the value of unity at the stagnation line, when the mainstream had low turbulence levels. Interestingly, these papers indicated that measurements on heat transfer coefficient at constant wall temperature did not engender the same results than the constant heat flux condition for $x/d > 6$. It was reasoned that the temperature distribution on the leading edge surface affected the heat transfer coefficient. This emphasizes the importance to run a conducting leading edge model with no film cooling since a conducting model is neither at constant wall temperature nor constant heat flux.

1.2.7 Experimental Study of Heat Transfer Coefficient Augmentation

Several studies have been done at the Turbulence and Turbine Cooling Research Laboratory (TTCRL) on the measurement of heat transfer near the leading edge of a turbine airfoil.

Yuki (1998) focused on the heat transfer coefficient using a quarter cylinder described above. One row of hole was positioned at the stagnation line and the other one at 25º. The model was designed with a 20 º injection angle. Yuki limited his study to low turbulence intensity ($Tu = 0.5\%$) at a Reynolds number of 65,000. Density ratio was one to reduce uncertainty. Heat transfer foils were set up on the model. The heat flux distribution was uniform except close to the holes, since the amount of current passes through the holes within a smaller area. The heat transfer coefficient augmentation was found 20% and 50% higher between the two rows of holes at $M = 0.8$ and $M = 1.9$, whereas downstream of the off-stagnation line, the heat transfer coefficient augmentation was 40% and 60%, at respectively $M = 0.8$ and $M = 1.9$. Yuki also observed that the heat flux was significantly reduced between the two rows of holes, whereas after $x/d > 8$, the blowing did not affect the heat load. Johnston (1999) pursued Yuki's work using a high turbulence intensity of 17%. The heat transfer coefficient augmentation turned out to be twice as low as Yuki's. This was due to the heat transfer coefficient with no blowing $h0$, which is really sensitive to the turbulence intensity (30-50% higher compared to the low Tu case). Johnston (1999) indicated a heat transfer augmentation of 1.1 between the holes at $M = 1.5$ and $Tu = 17\%$. The highest value of h_f/h_0 was obtained at $x/d = 5$. The heat transfer coefficient augmentation finally decreased from 1.3 to 1.1 downstream of the holes. Increasing mainstream turbulence level diminished the effect of blowing on the augmentation of the heat transfer coefficient, because of the change in h_0. At $Tu = 17\%$, the heat transfer coefficient h_0 was 25% higher than at $Tu = 0.5\%$, however, h_f at $Tu = 17\%$ was also 15%-40% higher than at the lower turbulence intensity.

Mouzon (2005) also complemented Yuki's study by using a half cylinder instead of a quarter cylinder. The simulated leading edge incorporated shaped holes. The same geometry was conserved with now two rows of holes located at ± 25 º, and the stagnation row of holes. To palliate the non-uniform temperature distribution between the holes, two separate foils were used. The Reynolds number was 32,000 and two turbulence intensities were maintained: $Tu = 0.5\%$ and $Tu = 7\%$. Mouzon presented his results using the Frossling number and the heat transfer coefficient augmentation. The Frossling number was always included between 0.75 and 2.5 for both turbulence intensities at the four blowing ratios examined, $M = 0.5, 1.0, 1.5, 2.0$. At $M = 2.0$, just downstream of the coolant holes, the Frossling number reached the highest value of 2.5 and decreased up to Fr = 1.0 at x/d = 12. For $M > 1.0$, it is interesting to notice that the low and high Tu are the same in terms of Fr. At M = 2, the heat transfer augmentation at the high turbulence intensity reached 30%-40% between the holes, decreased up to 25% at x/d = 10 to finally increased up to 35% at x/d = 12. At Tu = 0.5, h_f/h_0 was 60-80% between the holes, and decreased from 90% at x/d = 4 to 60% at x/d = 9 before increasing up to 220% at x/d = 12. These variations were mainly due to the change in h_0. As the boundary layer was already turbulent due to the coolant injection, h_f was less sensitive to the mainstream turbulence intensity. Therefore, the change in the ratio h_f/h_0 at higher Tu is dominated by the variation of h_0 from low to high turbulence.

Although Mouzon (2005) and Yuki (1998) did not use the same geometry, comparison was done between the two studies. It was found that the shaped holes showed a slight increase in heat transfer coefficient augmentation compared to the round holes configuration. However, the variations in h_f/h_0 for both analyses were in the same range, i.e. between 0.75 and 2.5. Johnston (1999) also gave similar values than Mouzon (2005) for h_f/h_0, although Johnston (1999) conducted experiments on cylindrical holes at a much higher turbulence intensity (Tu = 17%). The values for both studies differed by no more than 20%, which was imputed to the different holes configurations and turbulence intensities.

Mehendale and Han (1992) carried out several experiments on leading edge heat transfer. They used an array of embedded thermocouples. The geometry consisted in four rows of holes, two located at ± 15 º and two at ± 40 º. The main difference compared to the current study was the absence of film coolant holes on the stagnation line. The cylindrical holes were inclined by 30 º in the spanwise direction. Mehendale and Han (1992) focused their study on the influence of mainstream turbulence intensity on heat transfer coefficient. A constant heat flux was applied through heat transfer foils attached to the surface. Holes were cut in the foil and the foils were electrically connected by copper bars in series. Three different blowing ratio were investigated from $M = 0.4$ to $M = 1.2$. For low Tu ($Tu = 0.75\%$), $M = 0.4$ performed better regarding of the heat load reduction downstream of the holes but did poorly between the holes. The authors attributed this to the small amount of coolant ejected from the first row of film holes as compared to the second row of holes at such a small blowing ratio. They also found that the Frossling number near the holes increased with blowing ratio, while the performance decreased with higher blowing ratio downstream of the holes. For high maisntream turbulence intensity ($Tu = 10\%$), the blowing ratio had less impact. The Frossling number was also seen to rise up to 15% as the turbulence intensity increased, with the most significant effect at the middle blowing ratio tested, $M = 0.8$. For all blowing ratios, there was a lower heat transfer coefficient region between the two rows of holes. As Mouzon (2005), the values of the Frossling number varied from $Fr = 1.0$ to $Fr = 3.0$, with a peak in heat transfer coefficient at the holes location.

Ou and Rivir (2001) conducted experiments on a model, which was very similar compared to the current study. A circular leading edge with two rows of holes at ± 21.5 º and one row at the stagnation line was used. The holes were inclined with a 20 º angle to the spanwise direction and 90 º with the streamwise direction. Two different mainstream turbulence intensity of *Tu* = 1.2% and *Tu* = 20.2% were operated. The Reynolds number were set up to *Re* = 30,000 and *Re* = 60,000 and blowing ratios from *M* = 1.0 to 2.5. The distribution of heat transfer coefficients were obtained by the transient liquid crystal. Downstream of the holes, the Frossling number was slightly affected by turbulence at the low Reynolds number with a highest dissimilitude of 20% at *M* = 2.5. At high Reynolds number, the main difference between the two turbulence intensity occurred between the holes, where a 50% increase of the Frossling number was shown at *M* = 1. At *M* = 2.0, the Frossling number reached the value of 4.0, close to the holes location and went down to 1.0 far away from the holes (*x/d* = 10).

The measurement of heat transfer coefficients on a film-cooled leading edge has already been done in the past. The results discussed above have been obtained from two different experiments: the constant heat flux method and the transient liquid crystal technique. They both saw a peak of very high *Fr* values at the off-stagnation hole. Surprisingly, papers showed significant disparities among them. At *M* = 2.0, Mouzon (2005), Yuki (1998), Johnston (1999) and Mehendale and Han (1992) predicted a range of laterally averaged Frossling number between 0.75 and 3, whereas Ou and Rivir (2001) found a maximum value of $\overline{Fr}$ = 4.0 at the same blowing ratio. However, downstream of the holes location (*x/d* = 10), all experiments found that laterally averaged *Fr* converged towards the same value of unity. Moreover, all studies showed a peak in the laterally averaged Frossling number just downstream of the holes. Also, the $\overline{Fr}$ trend was similar for both methods, with a lower value between the two holes and a constant decrease downstream of the holes. It should be noticed that both experiments present issues: the constant heat flux applied is done at DR = 1.0 and does not represent the surface temperature distribution seen on a real conducting model, while the transient technique assumed a semi-infinite solid 1-D assumption, which is not often valid on models with strong radius curvature as the leading edge.

1.3 OBJECTIVE

This thesis had two major objectives. The first purpose of this thesis was to evaluate the accuracy of the CHT simulation to predict the surface temperature for a film cooled turbine blade leading edge model. This was accomplished by comparing the numerical predictions with experiments using a high conductivity model by Maikell (2008) and using a low conductivity model (adiabatic) model by Davidson and Dyson (2009). Two different film cooling configurations were studied. The first configuration consisted of one row of holes centered on the stagnation line. The second configuration had two additional rows located ± 25º from the stagnation line. The external heat transfer coefficients were also of interest in this thesis because the correct prediction of h_f was critical to predict the correct external surface temperature. This thesis also studied the validity of the assumption that the driving temperature for heat transfer is the adiabatic wall temperature. This was done by comparing the heat flux using T_{aw} as the driving temperature and the heat flux obtained from the CHT simulation.

The second objective of this study was to experimentally measure the cooling of a simulated turbine blade leading edge with no film cooling, i.e. with only internal impingement cooling. This was done to provide a reference case to gain a better understanding of the additional cooling provided when film cooling was added to the model. Two sets of experiments were conducted on a non-film cooled leading edge. Internal and external heat transfer coefficients were calculated from 1-D conducting analysis. Heat flux gauges were also used to confirm external heat flux values obtained from the 1-D conducting analysis. The influence of mainstream turbulence intensity on overall effectiveness was also investigated.

Chapter 2: Numerical Simulation of a Film Cooled Turbine Leading Edge

2.1 INTRODUCTION

Recently, Harrison (2006) indicated that the adiabatic wall temperature as the driving temperature was a poor assumption in some locations since conjugate heat transfer (CHT) effects were not taken into account. To address this issue, recent experimental studies have used high conductivity models, which match the Biot number of the engine, and therefore match the normalized temperature, ϕ, of the engine.

The primary objective of this study was to determine the accuracy of computational simulations, using CHT analysis, of the film cooling performance of a conducting model of a turbine blade leading edge that had been experimentally tested by Maikell (2008). The conducting model of Maikell (2008) was designed to match the Biot number for engine conditions, $Bi = 1.8$. Their experimental study used two leading edge film cooling configurations, one with a single row along the stagnation line, and the other with three rows of holes. A key aspect of this study was that all the experimental conditions needed to establish accurate boundary conditions were provided since the experiments and the simulations were conducted in the same laboratory (the Turbulence and Turbine Cooling Research Laboratory).

All the simulations discussed in this study are summarized in Table 2.1.1.

Table 2.1.1: Summary of the numerical simulations

Simulation name	Simulation Description	*DR*	*M*	# of rows	Results
S.1.a	Constant heat flux experiment without film cooling	N/A	N/A	N/A	h_0, Fr
S.1.b	Temperature boundary condition without film cooling	N/A	N/A	N/A	h_0, Fr
S.2.a	Adiabatic leading edge model with film cooling	1.5	1.0 2.0	1 row 3 rows	η, T_{aw}
S.2.b	Near-adiabatic leading edge model with film cooling (k = 0.48W/mK)	1.5	1.0 2.0	3 rows	η, T_{aw}
S.3.a	Conducting leading edge model with film cooling, $Bi = 1.8$	1.5	1.0 2.0	1 row 3 rows	ϕ, q''_{cond}, h_f/h_0
S.3.b	Conducting leading edge model with film cooling, $Bi = 0.44$	1.5	2.0	3 rows	ϕ
S.3.c	Conducting leading edge model with varying T_{plenum}	1.5	2.0	3 rows	ϕ
S.3.d	Conducting leading edge model with change in internal wall temperature boundary condition	1.5	2.0	3 rows	ϕ
S.3.e	Conducting leading edge model with film cooling without impingement plate	1.5	2.0	3 rows	ϕ
S.4	Adiabatic- Constant heat flux simulations with film cooling	1.0	1.0 2.0	3 rows	q''_{pred}, h_f/h_0

Simulations were conducted on a leading edge model with no film cooling (S.1.a – S.1.b) to determine the reference non filmed cooled heat transfer coefficient, h_0. A simulation was run to determine the adiabatic wall temperature distribution at $DR = 1.5$ (S.2.a). As explained in chapter 1, experiments are typically conducted on a near adiabatic model. Therefore, a CHT simulation was done using the very low thermal conductivity of the near-adiabatic material used for the experiment (S.2.b) to better match the experimental conditions of Davidson and Dyson (2009) than with an adiabatic model.

Then, the material thermal conductivity was changed to match the Biot number of Maikell's (2008) experimental conducting model. The wall temperature distribution was found using the CHT simulation from FLUENT (S.3.a). It is important to recognize that the experiments were done with an impingement plate, which was not included in the simulation. However, the effect of the impingement cooling was accounted for in the computational simulation by using the experimentally measured internal surface temperatures as a boundary condition for the computational simulation. By using the experimentally measured internal wall temperature as a boundary condition, the computational simulations were simplified, and also removed the issue of whether the internal impingement cooling was being correctly simulated.

Several other simulations were run varying different parameters, such as the Biot number, Bi (S.3.b), the plenum temperature, T_{plenum} (S.3.c), as well as the internal wall temperature (S.3.d). These simulations were conducted to determine the sensitivity of these different parameters. The influence of the impingement plate was determined by running a simulation with no impingement plate (S.3.e). The internal surfaces for the solid and the fluid were coupled, i.e. the convective heat transfer related to the fluid was equal to the conducting heat transfer in the solid at the internal wall. Finally, to simulate experiments used to determine heat transfer coefficient, a simulation was done using a constant heat flux boundary condition applied to the external surface (S.4). This was done at a unity density ratio since experimental data were obtained at DR = 1.0 due to the difficulty of obtaining accurate results at high DR. The computations conducted in this thesis are summarized in Table 2.1.1 as well as the outputs resulting from these simulations.

The secondary objective of this thesis was to determine if T_{aw} is the appropriate driving temperature for heat transfer for leading edge film cooling. As far as the author knows, no study in the past has evaluated the assumption of T_{aw} as an accurate heat transfer driving temperature on a leading edge model. Harrison (2006) limited her analysis to a flat plate. A comparison was done between the conducting heat flux, q''_{cond}, and the heat flux that the adiabatic wall temperature, T_{aw}, and heat transfer coefficient, h_f, predicts, q''_{pred}. The adiabatic wall temperature obtained from (S.2.a), the wall temperature from the conducting simulation (S.3.a) and the heat transfer coefficient from the constant heat flux simulation (S.4) were combined to obtain q''_{pred}, defined by Equation 1.1.4.1. The predicted heat flux and the heat flux obtained from the conjugate analysis were compared to determine how well the adiabatic wall temperature predicted the heat transfer that is expected to actually occur.

2.2 COMPUTATIONAL SETUP AND PROCEDURE

The geometry was first meshed with Gambit, a mesh generation software that is part of the FLUENT package. Then, the computational dynamic software FLUENT was used to run the simulations. This CFD code is based on finite volume method.

2.2.1 Description of the Model

The main purpose of this thesis is to compare the simulations obtained with measurement values. The geometry of the leading edge was then generated based on the physical model of Maikell (2008). The simulated blade leading edge model had a round leading edge with a diameter of 50.8 mm. As shown in the schematic of the mesh in Figure 2.2.1.1, the leading edge thickness was 12.7 mm.

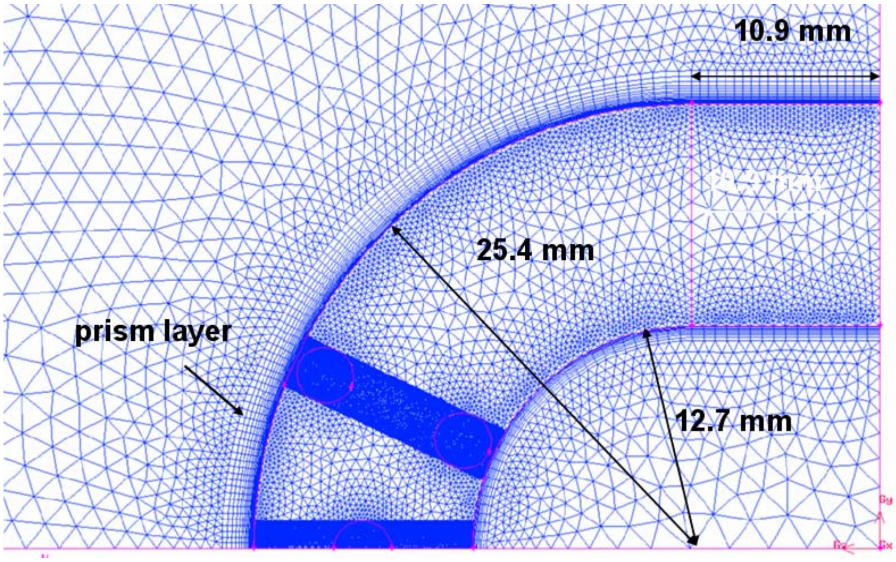

Figure 2.2.1.1: Mesh of the 3 row leading edge model

Two different film cooling configurations were employed. The first configuration consisted of one row of holes centered on the stagnation line. The second configuration had two additional rows located ±25° from the stagnation line. The coolant hole diameter was d = 3.15 mm. The holes were oriented radially, i.e. with a 90 ° compound angle. The model was designed with a 20 ° injection angle, as seen in Figure 2.2.1.2. Two different blowing ratio were investigated, M = 1.0 and M = 2.0. The density ratio was set to DR = 1.5. The Reynolds number matched Maikell's experiment of Re = 48,500.

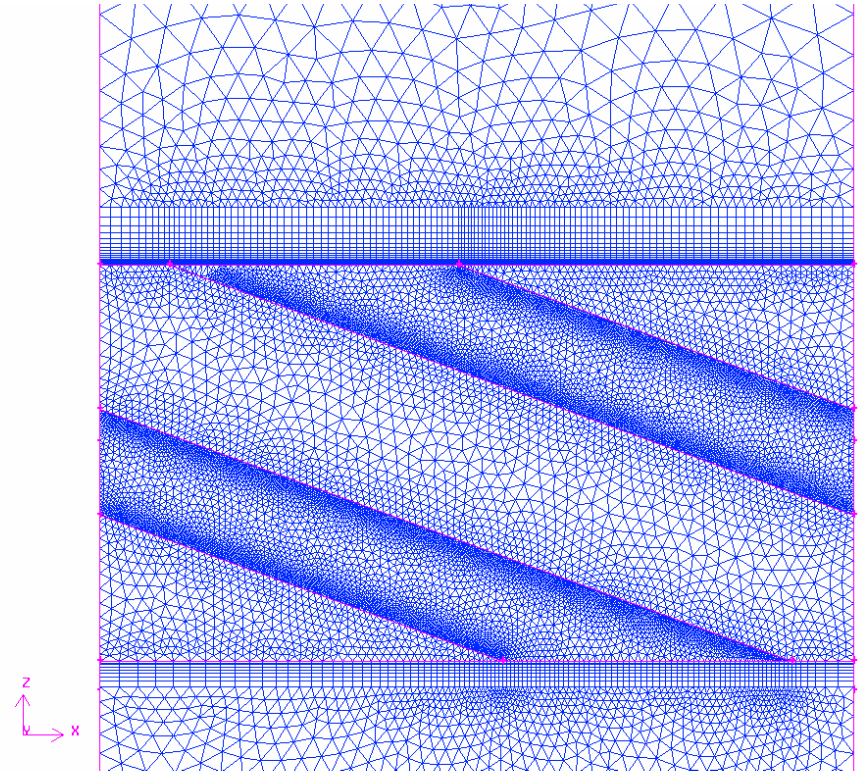

Figure 2.2.1.2: Mesh of the symmetry plane

The computational domain, shown in Figure 2.2.1.3 simulated the leading edge model including the plenum, the coolant holes and the wind tunnel test section. Indeed, Walters and Leylek (1997) suggested that better results would be obtained if the simulated model incorporates as many details as possible. Using realistic conditions such as including a plenum versus an inlet tube for injection was critical to obtain accurate results. Thus, the plenum and the coolant holes were included. Several attempts were first conducted to mesh the domain with hexahedral cells, since hexahedral meshing is known to deliver more accurate results. However, the complexity of the domain with sharp angles and strong curvature generated high skewed hexahedral cells and the FLUENT software was unable to run simulations with such high skewed cells. Thus, three-dimensional tetrahedral meshes were created with Gambit. To prevent high skewness and obtain high quality grid, two successive cells could differ by no more than 20%. A prism layer was also attached on the external surface of the leading edge to approximate a $y+$ value of 1 to accurately solve the viscous sublayer. The final mesh consisted of 4,236,174, where half of the cells were contained in the prism layer and the coolant holes.

To save computational time, periodic and symmetry conditions were applied to simulate rows of film cooling holes. The side walls were defined as periodic boundaries, spaced by the coolant hole pitch distance of p/d = 7.6. A symmetry boundary condition was applied at the symmetry plane. In all simulations, a no-slip condition was imposed at the top of the wind tunnel, while an adiabatic wall boundary was set up for the downstream end of the leading edge model.

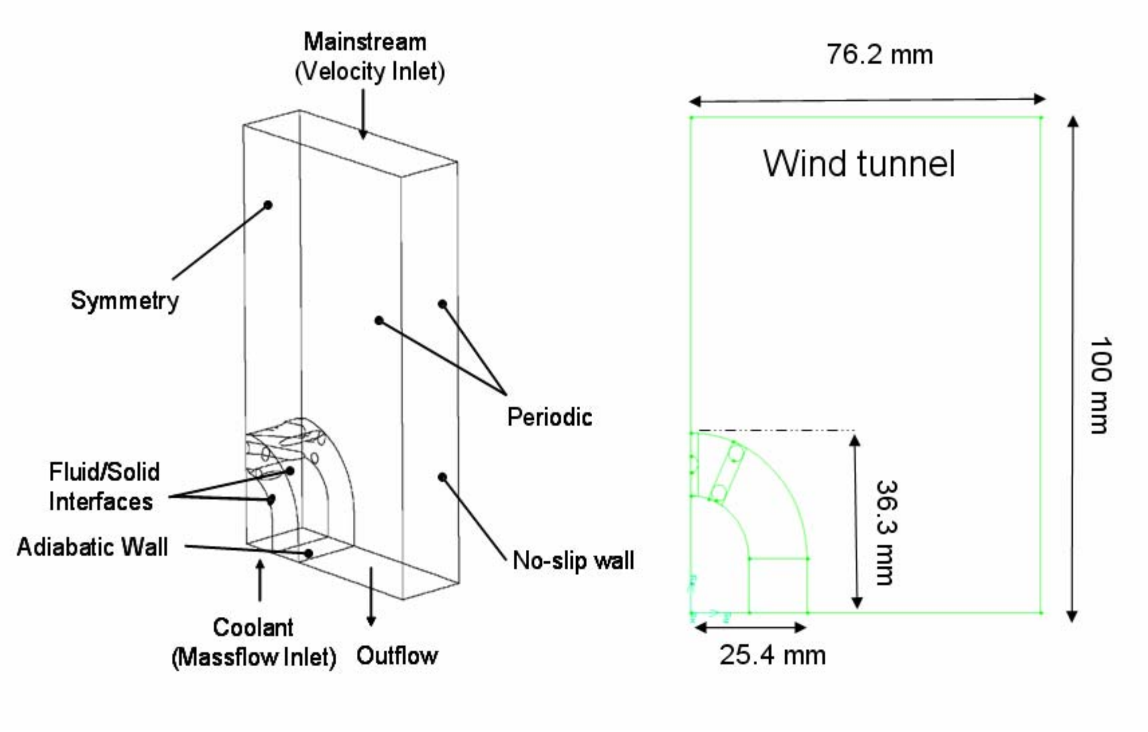

Figure 2.2.1.3: Computational domain of the CFD leading edge model (from Terrell, 2004)

The realizable k-ε turbulence model was selected due to its superior performance in predicting heat transfer coefficient in open literature over other models. Indeed, York and Leylek (2002) found in two separate papers that the realizable k-ε turbulence model gave better results than the standard k-ε turbulence model for adiabatic effectiveness and heat transfer coefficients predictions for film-cooled leading edge. The two layer enhanced wall treatment function was preferred since resolution into the viscous layer was required to achieve accurate heat transfer coefficient predictions. Harrison (2006) indicated that the realizable k-ε turbulence model gave the best prediction of h_f/h_0 for a flat plate with film cooling. Also, Ferguson et al. (1998) predicted that the enhanced wall treatment function better caught the separation along the centerline. The FLUENT manual advocates the use of the realizable k-ε turbulence model when favorable pressure gradients are involved. The simulations were run with the node-based, segregated, steady-state and implicit solver. The criteria were solved using a second order scheme.

Special attention was paid on the boundary conditions to match the experiments of Maikell (2008). The simulated boundary conditions are summarized in Table 2.2.1.1. The temperature of the tunnel mainstream was always 300K and the velocity of the approaching flow was 15m/s. The plenum temperature was 200K to obtain the correct density ratio of $DR = 1.5$. The coolant velocity was varied to match the blowing ratio of $M = 1.0$ or $M = 2.0$. The coolant turbulence intensity was not measured and presumed to be 6% with an arbitrary integral length scale of 9.5mm whereas the tunnel turbulence intensity was 4% with a mainstream integral length scale of 19mm, measured by Maikell (2008). Since there were large variations in air temperatures in these simulations, air properties were set up to vary with temperature, based on Mills' data.

Table 2.2.1.1: Operating parameters for the computational simulation

Mainstream velocity (m/s)	15
Mainstream temperature (K)	300
Mainstream turbulence (%)	4
Mainstream Integral length scale (mm)	19
Coolant temperature (K)	200
Coolant turbulence (%)	5
Coolant Integral length scale	9.5
Thermal conductivity (W/mK)	1.6

For the adiabatic case, the solid was deactivated in order to save computational time since no equations needed to be solved inside the solid. For the conducting case, the conjugate heat transfer analysis was employed and the solid was included in the simulation. The coupled function allowed solving simultaneously the convection heat transfer and the conduction occurring in the solid. Some adjustments were implemented for the conducting case as opposed to the adiabatic case. For the flow into the internal plenum, a boundary layer profile with an arbitrary displacement thickness of $\delta/d = 1$ was used adjacent to the plenum wall. The boundary layer profile was created to prevent any temperature discontinuity between the solid and the fluid.

The approximate integral method was employed to obtain the velocity profile at the plenum inlet. The boundary layer was assumed laminar. The velocity profile was represented by the equation 2.2.1.1:

$$\frac{u}{u_e} = \frac{3}{2}\frac{y}{\delta} - \frac{1}{2}\left(\frac{y}{\delta}\right)^3 \tag{2.2.1.1}$$

where δ is the edge of the hydro-dynamic boundary layer and u_e is the velocity outside the boundary layer. The velocity u_e was selected to have the appropriate mass flow rate.

The blowing ratio was also checked at the end of the simulations. The density and the velocity were obtained at the exit of the holes. An averaged blowing ratio of $M = 1.0$ and $M = 2.0$ was found. However, as shown in Table 2.2.1.2, the blowing ratio for the stagnation row is lower than for the off-stagnation row.

Table 2.2.1.2: Actual blowing ratio through each row

Averaged M	Stagnation	Off-stagnation
M=1.0	0.89	1.05
M=2.0	1.95	2.03

The major difference between experiment and simulation came from the impingement plate, which was not included in the simulation. As explained in the introduction, the impingement plate should have a negligible effect on the adiabatic film effectiveness simulation. Indeed, the dynamic effects are not taken into account when the impingement plate is not simulated. But, the length of the hole was long enough so that nay effect at the entry of the hole would be lost at the exit of the hole. Therefore, the impingement plate was not an issue for the adiabatic model, unlike the conducting model. For the conducting case, the thermal effects of the impingement plate were taken into account by artificially simulating it. This was done by using the internal surface temperatures experimentally measured by Davidson and Dyson (2009) as a boundary condition for the CFD simulations. Thermocouples were used to measure the internal surface temperature at eight different locations: 0º, 12.5º, 25º, 35º, 45º, 57.5º, 70º and 90º. A trend line for the internal temperature profile was generated based on these eight data points. The symmetry condition imposed a zero slope at the stagnation line. Also, a constant temperature was imposed on the internal surface for the flat part of the leading edge. This constant value was the one measured at 90º. The internal temperature profiles measured and prescribed are presented in Figure 2.2.1.4 for the two blowing ratios simulated, $M = 1.0$ and $M = 2.0$.

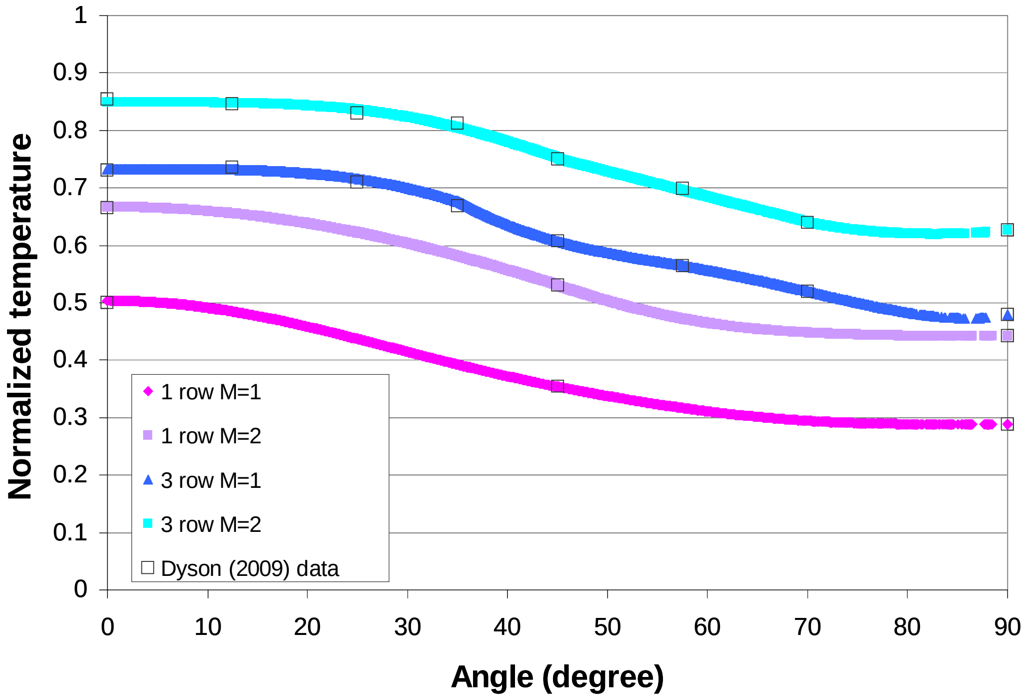

Figure 2.2.1.4: Internal surface temperatures (normalized) measured and used as the internal wall boundary condition.

By using the experimentally measured internal wall temperature as a boundary condition, the computational simulations were simplified and also removed the issue of whether the internal impingement cooling was being correctly simulated. However, in the actual leading edge mode, the impingement cooling causes an increase in coolant temperature before it enters the coolant holes. This increased coolant temperature was measured by Terrell et al. (2004). The temperature at the entry of the hole was $T = 215$K at $M = 1$ and $T = 210$K at $M = 2$. An adiabatic boundary condition was imposed on the internal surface related to the fluid to prevent any heat transfer. Therefore, the plenum temperature was set up, to impose the correct temperature at the entry of the coolant hole, since no heat transfer inside the plenum was allowed. Thus, any discrepancies between the experiment and the simulation could not be attributed to the internal cooling since it was artificially imposed with the internal temperature and the coolant temperature at the entry of the holes.

All these boundary conditions were imposed in order to match Maikell's (2008) experiment. The uniqueness of these simulations lies in the fact that the author obtained all the experimental measurements that she needed to simulate the leading edge model.

2.2.2 Convergence

A few papers expressed the convergence criteria that they adopted to obtain convergence. Mazur et al. (2006) assumed that the convergence was reached when the residual for energy was 10^{-7} and the residuals for all other entities were below 10^{-4}.

Residuals are the ratio of the difference in two successive iterations to the first iteration. The author judged these criteria insufficient since residuals are defined by the difference of the results obtained for two successive iterations normalized by the difference obtained for the previous iteration. Clearly, if the initial guess of the results was much different that the converged values, the difference obtained for the first iteration would be large and the residuals would be artificially low even though the solution was not converged. In this thesis, the strict criteria used by Harrison (2008) were adopted since no particular study was done in this area. The residuals were kept below 10^{-9} for the energy and 10^{-7} for all other residuals. At convergence, the average temperature on the surface of the leading edge and the normalized temperature at the exit of the stagnation hole changed no more than 0.005% for at least 100 iterations. This position was selected because of the very large temperature gradient in this region.

Simulations on the adiabatic and conducting models were run at M = 1.0 and M = 2.0. The $y+$ values were approximately unity so that enhanced wall treatment could be correctly used. A small region close to the off stagnation row had $y+$ values slightly higher than unity.

Grid independence was established by comparing results with a refined mesh of 9,150,000 cells was created with higher resolution in the holes and the prism layer. Grid independence was established as shown in Figure 2.2.2.1 which presents the laterally averaged adiabatic effectiveness and overall effectiveness at M = 2.0 for the three row leading edge model. The only discrepancy between the current grid and the refined grid was localized at the holes and was small enough to be considered negligible. The final mesh consisted of 4,236,174 cells where half of the cells were contained in the prism layer and the coolant holes. The typical number of iterations required for convergence was 4,000 iterations for the adiabatic model and 8,000 iterations for the conducting model.

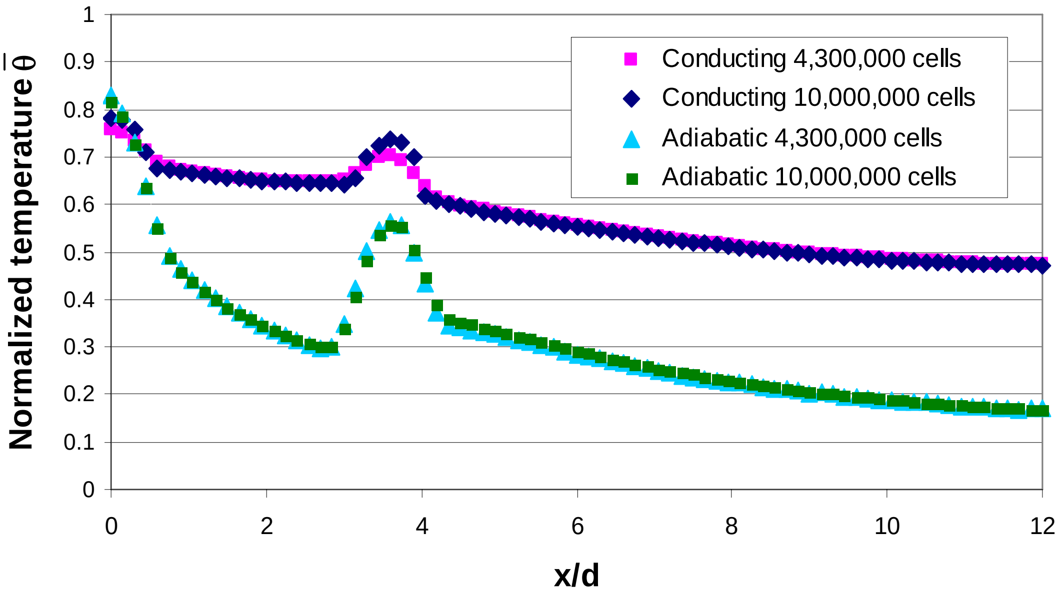

Figure 2.2.2.1: Validation of grid independence for the adiabatic and conducting model at *M* = 2.0, *DR* = 1.5

The grid independence was also checked for the no blowing case, which was a 2-D simulation. The no blowing cases were adapted separately since they had different geometries and therefore different meshes. Four different grids were simulated with the inclusion of a prism boundary layer. The difference between the grids was the height of the first cell attached to the wall, in other term *y+*. The smaller the height was, the better the resolution was. Table 2.2.2.1 indicates the characteristics of the four different prism layers.

Table 2.2.2.1: Characteristics of the four prism layers tested

	1st mesh	2nd mesh	3rd mesh	4th mesh
first cell (mm)	0.01	0.0075	0.005	0.0025
y+	0.60	0.45	0.3	0.15
growth factor	1.2	1.2	1.2	1.2
Number of rows	20	20	20	20
Prism layer size (mm)	1.87	1.4	0.93	0.47

Also, the prism layers were meshed so that the thermal and hydrodynamic boundary layers were included in the prism layer. The solution was considered grid independent since the results for the Frossling number changed by no more than 2.5% as shown in Figure 2.2.2.2.

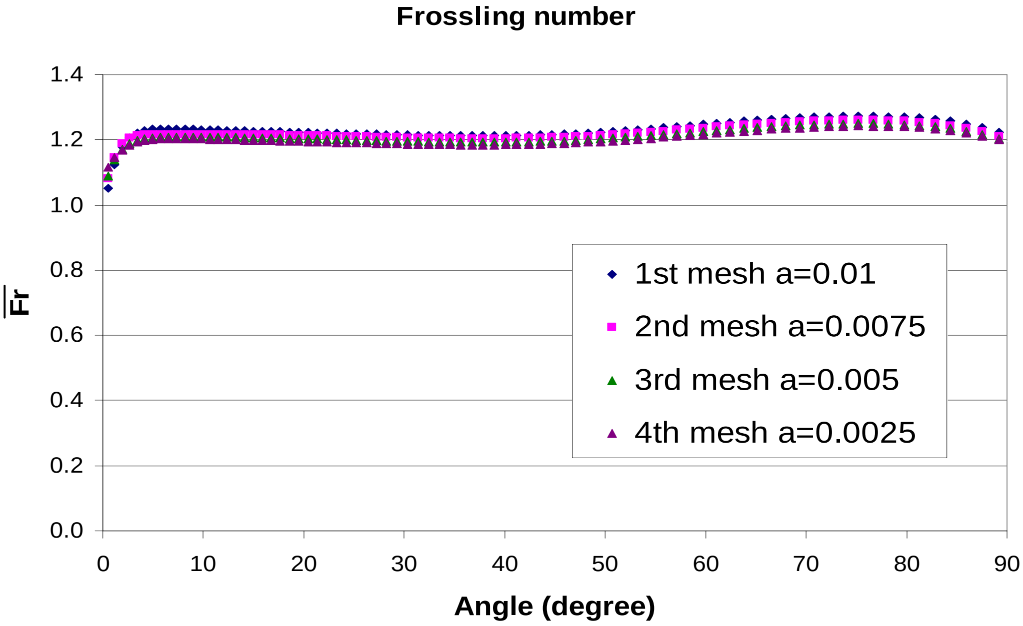

Figure 2.2.2.2: Validation of grid independence for the no blowing case

Chapter 3: Computational Results

The main focus of this study was to evaluate the accuracy of numerical simulations prediction of ϕ on a film cooled leading edge. The external heat transfer coefficients were also of interest because the correct prediction of h_f was critical to predict the correct external surface temperature. This chapter presents the results of adiabatic, constant heat flux and conducting simulations. All the simulated data were compared to experimental measurements to see how well the CHT analysis of the numerical simulations perform.

3.1 VALIDATION WITH EXPERIMENTS AND COMPARISON WITH OTHER COMPUTATIONS

In the following section, computational results for adiabatic effectiveness and overall effectiveness have been compared to experimental measurements using the three-row leading edge configuration. For the single row leading edge model, only overall effectiveness was experimentally measured. Computational predictions were compared to these measurements. Also, a few other simulations were included to offer a wider range of comparison. Finally, computational predictions of adiabatic effectiveness for the single row configuration are compared to the predictions for the three-row configuration to determine the interaction between the stagnation and off-stagnation rows of holes.

3.1.1 Predictions of Adiabatic Effectiveness for the Three Row Configuration

Simulated and experimental measurements of the spatial distributions of η are compared for a blowing ratio of $M = 1.0$ and $M = 2.0$ in Figures 3.1.1.1 and 3.1.1.2. For both blowing ratios, the general pattern of the η contours were similar for the computational predictions compared to the experiments. Although the profiles looked similar, there were distinct differences in some locations. At $M = 2.0$, the computational simulations show a greater lateral spreading of the coolant jets along the stagnation line than the experimental data. At the exit of the off-stagnation holes, the simulation predicted high values of $\eta > 0.9$, while the experimental measurements showed values $\eta < 0.8$. This disparity might be attributed to insufficient turbulent dispersion of the coolant in the predictions or to the separation of the coolant jet at the exit that is not fully captured by the computational simulations.

(a) Experimental data

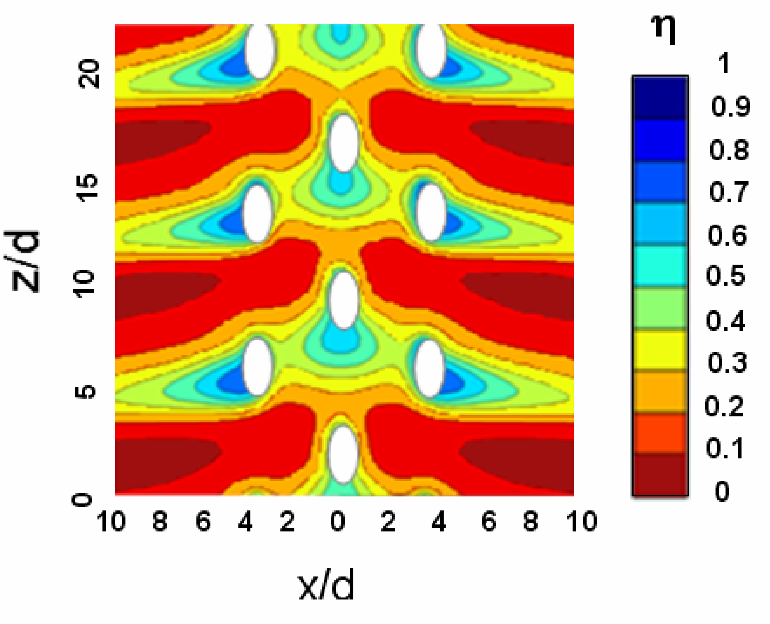

(b) Simulated data

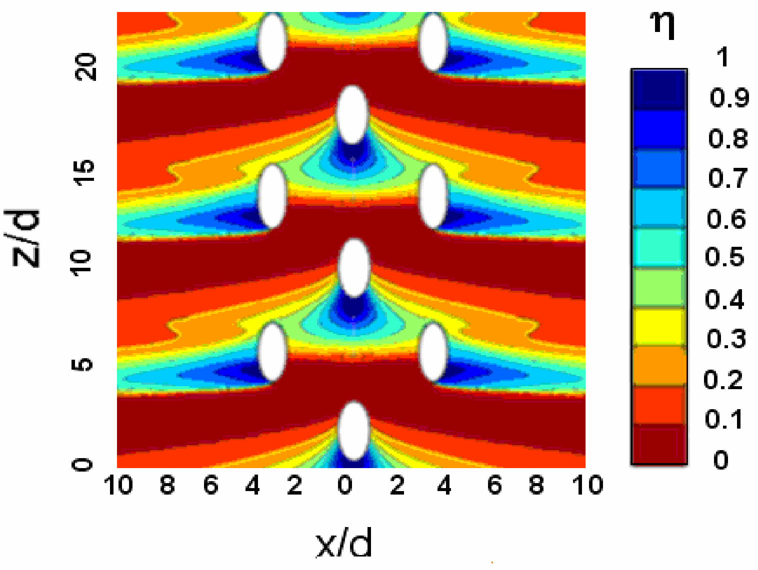

Figure 3.1.1.1 Contours of (a) experimental (from Davidson and Dyson, 2009) and (b) simulated adiabatic effectiveness at the blowing ratio of *M* = 1.0

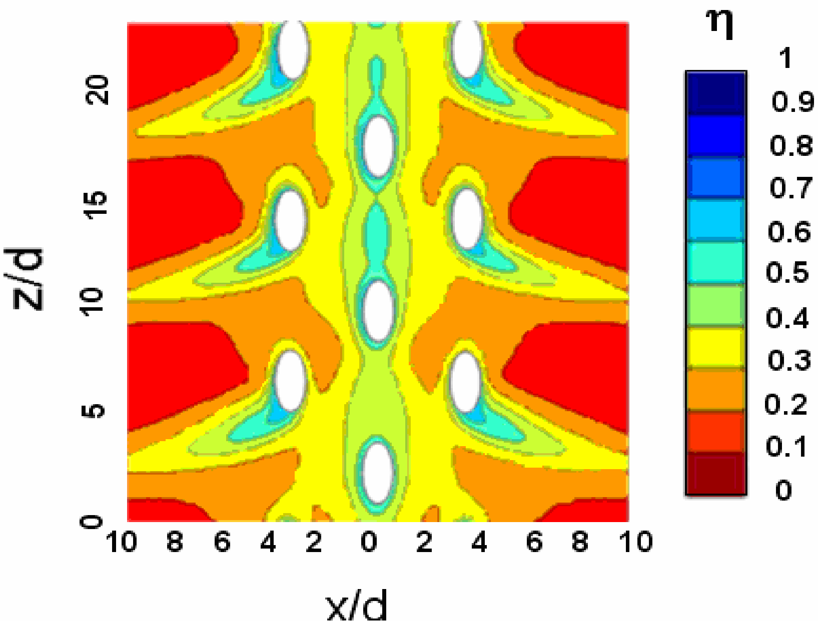

(a) Experimental data

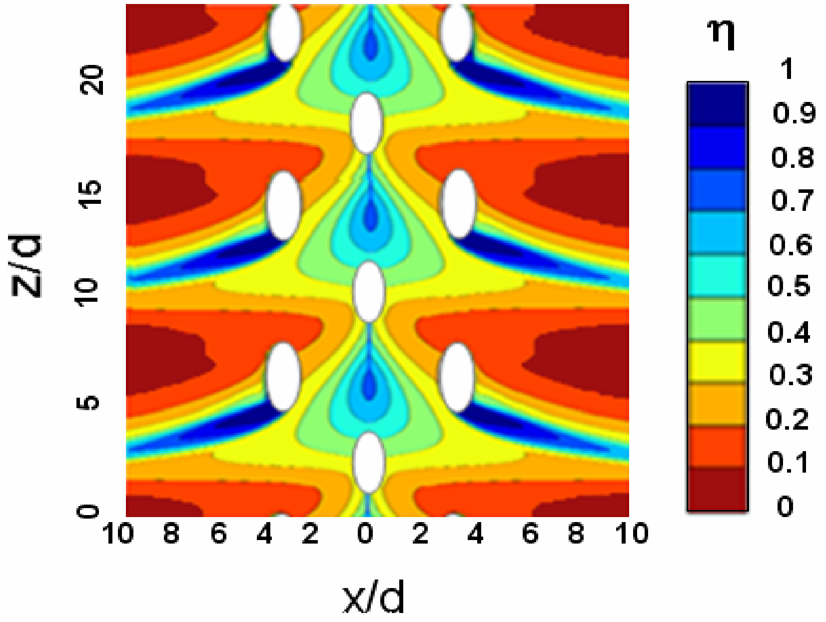

(b) Simulated data

Figure 3.1.1.2 Contours of (a) experimental (from Davidson and Dyson, 2009) and (b) simulated adiabatic effectiveness at the blowing ratio of $M = 2.0$

A cross section of the thermal profile at the exit of the off-stagnation is presented in Figure 3.1.1.3 for the three-row model at $M = 2.0$. It helps to visualize the trajectory of the jet at the exit of holes. Clearly, the jet did not separate since a high film effectiveness region of $\eta \approx 1$ is observed directly aft of the off-stagnation hole. For the experiment, there were much lower η values downstream of the exit of the holes, implying that the jet separated. The inability of the numerical simulation to predict the separation jet clearly affects the adiabatic effectiveness prediction.

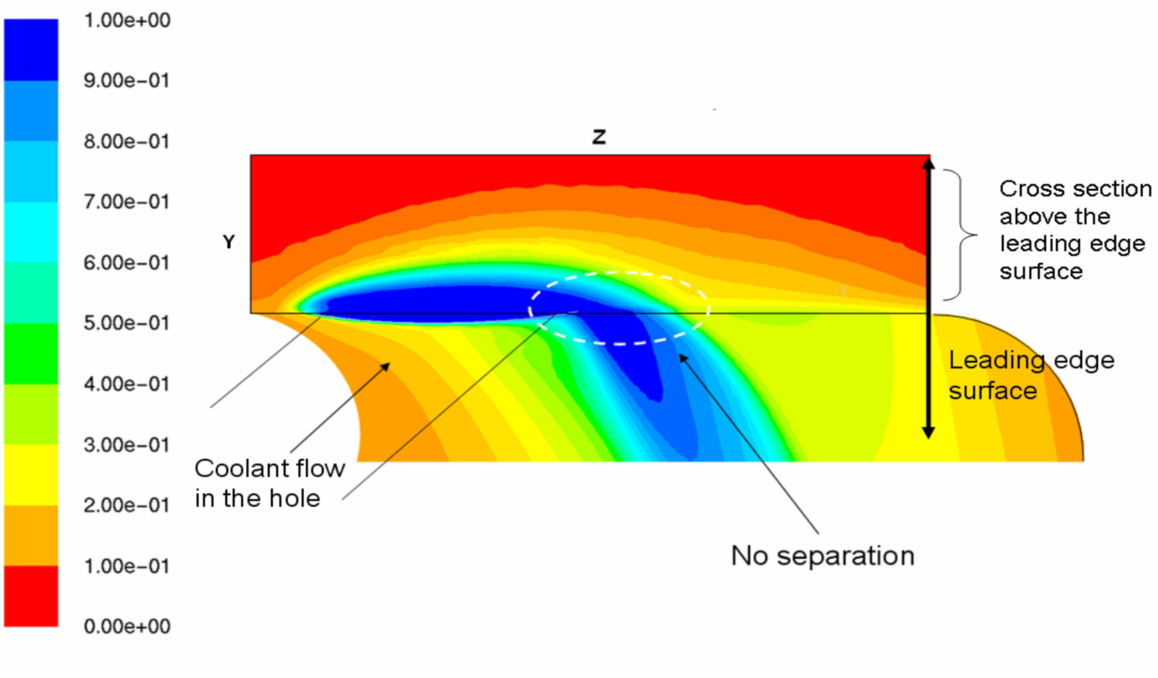

Figure 3.1.1.3 Contours of the leading edge surface at $M = 2.0$ and $x/d = 3.8$

Another difference between the computations and experimental measurements occurs for the $M = 1.0$ case where the experiments showed $\eta > 0.2$ along the stagnation line, but the CFD predictions showed $\eta < 0.1$ for a long region between holes. This discrepancy is partially explained by the conduction error for the experiments, since the holes are at a shallow angle to the surface. Indeed, the foam used for the experiment has a small thermal conductivity, which slightly affects the surface temperature. To address this issue, simulated computations were conducted using the low thermal conductivity of the experimental foam to perfectly match the experiments with the near-adiabatic model. The manufacturer reported a thermal conductivity of $k = 0.048$W/mK. The contours of the overall effectiveness with the low thermal conductivity are presented in Figure 3.1.1.4 for the blowing ratios of $M = 1$ and $M = 2$.

(a) *M*=1

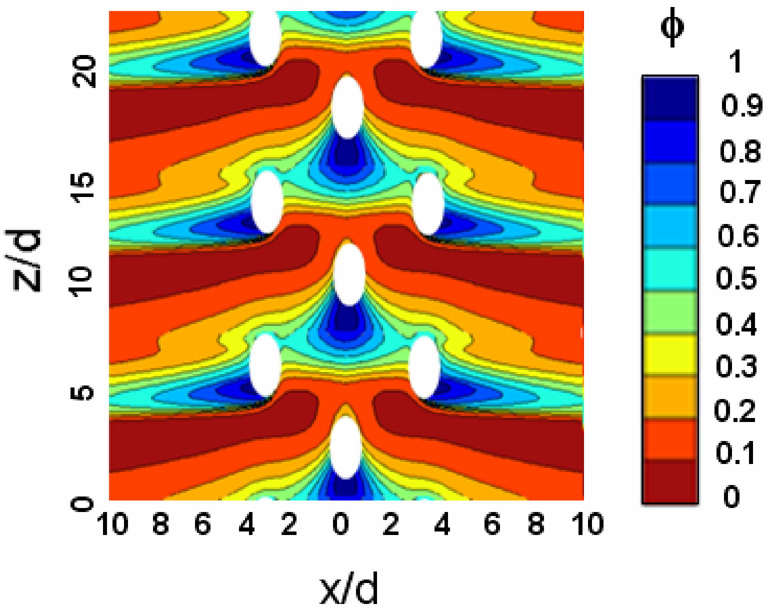

(b) *M*=2

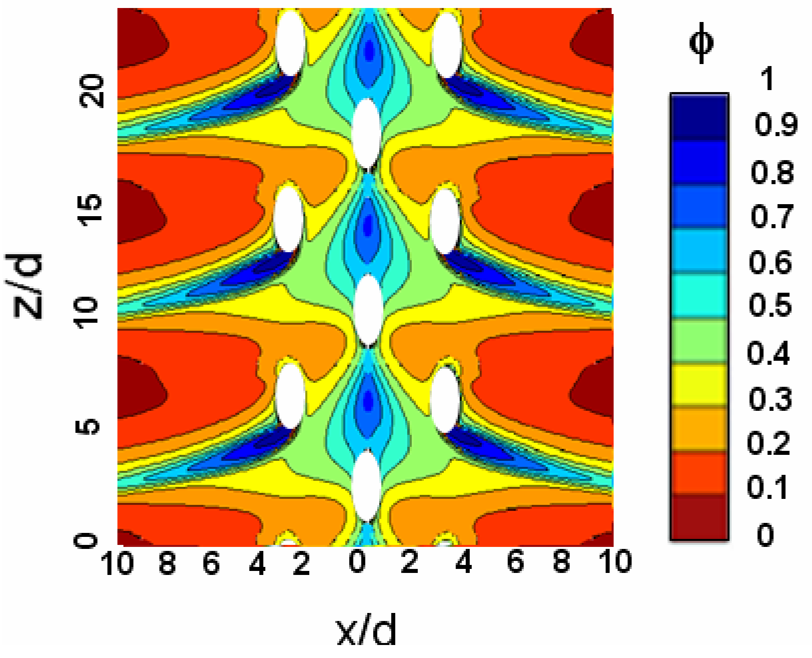

Figure 3.1.1.4 Contours of simulated overall effectiveness for the low thermal conductivity (k = 0.048W/mK) at the blowing ratio of (a) M = 1.0 and (b) M = 2.0

The simulations taking into account the thermal conductivity of the foam did not explain all the discrepancies between the experimental and the computational adiabatic predictions. However, at $M = 1.0$, conduction effect clearly affected the surface temperature resulting in a long region along the stagnation where $0.1 < \phi < 0.2$. The same region was observed for the experimental data; however for the experimental measurements, the magnitude of the normalized temperature was slightly higher with $0.2 < \phi < 0.3$. The small conduction effect started to slightly reduce the temperature gradients over the surface; however this effect was negligible for the three-row model at $M = 2.0$.

For the most part, the differences between the experimental measurements and the computational predictions were localized, and there was good prediction of the coolant distribution between the holes along the stagnation line and downstream propagation of coolant fluid.

Also, experimental and simulated data for laterally averaged film effectiveness, $\overline{\eta}$, were plotted at both blowing ratios of $M = 1.0$ and $M = 2.0$. Also, included are the results of the laterally averaged adiabatic effectiveness for the low thermal conductivity model. As shown by Maikell (2008), the process to determine the x/d location for these types of experiments was defined with an uncertainty of $\Delta x/d = \pm 0.3$. The experimental data were shifted by $x/d = 0.3$ so that the peaks of both the experimental and computational curves coincided at the same location, $x/d = 3.8$. The results, presented in Figures 3.1.1.5 and 3.1.1.6, showed a very good correspondence between computation and experiment. The reader should keep in mind that the comparison should be done between the experimental measurement and the simulation taken into account the thermal conductivity of the foam, since the simulation of the adiabatic three-row model does not exactly reflect the experiment. Downstream of the off-stagnation holes, the experimental and simulated curves collapsed at $M = 1.0$ given the uncertainty of the experimental data of $\Delta\theta = 0.03$. Concerning the blowing ratio $M = 2.0$ downstream of the off-stagnation holes, the computational predictions gave slightly higher η values than the experimental data. Between the holes, simulated predictions and experimental data for the laterally averaged adiabatic effectiveness differed by no more than 25% at $M = 2.0$ and 20% at $M = 1.0$. The main disparity occurred immediately after the stagnation hole. It is interesting to notice how the laterally averaged adiabatic effectiveness gave good agreement with experimental data, whereas plots of the contours of η clearly showed distinct discrepancies between experiment and computation. Overall, simulated data agreed fairly well the experimental measurements of η by Davidson and Dyson (2009).

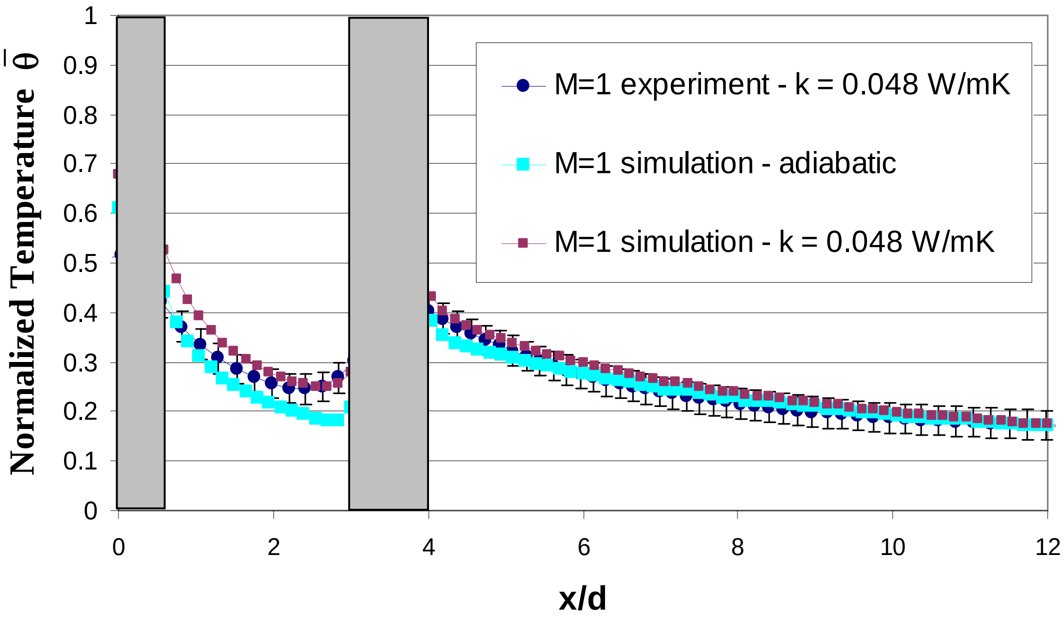

Figure 3.1.1.5: Comparison of laterally averaged normalized temperature for the CFD predictions and experimental data (Davidson and Dyson, 2009) at *M* = 1.0

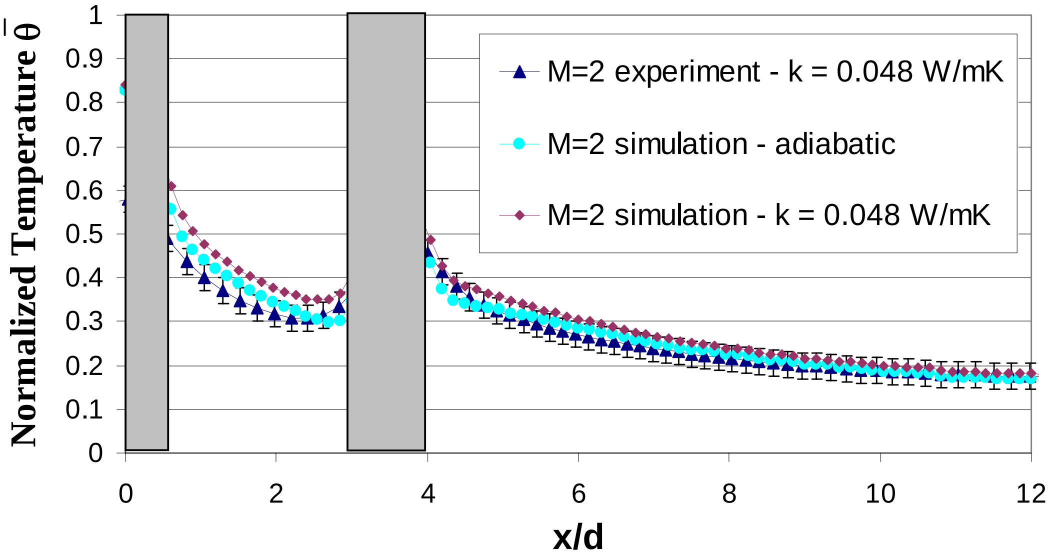

Figure 3.1.1.6: Comparison of laterally averaged normalized temperature for the CFD predictions and experimental data (Davidson and Dyson, 2009) at *M* = 2.0

When comparing experimental results for laterally averaged adiabatic effectiveness for M = 1.0 and M = 2.0, the two different blowing ratios collapsed to a single value at downstream location. Despite of the increasing blowing ratio, the laterally averaged adiabatic effectiveness neither decreased nor increased. This might be due to a balance between jet separation and increase of coolant from M = 1.0 to M = 2.0. This experimental oddity was also observed computationally with the laterally averaged adiabatic effectiveness plotted in Figure 3.1.1.7.

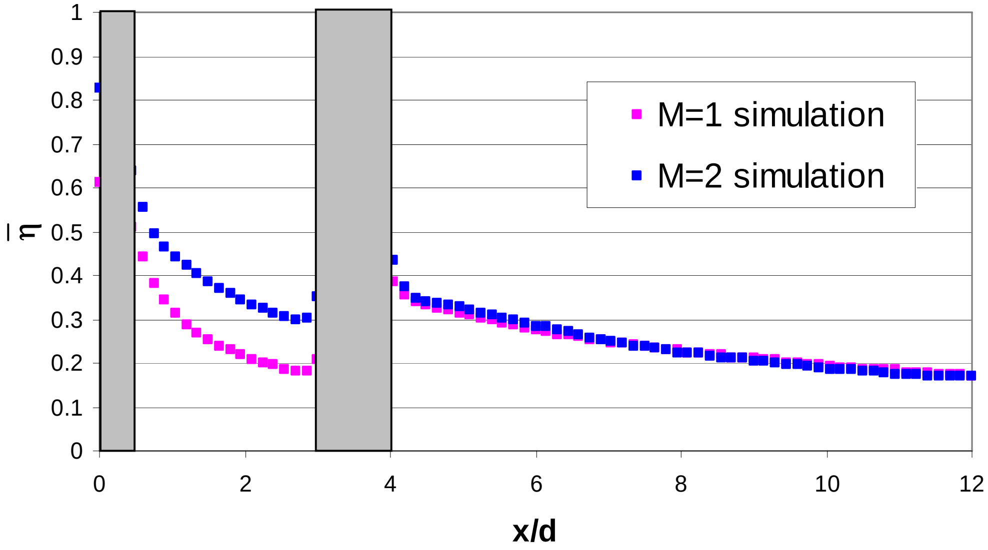

Figure 3.1.1.7: Comparison of laterally averaged normalized temperature for the CFD predictions at M = 1.0 and M = 2.0

The current computational predictions were compared to previous CFD predictions found in the literature for similar leading edge configurations. Several computations have been done in the past to predict the adiabatic effectiveness of the leading edge surface. The current simulation were compared to Martin and Thole (1997) and York and Leylek (2002), who both used FLUENT. They were selected since they proved to be the most accurate prediction of adiabatic effectiveness in the past. Although the same geometrical model was employed, inlet boundary conditions were different. Flow parameters for the various studies are presented in Table 3.1.1.1

Table 3.1.1.1: Flow parameters for various computational studies and experiments

Study	Grid Size (cells)	*DR*	*Re*	*Tu*	Tu model
Current study	3,000,000	1.5	48,000	4%	Realizable k-ε Enhanced wall treatment
Martin and Thole (1997)	200,000	1.8	32,000	0.5%	Standard k-ε
York and Leylek (2002)	3,600,000	1.8	32,000	0.2%	Realizable k-ε Enhanced wall treatment

All three studies used tetrahedral cells for their mesh. Moreover, York and Leylek (2002) and this current study used prism layers. Martin and Thole (1997) only investigated the blowing ratio of $M = 2.0$. Under the assumption that the density ratio has a small effect on adiabatic effectiveness, comparison was done with these two simulations even though they used a higher density ratio of $DR = 1.8$. The general patterns of Martin and Thole (1997) and the current study were almost identical as seen in Figure 3.1.1.8. Although the magnitudes of η were similar for both computational predictions, some distinct disparities were observed. At the stagnation line, the standard k-ε model, used by Martin and Thole (1997), did not predict separation region, which resulted in η values higher than $\eta = 0.9$ just downstream of the stagnation holes. Moreover, the coolant footprint of the off-stagnation row for Martin and Thole's (1997) simulation was different than the present study.

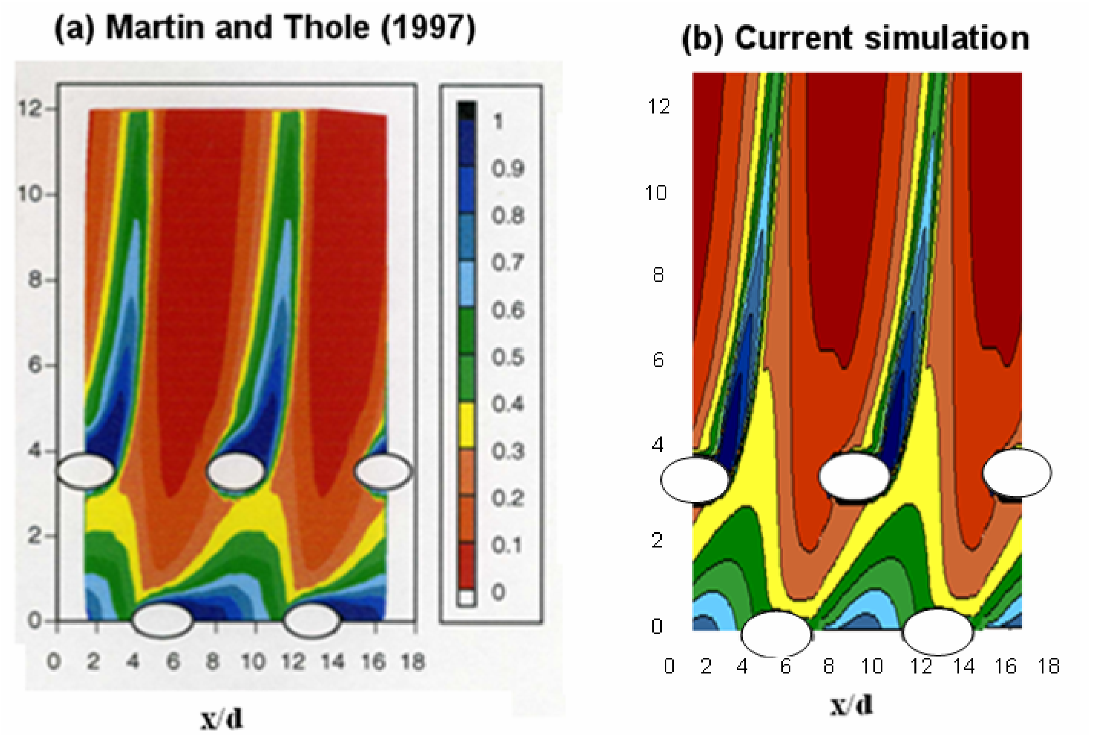

Figure 3.1.1.8 Comparison of the simulation of (a) Martin and Thole (1997) and (b) the current simulation for $M = 2.0$

The agreement with the simulation of York and Leylek (2002) was closer, as seen in Figures 3.1.1.9 and 3.1.1.10 for blowing ratios of $M = 1.0$ and $M = 2.0$, respectively.

For both blowing ratios, the contours of η were similar. However, the η values of the current simulation were lower than those of York and Leylek (2002). Thus, the current simulation matched the experimental values better than their simulation. At M = 2.0, York and Leylek (2002) predicted slight separation along the stagnation line and no separation for the off-stagnation holes, as the current computational simulation predicted.

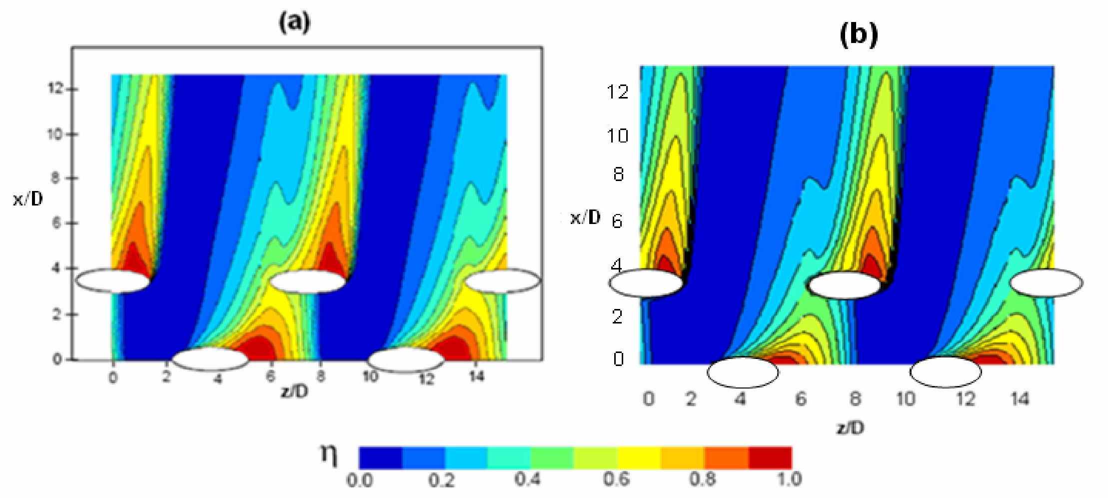

Figure 3.1.1.9 Comparison of the simulated contours of η of (a) York and Leylek (2002) and (b) the current simulation for M = 1.0

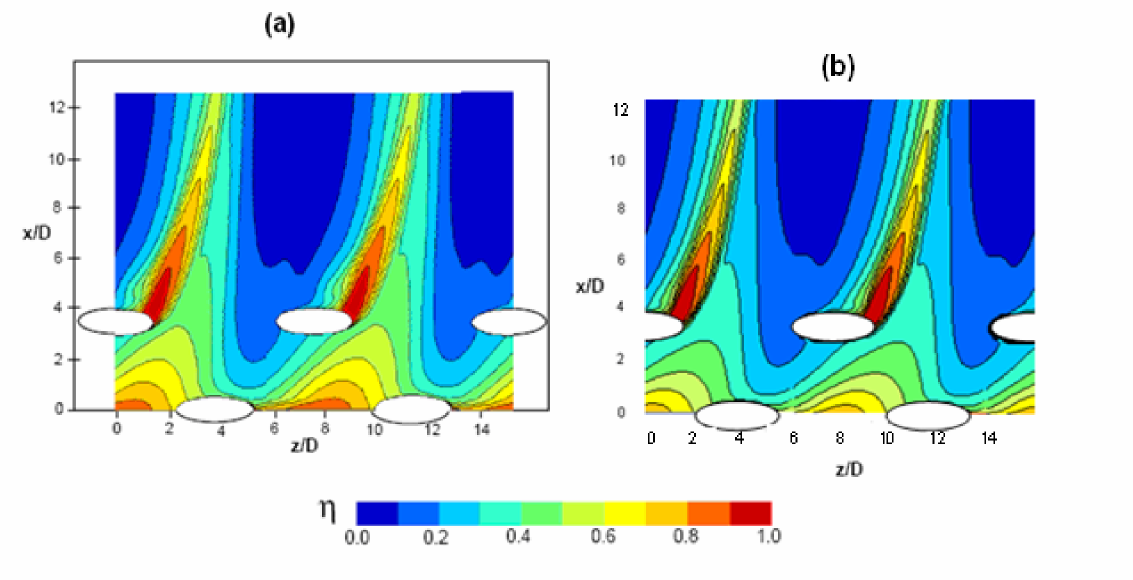

Figure 3.1.1.10 Comparison of the simulated contours of η (a) York and Leylek (2002) and (b) the current simulation for M = 2.0

The current simulation provided a noticeably better prediction of adiabatic effectiveness than the previous studies of Martin and Thole (1997) and York and Leylek (2002) to predict adiabatic effectiveness.

3.1.2 Predictions of Overall Effectiveness for the Three Row Configuration

The primary issue of concern in this thesis is the evaluation of the accuracy of numerical predictions of the overall film effectiveness. The experimental results were obtained in the Turbulence and Turbine Cooling Research Laboratory (TTCRL) using a high conductivity model with the same three-rows cooling hole configuration and using blowing ratios of M = 1.0 and M = 2.0. Contours of overall effectiveness, ϕ, for the CFD predictions and the experimental measurements are presented in Figures 3.1.2.1 and 3.1.2.2. For the M = 1.0 case, the computationally predicted ϕ distributions were very similar to the experimental measurements with the primary difference being lower ϕ values for the computational predictions between coolant jets. The contours of the computational ϕ values in Figure 3.1.2.1 showed a large region between the holes of $\phi >$ 0.5, which was not observed experimentally. Similarly, the numerical predictions of ϕ for M = 2.0 showed a continuous region of $\phi > 0.6$ along the stagnation line, whereas the experimental ϕ values were below $\phi < 0.6$. For both blowing ratios, the simulated computational overall effectiveness showed lower values than the experimental data after $x/d > 7$. Indeed, for the blowing ratio of $M = 2.0$, for $x/d > 7$, $\phi < 0.3$ for the computation and not for the experiment. This might be due to the impingement plate, which acts like a heat sink for the experiment. This was not taken into account in the simulation; in the simulation the boundary at the end of the leading edge was presumed to be adiabatic.

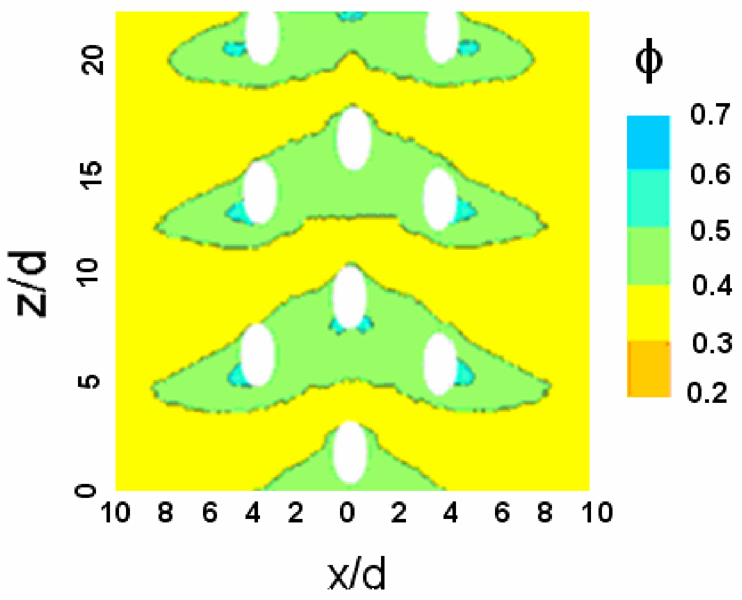

(a) Experimental data

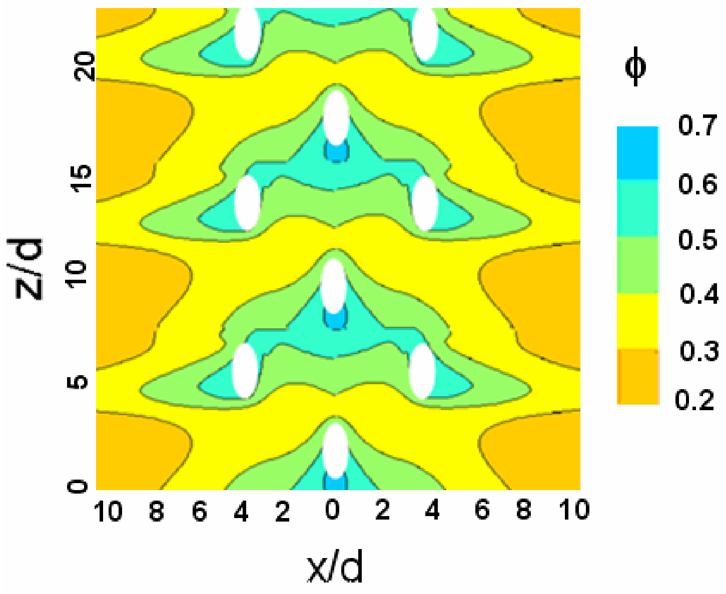

(b) Simulated data

Figure: 3.1.2.1. Contours of (a) experimental (Davidson and Dyson, 2009) and (b) simulated overall effectiveness at the blowing ratio of M = 1.0

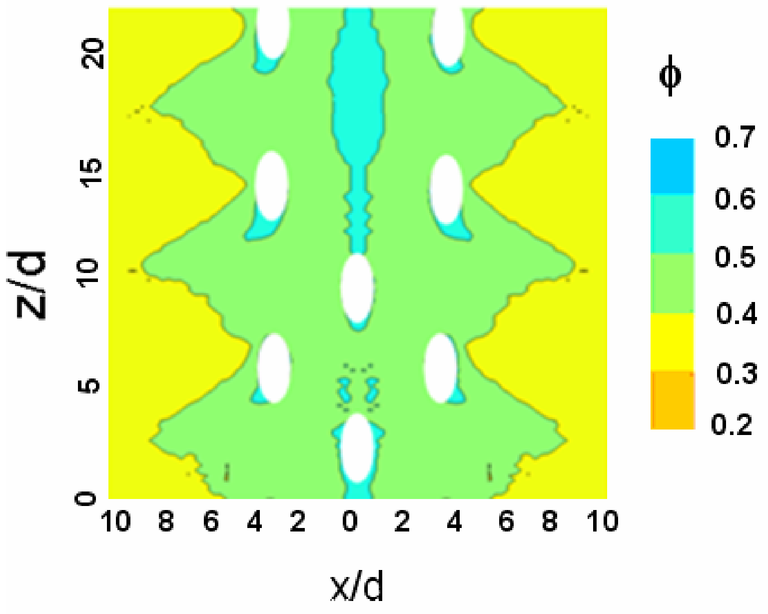
(a) Experimental data

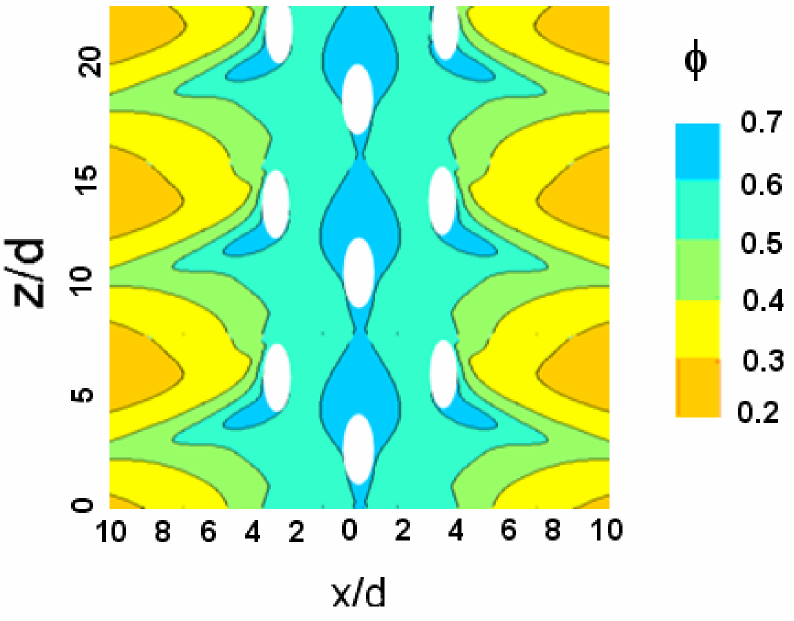
(b) Simulated data

Figure 3.1.2.2. Contours of (a) experimental (Davidson and Dyson, 2009) and (b) simulated overall effectiveness at the blowing ratio of M = 2.0

The results of overall effectiveness are also presented in terms of laterally averaged overall effectiveness, $\overline{\phi}$, in Figure 3.1.2.3 and 3.1.2.4 for both blowing ratios. Comparisons between the experimental data and the computational predictions revealed that for both blowing ratios, experimental $\overline{\phi}$ values were consistently lower than the simulated data between the stagnation row and off-stagnation row. Downstream of the stagnation row, the $\overline{\phi}$ values were slightly higher for the computational prediction than for the experimental values, whereas farther downstream at $x/d > 8$, computational $\overline{\phi}$ values were lower.

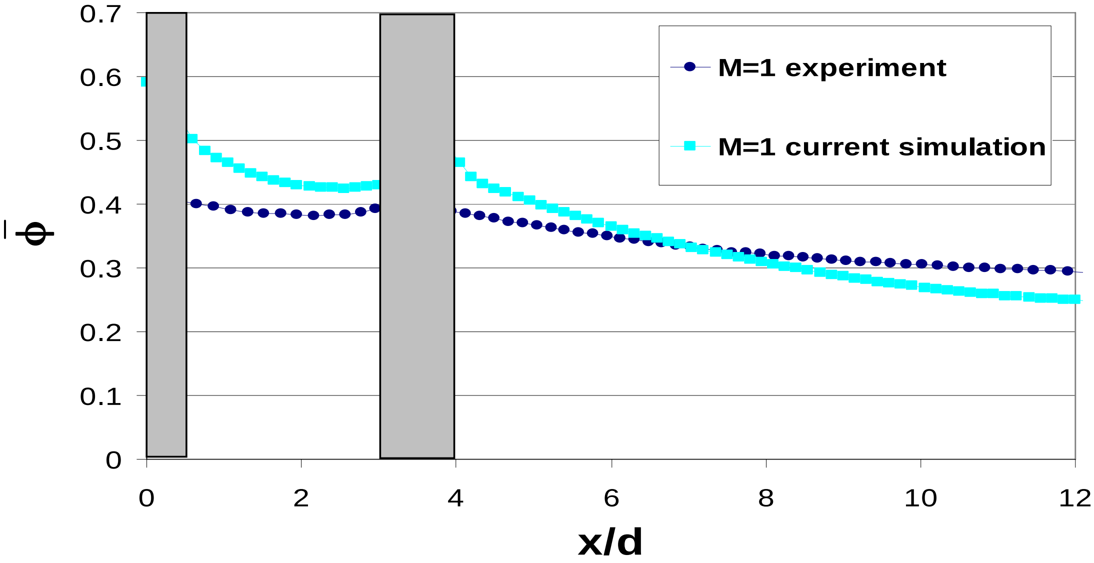

Figure 3.1.2.3: Comparison of laterally averaged overall effectiveness for the CFD prediction and experimental data (Davidson and Dyson, 2009) at *M* = 1.0

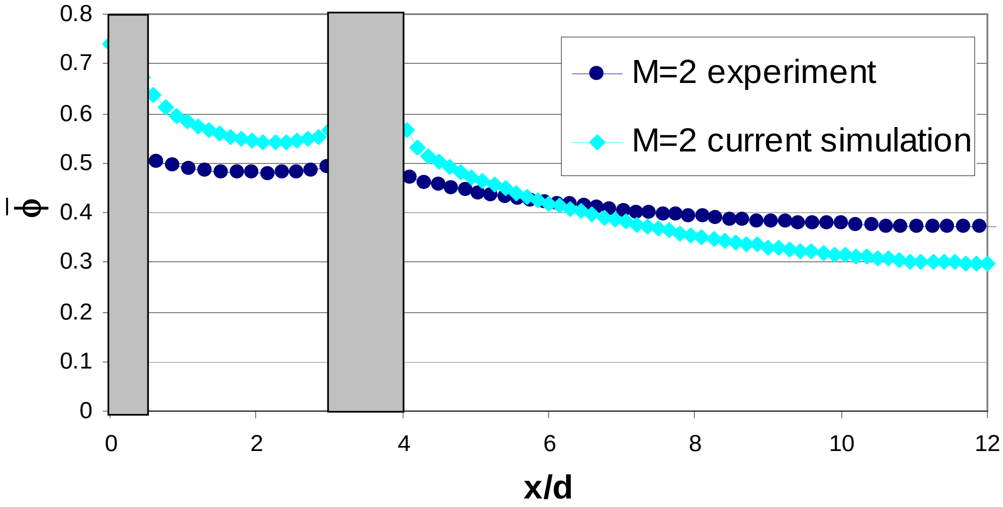

Figure 3.1.2.4: Comparison of laterally averaged overall effectiveness for the CFD prediction and experimental data (Davidson and Dyson, 2009) at *M* = 2.0

As for the adiabatic model, the two blowing ratios are plotted together in Figure 3.1.2.5. As expected, M = 2.0 gave higher performance than M = 1.0. Contrary to the adiabatic case, the curves for the two blowing ratios did not collapse downstream of the off-stagnation row holes. This was presumed to be due to the internal cooling much higher cooling at M = 2.0 than M = 1.0. Indeed, higher velocity jets resulted in higher internal heat transfer coefficients and thus lower internal wall temperature, which was experimentally measured.

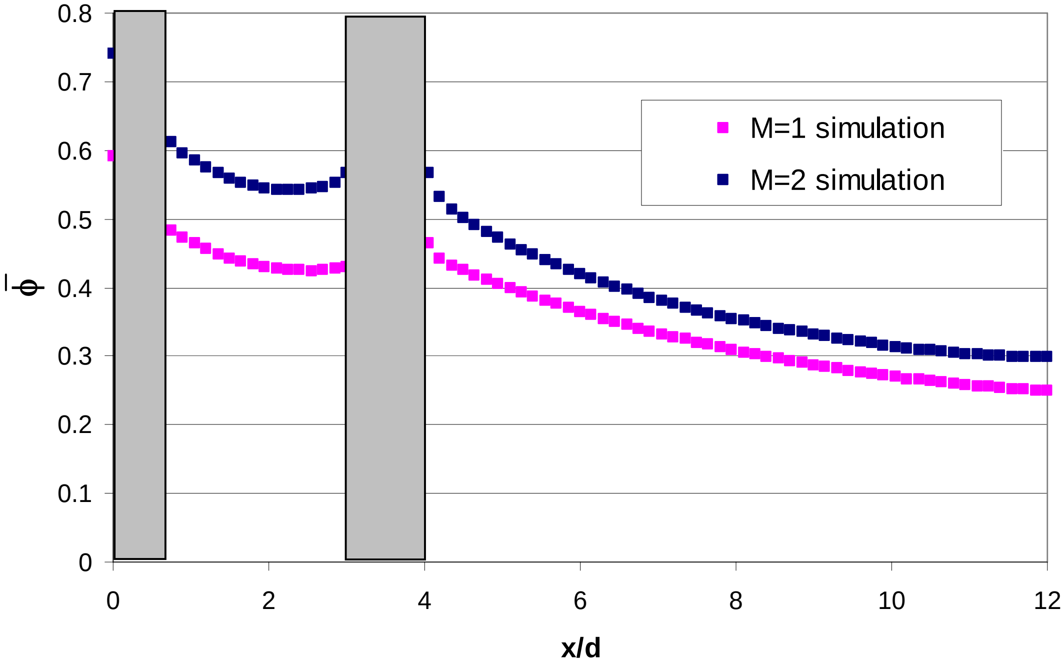

Figure 3.1.2.5: Comparison of laterally averaged overall effectiveness for the CFD prediction for both blowing ratios, *M* = 1.0 and *M* = 2.0

There have been previous CFD predictions incorporating conjugate heat transfer effects on a film cooled leading edge model with cylindrical holes. The closest study was done by Terrell (2004), who simulated a leading edge model with shaped holes based on Mouzon's (2005) geometry. Terrell (2004) found good agreement with the experiment for the contours of overall effectiveness. At $M = 2.0$, Terrell's (2004) simulated overall effectiveness prediction was lower than his experimental value after $x/d > 5$ and the maximum deviation was $\Delta\phi = 0.1$. Between the holes, Terrell (2004) found that the simulated overall effectiveness showed agreement with experimental values within 10%

for M = 2.0, whereas the current simulation presented a 20% discrepancy between experimental and computational data at the same location. Since the shaped holes simulated by Terrell (2004) would have reduced jet separation, the difficulty in predicting jet separation with numerical simulations was not an issue for Terrell's (2004) simulation, contrary to the current simulation of cylindrical holes. This could explain why Terrell (2004) gave a better simulated prediction than this current study.

3.1.3 Coolant Heat Transfer Results

Several interesting observations on conjugate heat transfer effects are evident from Figure 3.1.3.1. This figure represents thermal profiles of the conducting model at different spanwise directions for M = 2.0. These temperature contours highlight the temperature gradients through the solid and consequently indicate the heat flow through the solid.

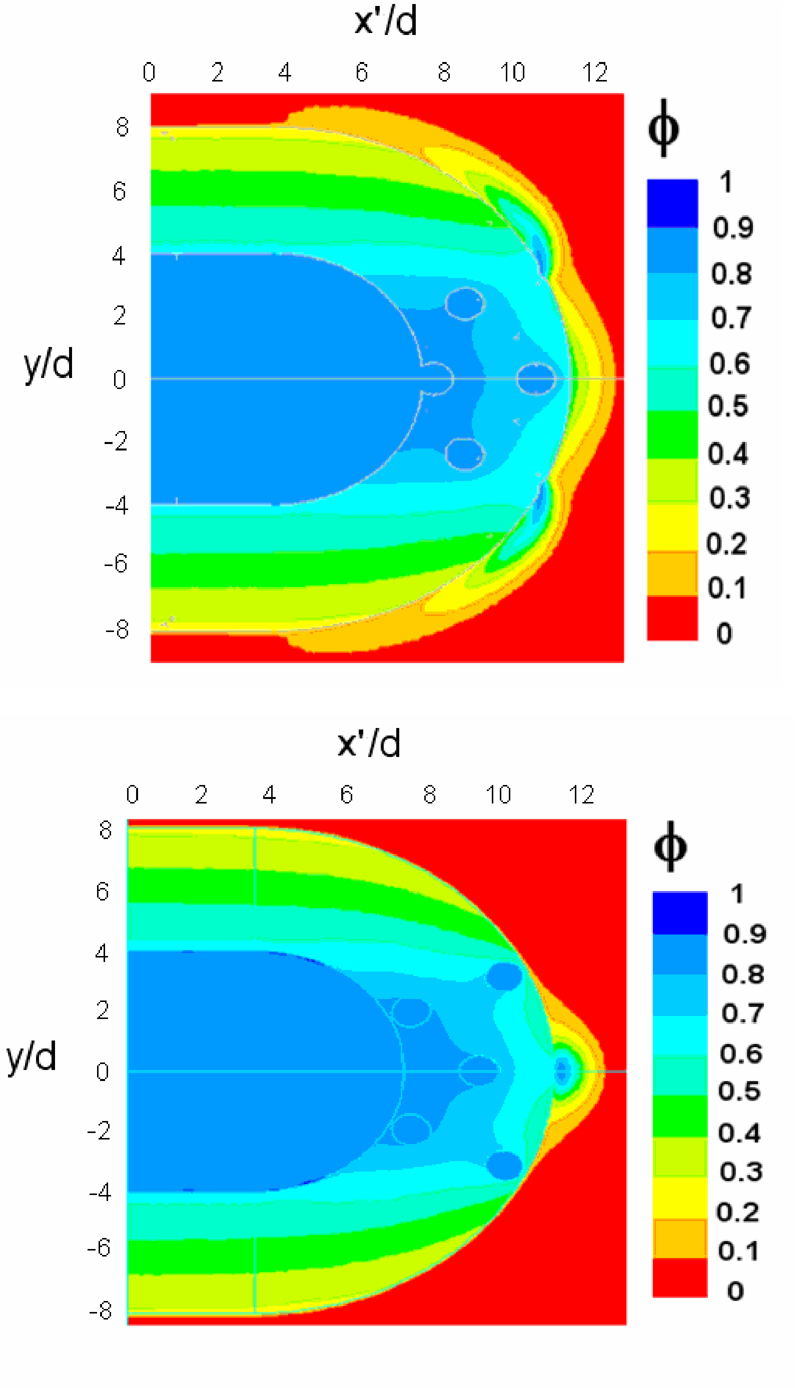

Figure 3.1.3.1: Thermal field cross-sections for blowing ratio of $M = 2.0$

First, the parallelism of the isotherms in the flat part of the leading edge model indicates that the coolant holes did not affect this region. As a result, heat was directly removed from the mainstream to the plenum in the flat region of the leading edge. However, in the leading edge regions, the isotherms indicate that the coolant holes clearly affected the heat flow from the external to the internal surface. This is indicative of the large contribution provided by the convective cooling within the cooling holes to the overall cooling of the leading edge. Calculations of the convective heat transfer and internal heat transfer were conducted to determine the contribution of the convective cooling to the overall cooling of the leading edge.

The convective cooling was obtained from three different algorithms. The first method relies on the area-average hole entrance and exit temperatures, respectively $\overline{T}_{c,in}$ and $\overline{T}_{c,out}$. The heat transfer, $q_{hole,\ average}$ was calculated using Equation 3.1.3.1 defined below:

$$q_{hole,average} = \dot{m}_c c_{p,c} (\overline{T}_{c,out} - \overline{T}_{c,in}) \qquad (3.1.3.1)$$

where $c_{p,c}$ = 1009 J/kgK and $\dot{m}_c$ is the coolant mass flow rate through each hole given by the CFD prediction. The exit temperature was taken 1mm below the exit of the holes, since the mainstream slightly entered the coolant hole. To obtain the temperature of the coolant, simulated data were taken 1 mm from the exit of the hole, which corresponds to 8% of the total hole length. The second method to calculate the heat transfer coefficient through the holes involves the calculation of the bulk temperature. FLUENT’ area integration ability was used to integrate the density, velocity and temperature product across the entrance and exit planes of each hole. The heat transfer occurring through the holes was calculated with Equation 3.1.3.2:

$$q_{\text{hole,integral}} = c_{p,c}\left(\int\limits_{A,out} \rho_c u_c \overline{T}_{c,out} dA - \int\limits_{A,in} \rho_c u_c \overline{T}_{c,in} dA \cdot \right) \qquad (3.1.3.2)$$

where $c_{p,c}$ = 1009 J/kgK, u_c is the coolant velocity normal to the entrance or the exit planes. The last method was obtained from the FLUENT code by isolating the coolant hole surfaces and reporting the area-averaged heat transfer through the coolant holes. Unlike the two previous methods, the internal and external heat transfers could be obtained from this method. The area-averaged heat transfer of the internal solid surface gave the internal heat transfer, q_{int}. This was possible because the internal wall temperature was imposed and the heat flux was only driven by the wall temperature conditions. The 2nd and 3rd method are the most accurate since the first one did not take into account the interdependence of the temperature, the velocity and the density.

Table 3.1.3.1 presents the results given by the three methods defined above at the two blowing ratios of M = 1.0 and M = 2.0. The area correction for the last method was done since FLUENT constrained the prediction of the heat transfer for the whole hole, whereas the two first methods evaluated the exit temperature 1mm below the real exit. This 1mm led to an 8% decrease in the coolant hole area. Assuming that the heat flux is constant through the whole area, this would also lead to an 8% decrease in q_{hole}. The last column allows checking the accuracy of the numerical simulation.

Table 3.1.3.1 Summary of the heat transfer for both blowing ratios

$M = 1$	q_{int} (W)	q_{ext} (W)	q_{hole} (W)	$q_{ext} - q_{int}$ (W)
Average method	X	X	4.43	X
Integral method	X	X	3.21	X
Heat transfer from Fluent	2.23	5.91	3.70	3.68
Heat transfer from Fluent (area correction)			3.40	

$M = 2$	q_{int} (W)	q_{ext} (W)	q_{hole} (W)	$q_{ext} - q_{int}$ (W)
Average method	X	X	4.40	X
Integral method	X	X	3.59	X
Heat transfer from Fluent	3.24	7.55	4.33	4.31
Heat transfer from Fluent (area correction)			3.98	

It is worth noticing that the three methods delivered similar results for the convective heat transfer in the holes. The integral method, as well as the heat flux obtained directly by FLUENT should have given approximately the same answer since c_p was a constant in the range $200 < T_c < 300$. At $M = 2.0$, a 10% difference was observed between both methods. This might be explained by the area correction analysis, which assumed that the heat flux was constant through the entire hole area, whereas the actual heat flux would increase close to the exit of the hole.

Table 3.1.3.1 also indicates of the large contribution provided by the convective cooling within the cooling holes to the overall cooling of the leading edge. Quantitatively, for a blowing ratio of $M = 2.0$, the computational simulations predicted 57% of the total heat flow into the coolant was via convective cooling within the coolant holes, and the remaining 43% via convective cooling through the internal walls of the leading edge. For a blowing ratio of $M = 1.0$ the percentage convective cooling through the holes was much larger, 63%, with 38% via cooling through the internal walls.

The intensive cooling along the stagnation line is more evident in Figure 3.1.3.2, which shows a cross-section of temperature contours along the stagnation line for blowing ratios of $M = 1.0$ and 2.0. For the higher blowing ratio, the cooling around the holes is sufficient so that the temperature difference between the coolant and holes was less than the increment in colors for the temperature contours, i.e. $\Delta\theta < 0.1$. For the lower blowing ratio, $M = 1.0$, there was a distinctly larger temperature difference between coolant and inside surface of the holes. Consequently, the computational simulations found a slightly larger total heat transfer to the coolant within the holes for $M = 1.0$ compared to $M = 2.0$, even though the heat transfer coefficient for the $M = 2.0$ case is larger.

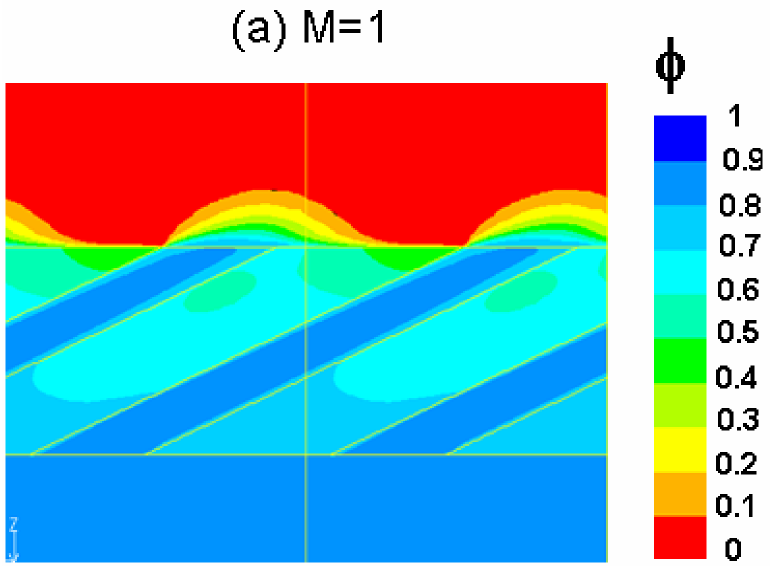
(a) M=1

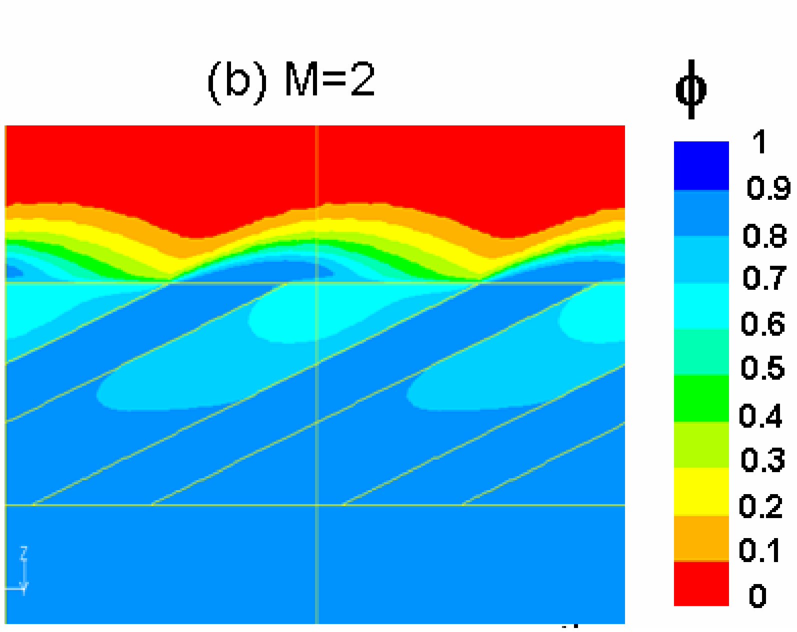

Figure 3.1.3.2: Thermal field cross-section along the stagnation line for *M* = 1.0 and *M* = 2.0

3.2 EXPLANATION OF THE DISCREPANCIES

Several factors can explain the discrepancies in ϕ between the numerical simulations and the experiments. This section analyses the different parameters, which influences the ϕ results.

3.2.1 Prediction of the Jet Separation

One of the reasons which could explain the discrepancy in the ϕ values is the jet separation that was not well predicted by the numerical simulations. In Figure 3.2.1.1, thermal profiles of the symmetry plane for both blowing ratios are presented. The temperature contours give no indication of jet separation at $M = 1.0$. Although there were no experimental measurements of the thermal field above the wall for this configuration, a previous experimental study of the thermal fields for film cooled vane model by Cutbirth and Bogard [25] showed a distinct separation of the coolant jets along the stagnation line even for blowing ratios as low as $M = 0.8$. Moreover, the experimental measurements of $\eta < 0.7$ for a blowing ratio of $M = 1.0$, shown in Figure 3.1.1.1 (a), suggests separation.

At $M = 2.0$, Figure 3.2.1.1 (b) shows a slight jet separation on the stagnation line. Again, experimental measurements of $\eta < 0.6$ along the stagnation line for $M = 2.0$, seen in Figure 3.1.1.2 (a), suggest a stronger jet separation than the numerical simulation predicted. The failure of the computational simulation to predict the coolant jet detachment along the stagnation line may explain why the predictions of adiabatic effectiveness and overall effectiveness were too high in this region.

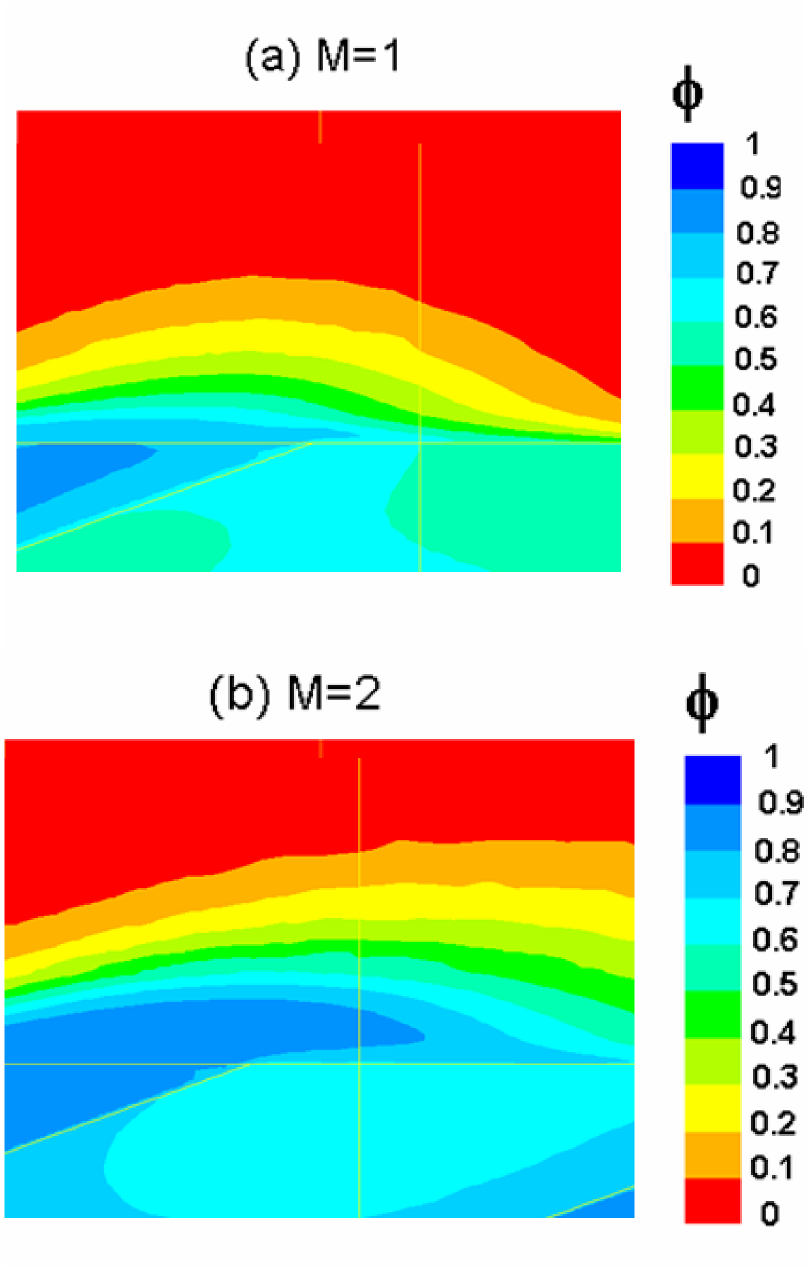

Figure 3.2.1.1: Thermal profiles on the stagnation line at the exit of the coolant hole for (a) M = 1.0 and (b) M = 2.0

Recall that the discrepancy between the computational predictions and the experimental measurements of η were attributed to coolant jet separation not being well predicted by the numerical simulations. Therefore, an analysis was done to see if the higher ϕ values predicted computationally in the region $0 \leq x/d \leq 5$ can be explained by the higher η levels predicted by the computational simulations. As shown previously in Figure 3.1.1.2, computationally predicted adiabatic effectiveness levels were also lower than experiments between coolant jets for M = 2.0. At the same blowing ratio, the computational simulations predicted higher overall effectiveness than measured experimentally in the region between $0 < x/d < 5$. A 1-D heat transfer analysis was done to see if the discrepancy in η could explain the discrepancy in ϕ. Using Equation 1.1.3.10, the change in η is related to the change in ϕ by the following equation:

$$T_w = \frac{T_{aw} + \frac{T_{\text{int}} k}{h_f l}}{1 + \frac{k}{h_f l}} \tag{3.2.1.1}$$

At the exit of the off-stagnation hole, a discrepancy of $\eta_{comp} - \eta_{exp} = 0.3$ was observed between the computation and the experiment for the near adiabatic three-row leading edge model (k = 0.048W.mK) for M = 2.0. According to the 1-D analysis (Equation 3.2.1.1), this would lead to a discrepancy of nominally $\phi_{comp} - \phi_{exp} = 0.2$ between the simulated and experimental ϕ values, which was higher than the discrepancy observed in the contours of ϕ values as seen in Figure 3.1.2.2. Similarly, for a blowing ratio of M = 1.0, at the exit of the stagnation hole, the discrepancy between the computational and experimental adiabatic effectiveness values was $\eta_{comp} - \eta_{exp} = 0.3$. At this location, this would be expected to cause a difference in ϕ values of $\phi_{comp} - \phi_{exp} = 0.2$ between the computation and the experiment. This expected discrepancy was very similar to that observed in Figure 3.1.1.1. Therefore, the inaccuracies in predictions of ϕ appear to be a result of the inaccuracies in predicting η.

Although the higher ϕ values predicted computationally in the region $0 \leq x/d \leq 5$ can be explained by the higher η levels predicted by the computational simulations, a full explanation requires an examination of other factors. Some insight of the discrepancies can be gained by analyzing the different parameters which affects the conjugate heat transfer analysis.

3.2.2 Prediction of the in-Hole Convective Cooling for the Three Row Configuration

One possibility that could contribute to the disparity is the computed convective cooling within the holes being larger than what actually occurs in the experiment. Since the total convective heat transfer is proportional to the increase of bulk temperature from the entry to the exit of the hole, comparing the increase in bulk temperature along the length of the holes gives an indication of the accuracy of the computed convective heat transfer occurring though the holes. Terrell (2004) data were used as experimental baseline, since they conducted experiments using a conducting model with a Biot number that was very similar to the current simulation. The only difference was the shape of the holes at the exit. Terrell (2004) used shaped holes, versus cylindrical holes for Maikell (2008). As shown in Figure 3.2.2.1, Terrell (2004) took his exit temperature measurements with a traversing thermocouple probe, at a location, where the shape of his holes was still very close to a cylinder.

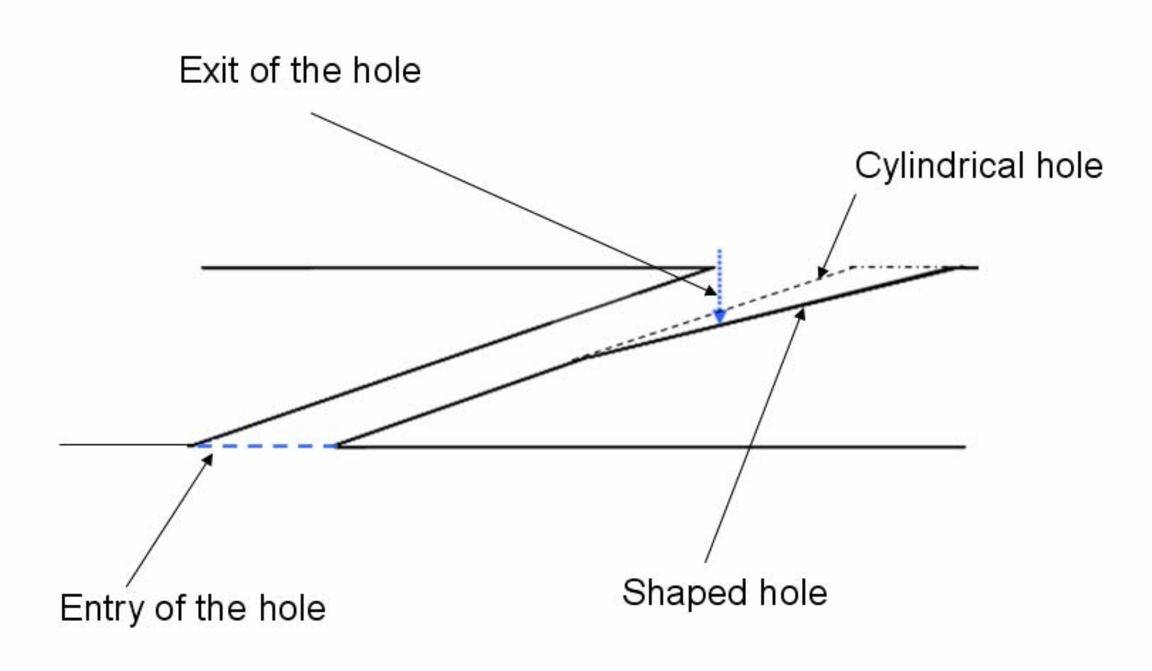

Figure 3.2.2.1: Coolant hole entrance and exit measurement locations for the shaped holes model of Terrell (2004) and the current simulation

Consequently, the section of the hole upstream of the exit plane measured by Terrell (2004) was essentially cylindrical and comparable to the holes used in this study. Therefore, the increase of the bulk temperature through the holes between Terrell's (2004) experimental data and the current simulated computation was compared. The results are presented in terms of the dimensionless gas temperature, θ, in Table 3.2.2.1. For the blowing ratios of $M = 1.0$, the predicted increase in temperature for the current simulation was similar to the experimental values of Terrell (2004), especially for the off-stagnation hole. But for a blowing ratio of M = 2.0, current computational simulations predicted a lower average temperature increase along the length of the coolant holes. Simulated predictions of Terrell (2004) gave better agreement for the stagnation hole than the current simulation in terms of $\Delta\theta$, whereas the increase in temperature for the off-stagnation hole was better predicted by the current simulation than Terrell's (2004) simulation. These results indicate that the current computational simulations accurately predicted the total convective heat transfer from the walls of the film cooling holes into the coolant gas for the lower blowing ratio, but at the higher blowing ratio, the predicted total convective cooling in the hole was too low. Consequently the convective cooling within the coolant holes did not explain the higher values of $\bar{\phi}$ between the two rows of holes predicted numerically.

Table 3.2.2.1 Temperature increases, Δθ, from inlet to exit of the coolant holes compared to experimental and simulated data from Terrell (2004)

	$M = 1$		$M = 2$	
	Stag	Off-stag	Stag	Off-stag
Experiment Terrell (2004)	0.103	0.086	0.061	0.068
Simulation Terrell (2004)	0.118	0.078	0.043	0.037
Current simulation	0.084	0.089	0.037	0.054

3.2.3 Prediction of the Heat Transfer Coefficient Augmentation using a Constant Heat Flux Simulation

Another factor investigated was the external heat transfer coefficient. The computational simulation was compared to experimental measurements of Johnston et al. (1999). They evaluated the heat transfer coefficient augmentation, $\frac{h_f}{h_0}$ at two turbulence levels, *Tu* = 0.5% and *Tu* = 17%. The turbulence level of the current simulation, *Tu* = 6%, falls in the range of the two turbulence levels studied by Johnston et al. (1999). It is also important to notice that the experiments were conducted applying a constant heat transfer on the surface, and a density ratio of *DR* = 1.0 was used. In this case, the driving temperature was the freestream temperature and the heat transfer coefficient was defined by the following equation:

$$h_f = \frac{q''}{T_\infty - T_w} \tag{3.2.3.1}$$

For both, the computational predictions and experimental measurements, the reference non-film-cooled heat transfer, h_0, was obtained from the non-film-cooled model with constant heat flux. The first step for this study was to investigate the sensitivity of h_0 to different turbulence models. The results are presented in terms of *Fr* for a fixed *Re*. The fluid properties were in the Nusselt number, *Nu,* were evaluated at the film temperature. In Figure 3.2.3.1, predictions of *Fr* with the realizable k-ε with enhanced wall treatment, the SST k-ω and the RSM turbulence models, as well as the laminar model were compared to the experimental data of Mouzon (2005). Mouzon used the same leading edge model as simulated in this thesis and used mainstream turbulence levels of $Tu = 0.5\%$ and $Tu = 7\%$. In this study, the turbulence intensity was kept at $Tu = 6\%$ to match Maikell's (2008) experiments, except for the "laminar" simulation. The mainstream flow for the "laminar" simulation case had zero turbulence intensity, because non-zero turbulence intensity could not be imposed using the FLUENT code. For the low turbulence case, the "laminar" model matched the experimental data for $Tu = 0.5\%$ within 10%. The numerical predictions for the k-ε and RSM turbulence models agreed reasonably well with the experimental data of Mouzon (2005) at $Tu = 7\%$ up to $x/d = 6$. Beyond this point, the slope for the experiment was much steeper than the one predicted by the k-ε and RSM turbulence models. The SST k-ω turbulence model showed a consistent offset when compared to the experiments.

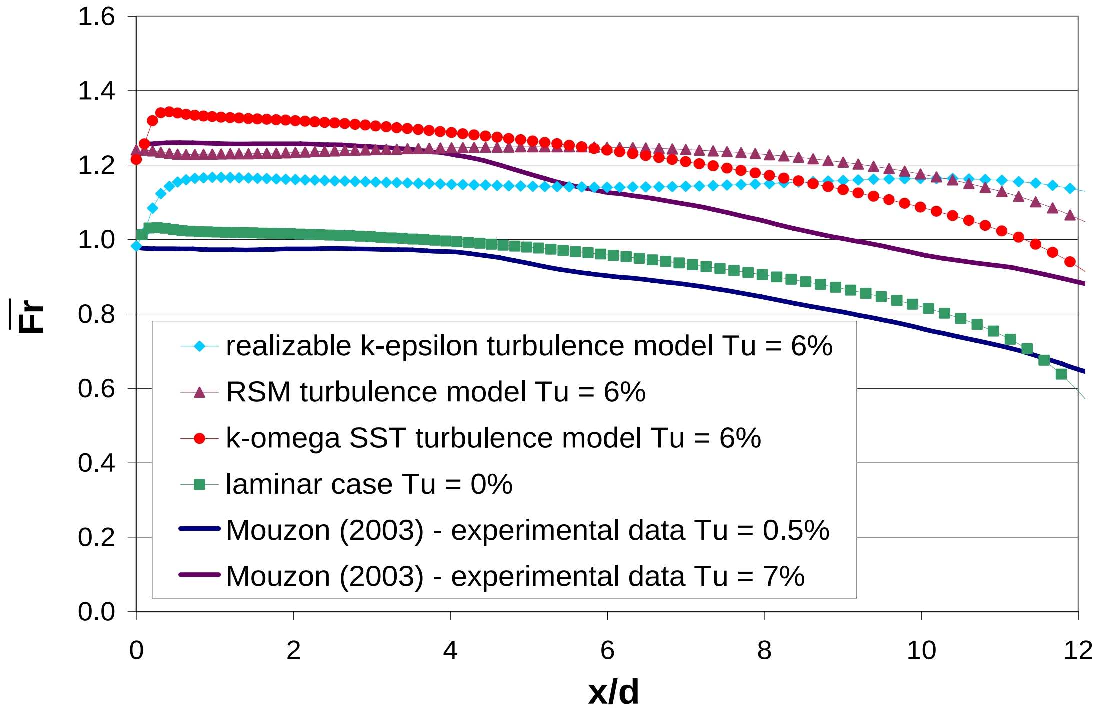

Figure 3.2.3.1: Laterally averaged Frossling number for the no blowing case model at *Tu* = 6%

Surprisingly, an abrupt slope was observed on the stagnation line for the “laminar”, k-ε and k-ω turbulence models. The author attributed the steep slope to the symmetry condition. Indeed, an additional simulation with a complete leading edge was run and this simulation gave the zero slope characteristic of the Frossling number at the stagnation line, as seen in Figure 3.2.3.2. Interestingly, the k-ε turbulence model gave a similar prediction for *Fr* as obtained in the computational simulations of York and Leylek (2002). However, the current simulation was slightly better since the realizable k-ε turbulence simulation did not show an increase in *Fr* after 50 degrees, as was seen in the York and Leylek (2002) prediction.

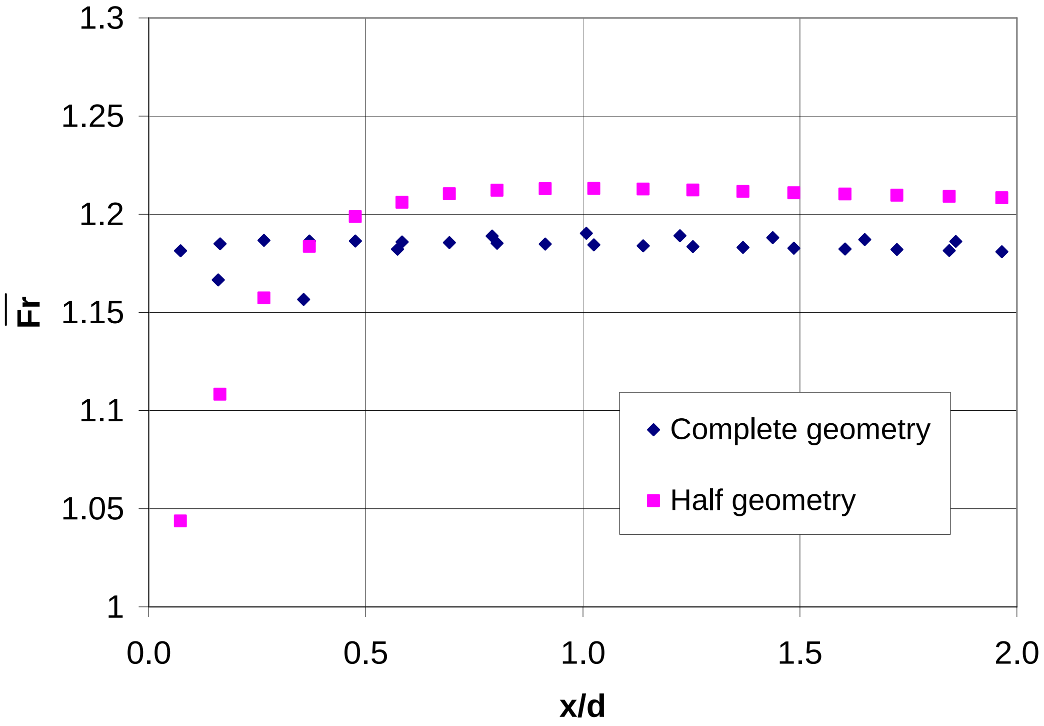

Figure 3.2.3.2 Influence of the symmetry condition on the stagnation line for the no blowing case model at *Tu* = 6% with the realizable k-ε turbulence model

Since the computationally prediction of h_0 with the laminar case was very similar to the experimental data of Mouzon (2005), the laminar model was selected as the reference for the non-film cooled heat transfer and further analyzed to check its accuracy. Another simulation was conducted where a constant temperature was imposed on the external surface. Figure 3.2.3.3 presents the influence of the temperature distribution on the Frossling number, *Fr*. The simulated data were compared to the measurements of

Papell (1981) around a cylinder. The comparison was limited after 60 degrees due to the dissimilitude in geometry between the cylinder of Papell (1981) and the leading edge of the current study. Experimental data proved that the iso-heat-flux external wall condition led to slightly higher heat transfer coefficients than the isothermal case. As noted by Papell (1981), the iso-heat flux wall had a smaller thermal boundary layer growth and therefore a higher heat transfer coefficient than the isothermal wall condition. At a position of 80º, the CFD predictions also showed a Frossling number for the iso-heat flux 30% higher than for the isothermal wall. The computational data gave similar values than for the experiments close to the stagnation line. Overall, the laminar model was able to reproduce the difference between the iso-heat flux and the isothermal wall (with the iso-heat flux condition delivering higher values of Frossling number than the constant wall temperature boundary condition). Therefore, for both the computational predictions and experimental measurements, the reference non-film-cooled heat transfer coefficient, h_0, which was used in the augmentation factor, was obtained from a non-film cooled case with constant heat flux and low mainstream turbulence. Since the computational and experimental h_0 were essentially the same, differences in h_f/h_0 would be due to differences in h_f.

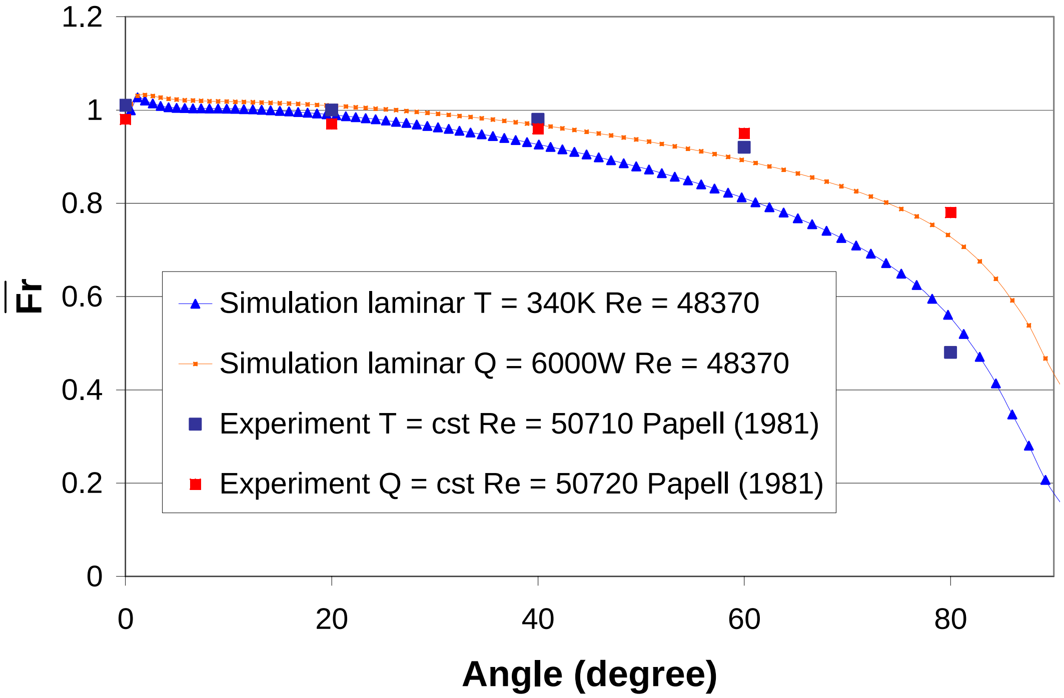

Figure 3.2.3.3: Influence of the temperature distribution on the Frossling number for the no blowing case model using the laminar model

Once the reference non-film-cooled heat transfer coefficient, $h_{0,}$ was computationally determined, a simulation was run to predict the correct external heat transfer coefficient with film cooling, h_f. Since no experimental data were available to predict the external heat transfer coefficient for a conducting model, another simulation was conducted to match the experimental protocol of Johnston (1999). A constant heat flux of $q'' = 3000$ W/m^2 was imposed on the external surface at $DR = 1.0$. This value of q'' was chosen to nominally match the averaged heat flux entering the external surface for the three row conducting model. The data are presented in terms of $\frac{\overline{h_f}}{h_0}$ in Figure 3.2.3.4. The turbulence intensity of the mainstream for the simulation was *Tu* = 6%, which was the same as Maikell's (2008) experiment. Johnston's (1999) experiments were conducted with approach flow turbulence levels of *Tu* = 0.5% and 17% which bracket the turbulence level of *Tu* = 6% used in the computational simulation. He reported an uncertainty of $\Delta\frac{\overline{h_f}}{h_0}$ = ± 0.05. If the numerical predictions of $\frac{\overline{h_f}}{h_0}$ at *Tu* = 6% are presumed to be at the midspan between measurements at *Tu* =0.5% and 17%, with an uncertainty of ± 0.1, the numerical prediction gave values of $\frac{\overline{h_f}}{h_0}$ within the experimental uncertainty for 0 < *x/d* < 8, except at *x/d* = 3. After *x/d* = 10, the simulated heat transfer coefficient augmentation were higher than the experimental values of Johnston (1999) for *Tu* = 17%, which would be expected to be larger than $\frac{\overline{h_f}}{h_0}$ at *Tu* = 6%. Overall, the heat transfer coefficients were in the range of the uncertainty for the experimental values, except at *x/d* = 3, where predicted $\frac{\overline{h_f}}{h_0}$ was lower than measured and *x/d* > 10 where predicted $\frac{\overline{h_f}}{h_0}$ was greater than experimental data. The predictions of $\frac{\overline{h_f}}{h_0}$ values higher than actual values, after x/d > 10, would result in predictions of lower ϕ values. Hence, this error in the $\frac{\overline{h_f}}{h_0}$ predictions would contribute to the lower values of ϕ predicted for $x/d > 10$.

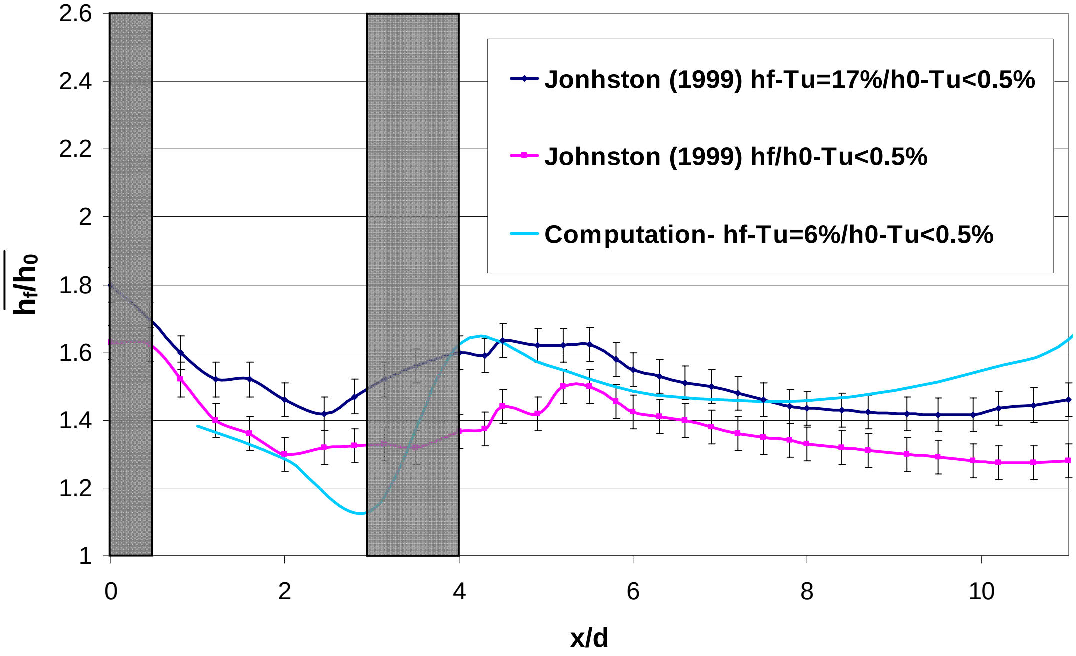

Figure 3.2.3.4 Laterally averaged heat transfer augmentation for the constant heat flux three-row model compared to experimental measurements (Johnston, 1999) at M = 2.0

3.3 PREDICTION OF OVERALL EFFECTIVENESS FOR THE ONE ROW CONFIGURATION

Simulations were also conducted for the single row leading edge model. The simulated data of ϕ distributions were compared to the measured values of Maikell (2008), as plotted in Figures 3.3.1 and 3.3.2 for, respectively, $M = 1.0$ and $M = 2.0$. As for the three-row leading edge model, the stagnation line shows much higher values of ϕ

for the CFD predictions at both blowing ratios. Although the contours of ϕ showed, for the computation and experiment for $M = 1.0$, a maximum ϕ value at the same location, i.e. just after the exit of the stagnation holes; the magnitude of this maximum was significantly different with $0.45 < \phi < 0.5$ for the computation and $0.25 < \phi < 0.3$ for the experiment. After $x/d = 8$, the CFD simulations predicted ϕ lower values than the experimental data for $M = 1.0$. Unlike $M = 1.0$, the position of the maximum value, for $M = 2.0$, was different for the experimental and computational ϕ values. The magnitude of these maximum was also different with the computed $\phi > 0.6$ compared to the experimental $\phi > 0.35$. Again, these trends were similar to the three-row leading edge model.

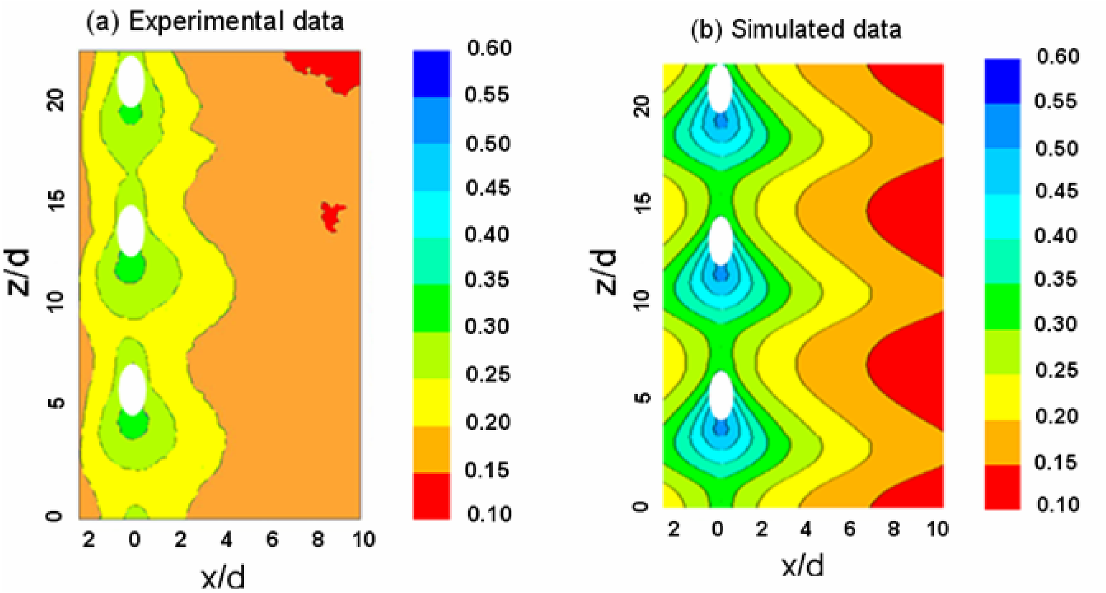

Figure 3.3.1: Contours of (a) experimental and (b) simulated overall effectiveness for the blowing ratio of *M* = 1.0 for the one-row leading edge model

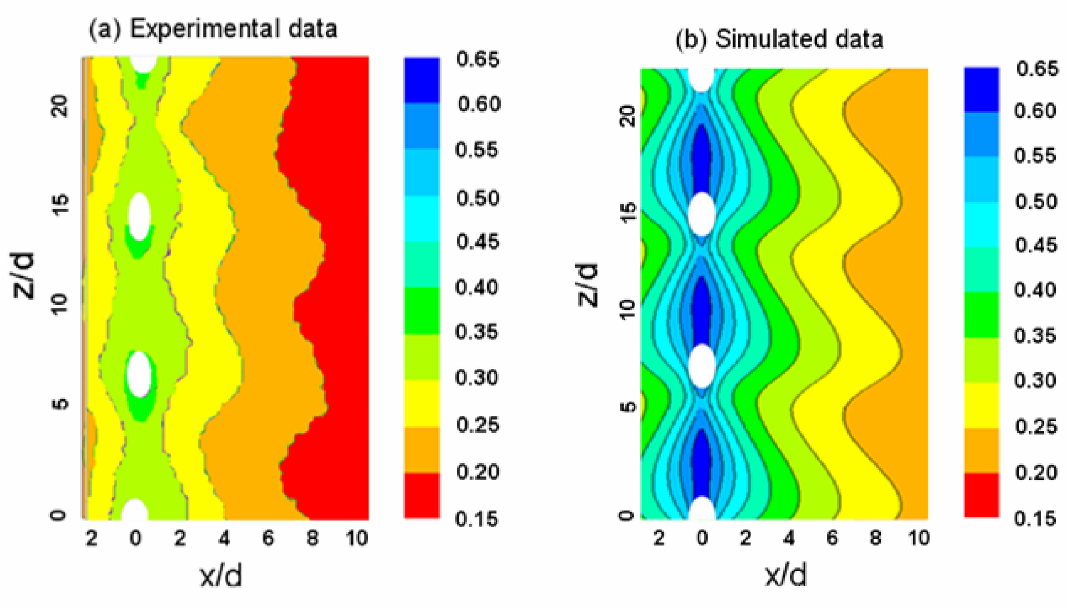

Figure 3.3.2: Contours of (a) experimental and (b) simulated overall effectiveness for the blowing ratio of *M* = 2.0 for the one-row leading edge model

Distributions of the laterally averaged overall effectiveness for the one-row leading edge model are presented in Figure 3.3.3 and 3.3.4 for, respectively, M = 1.0 and M = 2.0. The simulation predicted much higher $\overline{\phi}$ values than the experimental data at the stagnation line, but similar values for $x/d > 5$ when M =1.0 and x/d > 10 when M = 2.0. For M = 1.0, the experimental data showed higher ϕ values than the computation values, which was probably due to conduction through the impingement plate that was not simulated in the computational case. The impingement plate cooled down the experimental model, since it was made with a highly conducting material (aluminum). The slopes of the laterally averaged overall effectiveness for the CFD predictions were much steeper than for the experimental data at both blowing ratios. Comparisons of adiabatic effectiveness contours would have been useful to prove the inability of the numerical simulations to determine whether poor predictions of ϕ along the stagnation line might be attributed to poor predictions of η, as was the case for the three row model. However, no measurements of η were conducted for the single row model. To help confirm that the adiabatic effectiveness along the stagnation line for the one row configuration would be the same as for the three row configuration, a computational simulation was done of an adiabatic single row configuration. Contours of η for the one and three row configurations are presented in Figures 3.3.5 and 3.3.6 for blowing ratios of M = 1.0 and 2.0, respectively. It is remarkable how the stagnation line is perfectly identical for both models regardless of the blowing ratio. This proves that the off-stagnation coolant path did not interfere with the coolant flow in the stagnation region. Since the jet separation was not well predicted for the three row adiabatic model, and the one row and three row models showed the exact same contours of adiabatic effectiveness on the stagnation line, the poor prediction of jet separation could also explain the discrepancy between the measurements and the computations for the one row model.

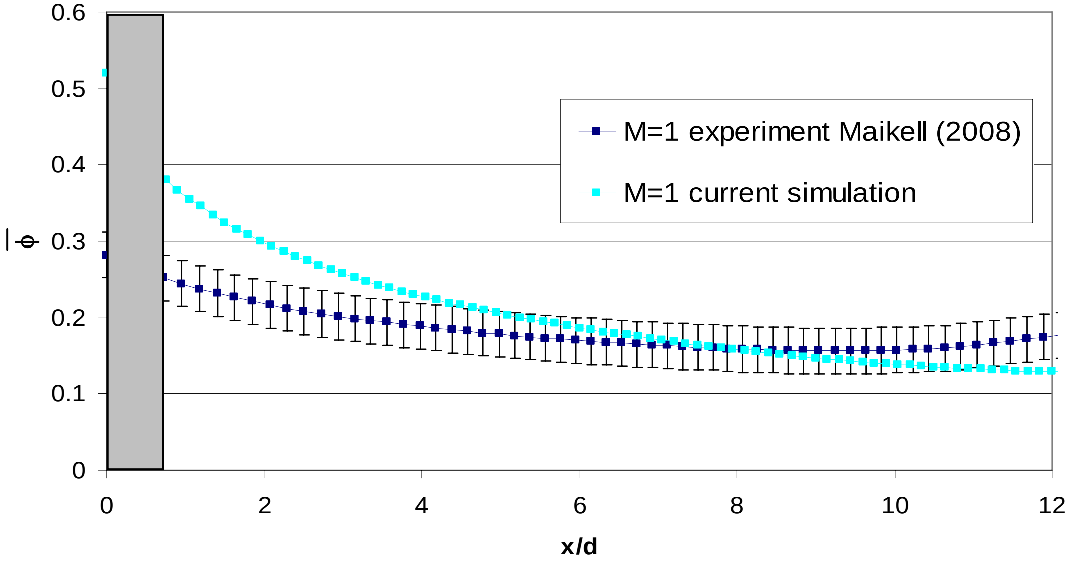

Figure 3.3.3: Comparison of laterally averaged overall effectiveness for the CFD prediction and experimental data at *M* = 1.0

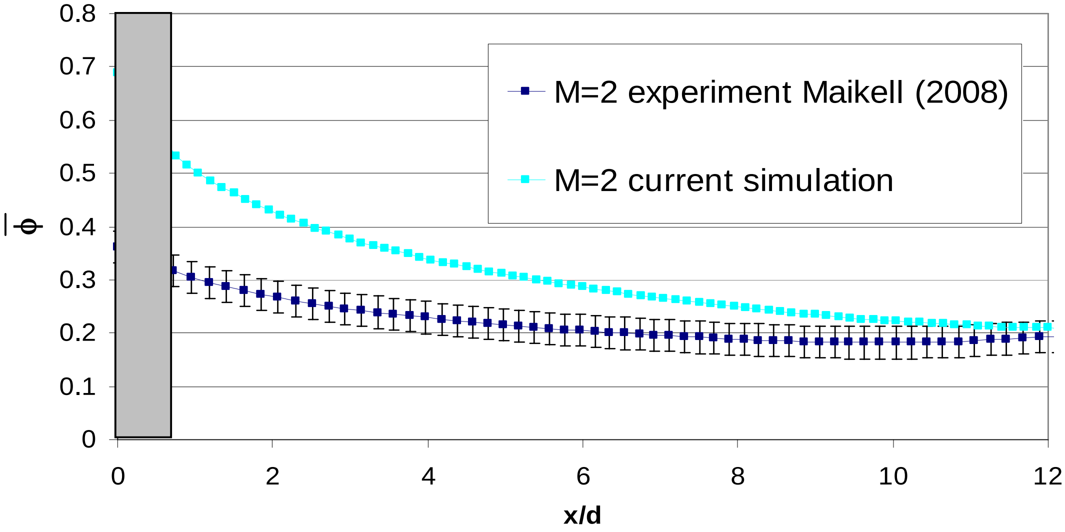

Figure 3.3.4: Comparison of laterally averaged overall effectiveness for the CFD prediction and experimental data at *M* = 2.0

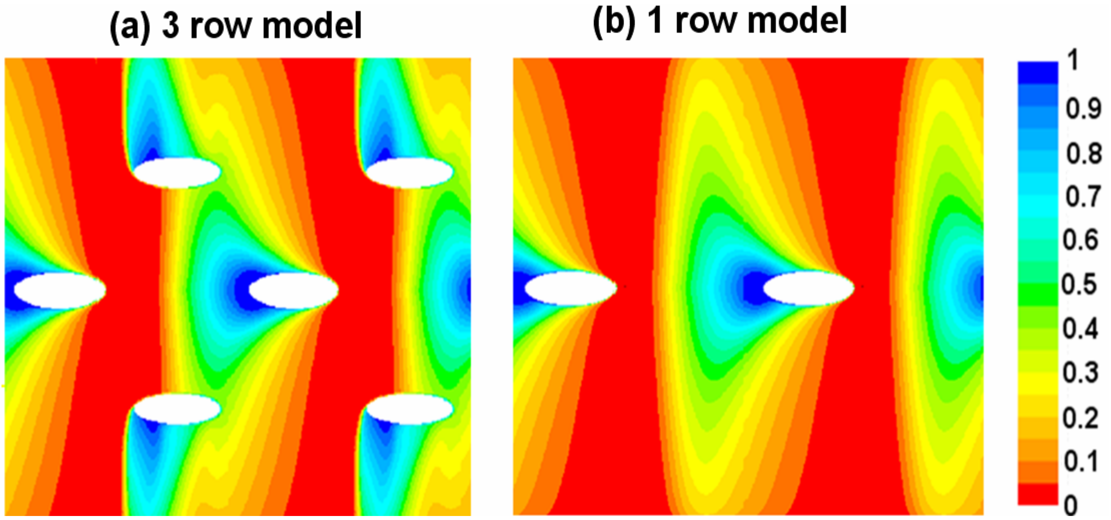

Figure 3.3.5: Contours of simulated adiabatic effectiveness at *M* = 1.0 for (a) the three-row model and (b) the one-row model

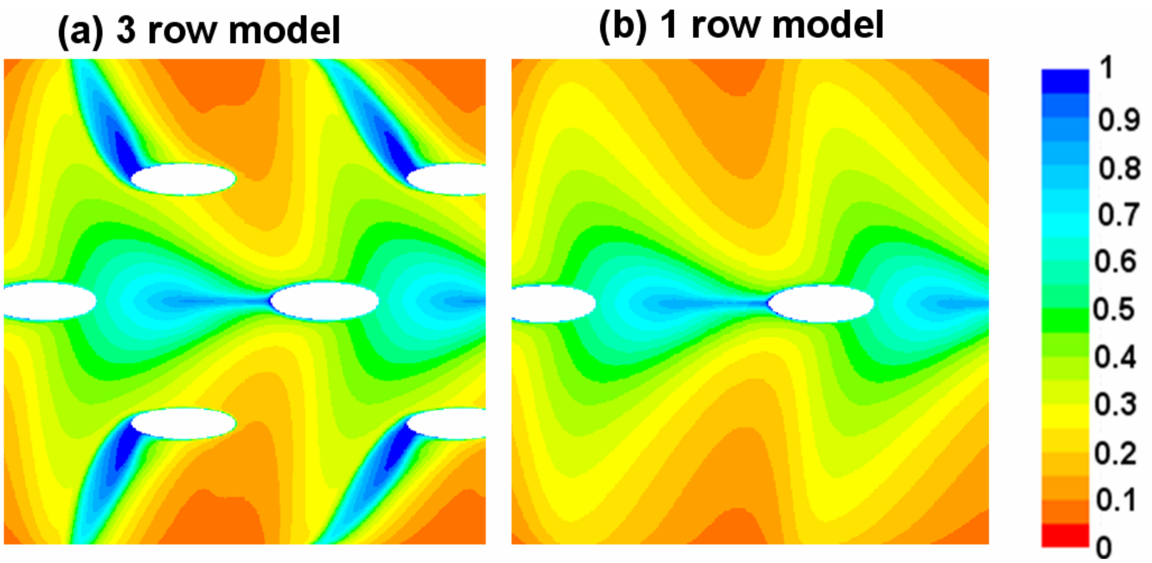

Figure 3.3.6: Contours of simulated adiabatic effectiveness at M = 2.0 for (a) the three-row model and (b) the one-row model

3.4 INFLUENCE OF PARAMETERS ON THE CONJUGATE HEAT TRANSFER ANALYSIS

Some insight about the three row model can be gained by analyzing the different parameters which affect the heat transfer through the solid leading edge. Figure 3.4.1 presents a schematic of a 1-D analysis of heat transfer using thermal resistances. The external heat transfer coefficients and the adiabatic wall temperature were already discussed in the previous section. The internal heat transfer coefficient sensitivity was not relevant in this thesis since the internal wall temperature was imposed. Of interest in this section were the thermal conductivity of the material, the impingement plate and the coolant temperature.

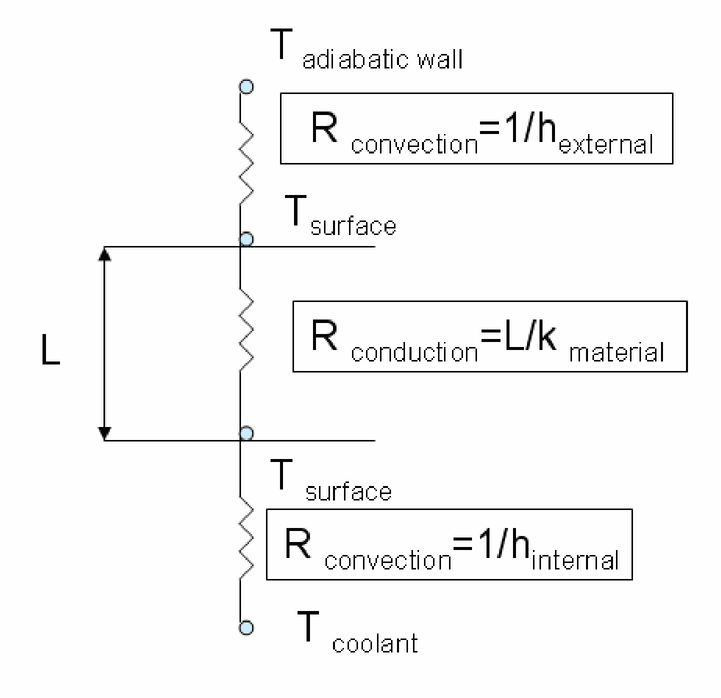

Figure 3.4.1: Schematic summarizing the key parameters for conjugate heat transfer

3.4.1 Sensitivity to the Thermal Conductivity of the Solid

Even though predictions of ϕ values were high close to the stagnation line, the numerical simulations proved to be a useful tool to predict the solid wall temperature using a CHT analysis. Thus, a three-row conducting model with high conductivity material was simulated to establish the sensitivity to varying solid thermal conductivity. For this analysis the thermal conductivity was increased nominally by a factor of four, i.e. k = 4.3 W/mK. This analysis was also a test of the Biot number sensitivity since the high thermal conductivity corresponds to Bi = 0.44, while the low thermal conductivity of k =

1.04W/mK corresponds to Bi = 1.8. The thermal conductivity was chosen to be in the range of possible Biot number when different engine operating conditions (k, Re, T) were taken. The internal boundary condition was kept the same for both simulations to focus on the effect on the external wall temperature. Contours of ϕ surface distributions calculated using the Bi = 0.44 model are presented in Figure 3.4.1 for blowing ratios of M = 1.0 and 2.0. These ϕ distributions can be compared with the ϕ distributions for Bi = 1.8 presented earlier in Figures 3.1.2.1 (b) and 3.1.2.2 (b). Clearly, the ϕ values were larger for the lower Bi model, and this was expected due to the decrease in thermal resistance through the solid. Also, the metal temperature tends to be more homogeneous with high Bi.

Besides, the metal temperature for actual engine operation is assumed to be relatively constant because of the large thermal conductivity of metal blades and vanes. This presumption is clearly not correct at the higher Bi, and is still questionable even when Bi is decreased by a factor of four.

The laterally averaged overall effectiveness, $\overline{\phi}$, are compared in Figures 3.4.1.2 and 3.4.1.3 for both Biot number, Bi = 0.44 and Bi = 1.8, at M = 1.0 and M = 2.0. The results showed that the higher the thermal conductivity was, i.e. lower Bi, the surface temperature decreased.

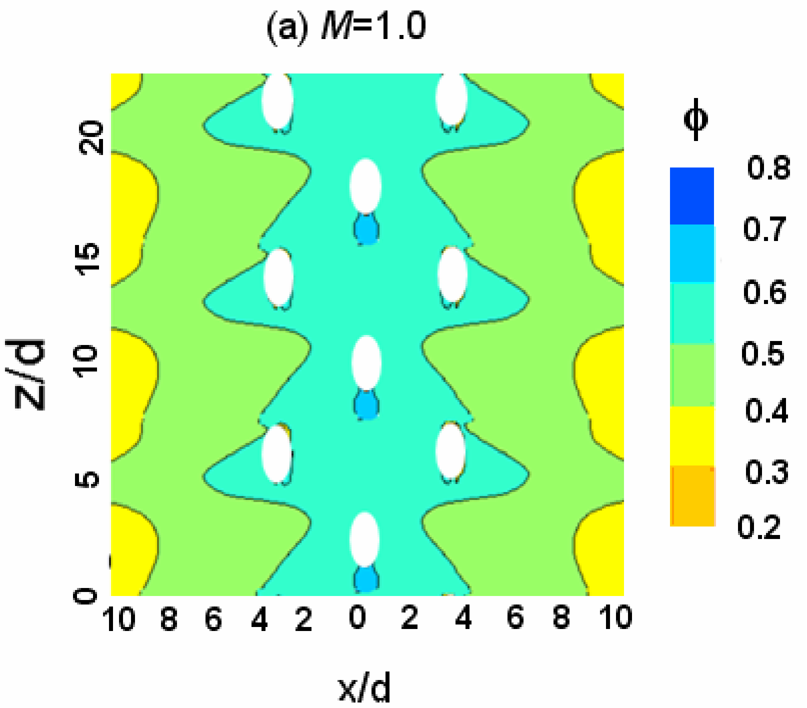
(a) M=1.0

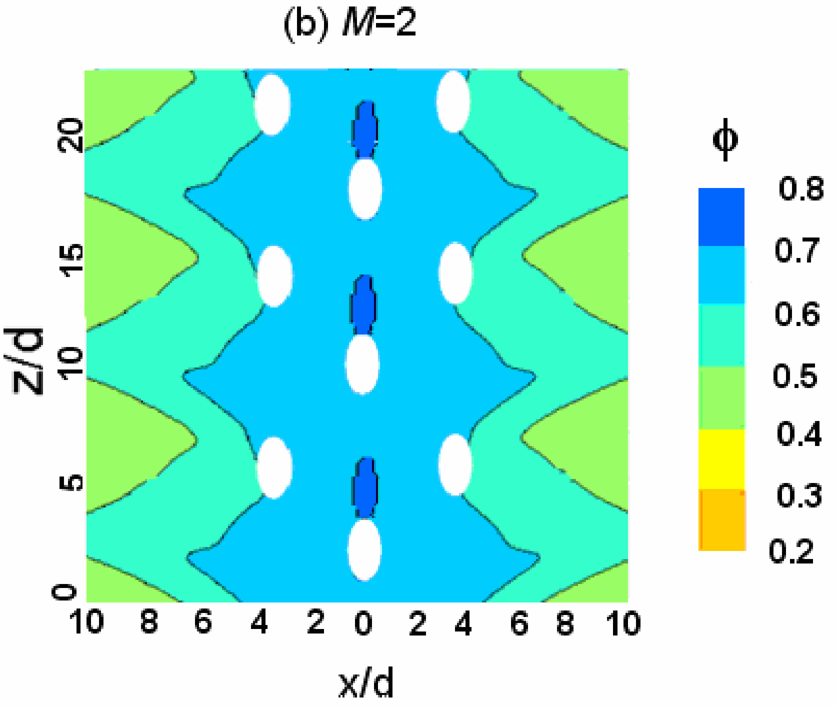
(b) M=2

Figure 3.4.1.1: Contours of simulated overall effectiveness for the three-row model at a blowing ratio (a) *M* = 1.0 and (b) *M* = 2.0 for *Bi* = 0.44.

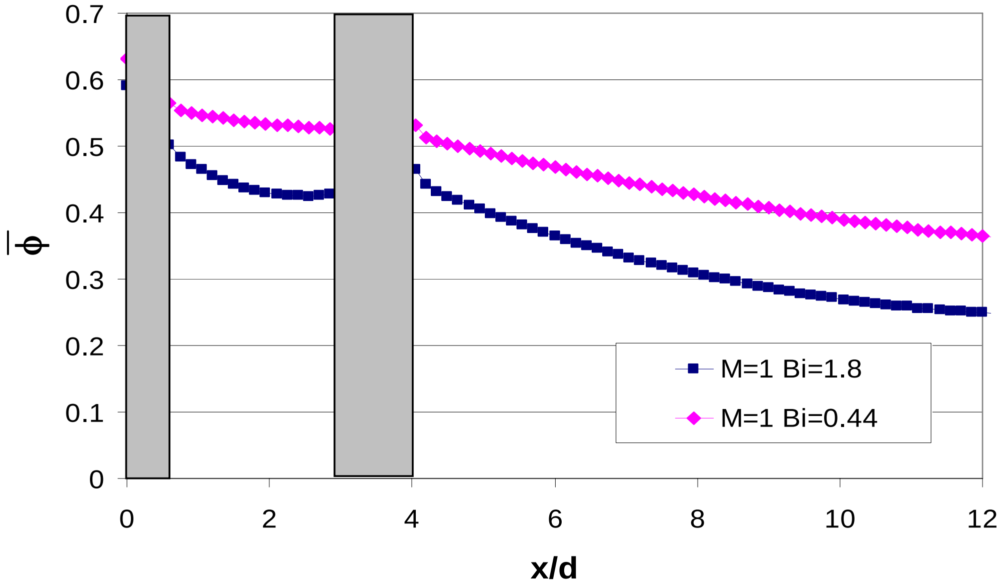

Figure 3.4.1.2: Comparison of simulated laterally averaged overall effectiveness for both Biot number at *M* = 1.0

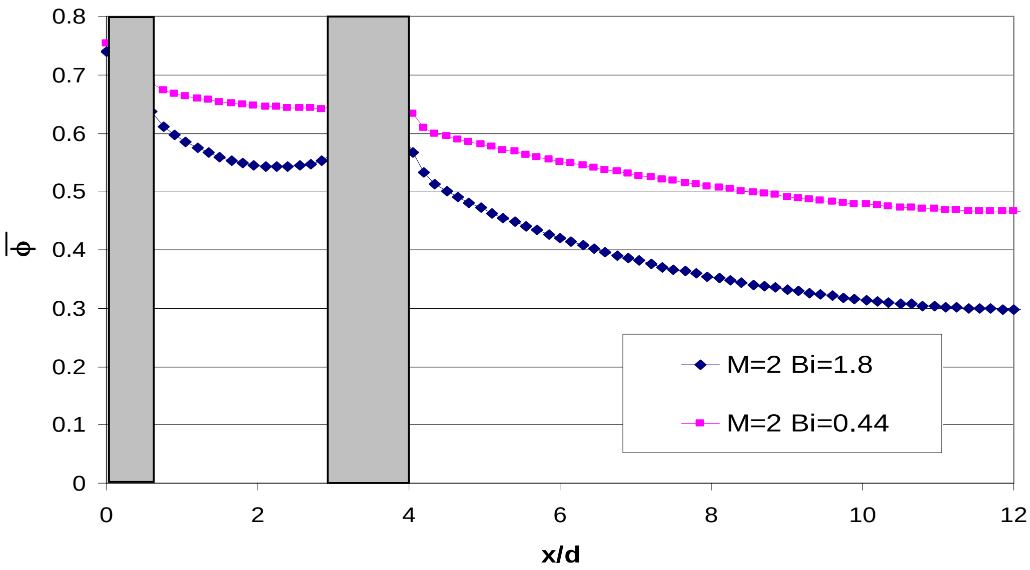

Figure 3.4.1.3: Comparison of simulated laterally averaged overall effectiveness for both Biot number at M = 2.0

3.4.2 Sensitivity to the Coolant Temperature at the Entry of the Hole

For the previous simulated predictions, the coolant temperature at the entry of the hole was adjusted so that the experimental and computational coolant temperatures at the entrance of the holes were similar. An analysis was conducted to determine how the coolant temperature at the entry of the hole affects the external temperature, i.e. ϕ. Three different coolant temperatures at the entry of the hole were tested: $T_{c,in}$ = 205K, $T_{c,in}$ = 210K and $T_{c,in}$ = 234K. In all simulations, the internal wall temperature (imposed on the solid surface) was kept identical in order to isolate the influence of the coolant temperature. For the internal cavity, an adiabatic wall was used for the fluid surface. The

CFD simulations predicted that the coolant temperature had a small influence on the overall effectiveness ϕ, as presented in Figure 3.4.2.1. A 35% increase in plenum temperature led to a 15% decrease in the simulated $\overline{\phi}$ between the rows of holes. The coolant temperature also affected the $\overline{\phi}$ values up to x/d = 8. Farther downstream, the curves collapsed to a single curve. This proves that the temperature of the coolant affects the distributions of ϕ up to x/d = 8. After x/d = 8, Taw had a very little effect on the external ϕ values as seen in Figure 3.1.1.2 (b). The internal cooling dominated the cooling process.

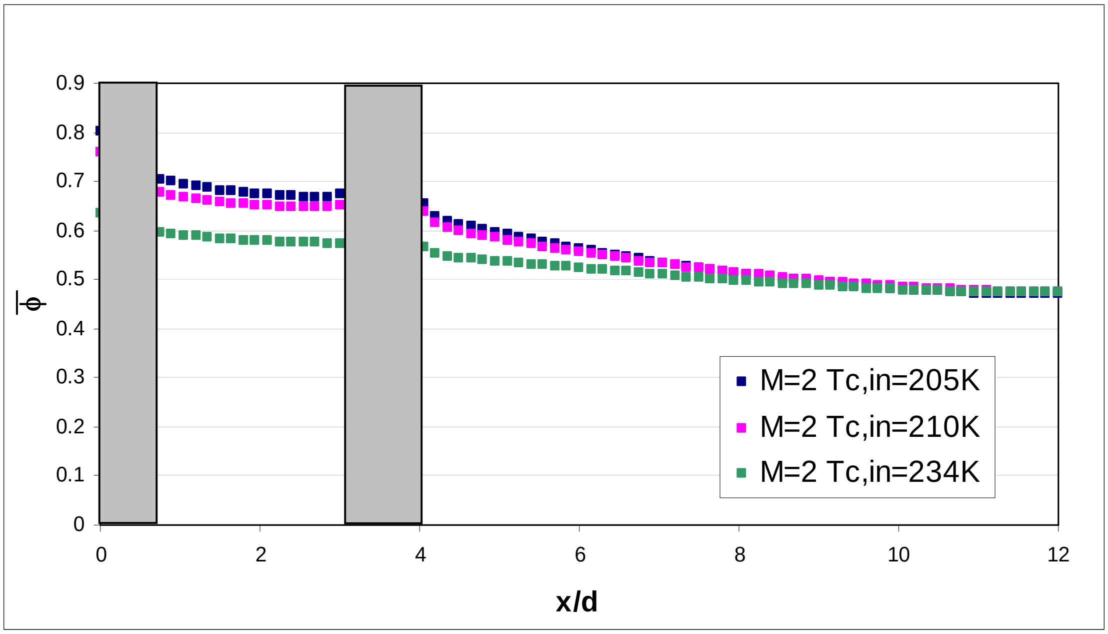

Figure 3.4.2.1: Laterally averaged overall effectiveness for different coolant temperature at the entry of the hole for the three row model at *M* = 2. 0

3.4.3 Sensitivity of the Impingement Plate with the Internal Wall Temperature

The sensitivity of the impingement plate was of interest in this section. A three row conducting model with a different internal temperature than the one measured experimentally was simulated with FLUENT. This was also a check of the sensitivity of the uncertainty in the experimental internal wall temperature values. The new internal wall temperature was obtained from erroneous experimental internal wall temperature, which gave an opportunity to check the internal wall temperature sensitivity. The new data set were roughly $\Delta\theta = \pm 0.05$ different than the nominal value across the whole inside surface. At $M = 2.0$, the new internal wall temperature boundary condition was warmer than the internal wall temperature experimentally measured and imposed for the three row model, whereas for the case $M = 1.0$, the new internal temperature boundary condition was colder, resulting in higher θ values. A plot of the internal temperatures imposed is shown in Figure 3.4.3.1.

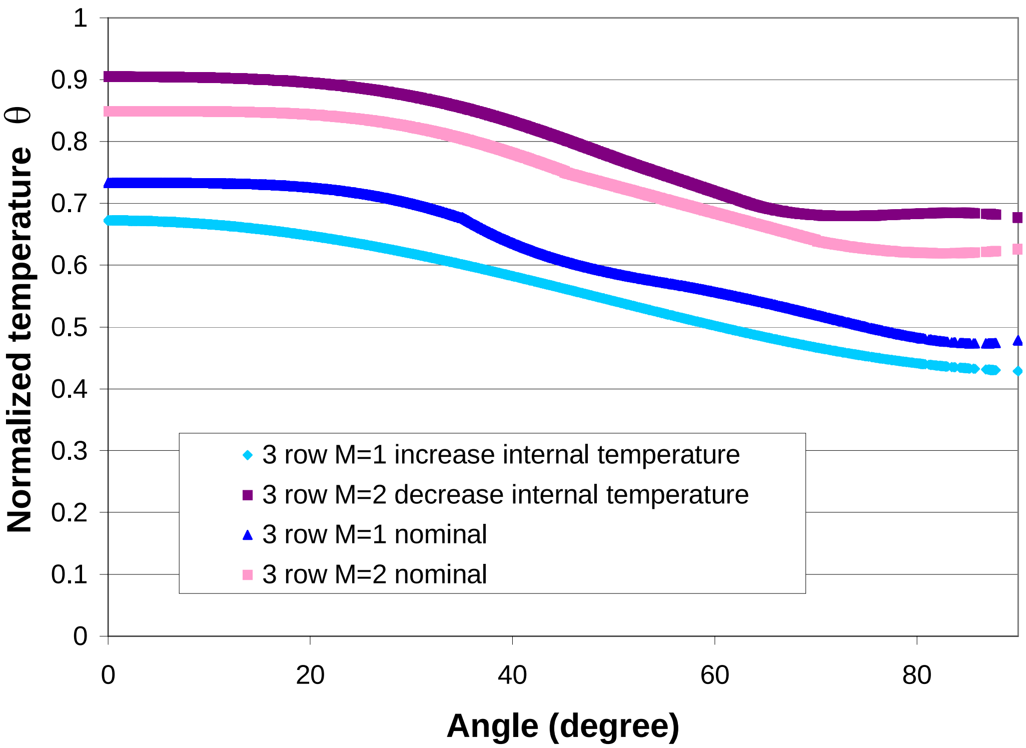

Figure 3.4.3.1: Internal surface temperatures (normalized) and used as the internal wall boundary condition

The computational predictions revealed a small sensitivity to the internal temperature, as seen with the contours of ϕ for both simulations in Figures 3.4.3.2 and 3.4.3.3 at respectively M = 1.0 and M = 2.0. The author is aware that the scale does not necessarily help visualizing the change in ϕ since the change in normalized internal wall temperature is smaller than the color bar resolution. However, any change in trend is still noticeable with this color bar resolution, but the magnitude of the change is not evident. The trends were very similar regardless of the internal temperature imposed. Small differences were observed at the stagnation line. At M = 1.0, the higher internal temperature (case b) did show an entire region of $0.5 < \phi < 0.6$ between the stagnation hole and off stagnation holes, whereas the colder internal wall temperature led to a region on the stagnation line of $0.4 < \phi < 0.5$. Also, Figure 3.4.3.3 revealed that at $M = 2.0$, a higher internal wall temperature than the experimental data (case a) resulted in a less expanded region of high values of $\phi > 0.6$.

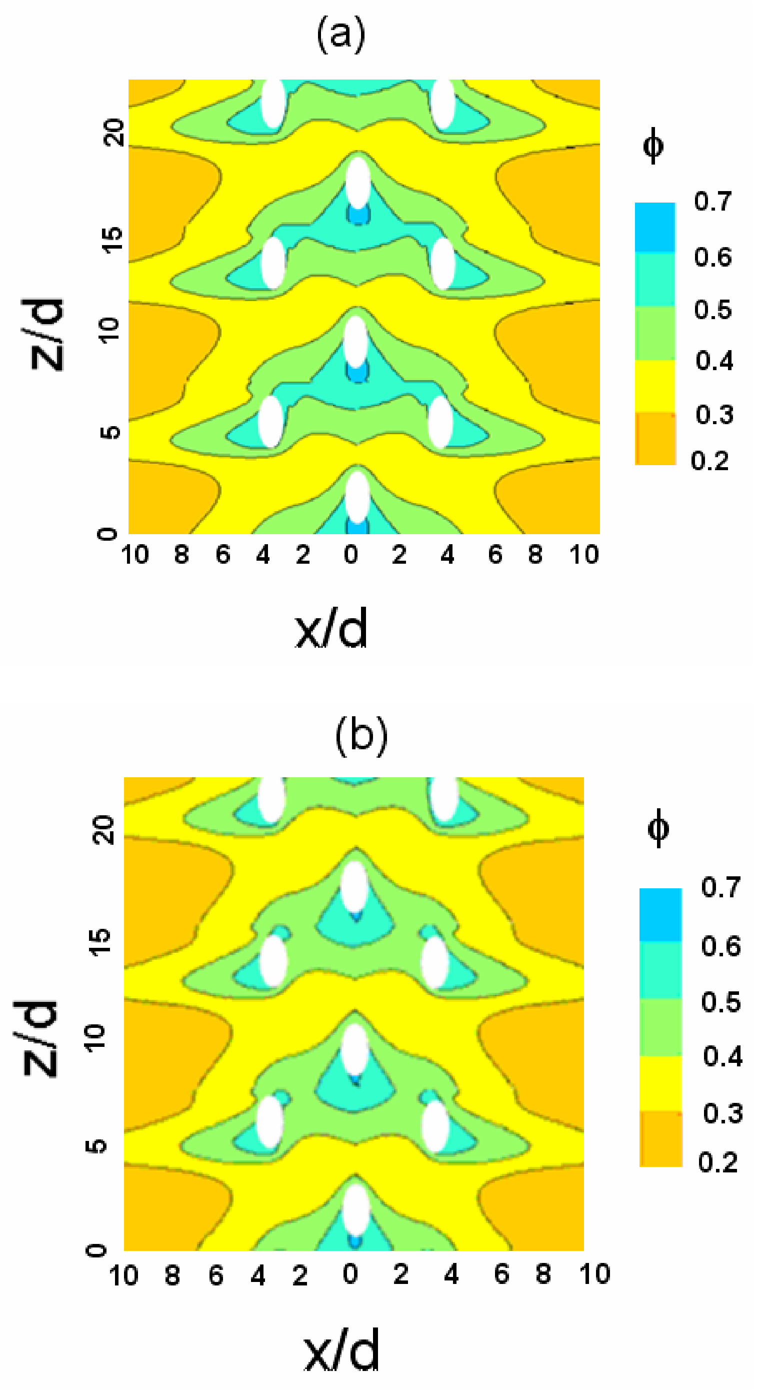

Figure 3.4.3.2: Contours of simulated overall effectiveness for the three-row model at a blowing ratio of M = 1.0 with as the internal temperature, (a) the nominal case and (b) nominal internal θ– 0.05

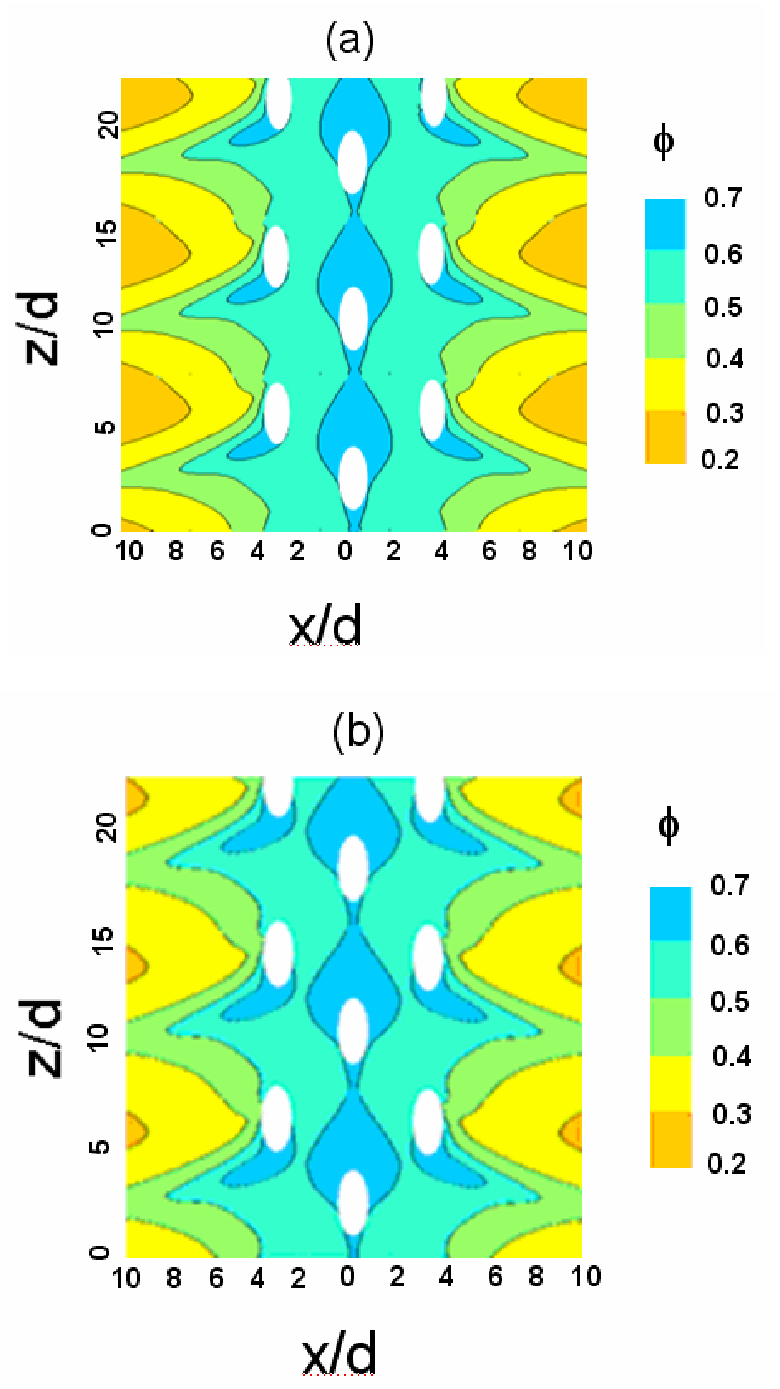

Figure 3.4.3.3: Contours of simulated overall effectiveness for the three-row model at a blowing ratio of $M = 2.0$ with a s the internal temperature, (a) the nominal case and (b) nominal internal $\theta + 0.05$

The laterally averaged overall effectiveness for both internal wall temperature boundary conditions at M = 1.0 and M = 2.0 are plotted in Figures 3.4.3.4 and 3.4.3.5, respectively. The simulated results showed almost no change in $\bar{\phi}$, although there was a significant change in the internal wall temperature boundary condition. This proves that the uncertainty in the experimental internal wall temperature measurements, which was smaller than $\Delta\theta = \pm0.05$, was not an issue to predict ϕ. As expected, lower internal wall temperature led to lower ϕ values for the M = 1.0 case, and higher internal wall temperature resulted in higher ϕ values for M = 2.0.

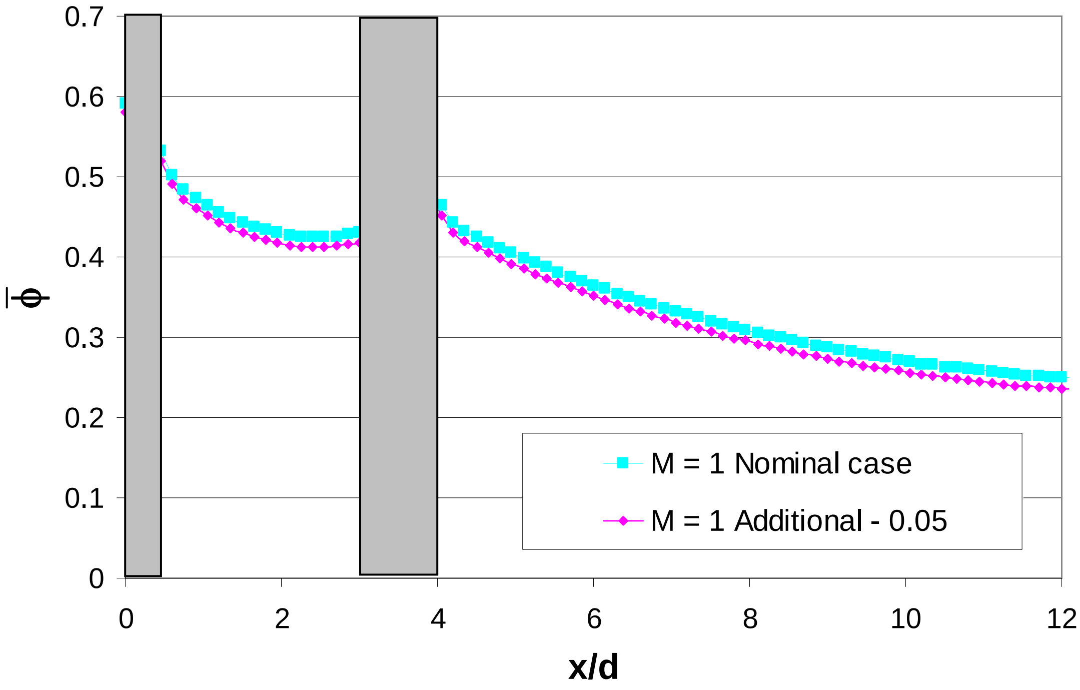

Figure 3.4.3.4: Laterally averaged overall effectiveness at *M* = 1.0 for both internal wall temperature boundary conditions

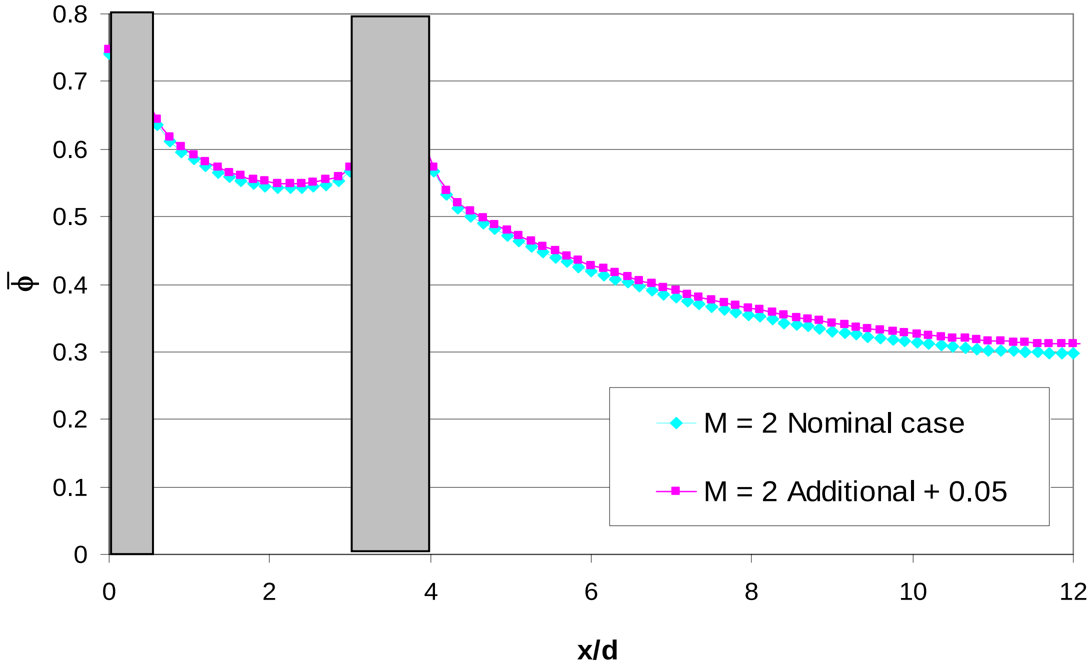

Figure 3.4.3.5: Laterally averaged overall effectiveness at *M* = 2.0 for both internal wall temperature boundary conditions

An analysis of the effects of changing the internal surface temperature on total heat transfer was also conducted and is presented in Table 3.4.3.1. The heat flux was obtained from the direct method of FLUENT, described in Section 3.2.2. As a check, the author verified that the heat flux entering the solid, named "External heat transfer", was equal to the heat flux leaving the solid, represented by "Convective cooling" plus "Internal cooling". As expected, the colder internal wall temperature resulted in a higher external heat transfer. Indeed, the colder internal wall temperature cooled down the external wall temperature, which led to a higher temperature gradient (T_{aw} - T_w) and therefore to a greater external heat transfer. Interestingly, for a blowing ratio of $M = 2.0$, the change in internal wall temperature caused a 28% increase in internal heat transfer, but only a 5% increase in external heat transfer. This was due to a 12% decrease in convective cooling, since the colder internal temperature cooled down the solid, resulting in a smaller temperature difference between the solid wall and the coolant in the holes. Therefore, less heat was extracted through the coolant holes. The 5% increase in external heat transfer led to the very small decrease in ϕ. Less than 0.01 of change in $\overline{\phi}$ was observed between the nominal internal wall temperature and the one with the additional $\Delta\theta = \pm 0.05$. Overall, a large change in internal wall temperature does not necessarily lead to a large change in external wall temperature, since the convective cooling compensates the change in internal cooling by responding in the opposite direction, i.e. a increase in internal cooling is associated by a decrease in convective cooling within the holes, and conversely. Table 3.4.3.2 summarizes the temperature rise through the coolant holes for both blowing ratios and both internal wall temperatures prescribed. It is interesting to notice that the stagnation hole exit temperature was smaller than the one for the off-stagnation hole.

Table 3.4.3.1: Summary of the heat transfer for both blowing ratios and both internal wall temperature boundary condition

θ internal $\Delta\theta = \pm 0.05$	**Internal θ decreased**		**Internal θ increased**	
	M=1		M=2	
HEAT TRANSFER (W)	Heat transfer (W)	% compared to the external heat transfer	Heat transfer (W)	% compared to the external heat transfer
Internal cooling	1.4	**25**	4.1	**52**
Convective cooling	4.1	**75**	3.8	**48**
External heat transfer	5.5		8.0	

Nominal θ internal	**Nominal θ internal**		**Nominal θ internal**	
	M=1		M=2	
HEAT TRANSFER (W)	Heat transfer (W)	% compared to the external heat transfer	Heat transfer (W)	% compared to the external heat transfer
Internal cooling	2.2	**38**	3.2	**43**
Convective cooling	3.7	**63**	4.3	**57**
External heat transfer	5.9		7.6	

Table 3.4.3.2: Summary of the temperature rise through the holes for both blowing ratios and both internal wall temperature boundary condition

θ internal $\Delta\theta = \pm 0.05$	**Internal θ decreased**		**Internal θ increased**	
	Stagnation hole		Off-stagnation hole	
TEMPERATURE (K)	M=1	M=2	M=1	M=2
Tc,entrance	216.2	210	216	210.1
***Tc,exit	225.7	213.8	226.4	215.2
ΔT	**9.5**	**3.8**	**10.4**	**5.1**

Nominal θ internal	**Nominal θ internal**		**Nominal θ internal**	
	Stagnation hole		Off-stagnation hole	
TEMPERATURE (K)	M=1	M=2	M=1	M=2
Tc,entrance	215.8	210.2	215.7	210.2
***Tc,exit	225.3	214.4	224.6	215.8
ΔT	**9.5**	**4.2**	**8.9**	**5.6**

3.4.4. Sensitivity to the Impingement Plate

The effect of the internal impingement was of interest in this section. A simulation with no impingement plate was conducted to determine the effects of the impingement plate on the overall effectiveness. In this simulation, the solid surface and fluid surface were coupled. In the past, Mouzon (2005) measured the influence of the impingement plate on a three row conducting model with shaped holes. For a higher blowing ratio of $M = 2.0$, he found that the impingement plate has no noticeable effect on the stagnation line. His measurements showed that the impingement plate model delivered slightly higher laterally averaged overall effectiveness than the no-impingement case with a 15% increase at $x/d = 12$ for $M = 2.0$. This difference farther downstream can be explained by the impingement plate acting like a heat sink. The impingement plate is made of metal, which conducts a certain amount of heat from the external surface to the internal surface. This phenomenon was studied by Dyson and Davidson (2009) for an adiabatic model. They measured an increase in coolant temperature of $\Delta T = 5.5\text{K}$ at $M = 2$ due to the conduction error induced by the impingement plate. This effect was also observed computationally for the conducting model. At $M = 2$, the simulated convective cooling through the walls led to a $\Delta T = 3.5\text{K}$ increase in coolant temperature. Terrell (2004) measured the coolant temperature at the entry of the hole and found $T_c = 210\text{K}$. The discrepancy between the experimental temperature of Terrell (2004) and the simulated temperature of $T_c = 203.4\text{K}$ was attributed to the conduction through the impingement plate, causing an increase in plenum temperature of $\Delta T = 6.5\text{K}$. As expected, the conduction error was higher for the conducting model than for the adiabatic model, since the model also warmed up the impingement plate for the conducting case. The schematic in Figure 3.4.4.1 illustrates the conduction effect of the impingement plate. Not only is heat coming from the external to the internal surface, but also from the model, which was warmer than the impingement plate. It resulted in an artificial increase in the coolant temperature.

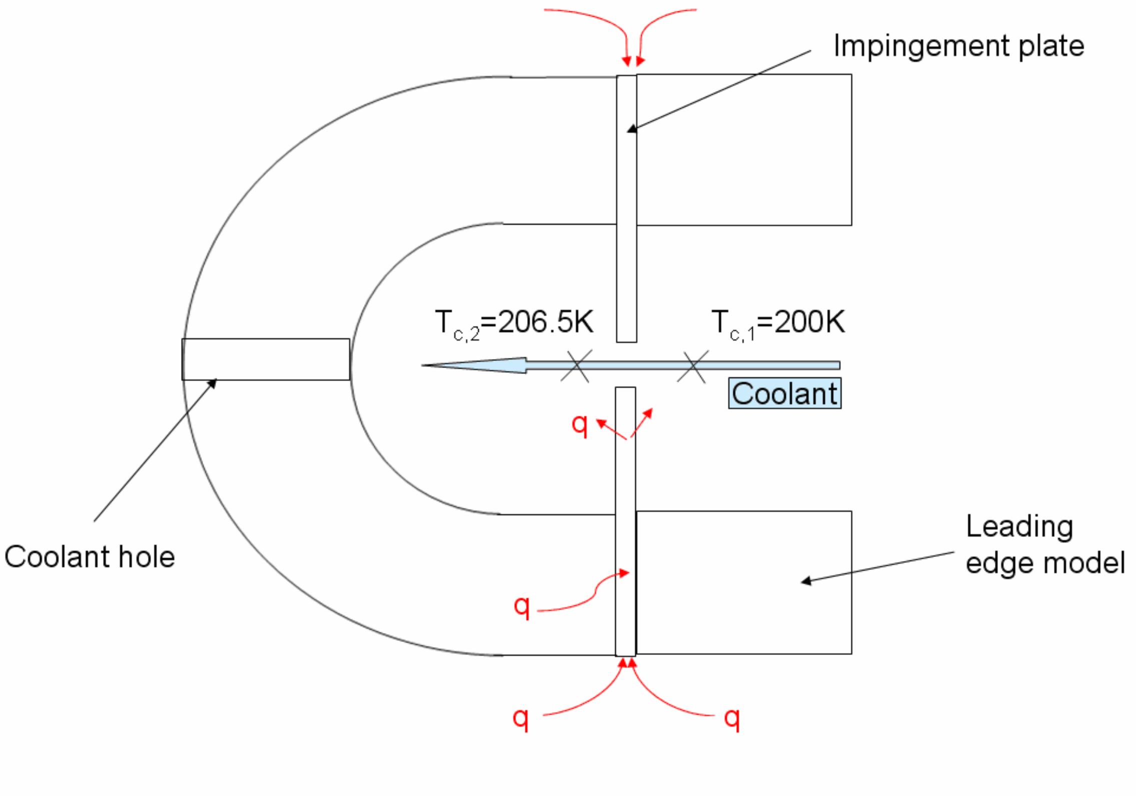

Figure 3.4.4.1: Schematic illustrating the warming up of the coolant due to the impingement plate for a blowing ratio of *M* = 2.0

To be able to compare the impingement and no-impingement cases, the conducting error generated by the impingement was isolated. Therefore, a new normalized temperature for the impingement plate simulation was defined as follows:

$$\Phi' = \frac{T_\infty - T_{w,out}}{T_\infty - T_{c,impingement}} \qquad (3.4.4.1)$$

where $T_{c,impingement}$ is the coolant temperature, which takes into account the conduction error induced by the impingement plate. Therefore, $\mathrm{T}_{\mathrm{c,impingement}}$ is equal to the initial plenum temperature $T_{c,1}$, and the correction temperature, $\Delta T_{\mathrm{correction}}$ where $\Delta T_{\mathrm{correction}}$ = 6.5K for M = 2.0, as seen in Figure 3.4.4.1.

Contours of normalized temperature for the impingement and no-impingement cases are presented in Figure 3.4.4.2 for a blowing ratio of M = 2.0 and a thermal conductivity of k = 1.04W/mK. As Mouzon (2005) found experimentally, contours of normalized temperature for both cases were very similar. The main difference was observed farther downstream of the holes, where the impingement plate acted like a sink. Laterally averaged overall effectiveness for both cases is plotted in Figure 3.4.4.2. At x/d = 12, computational predictions showed a 25% increase of overall effectiveness due to the impingement plate whereas Mouzon (2005) measured a 15% increase.

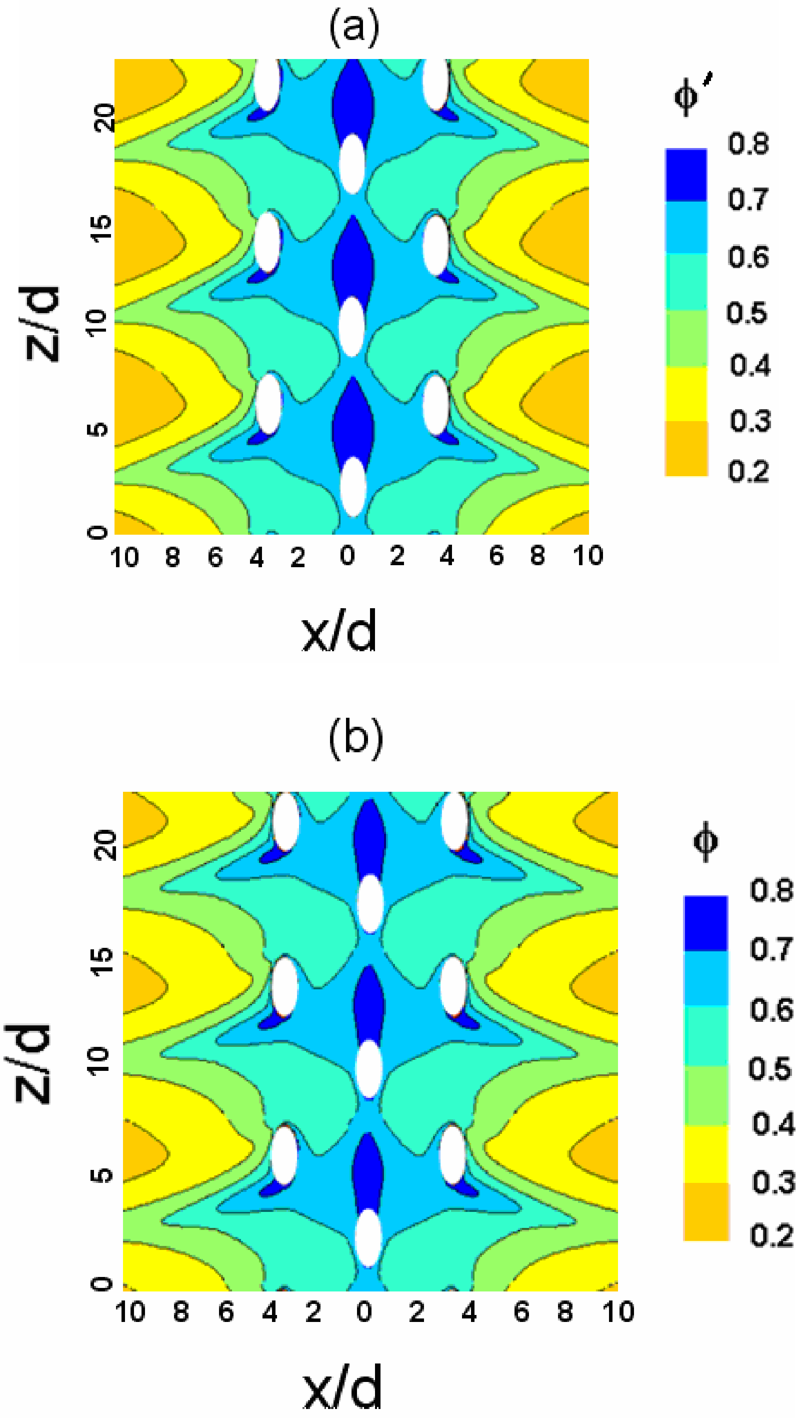

Figure 3.4.4.2: Contours of overall effectiveness at *M* = 2.0 for *k* = 1.04W/mK (a) without impingement plate and (b) with impingement plate.

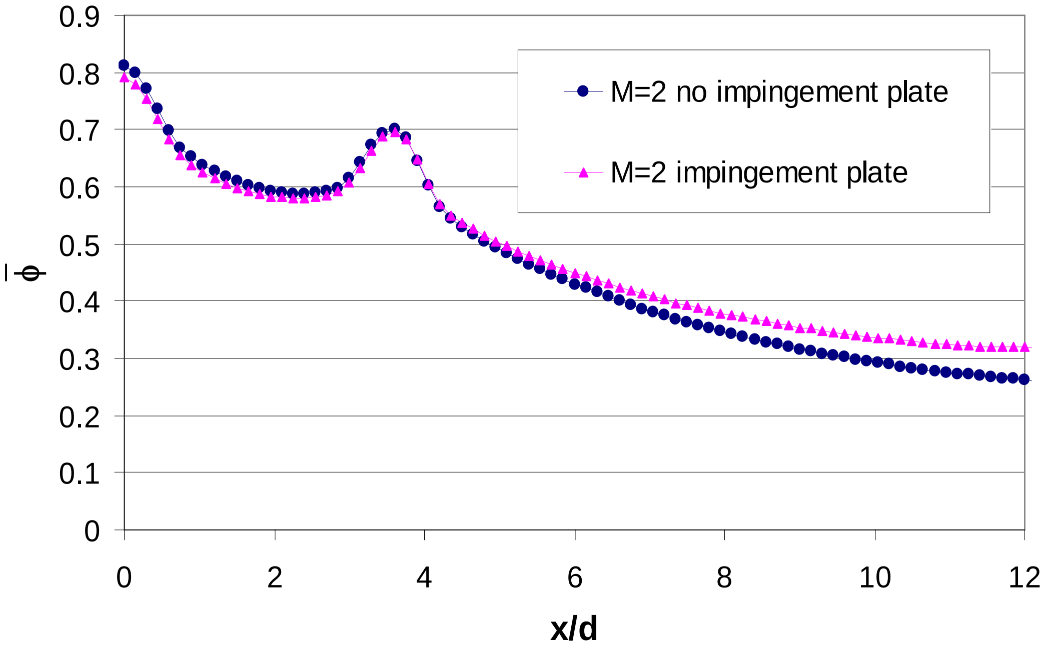

Figure 3.4.4.3: Laterally averaged overall effectiveness at *M* = 2.0 for the impingement case and the no-impingement case

An understanding why the internal impingement plate does not significantly decrease external surface temperatures can be gained with the visualization of the normalized internal wall temperature, as shown in Figure 3.4.4.4. For the impingement case, the internal wall temperature was obtained from Dyson' and Davidson' experiments. The internal wall temperature was normalized using ϕ' defined in equation 3.4.4.1 to allow the comparison with the internal wall temperature, ϕ, for the no-impingement case. It is interesting to notice that the no-impingement case showed a continuous region of very high ϕ values on the stagnation line, presumably due to the strong convective cooling through the holes. This highlights the inefficiency of the impingement jets on the stagnation line. The small temperature difference between the coolant jet and the internal wall led to a small convective heat transfer through the internal wall, regardless of the internal heat transfer coefficient. Therefore, the increase in heat transfer coefficient generated by the impingement plate had a small effect on the convective heat transfer through the internal wall since the temperature gradient was very small. Laterally averaged normalized temperatures are also presented in Figure 3.4.4.5. The higher normalized temperature for the impingement case downstream of the holes can be explained by two phenomena: the impingement plate acting like a heat sink and the stronger recirculation of the coolant inside the plenum.

Additionally, the increased internal heat transfer coefficients due to the use of the impingement jets have the effect of reducing the internal surface temperature and it was proved in the last section that the internal wall temperature has a small to negligible effect to the external temperature.

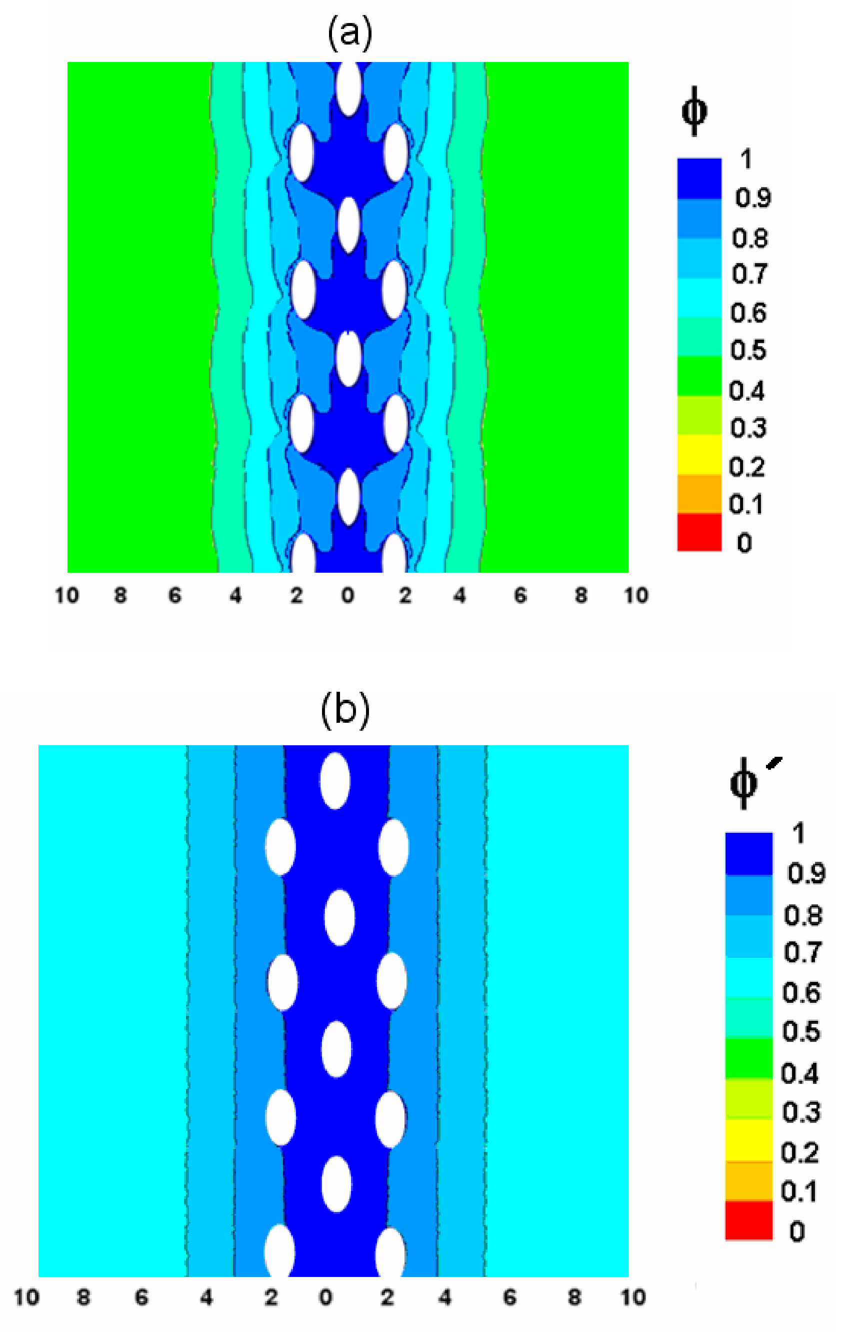

Figure 3.4.4.4: Contours of normalized temperature for the internal wall at *M* = 2.0 for *k* = 1.04W/mK (a) without impingement plate and (b) with impingement plate

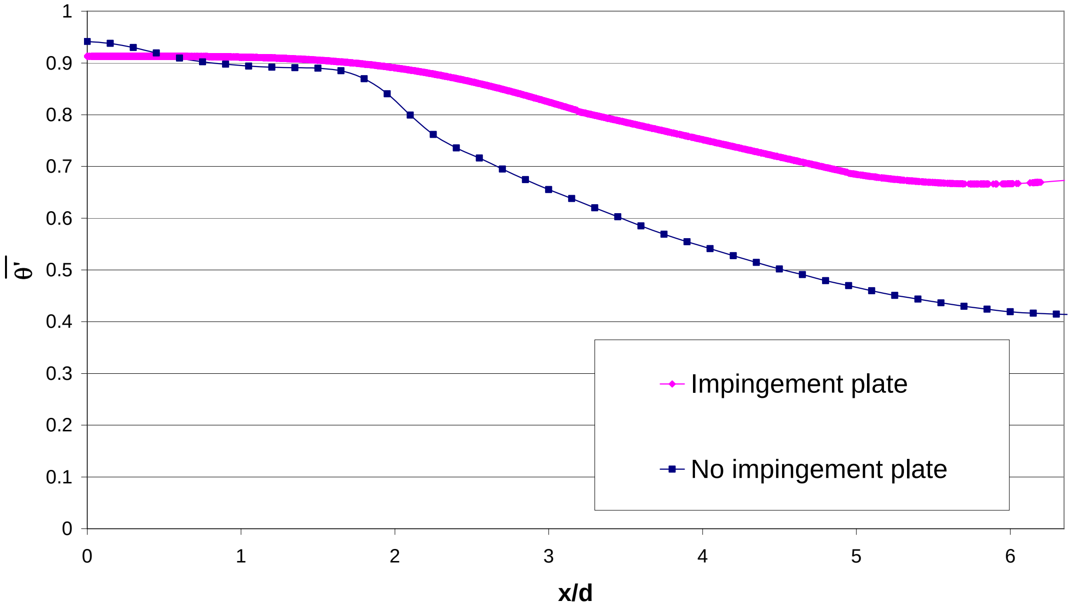

Figure 3.4.4.5: Laterally averaged normalized temperature for the internal wall at M = 2.0 for the impingement case and the no-impingement case

3.5 EVALUATION OF THE HEAT TRANSFER PREDICTED WITH T_{AW}

The main focus of this section is to question the legitimacy of T_{aw} as the driving temperature for the heat transfer coefficient. It has been taken for granted that T_{aw} is the appropriate driving temperature for heat transfer to a film cooled surface. According to Harrison (2006), assuming the adiabatic wall temperature to be the heat transfer driving temperature is generally a reasonable assumption; however, it can result in significant local errors. The Harrison (2006) study was limited to a flat plate case. In this section, the author focuses on the simulated leading edge of a blade.

To evaluate the validity of the adiabatic wall temperature assumption, a comparison was done between the heat flux predicted using T_{aw} and the heat flux obtained by the CHT analysis. The heat flux obtained from the CHT computation simulated the actual heat flux leaving or entering the leading edge. The predicted heat flux was derived from equation 1.1.4.1. The heat transfer coefficient in equation 1.1.3.1 was obtained from a simulation of a constant heat flux simulation, as is commonly done experimentally. A constant heat flux of $q'' = 3000$ W/m^2 was imposed. As explained earlier, this value corresponds to the averaged 'actual' heat flux, obtained from the computational predictions for the conducting wall. As the constant heat flux experiments are typically conducted using a density ratio of $DR = 1.0$, the coolant and mainstream temperatures were both set at $T = 300$ K. The heat transfer coefficient for the constant heat flux simulation was obtained from Equation 3.2.3.1. The driving temperature is for this case the mainstream temperature, since the simulations were run at $DR = 1.0$. Contours of the heat transfer coefficient for a blowing ratio of $M = 2.0$ are presented in Figure 3.5.1. These contours are very similar to the computational predictions of York and Leylek (2002), which was expected since they used the same realizable k-ε turbulence model. The plot of h_f/h_0 in Figure 2.3.5.1 reveals two regions of very high h_f/h_0 values located directly aft the off-stagnation hole. These very high values are explained by the strong vortex created by the mainstream flow, as it tripped over the coolant jet exiting the off-stagnation holes, as observed by York and Leylek (2002). However, the computational predictions did not agree well with the experimental data of

Yuki (1998). Indeed, h_f/h_0 measurements did not show such elevated values downstream of the off-stagnation hole. Not only did the magnitude differ between the experimental data and the computational predictions, but also the location of this very high region was different. In Yuki's experimental data, one single area of high values was observed just behind the off-stagnation hole, whereas the computational simulations showed two areas at both extremities of the off-stagnation hole. To this date, the origin of the discrepancies between the experimental data and the computational prediction is not clear and needs further examination.

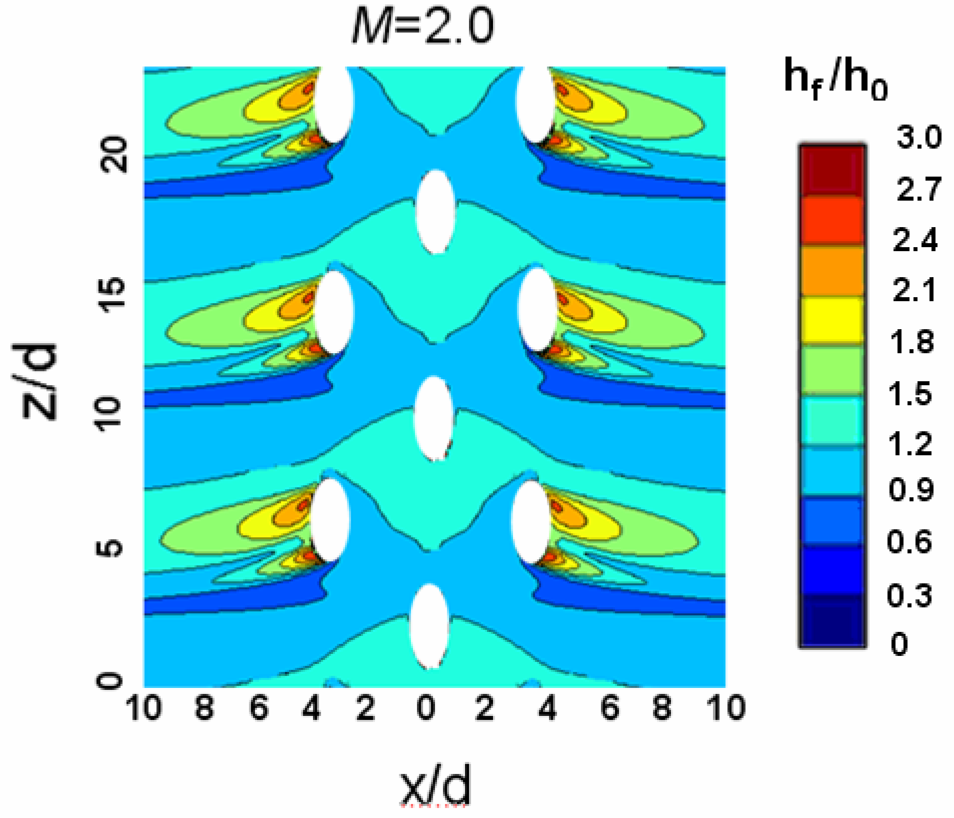

Figure 3.5.1: Contours of heat transfer coefficient obtained from the constant heat flux simulation at *M* = 2.0

Presented in Figure 3.5.2 and 3.5.3, are the other variables required for the prediction of *q"* using T_{aw} for a blowing ratio of $M = 2.0$. They are defined in terms of non dimensional temperature, ϕ_{aw} and ϕ. ϕ_{aw} was defined according to the following equation:

$$\phi_{aw} = \frac{T_\infty - T_{aw}}{T_\infty - T_c} \tag{3.5.1}$$

As a reminder, the adiabatic wall temperature used for q''_{pred} is defined according to Equation 1.1.4.2:

$$T_{aw} = T_{\infty} - \eta * \left(T_{\infty} - T_{c,out}\right) \tag{1.1.4.2}$$

where $T_{c,out}$ is the coolant temperature at the exit of the hole for the conducting model. ϕ_{aw} is different from η because the coolant reference is not the same. ϕ_{aw} take into account the increase in coolant temperature due to the convective cooling through the holes and the internal wall for the conducting leading edge model.

In general, the normalized temperature ϕ_{aw} was smaller than the overall effectiveness, ϕ, indicating that the predicted heat flux would mainly enter the plate. As explained before, the conducting wall presented much less variation in temperature than the adiabatic wall since the conducting wall was able to spread the heat, resulting in a more uniform wall temperature. On the stagnation line, ϕ_{aw} was in a similar range than ϕ, i.e between $0.6 < \phi < 0.7$. Therefore, a small heat flux was expected. Downstream of the off-stagnation hole, ϕ_{aw} was greater than ϕ, which would result in a positive predicted heat flux. Surface contours of the predicted heat flux, q''_{pred}, are shown in Figure 3.5.4. The heat flux was generally directed into the leading edge, which was defined as negative in the contour plot. However, downstream of the off-stagnation holes, there was a narrow region where the heat flux was positive. This region of positive heat flux corresponds to location of the coolant jet flowing downstream of the off-stagnation holes.

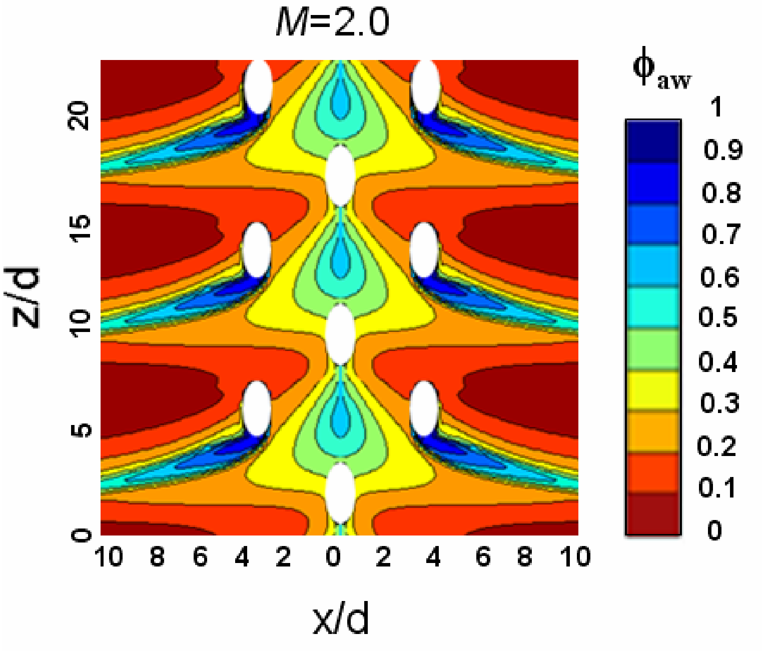

Figure 3.5.2: Contours of normalized temperature ϕ_{aw} at M = 2.0

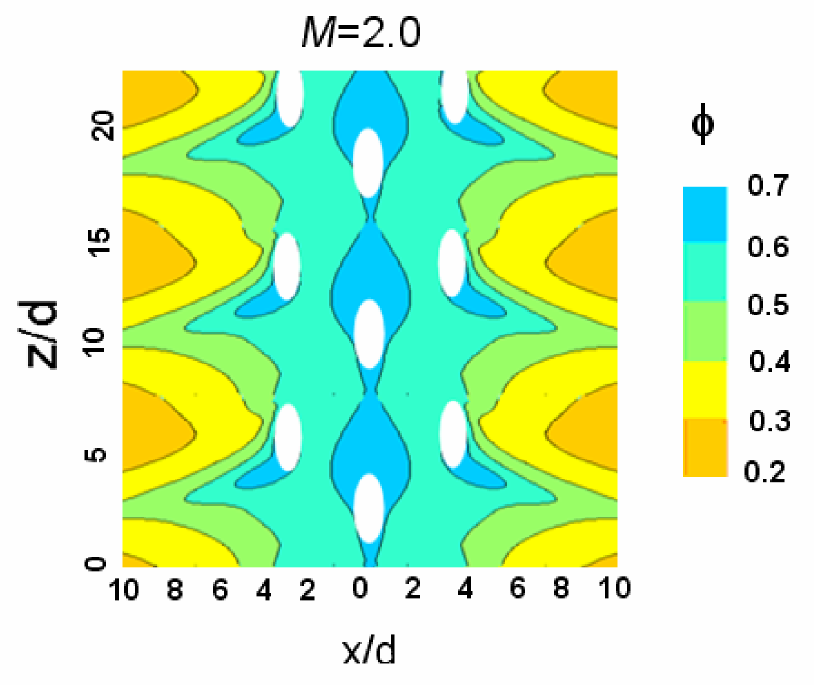

Figure 3.5.3: Contours of normalized temperature ϕ at M = 2.0

Contours of the heat flux into the surface for the conducting model, q''_{cond}, are presented in Figure 3.5.5. Comparison of contours plots of q''_{pred} and q''_{cond} provides an answer to the question of whether T_{aw} is the driving temperature for heat transfer. Contours of q''_{pred} and q''_{cond} look very much alike. After $x/d = 5$, the heat flux predicted using T_{aw} as the driving temperature gave similar results than the conducting heat flux obtained from the CHT analysis. The main disparity occurred between the stagnation and off-stagnation lines, where the predicted heat flux showed a large region of q'' between 0 and -3000 W/m^2. For the conducting simulation, the region of $-3000 < q'' <0$ was smaller and a positive heat flux was observed on the stagnation line. The conducting simulation also showed a region of very high heat flux entering the leading edge, $-9000 < q'' < -6000$, between the stagnation and off-stagnation holes, whereas the same region of high heat flux was very localized around the off stagnation hole for the predicted heat flux. Overall, the heat flux was well predicted with the use of the adiabatic wall temperature, which confirms that generally, the adiabatic wall temperature is the appropriate temperature for heat transfer.

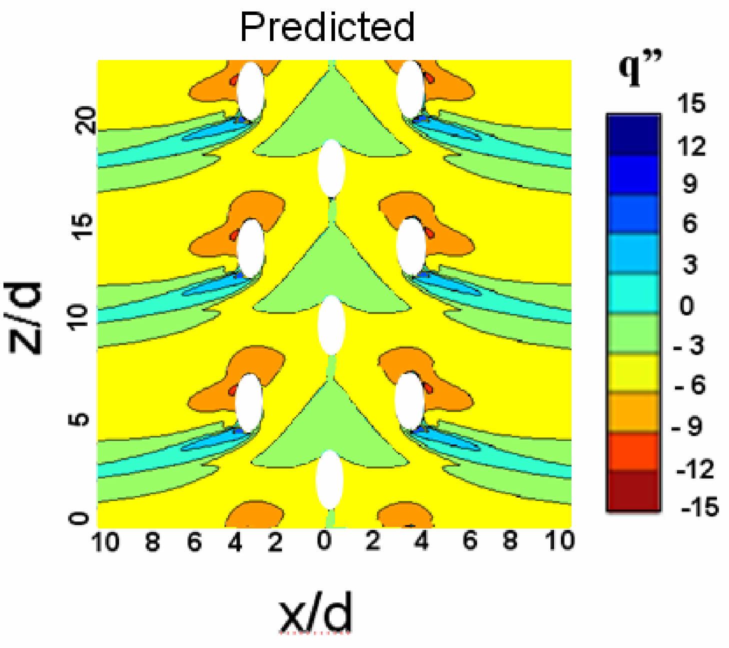

Figure 3.5.4: Contours of the predicted heat flux at *M* = 2.0 (kW/m2)

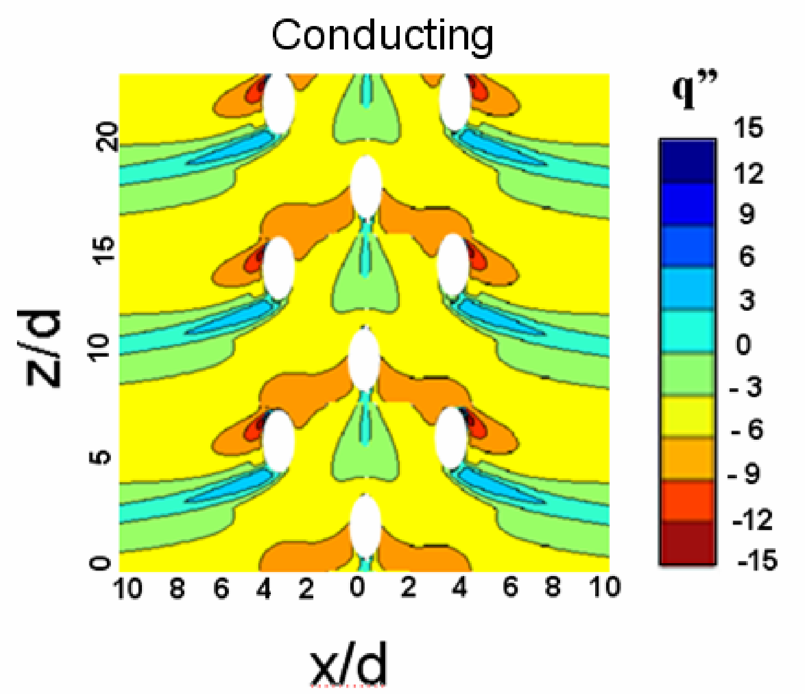

Figure 3.5.5: Contours of the conducting heat flux at *M* = 2.0 (kW/m2)

To gain a better understanding why T_{aw} is a reasonable assumption for the driving temperature for heat transfer, comparison of the predicted and actual heat flux was done at various lateral positions: $x/d = 1$, 5 and 9. It is evident that, at $x/d = 1$, the predicted heat flux was generally higher than the actual heat flux, as seen in Figure 3.5.6. The laterally averaged predicted heat flux was 12% higher than the laterally averaged actual heat flux at $x/d = 1$. However, local values showed discrepancies up to 30% between q''_{pred} and q''_{cond}.

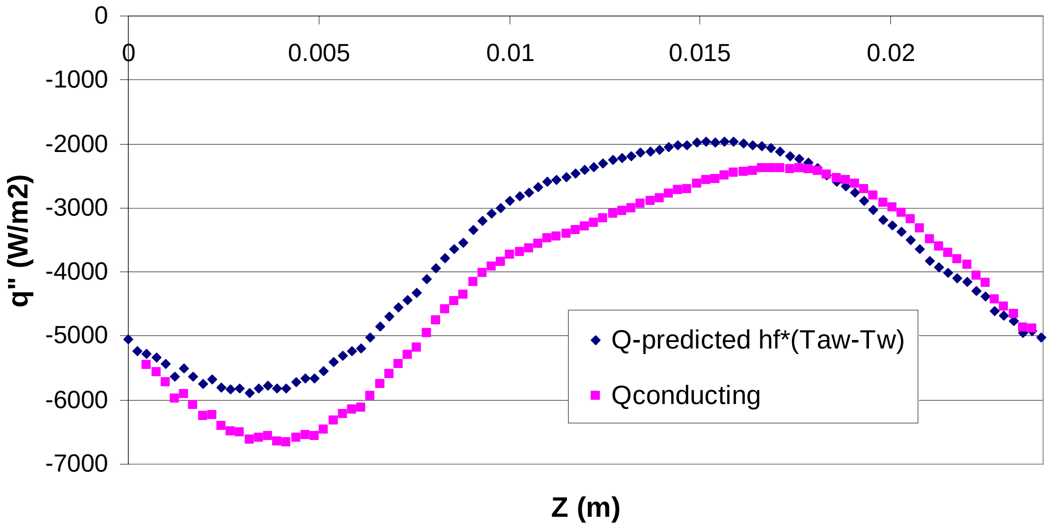

Figure 3.5.6: Lateral variation in predicted and actual heat flux for $M = 2.0$ and $x/d = 1.0$

Thermal boundary layer profiles were used to understand the disparity between the actual and predicted heat flux. In Figure 3.5.7, thermal profiles of the temperature above the adiabatic and conducting wall are presented at the location z = 15 mm. The constant heat flux thermal profile is also included in this figure to provide an indication of the extent of the thermal boundary layer for the constant heat flux condition. The adiabatic thermal profile was flat for a relatively short distance away from the wall. The constant heat flux simulation revealed that the thermal boundary layer had a thickness of about 0.1 mm. Note that over this distance of 0.1 mm, the air temperature for the adiabatic wall can vary from T = 249K (at the wall) to T = 263K. The effective freestream temperature for the conducting case would be larger than the adiabatic wall temperature of T_{aw} = 249K. Consequently, the driving temperature would be expected to be larger than T_{aw}, resulting in a higher q'' than the heat flux predicted with T_{aw}. This is consistent with the results in Figure 3.5.6.

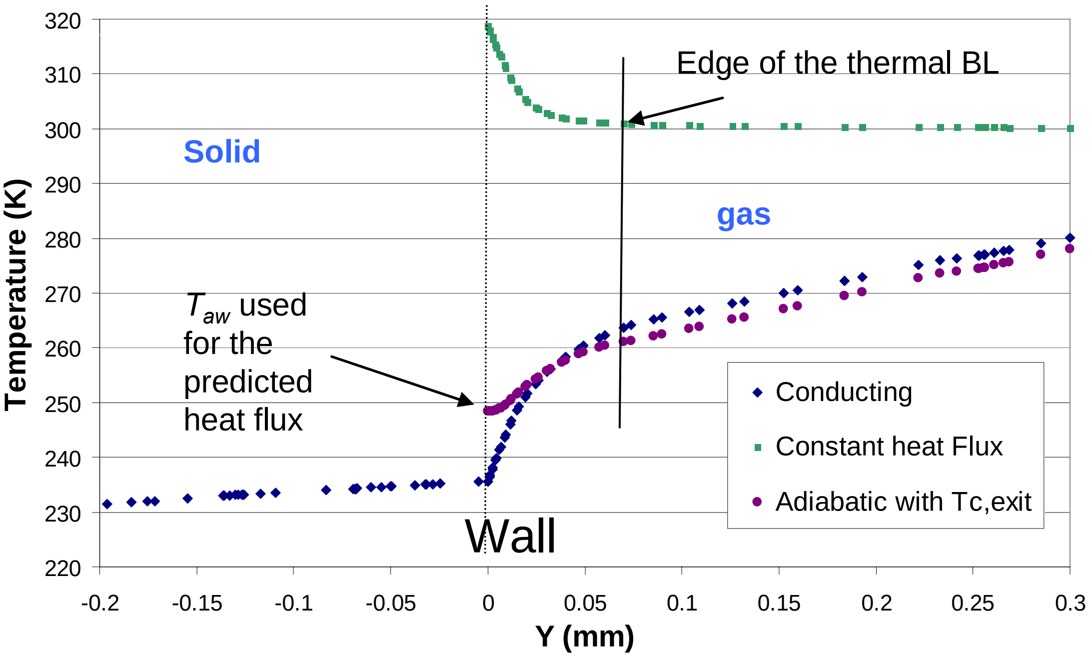

Figure 3.5.7: Thermal profiles above adiabatic, constant heat flux and conducting walls for M = 2.0 at x/d = 1.0 and z = 15 mm. (y = 0 corresponds to the wall)

Surprisingly, the thermal profiles for the adiabatic and conducting simulations did not merge beyond 0.1 mm from the wall where the constant heat flux simulation showed the edge of the thermal boundary layer. Indeed, the conducting wall should have only influenced the surrounding gas up to the edge of the thermal boundary layer. Thorough insight can be gained with the contours of the thermal profiles at $x/d = 1$ centered on $z =$ 15 mm presented in Figure 3.5.8. The simulations for the adiabatic and conducting simulations were run with the same grid. Figure 3.5.9 includes the grid mesh on top of the thermal profiles to show the identical grid mesh. The contours of thermal profiles for the adiabatic and conducting simulations in Figure 3.5.8 shows the same difference in temperature for both simulations above the edge of the constant heat flux thermal boundary layer. The author concluded that the difference resulted from numerical uncertainty. The criteria of convergence might not have been exactly the same and might have resulted in small discrepancies between adiabatic and conducting simulations.

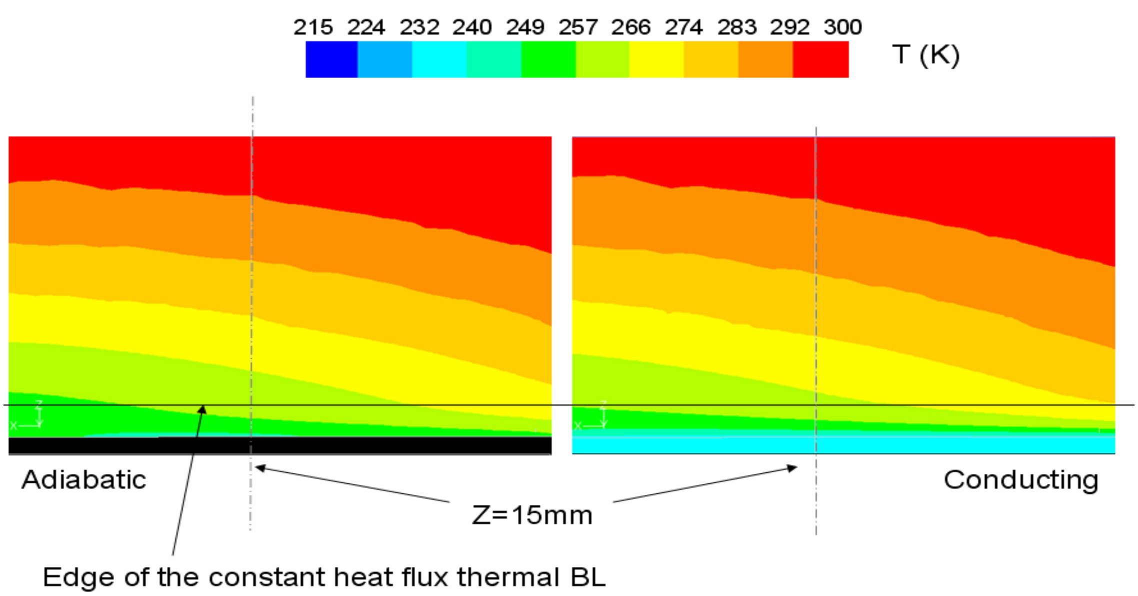

Figure 3.5.8: Thermal profiles above the adiabatic and conducting walls for M = 2.0 and x/d = 1.0

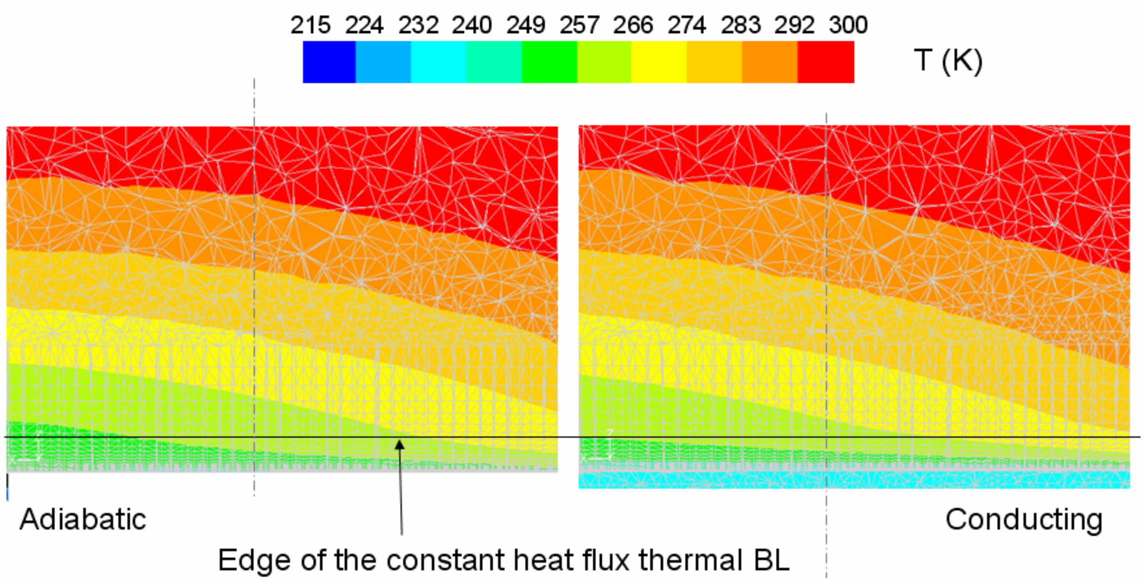

Figure 3.5.9: Thermal profiles above the adiabatic and conducting walls including the grid mesh for M = 2.0 and x/d = 1.0

The predicted and actual heat fluxes are shown in Figure 3.5.10 for *M* = 2.0 and *x/d* = 5. First, both curves matched very well. The magnitudes of the peaks were similar for both heat fluxes, q''_{pred} and q''_{cond}. This shows that the adiabatic wall temperature was an appropriate driving temperature for heat transfer at *x/d* = 5.0. However, it was surprising that the predicted and conducting heat fluxes gave the same values at the jet location. The conducting wall has developed a thermal boundary layer, which has warmed up the surrounding gas up inside the thermal boundary layer. Therefore, the behavior of the coolant jet for the conducting and the adiabatic cases would be expected to be different. The author would not have expected the adiabatic wall temperature to be the appropriate driving temperature at this particular location.

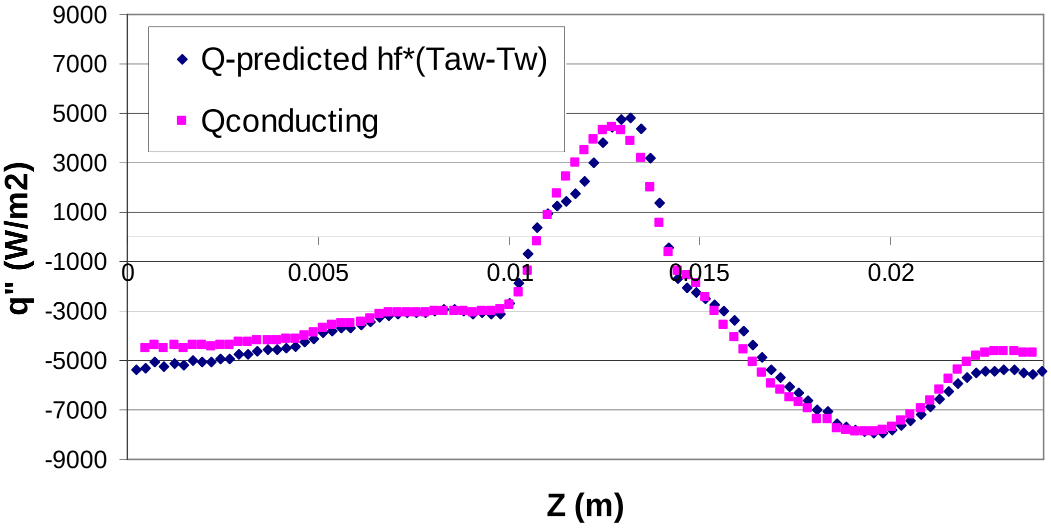

Figure 3.5.10: Lateral variation in predicted and actual heat flux for *M* = 2.0 and *x/d* = 5.0

A review of all the variables required to obtain the predicted heat flux values is presented in Figure 3.5.11. The two peaks observed in the heat transfer coefficient values were also seen in the contours of heat transfer coefficient in Figure 2.3.5.1. The lower peak located around *z* = 13 mm were close to the jet location at *x/d* = 5.0. By definition, the predicted heat flux curve crossed the *q"* = 0 line when the adiabatic wall temperature is equal to the wall temperature.

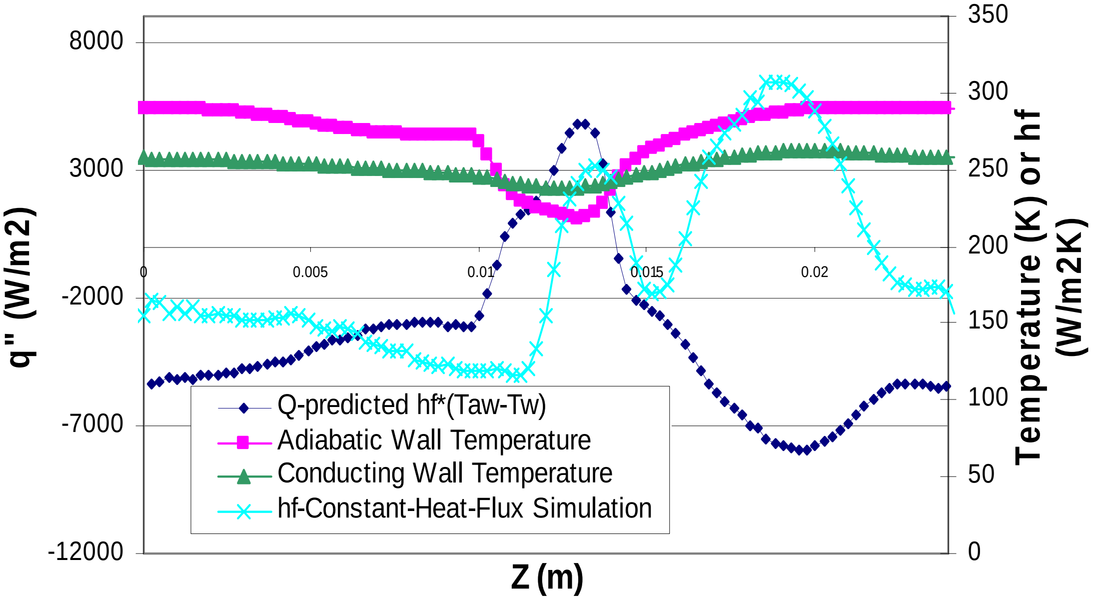

Figure 3.5.11: Lateral variation of all the variables included in the heat flux prediction using T_{aw} for $M = 2.0$ and at $x/d = 5.0$

As an insight, the thermal profiles over the adiabatic, constant heat flux and conducting walls are plot in Figure 3.5.12. The dashed line represents the wall location. The temperature profiles for the adiabatic and conducting cases merged at some distance away from the surface, which corresponded to the edge of the thermal boundary layer. It was surprising that T_{aw} gave a correct prediction of the actual heat flux, considering that the minimum gas temperature above the conducting wall, about 228 K, was much higher that $T_{aw} = 219$ K . The reason why T_{aw} gave a correct prediction of heat transfer has not been solved yet and needs further investigation.

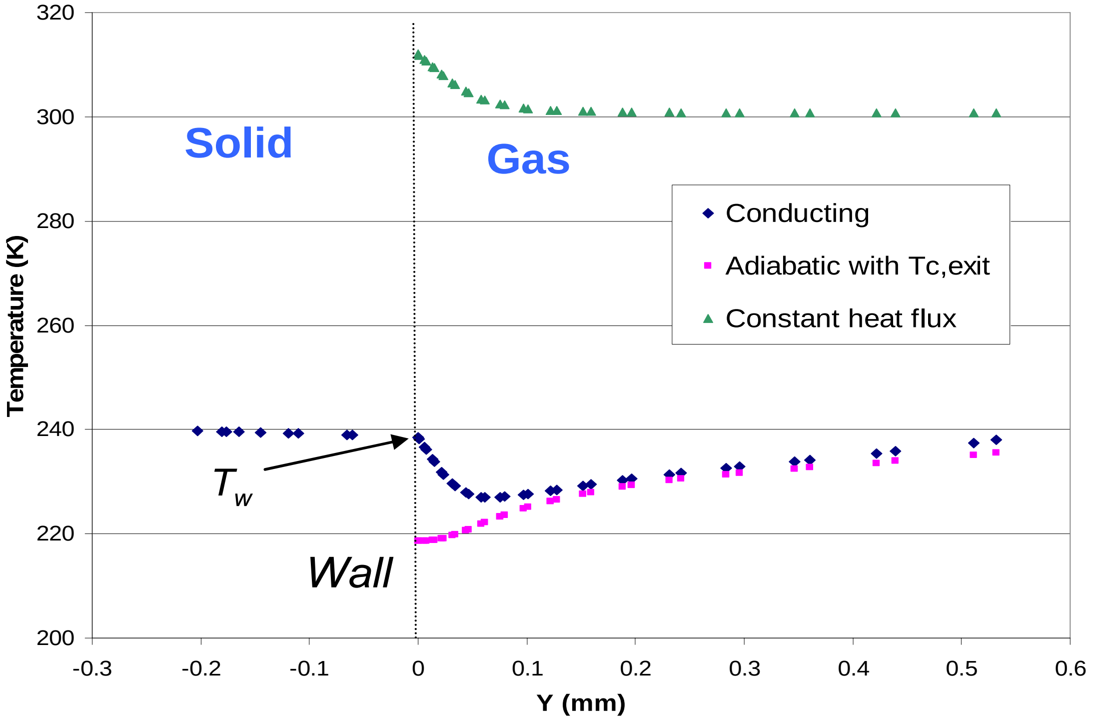

Figure 3.5.12: Thermal profiles above adiabatic, constant heat flux and conducting walls for $M = 2.0$ at $x/d = 5.0$ and $z = 13$ mm. ($y = 0$ corresponds to the wall)

Another thermal profile was done at *x/d* = 5.0 and *z* = 14.1 mm, where the predicted and conducting heat flux were zero. The results are shown in Figure 3.5.13, which reveals that, at a very short distance from the wall, y < 0.05 mm, the adiabatic and conducting thermal profiles were identical. As seen in Figure 3.5.10, the conducting heat flux was also zero at this location. This corresponds to the transition between two regions: a region where the heat flux is entering the solid and another one where the heat flux is leaving the solid. As no thermal boundary layer was created, a similar thermal profile for the conducting and adiabatic simulation was expected.

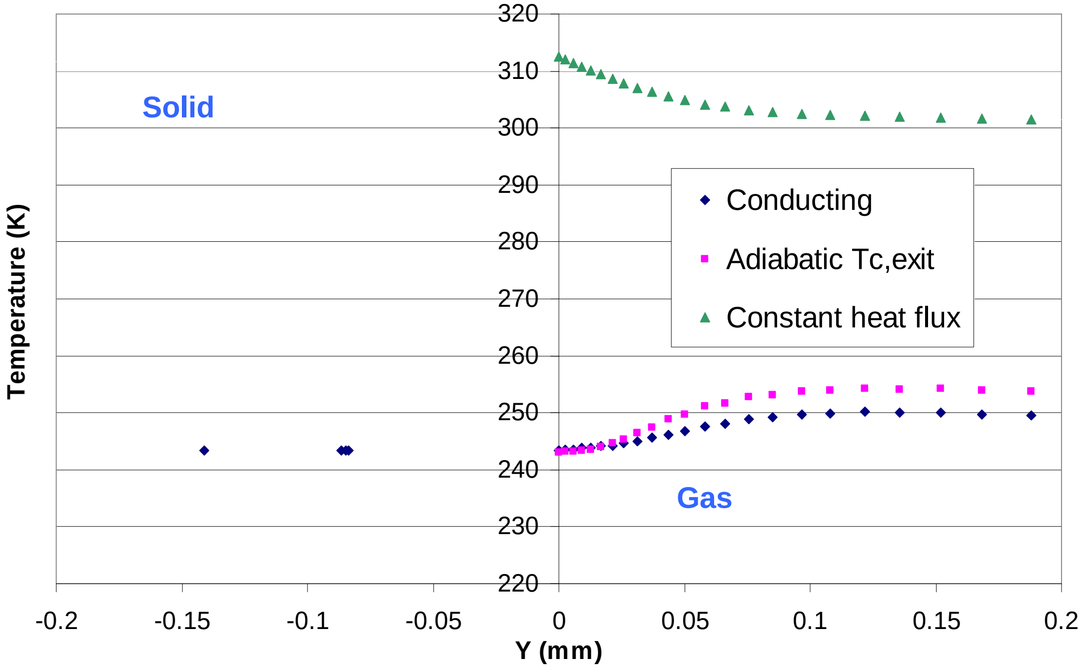

Figure 3.5.13: Thermal profiles above adiabatic, constant heat flux and conducting walls for *M* = 2.0 at *x/d* = 5.0 and *z* = 14.1 mm. (*y* = 0 corresponds to the wall)

The contours of thermal profiles are presented in Figure 3.5.14 to try to explain why the adiabatic and conducting thermal profiles differed farther away from the wall. No clear explanation was found. The shape of the off-stagnation coolant jet is clearly visible. The dashed line entitled z =14.1mm is located at the extremity of the coolant jet, where the jet did not cool the surface anymore. At this location, no heat flux left or entered the leading edge.

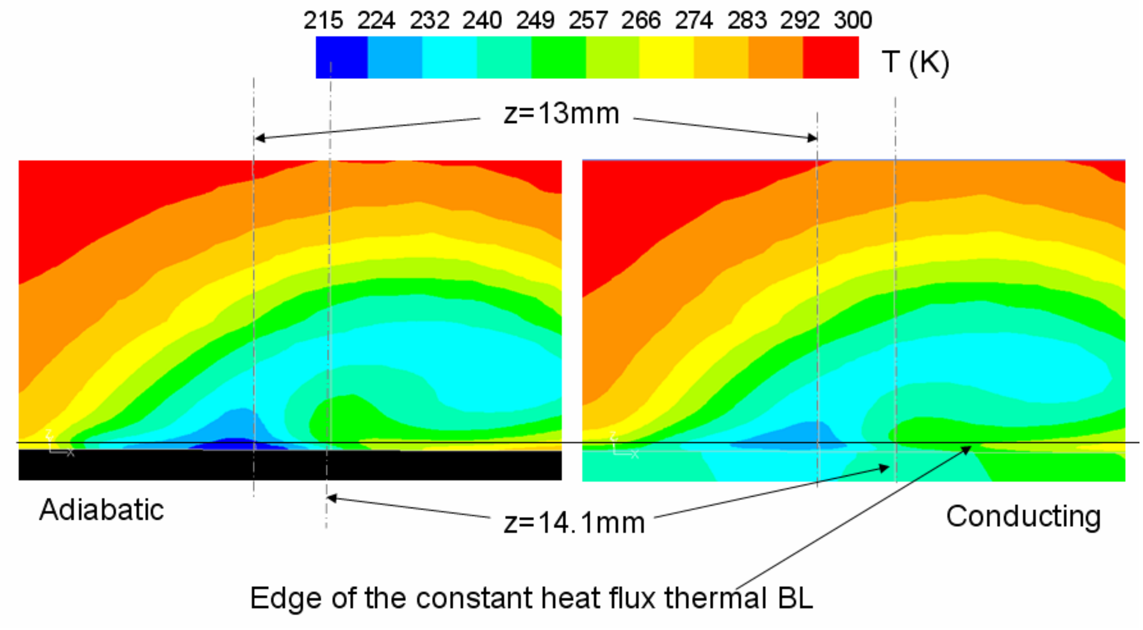

Figure 3.5.14: Thermal profiles above the adiabatic and conducting walls for *M* = 2.0 and *x/d* = 5.0

The predicted and actual heat flux values at *x/d* = 9.0 are presented in Figure 3.5.15. As for *x/d* = 5.0, the predicted heat flux agreed remarkably well with actual heat flux obtained with the CHT analysis. This also indicates that the adiabatic wall temperature is a reasonable driving temperature for the heat flux. Figure 3.5.16 shows the thermal profiles for the different computational predictions for *M* = 2.0 at *x/d* = 9.0 and *z* = 8.5 mm. Again, the minimum gas temperature above the conducting wall, 250K, is much higher than T_{aw} = 240 K. Consequently, it is surprising that T_{aw} leads to the correct heat flux. The fact that the adiabatic and conducting thermal profiles did not merge was also surprising. Contours of thermal profiles at *x/d* = 9 around z = 8.5 mm are plotted in Figure 3.5.17. The shapes of the thermal profiles for the adiabatic and conducting walls were very similar above a distance 1.4 mm from the wall, which was the extent of the thermal boundary layer for the constant heat flux case. No clear explanation was found to explain why both thermal profiles did not merge further away from the wall, where the conducting wall should have had no more influence on the coolant jet, so the differences were assumed to be due to numerical accuracy.

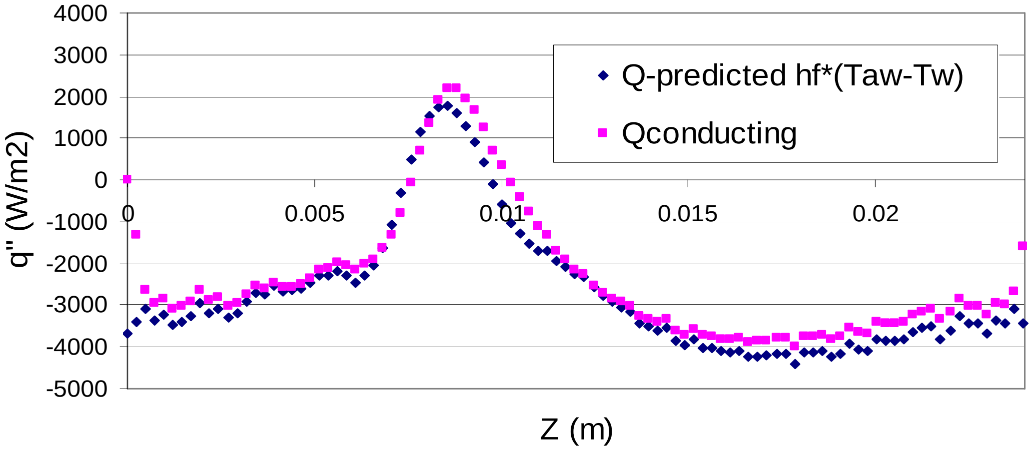

Figure 3.5.15: Lateral variation in predicted and actual heat flux for *M* = 2.0 and *x/d* = 9.0

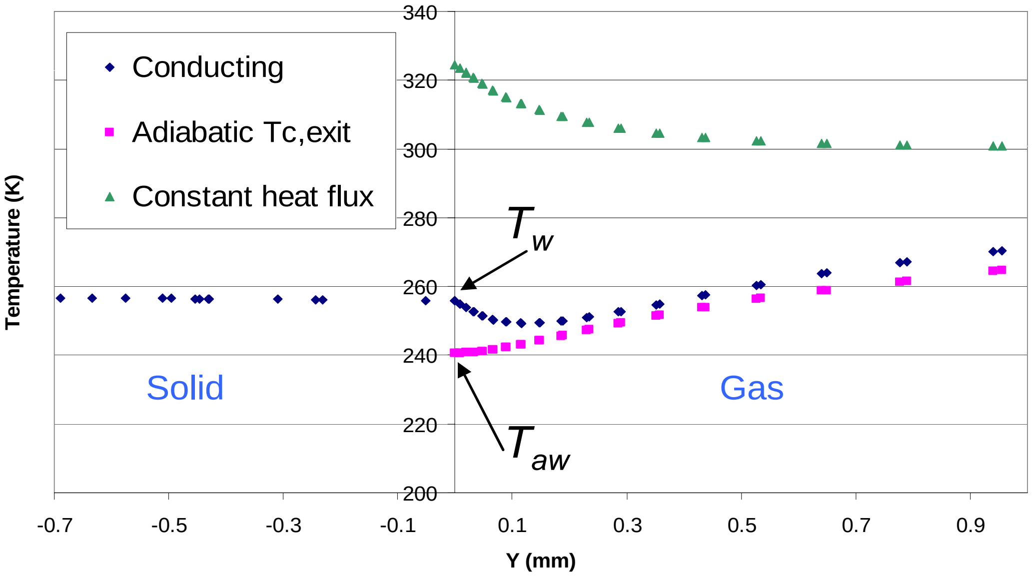

Figure 3.5.16: Thermal profiles above adiabatic, constant heat flux and conducting walls for *M* = 2.0 at *x/d* = 9.0 and *z* = 8.5 mm. (*y* = 0 corresponds to the wall)

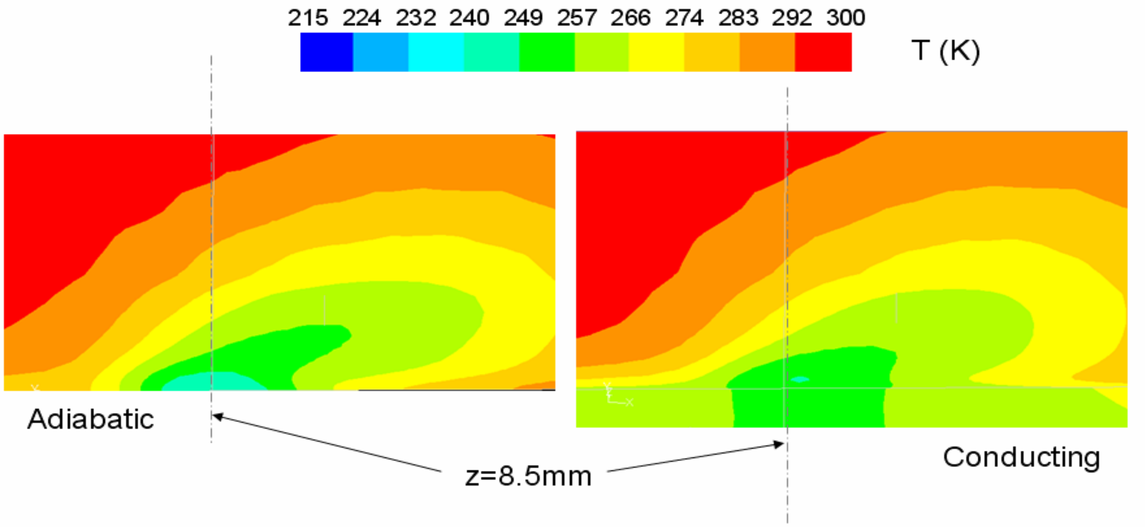

Figure 3.5.17: Thermal profiles above the adiabatic and conducting walls for *M* = 2.0 and *x/d* = 9.0

It is unclear why T_{aw} is the driving temperature for heat transfer close to the jet location. One explanation could be that the external heat transfer coefficient might have been under-predicted, even though Figure 3.2.3.4 revealed that the laterally averaged heat transfer augmentation obtained from the constant heat flux simulation was in the range of the experimental data of Johnston (1999). Indeed, the heat transfer augmentation was obtained using $DR = 1.0$, which does not address the issue of whether h_f from a $DR = 1.0$ constant heat flux surface is appropriate for the conducting surface.

Overall, the adiabatic wall temperature used as the heat transfer driving temperature gave fairly good heat flux values. The only concern remains close to the stagnation line where the predicted heat flux using T_{aw} and the heat flux into the conducting wall showed discrepancies up to 30% at some locations. This could lead to critical, but very localized, damage to the leading edge.

Chapter 4: Experimental Facility and Procedure

To isolate the internal cooling effect on the film cooled leading edge, a no blowing model was designed, constructed and tested. The experiment was also run to help resolve the discrepancy between the simulations and the experiments. Indeed, in a first attempt, the thermal conductivity for the simulations was set up to be k = 4.3W/mK, which was the value claimed by the manufacturer. The no blowing experiment described in this chapter revealed that the thermal conductivity was approximately 1/4 the value reported by the manufacturer, which explained the large differences between simulations and experiments, when k = 4.3W/mK was used for the simulations.

In this chapter, the wind tunnel facility, as well as the coolant supply, is described. Then, details on the geometry model are given. This section also specifies how the model was instrumented with thermocouples and heat flux gauges. Then, the experimental procedure and the data reduction procedures are presented. Finally, an uncertainty analysis on the results in this thesis is given.

4.1 TEST FACILITY

The experiments run for this thesis were realized using a closed loop wind tunnel from the Engineering Design Laboratory. The mainstream flow was driven by a 5hp variable speed axial fan. The flow first traveled through desiccant packs to reduce the humidity level, and therefore limit frost formation. Once the mainstream flow passed the desiccants, it circulated through a water cooled heat exchanger, which stabilized the temperature. Then, the mainstream flow passed through several honeycombs and screens that produced a low turbulence intensity of Tu = 0.5% in the test section. The mainstream then flowed around the leading edge model before recirculating in the wind tunnel.

Experiments were conducted with two mainstream turbulence intensity, Tu = 0.5% and Tu = 6%. The turbulence intensity of Tu = 0.5% was already achieved by the wind tunnel design, whereas Tu = 6% was obtained with the same turbulence generator that Maikell (2008) used. The turbulence generator consisted of cylindrical vertical bars of diameter b = 9.5mm and regularly spaced by m = 25mm. Turbulence measurement were not conducted since it has already been done in the past. Maikell (2008) claimed a turbulence intensity of Tu = 6%, when the model was 0.38m downstream of the bars grid. The calculation of the integral length scale gave Λ = 19mm. The turbulence generator was simply removed to test the model using the lower mainstream turbulence intensity.

A secondary loop, much more complex than the primary loop, provided the coolant gas to the leading edge. The coolant gas was nitrogen which was supplied by a liquid nitrogen Dewar. As it left the Dewar, the nitrogen was liquid but warmed up through the system and ended up to a gas when it reached the test section. The nitrogen gas was either directly injected to the leading edge or traveled through several pipes before reaching the model. Experiments are done at a constant density ratio, defined as the coolant to mainstream density ratio, $DR = \frac{\rho_c}{\rho_\infty}$. Thus, if the density ratio was judged too high, the coolant could be warmed up in the pipe. Also, the heat exchanger and resistive heaters were sometimes activated to accelerate the process of heating the coolant, i.e. decreasing *DR*. These two paths allowed having a better control on the density ratio. A main coolant valve controlled the mass flow rate injected to the plenum. The main valve controls the density ratio since it depends on the coolant temperature and the temperature of the coolant varies with the mass flow rate. A bypass valve was located just downstream the main coolant valve. This valve bypassed some of the coolant flow, keeping the same mass flow rate to the model. Once the density ratio was adjusted with the main coolant valve, the blowing ratio was mainly regulated using the bypass valve in order to keep the same amount of coolant and thus the same density ratio *DR*. The bypass valve was much more sensitive than the main coolant valve. The schematic below in Figure 4.1.1 summarizes the wind tunnel loops.

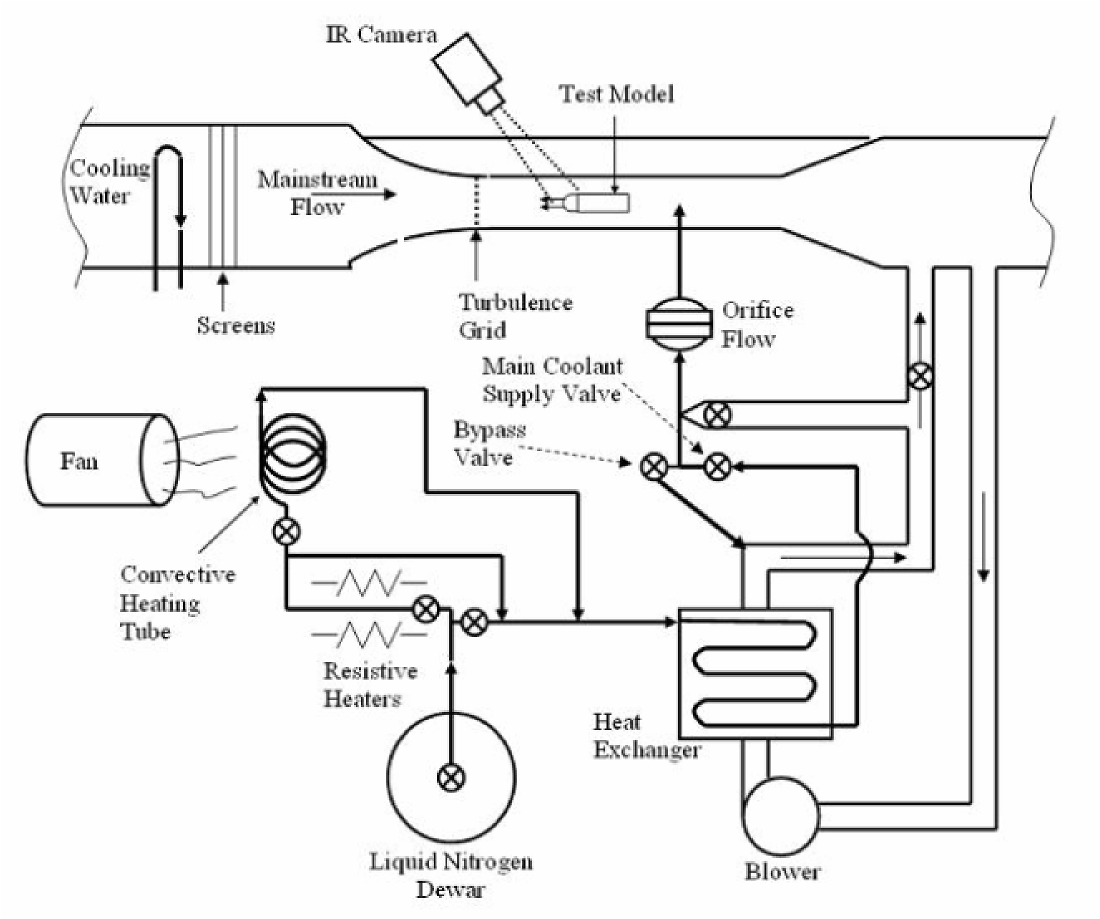

Figure 4.1.1: Schematic of the wind tunnel test section and secondary cooling loop

4.2 LEADING EDGE MODEL

The model consisted of a leading edge model attached to a coolant supply plenum. The plenum was designed in the continuity of the model such as the flow was not disturbed by its presence. The plenum was covered by foam, 8mm thick, to limit any heat transfer with the surrounding environment. An impingement plate was inserted between the leading edge model and the coolant supply plenum. The impingement plate was perforated with 16 holes 2*d* in diameter, spaced one pitch $p = 7.6d$ apart, where d = 2.5mm. The impingement plate generated these very high velocity jets, which considerably increased the internal heat transfer coefficient. This model was created to gain a much better understanding of the internal cooling effect, so the model did not include cooling holes designs. In a film cooled leading edge model, the coolant from the internal cooling was evacuated through the cooling holes and therefore a continuous flow was circulating. In the no blowing case model, the flow exited the plenum with 32 straight holes 1*d* in diameter. They were positioned far away from the stagnation line in order to limit the disturbance of the approaching flow. The holes were located at ±90º, between two impingement jets holes, as seen on Figure 4.2.1.

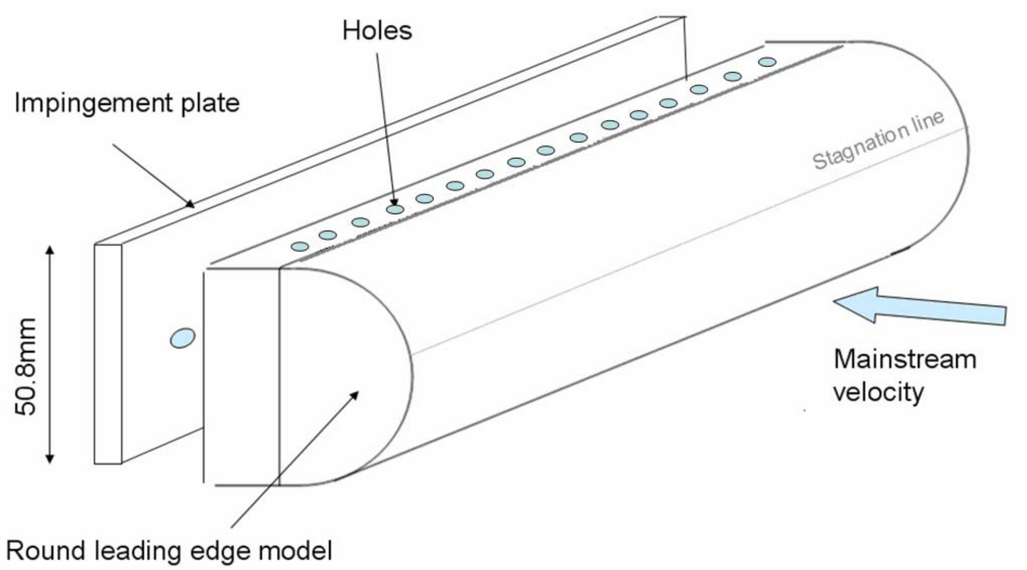

Figure 4.2.1: Schematic of the no blowing model with the impingement plate

4.3 THERMAL CONDUCTIVITY

Because the author suspected the thermal conductivity of the material to be different than the one claimed by the manufacturer, a facility was built to measure the thermal conductivity of the epoxy, designated as Polycast PC 287 by the manufacturer. The material for the model was the same than the one used by Maikell (2008). Thus, comparison could be done between the film cooled leading edge model and the current model. The material was a castable epoxy, which was chosen to match the real engine Biot number. Two identical flat plates of epoxy were cast. The thicknesss of the plates was 10mm, each. The thermal conductivity was obtained by applying a constant heat flux between the two epoxy plates and the temperature drop though the material was measured by four thermocouples, two on each side of the plate. The constant heat flux was imposed with a stainless foil heated electrically by a DC power supply. A schematic on Figure 4.3.1 shows the epoxy plate instrumented.

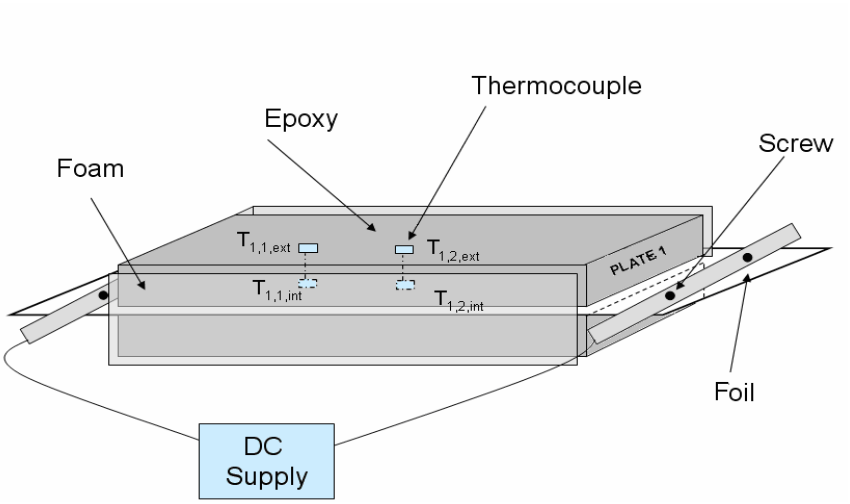

Figure 4.3.1 Schematic of the conductivity test on the epoxy material

The temperature drop needed to be large enough to limit uncertainty issues; therefore a large heat flux of $q'' = 2200$ W/m^{2}K was imposed. Figure 4.3.2 shows the temperature drop across plate 1 and plate 2. The difference in temperature drop between the two plates resulted from the difference in external heat transfer coefficients. The plate 1 on top had a much greater heat transfer coefficient than plate 2, which was very close to the ground. Special attention was given to obtain uniform temperatures and therefore ensure 1-D heat transfer. The edges were insulated. Two thermocouples on the same surface differed by no more than 2º, which was in agreement with the IR camera images taken on the external surface for the plate 1. Thus, the uncertainty in the temperature was $\Delta T = \pm 1^{\circ}$. The temperature drop across plate 1 was about 14º, as seen in Figure 4.2.2. Since the IR camera showed that the temperature gradients were small, lateral conduction through the plate was ignored. The surfaces were smoothed to improve the contact surface. The resistance used to measure the current and the voltmeter had an uncertainty of 0.25% and 0.5%, respectively, which gave an uncertainty in heat flux of less than a 1%. A thermal conductivity of $k = 1.04$W/mK was measured, 1/4th of the reported values. These measurements were accurate ± 6%. A test-to-test repeatability was done and a thermal conductivity of $k = 1.00$W/mK was found, which falls in the uncertainty range.

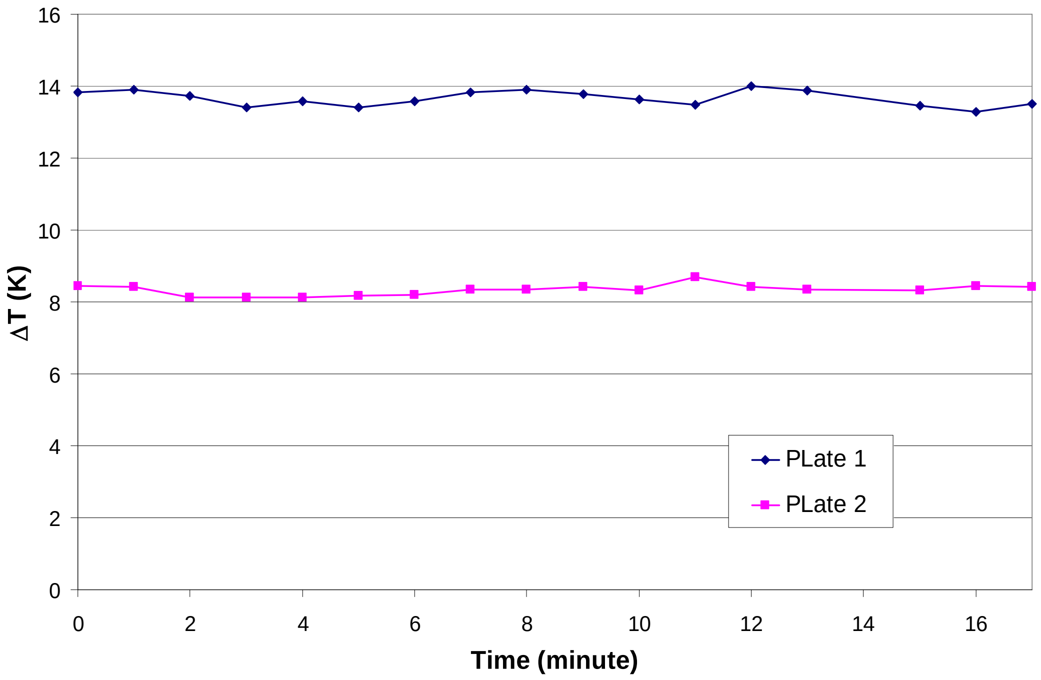

Figure 4.2.2: Temperature drop based on the averaged temperature measurement externally and internally across Plate 1 and Plate 2 after steady state

4.4 INSTRUMENTATION

The external surface temperature, the internal surface temperature and the heat flux on the external surface were measured on these tests.

The external surface temperature was obtained with an infrared (IR) camera. This camera looked through two different windows, an exterior window made of Zinc-Selenide (ZnSe) and an interior window made of Sodium-Chloride (NaCl). A schematic shown in Figure 4.4.1 represent the IR camera configuration.

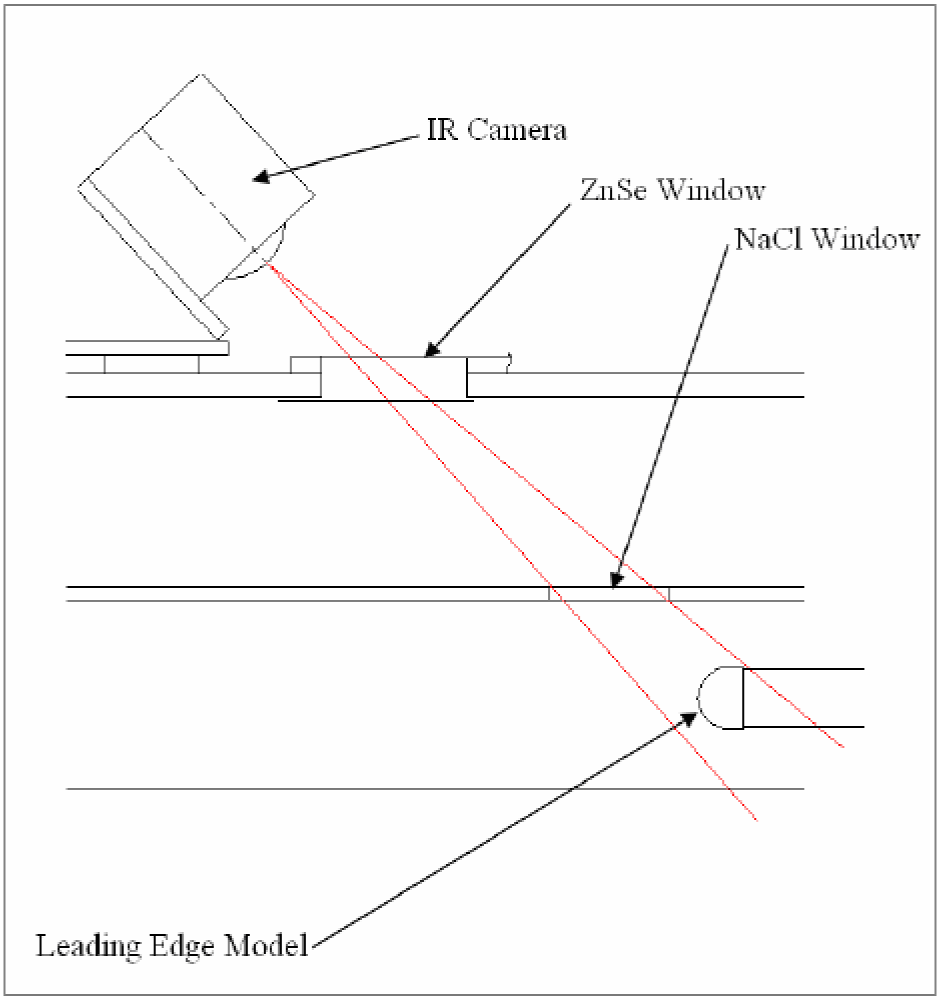

Figure 4.4.1: Schematic of the IR camera setup (from Maikell, 2008)

To obtain a uniform emissivity, the model was painted black. The IR camera was then calibrated with two external thermocouples since the IR windows were not perfect transmitters of IR energy. The IR camera recorded temperatures that were compared to the temperatures read by the two external thermocouples. The calibration curve for this experiment and the one used by Maikell (2008) are plotted in Figure 4.4.2. The disparity between the calibrations was observed for each experiment and attributed to the use of different NaCl crystal windows.

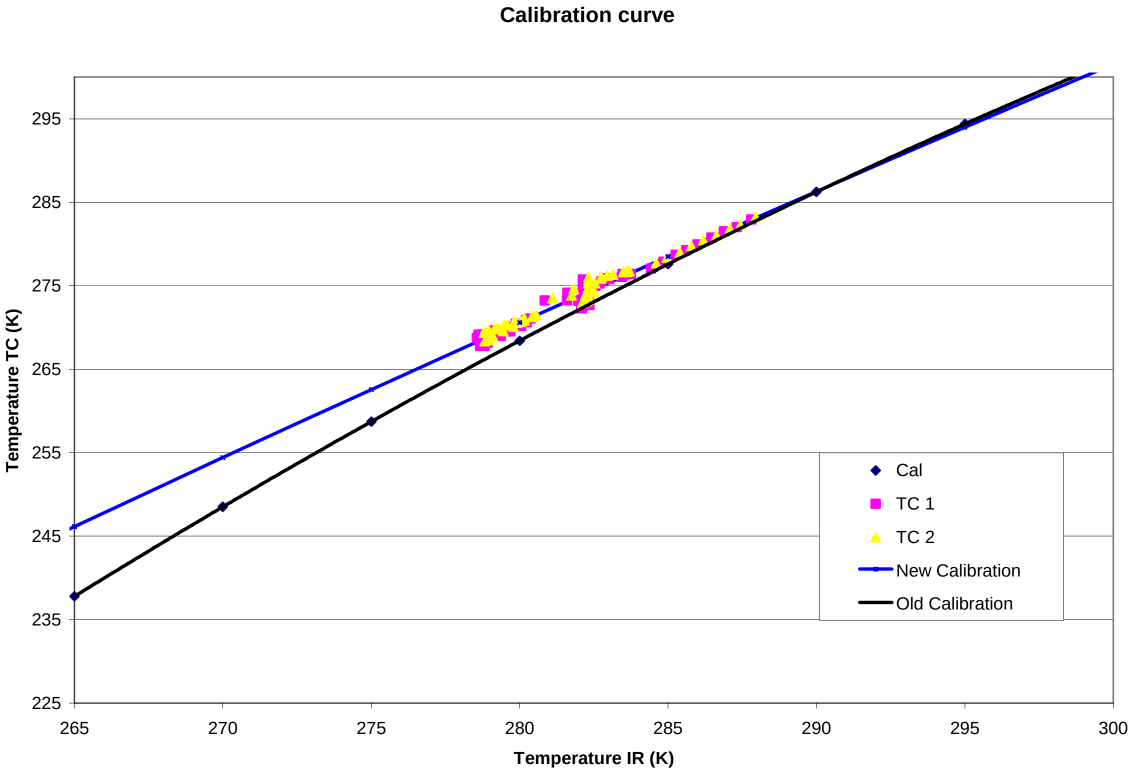

Figure 4.4.2: Calibration curve for the IR camera

Also, the leading edge model was instrumented with E-type thermocouples, which were connected to a National Instruments data acquisition system (DAQ). The measurements were then recorded and displayed with Labview. Thermocouples were used to measure mainstream and plenum temperatures. These thermocouples were 0.5mm diamater welded wires, whereas the ones used on the internal surface were welded ribbon type thermocouples, 5x5 mm large. They were glued on the internal surface at various angles, from $\beta = 0°$ to $\beta = 90°$, where β is the angle defined in Figure 4.4.3. There were two thermocouples on the stagnation line, one under an impingement jet and another one between two impingement jets. The schematic shown in Figure 4.4.4 summarizes the location of the other internal thermocouples.

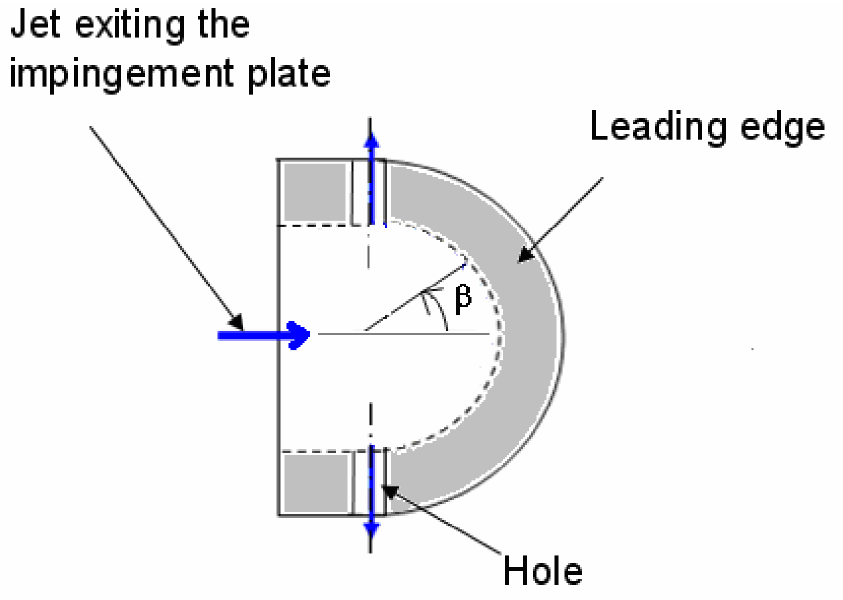

Figure 4.4.3: Definition of the angle β

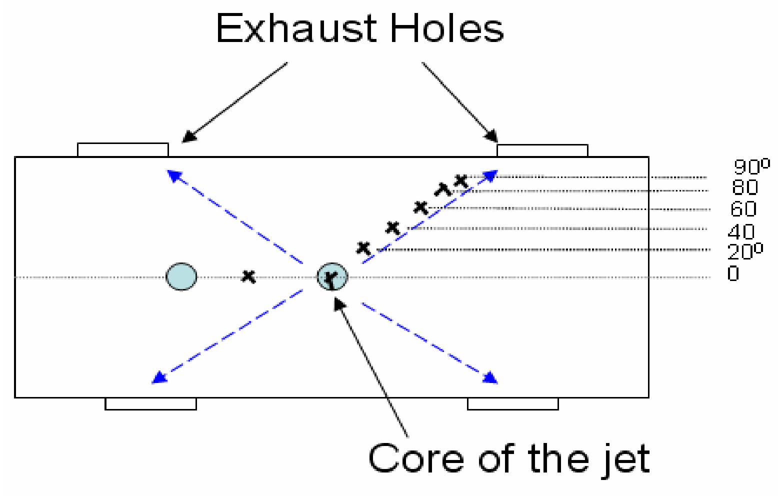

Figure 4.4.4: Location of the thermocouples on the internal surface

The instrumentation for this study also used two heat flux gauges located on the stagnation line and at $\beta = 90°$ located between two holes. These heat flux gauges were RdF Model 27132 micro-foil heat flux sensor. These heat flux gauges were previously calibrated using a constant heat flux device, which consisted of a stainless steel foil heated electrically with a DC power supply. This foil was taped on an insulating foam to minimize the conduction loss. The heat flux gauges were taped on the foil with a thin tape of 9 mils. To be able to reach high heat flux without producing excessive temperatures, the plate was put in a wind tunnel where a velocity of 15 m/s was set up. The high heat transfer coefficient allowed to reach heat fluxes up to $q'' = 4{,}000$ W/m^2 without melting the foam Therefore, the heat flux gauges were calibrating using a wide range of heat flux from $q'' = 0$ W/m^2 to $q'' = 4{,}000$ W/m^2. The heat flux imposed on the plate was obtained by measuring the voltage drop through the plate, as well as the current. The power was divided by the area of the plate, which gave a heat flux (W/m^2). This value was compared to the heat flux measured by the heat flux gauges. Surprisingly, the heat flux gauges calibration was consistently 10% to 50% lower than the one the manufacturer provided, depending on the heat flux gauges sensitivity. Also, several issues were addressed. The heat flux gauges measured voltage in the microvolt range, which required a very sensitive device. Heat flux data were measured with two different devices: A HP 3456 digital voltmeter able to measure voltage in the microvolt range and a National Instrument data acquisition board. The two devices agreed within 20%, which did not explain the 50% discrepancy of the calibration factor with the manufacturer. An analysis of the tape used to bond the heat flux gauges to the surface was done to ensure that it did not influence the measurements. Two experiments were conducted, one with one layer of tape and another one with an extra layer of tape. The tape did influence the measurement by no more than 10%. Finally, the conduction loss through the foam was estimated to be 2% of the heat generated by the foil. The graph in Figure 4.4.5 shows the calibration curve for three heat flux gauges presenting different sensitivity. The calibrated flux corresponded to the heat flux delivered by the DC power supply. The measured heat flux was obtained from the heat flux gauges. The voltage was converted to a heat flux using the sensitivity of the gauge given by the manufacturer. The heat flux gauge referenced 126 gave values within the uncertainty range. However, 107 and 161 measured only respectively 37% and 50% of the heat flux imposed.

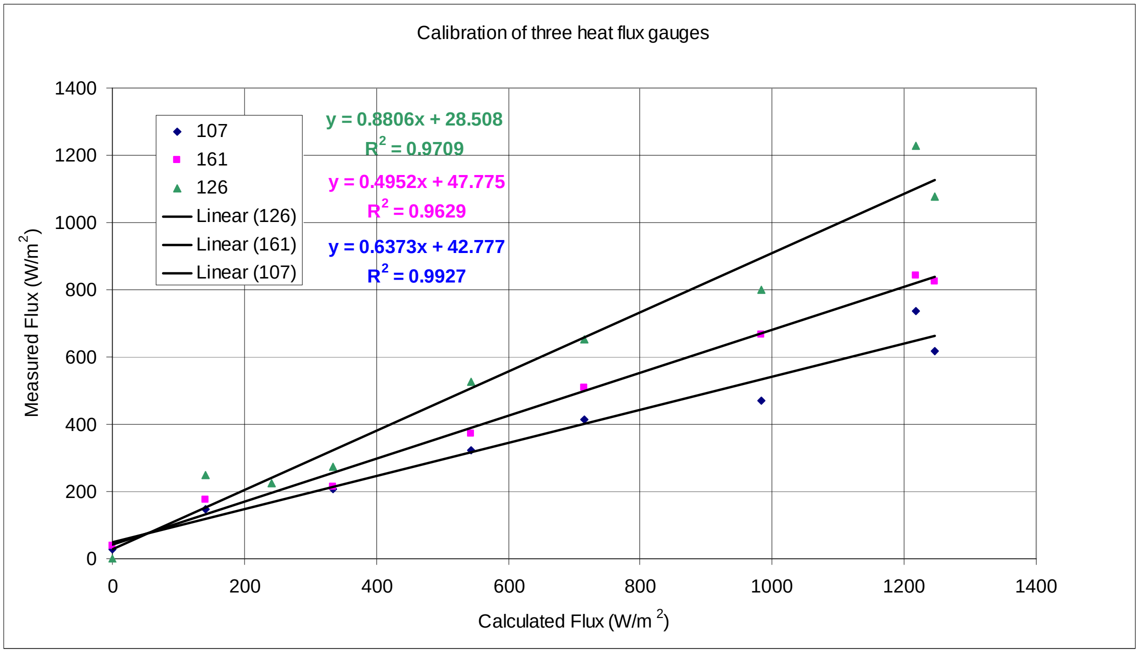

Figure 4.4.5: Calibration of three heat flux gages of different sensitivity

To stabilize the mainstream temperature, the mainstream heat exchanger was activated. The second step was to set up the correct coolant temperature so that the density ratio reached the desired value of *DR* = 1.5. This operation was done carefully in order to collect data to calibrate the IR camera. Thus, thermocouple data and IR images were recorded approximately every minute for calibration purpose. When the density ratio reached *DR* = 1.5, the ‘effective’ blowing ratio was adjusted with the bypass valve. As the no blowing model was used as a baseline of the internal cooling of the film cooled model, the jet velocity at the exit of the impingement plate was matched to the impingement jet velocity for specific blowing ratios for the film cooled models. Thus, the non-film cooled model was run at an “effective blowing ratio”, which corresponded to a similar impingement jet velocity for both experiments.

As several blowing ratios were tested, the model went through extreme operating conditions, as witnessed by the large variation of ϕ values for different blowing ratios. Therefore, steady state was necessary to produce accurate values. At each blowing ratio, several points were taken one minute apart until steady state was reached. The time response of the model to reach the new equilibrium was in the order of 8-10 minutes, which was attributed to the model response time to new operating conditions. Two time history plots are shown below (Figures 4.4.6 and 4.4.7). It can be noticed that, at a higher blowing ratio, the no blowing case model reached faster than for the low blowing ratio steady state. In Figure 4.5.1, the experiment was started at $M = 2.5$, which justifies why ϕ started high and then decreased. The time was reset to zero when the density ratio and the blowing ratio were within ± 0.05 of the desired DR and M.

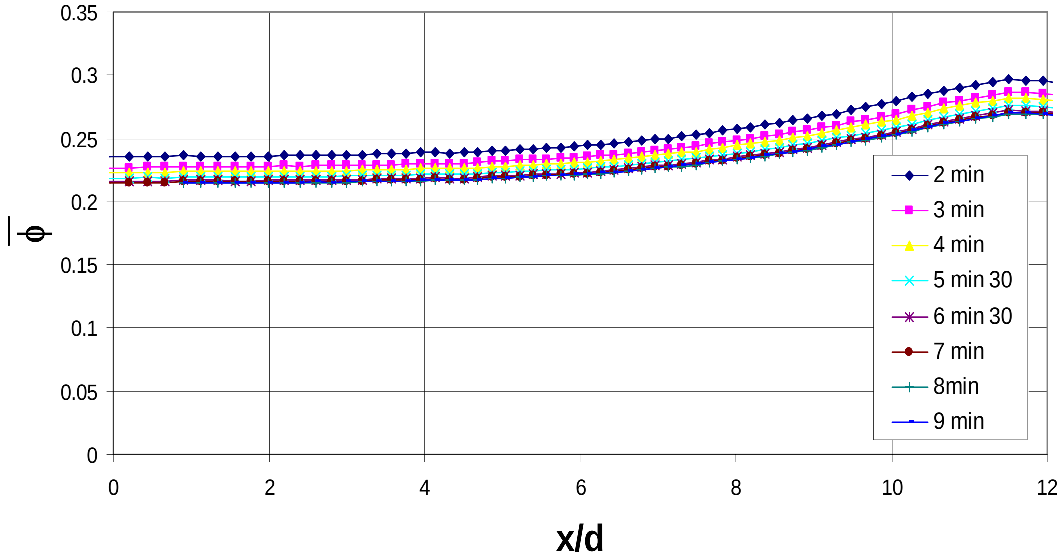

Figure 4.4.6: Determination of the steady state for the blowing ratio of *M* = 2.0 starting from *M* = 2.5

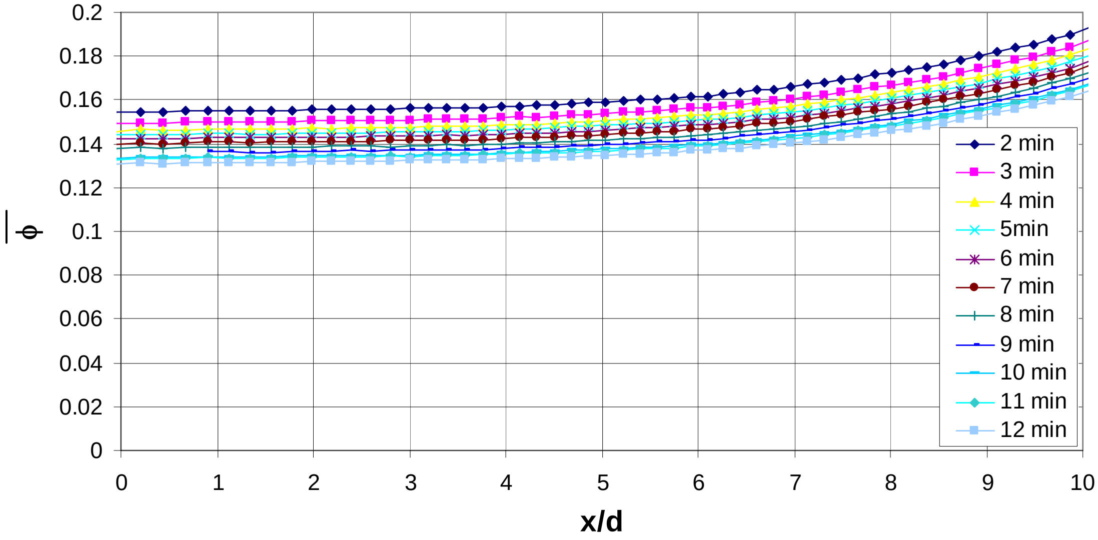

Figure 4.4.7: Determination of the steady state for the blowing ratio of *M* = 0.5 starting from *M* = 1.0

The highest blowing ratio that could be reached with the liquid nitrogen Dewar, was always the first attempted. The bypass was then opened to lower the blowing ratio. In test repeatability, which consists in repeating measurements in the same experiment, was done for all experiments to insure that steady state was reached.

4.5 DATA REDUCTION

Laterally averaged overall effectiveness, $\overline{\phi}$, and contours of ϕ were calculated from surface, mainstream, and coolant temperatures measurements. The program used to transform the images was the same one than Maikell (2008). First, the view area was defined. It generally consisted of a span of three pitches. The images were then unwrapped so the curvature of the model and the perspective of the camera did not affect the results. To establish the coordinates of the IR image pixels, lines corresponding to specific *x/d* positions were drawn on the model with a silver paint. These lines were visible on the images recorded by the IR camera. The software ThermaCam from Flir Systems then determined the location of these lines and associated each pixel value to a correct *x/d* value. Thus, a matrix of temperatures corresponding to the pixel location was generated. These matrixes served as input files for a Matlab program named *Blockscan.m,* which calculated laterally averaged overall effectiveness. This program was written by a previous TTCRL student (Rutledge, 2004). A plot of laterally average overall effectiveness was obtained for each blowing ratio.

Blockscan.m also gave the calibration curve shown in Figure 4.4.2. The locations of the two external thermocouples were used as inputs and the program compared the temperatures of the thermocouples with the temperature read by the IR camera at the location of the surface thermocouples. The new calibration was plotted with the previously determined calibration curve to check the validity of the experiment (cf Figure 4.4.2).

Contours of ϕ were visualized with another Matlab program, named *Temp2phi.m,* which was written by previous students in the lab. This program was input with the *x/d* correlation, the temperature matrices, and the mainstream and coolant temperatures. It assigned at the *x/d* coordinates, the z*/d* coordinates. The *z/d* coordinates were calculated from the Z pixels bounds of the Blockscan imput and the values of *p/d*. Contours of 2-D plots of ϕ values were then displayed with the Matlab program *phiplot.m*, also written by previous TTCRL students. Color bars were adjusted since the no film blowing model showed slight variation from the stagnation line to the flat part of the leading edge, compared to the traditional film cooled model.

4.6 UNCERTAINTY ANALYSIS

An uncertainty analysis was conducted to attribute a confidence level on the experimental data. The uncertainty for measurements presented in this thesis originates from the temperature and pressure measurements, the *x/d* uncertainties and the spatial resolution. The source of uncertainties will be discussed first, followed by repeatability measurements.

4.6.1 Uncertainty in Variables

The uncertainty in blowing ratio depends on pressure and temperature measurements. The pressure uncertainty for the small wind tunnel was $\delta p = \pm 1.35$ Pa. At 15 m/s, a $\delta p = \pm 1.35$ Pa resulted in a mainstream velocity uncertainty of $\delta U_\infty = \pm 0.1$ m/s. The sequential perturbation method, addressed by Moffat (1988) gave an uncertainty for the density ratio of $\delta DR = \pm 0.05$ based on temperature uncertainty of $\delta T = \pm 0.5^\circ$ for coolant and mainstream. The blowing ratio uncertainty was found using the same sequential perturbation method. The uncertainty of the pressure measurement for the orifice meter was taken to be $\delta p_c = \pm 2.5$ Pa. The uncertainties in DR, U_c and U_∞ resulted in an uncertainty of $\delta M = \pm 0.04$ at $M = 1.0$ and $\delta M = \pm 0.07$ at $M = 2.0$.

The use of the IR camera engendered another source of uncertainty, the x/d correlation. A wrong x/d correlation could shift the contours of ϕ. The uncertainty in x/d correlation is mainly due to the precision with which the x/d marks were placed on the model, and the pixel resolution. Since no modification was done since Maikell's analysis, his values were used for the x/d uncertainty. Maikell (2008) calculated the uncertainty based on the standard deviation of the measured pixel location of the x/d marks to the correlation used to calculate the location given a pixel location. He reported a value of δ

$x/d = \pm 0.34$. He also quoted a spatial resolution of 0.5 d. More detailed explanations were provided on Maikell's thesis.

The uncertainty in the Frossling number, Fr, was mainly due to the uncertainty in h, which was due to the uncertainty for the thermal conductivity of the solid model. The thermal conductivity measured for the castable epoxy was k =1.04W/mK with an uncertainty of $\delta k = \pm 0.06$ W/mK. This led to an uncertainty in h on the stagnation line of 7.8% at $M = 1.0$ and 7.1% at $M = 2.0$. Finally, the uncertainty in Frossling number was calculated using the sequential perturbation methods. This gave an uncertainty in Fr on the stagnation line of 7.9% at $M = 1.0$ and 7.2% at $M = 2.0$.

4.6.2 Repeatability

Measurement uncertainty was checked by investigating repeatability of tests. During the experiment, the operating conditions were changed. A repeatability test was done by returning to the original operating conditions at the end of the test. These tests are referred as in-test repeatability. In-test repeatability was done for each experiment. Figure 4.7.2.1 and 4.7.2.2 illustrated the in-test repeatability conducted for respectively the first experiment (test 1) at $M = 1.5$ and the second experiment (test 2) at $M = 1.0$. Since the IR camera was not removed, the x/d correlations were identical for the in-test repeatability. The in-test repeatability gave a biased uncertainty of $\delta\phi = 0.01$ and $\delta\phi = 0.03$ for respectively test 1 and test 2.

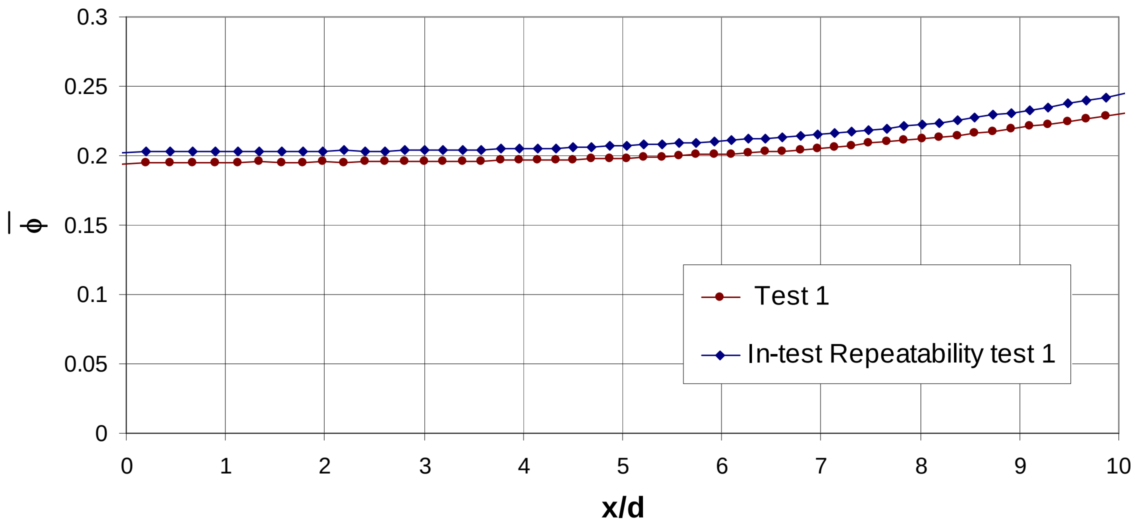

Figure 4.6.2.1: In-test repeatability, M = 1.5 Tu = 6%

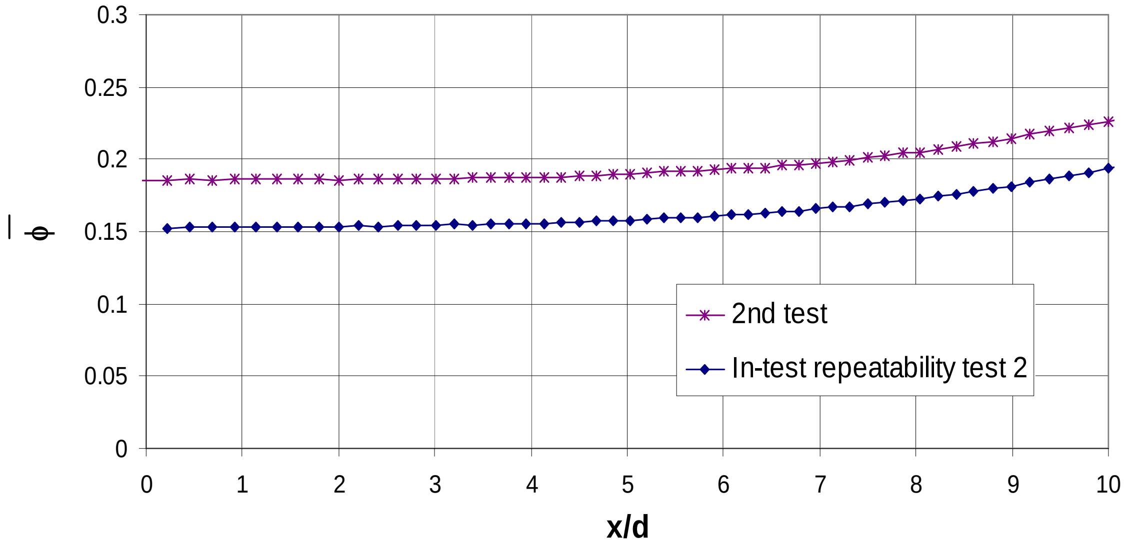

Figure 4.6.2.2: In-test repeatability, M = 1.0 Tu = 6%

Another repeatability test consisted in conducting the same experiment at the same conditions, which are called test-to-test repeatability. A test-to-test repeatability analysis was also conducted for these experiments. The same method employed by Maikell (2008) was followed to determine the uncertainty in ϕ. Two different tests were used with seven data points. Out of these seven data points, only one was in-test repeatability. The test-to-test repeatability was checked at three different locations, at $x/d = 0$, 4 and 8. The standard deviation gave an uncertainty of $\delta\phi = \pm 0.02$. Figures 4.7.2.3, 4.7.2.4 and 4.7.2.5 present a test-to-test repeatability done at three different blowing ratios. Maikell (2008) reported an uncertainty of $\delta\phi = 0.025$ for experiments on film cooled leading edge. The repeatability for $M = 1.5$ and 2.0 for these experiments on a non-film cooled leading edge was better than the uncertainty given by Maikell (2008). As discussed above, higher M reduced uncertainty. This might be due to the fact that the steady state at $M = 1.0$ was longer to achieve than $M = 2.0$. Further experiments should be done to reduce the uncertainty.

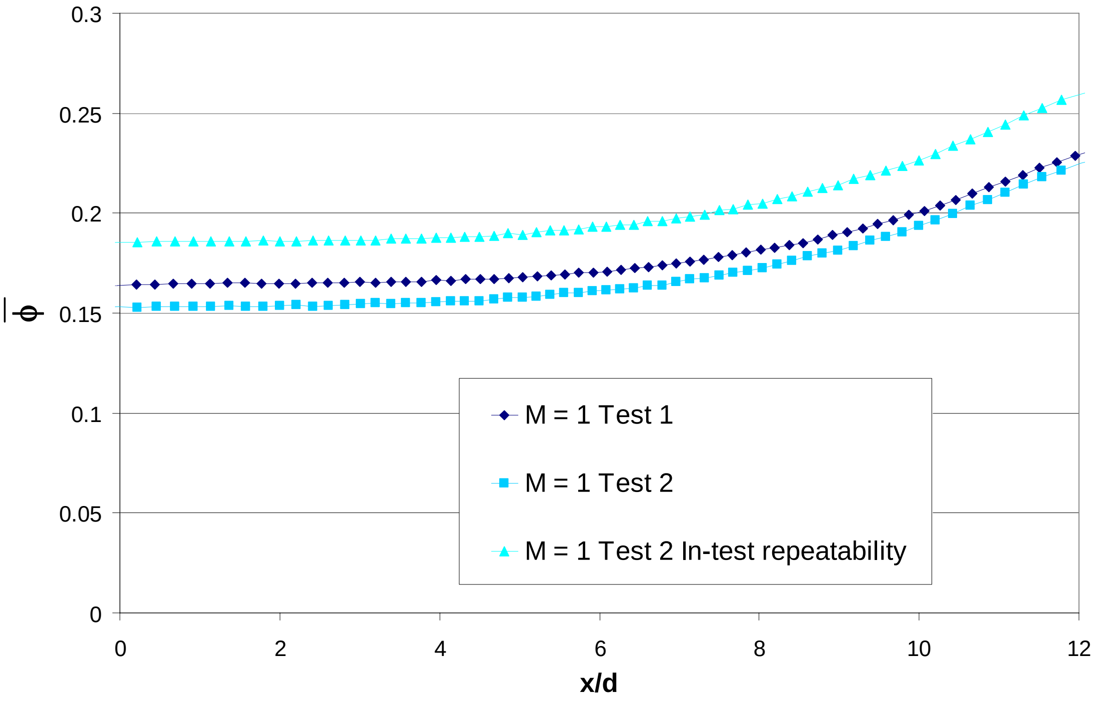

Figure 4.6.2.3: Test-to-test repeatability for *M* = 1 at *Tu* = 6%

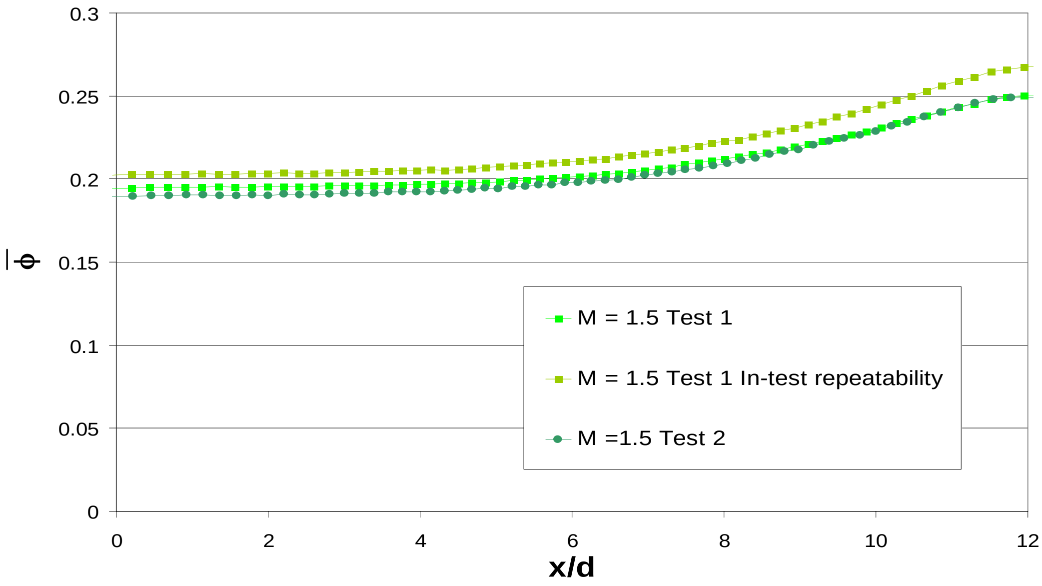

Figure 4.6.2.4: Test-to-test repeatability for *M* = 1.5 at *Tu* = 6%

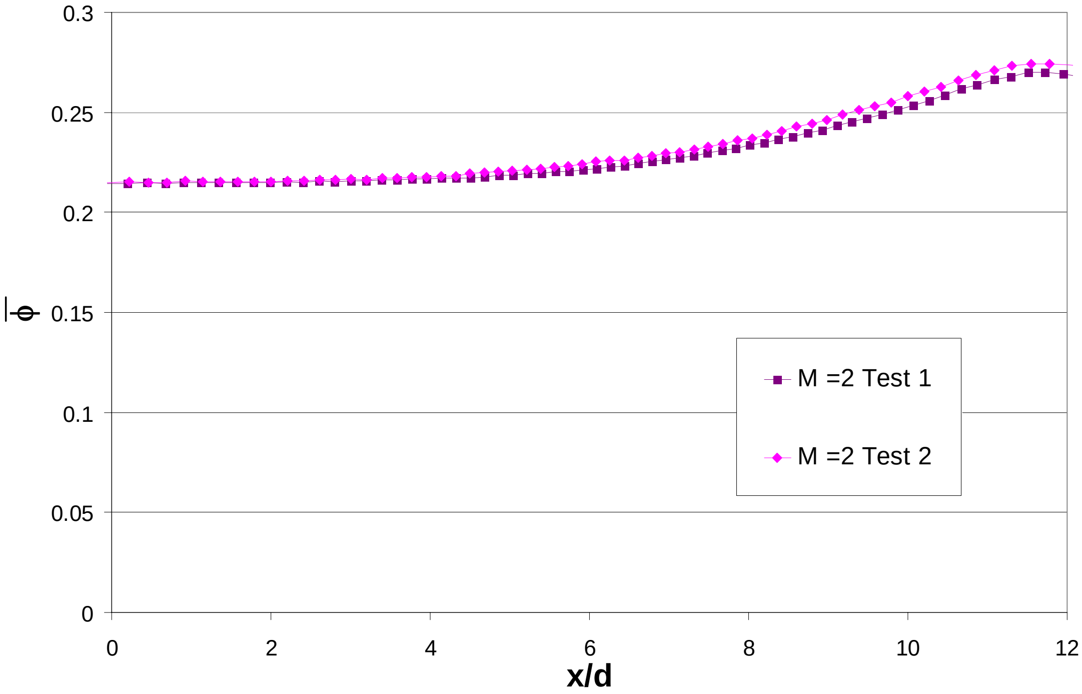

Figure 4.6.2.5: Test-to-test repeatability for *M* = 1.5 at *Tu* = 6%

Chapter 5: Experimental results

This chapter presents the results of the experiments conducted on the no blowing model with an angle of attack of α = 0º. The experiments were run at two different mainstream turbulence intensity levels, *Tu* = 0.5% and *Tu* = 6%. All the data were obtained from the first test (test 1), which presented better in-test repeatability than the second test (test 2). In some tests, holes were blocked to quantify the influence of the convective cooling. The heat flux was obtained from two different ways, a direct measurement of *q”* with heat flux gauges and a 1-D conduction analysis through the model. The results of heat transfer coefficients are expressed in terms of the Frossling number, *Fr*. Additional comparisons were made with previous studies done on the film cooled leading edge.

5.1 CONTOURS OF ϕ AND DISTRIBUTIONS OF $\overline{\phi}$

This section discusses the contours of ϕ obtained at four different effective blowing ratios: *M* = 0.5, 1.0, 1.5 and 2.0. There were no film cooling holes in this model, so blowing ratio for these tests indicates that the internal impingement jet had the same velocity as for film cooling tests with the given value of *M*. The turbulence intensity was maintained as the same level as Maikell’s studies with a film cooled leading edge, i.e. *Tu* = 6%. Figures 5.1.1 through 5.1.4 show the plots of ϕ for all blowing ratios. As expected, ϕ increased with higher *M*. The surface temperatures were relatively constant through all the leading edge. The plots revealed a higher ϕ around x/d = 8-10, which was attributed to the presence of the exhaust holes.

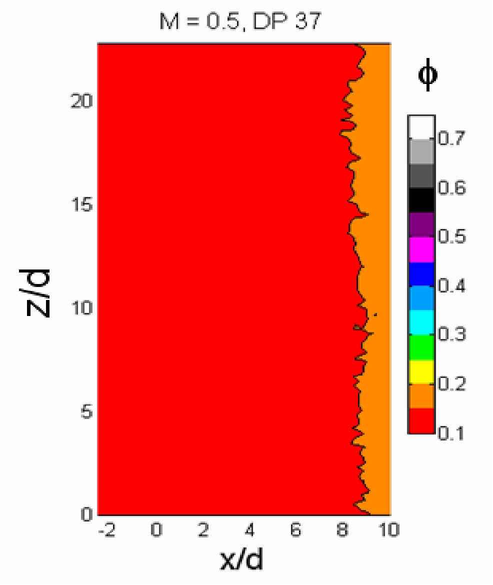

Figure 5.1.1: Spatial distribution of ϕ for M = 0.5 at Tu = 6%

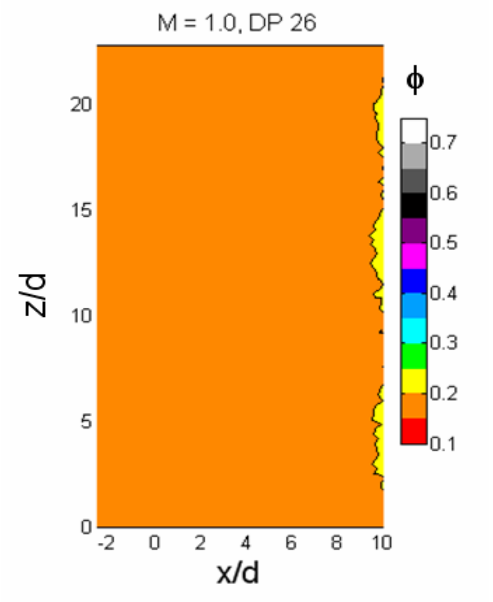

Figure 5.1.2: Spatial distribution of ϕ for M = 1.0 at Tu = 6%

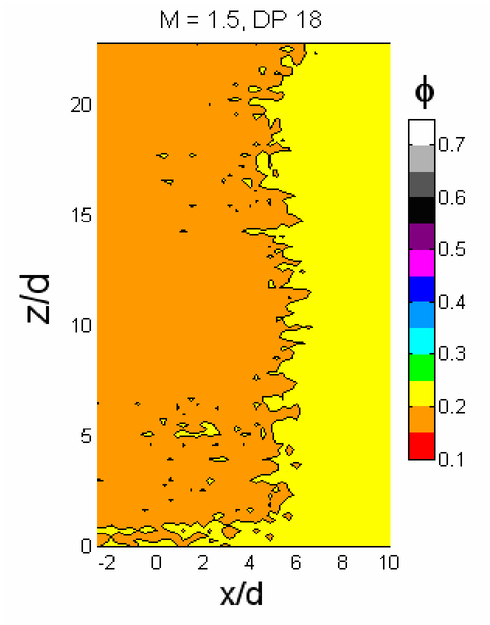

Figure 5.1.3: Spatial distribution of ϕ for M = 1.5 at Tu = 6%

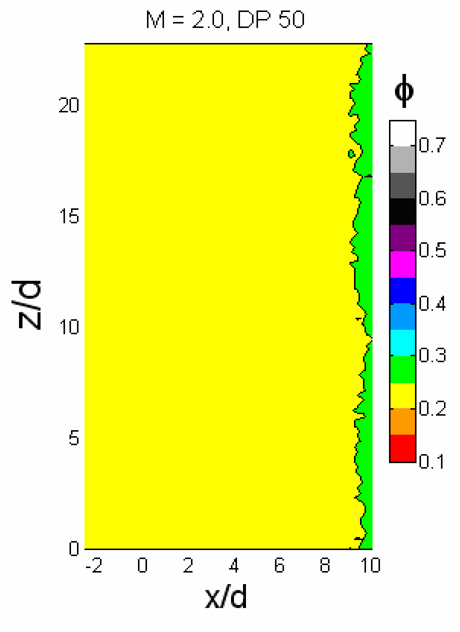

Figure 5.1.4: Spatial distribution of ϕ for M = 2 at Tu = 6%.

To help visualizing the contours, a refined color bar was selected to obtain higher resolution. All plots presented the same feature, as shown on Figure 5.1.5.

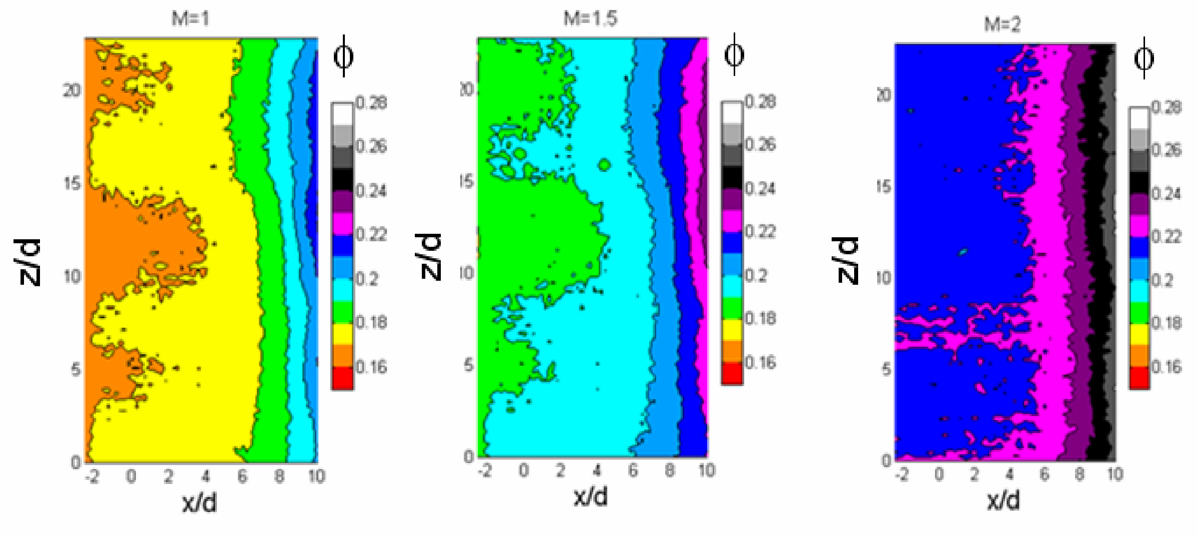

Figure 5.1.5: Spatial distribution of ϕ for M = 1.0, M = 1.5, M = 2.0 at Tu = 6%

The temperatures slightly changed laterally, but less than ±0.01. Note the distinct increase in ϕ from x/*d* = 6 to x/*d* = 10 evident in Figure 5.1.5. It should be recalled the presence of exhaust holes at *x/d* = 13. It is unclear on Figure 5.1.5 how the convective cooling through the exhaust holes affected the external ϕ values. To gain more understanding of this convective cooling effect, two exhaust holes were blocked and the contours of overall effectiveness were compared with the case with no exhaust holes blocked. Figures 5.1.6 and 5.1.7 show the contours of ϕ at respectively M = 1.0 and M = 2.0 for the case with no holes blocked and the case with two blocked exhaust holes. The comparison should be done at *z/d* = 19 and 27.

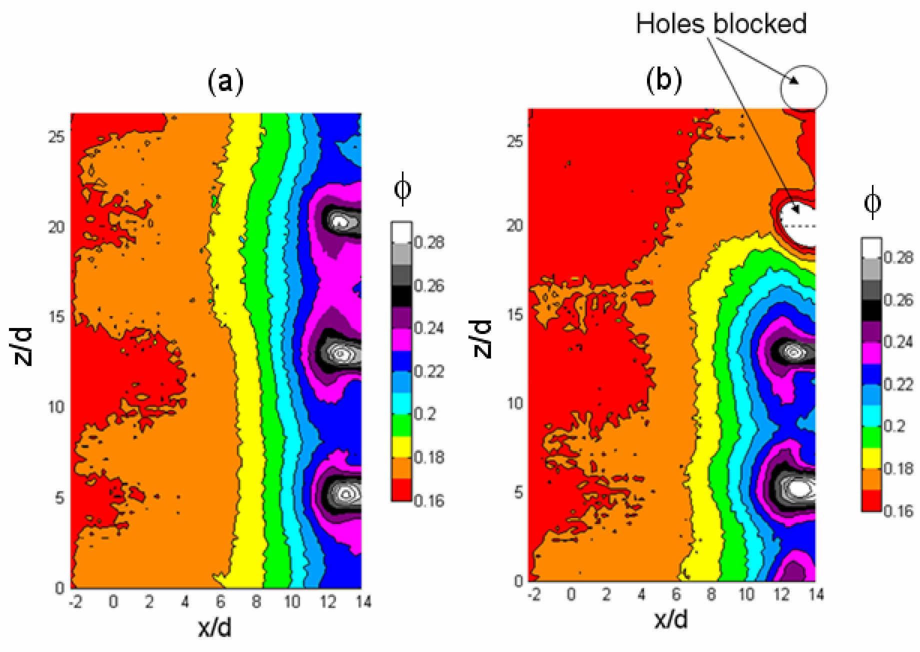

Figure 5.1.6: Spatial distribution of ϕ for M = 1.0 and Tu = 6% for (a) the non blocked holes and (b) the blocked holes case

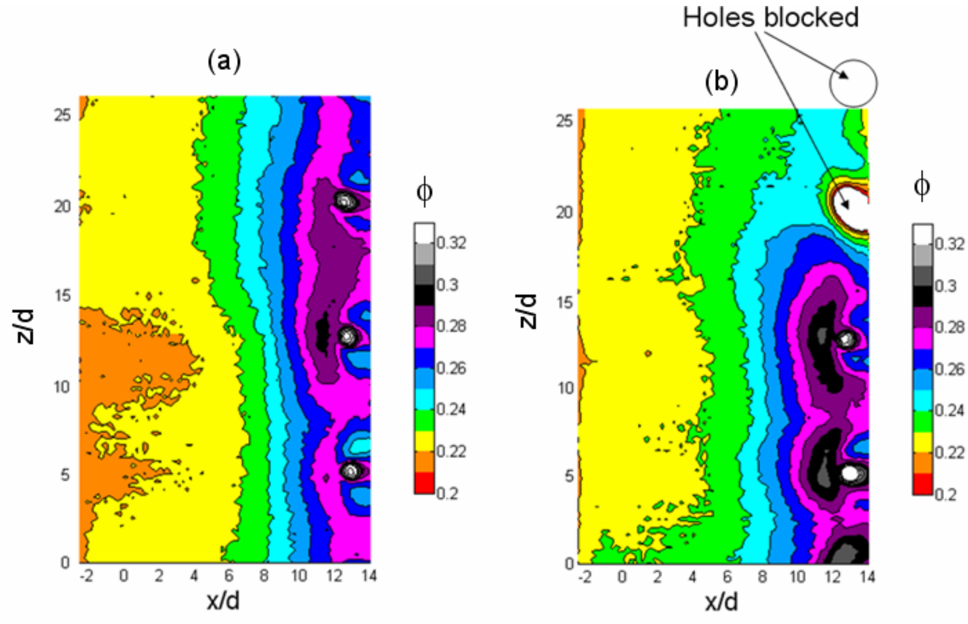

Figure 5.1.6: Spatial distribution of ϕ for M = 1.0 and Tu = 6% for (a) the non blocked holes and (b) the blocked holes case

The laterally averaged overall effectiveness, $\bar{\phi}$, was calculated for the four blowing ratios and presented in Figure 5.1.8. The convective cooling though the exhaust holes was isolated by blocking two exhaust holes, which allows determining a corrected $\bar{\phi}$ value. According to Figures 5.1.6.b and 5.1.7.b, the overall effectiveness was roughly constant through all the leading edge after isolating the convective cooling effect. From *x/d* = 0 to *x/d* = 6, a 50% increase in the blowing ratio from *M* = 1.0 to *M* = 1.5 resulted in a 12% increase in overall effectiveness, whereas a 100% increase in blowing ratio, from *M* = 1.0 to *M* = 2.0, generated a 30% increase.

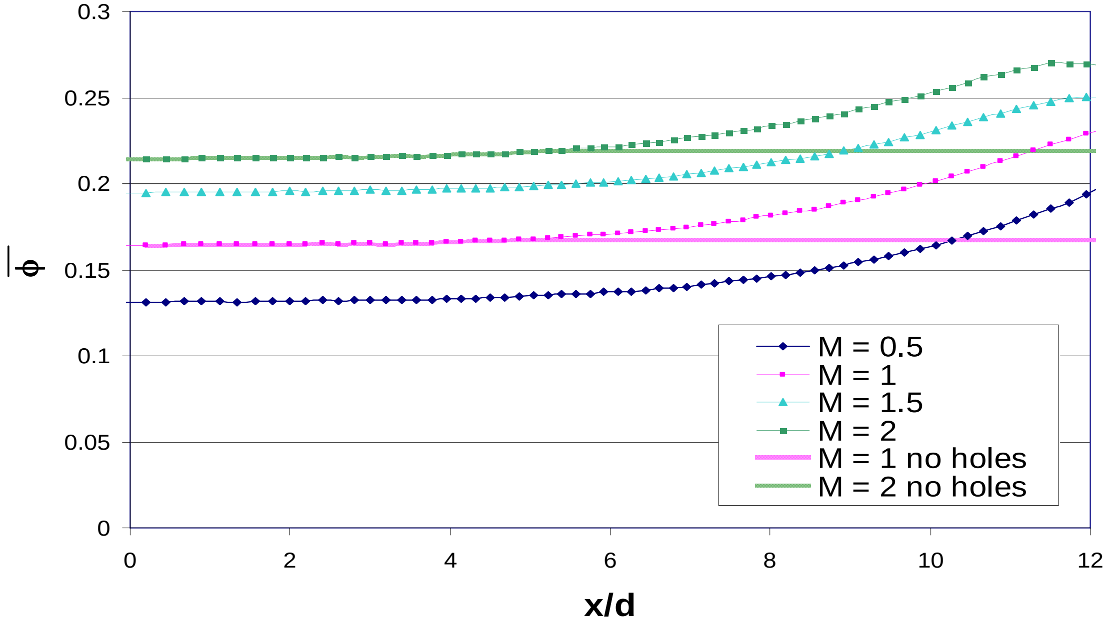

Figure 5.1.8: Laterally averaged overall effectiveness with varying *M* at *Tu* = 6%

Several parameters contributed to the overall effectiveness. The schematic on Figure 5.1.9 details all the parameters which affect the overall effectiveness. The higher effectiveness at higher blowing ratio resulted from an increase in the internal heat transfer coefficient, h_i. Thus, the internal temperature was lower at higher blowing ratio, as seen in Figure 5.1.10. The temperature on the stagnation line was averaged from measurements of the temperatures under the jet and between two impingement jets. Table 5.1.1 shows the normalized internal temperature variation along the stagnation line. As expected, the temperature read by the thermocouple under the jet was colder than the temperature of the thermocouple between the two impingement jets.

Table 5.1.1: Normalized internal temperature variation along the stagnation line

	θ (K) Under Jet	θ (K) Between Jets	$\Delta\theta$
M = 0.5	0.52	0.43	0.09
M = 1.0	0.62	0.53	0.08
M = 1.5	0.69	0.62	0.08
M = 2.0	0.73	0.64	0.09

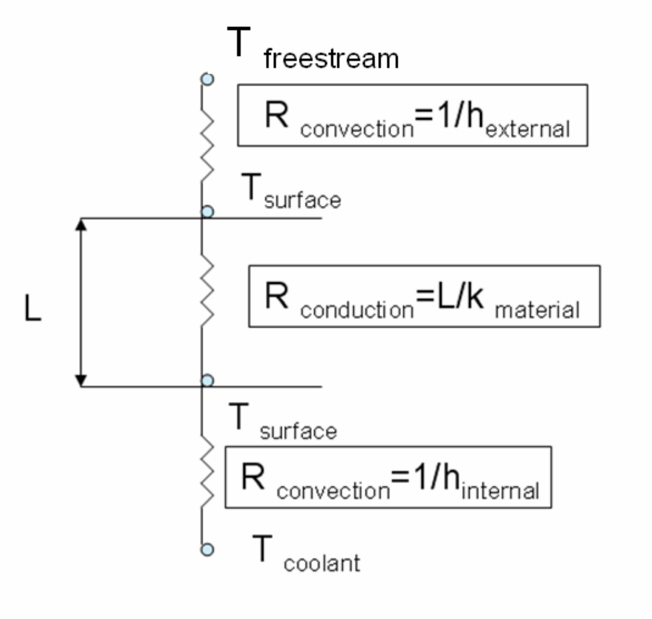

Figure 5.1.9: Schematic of the different parameters influencing ϕ

Figure 5.1.10 reveals that the internal normalized temperature, θ, slightly decreased from $\beta = 0°$ to $\beta = 60°$. All blowing ratios revealed the same general trend. The biggest jump in internal normalized temperature occurred from $M = 0.5$ to $M = 1.0$. The normalized temperature, θ, reached the lowest value at $\beta = 80°$ for all blowing ratios. The increase in θ at $\beta = 90°$ was explained by the presence of the exhaust holes at $\beta = 90°$, as seen in Figure 5.1.11. Plots of normalized internal temperatures in Figure 5.1.11 shows a constant decrease in temperature with increasing β, when the convective cooling effect was isolated, i.e. when the exhaust holes were blocked. This plot also shows the very localized region affected by the convective effect internally. All further analyses were done with the convective cooling isolated. Therefore, the convective cooling through the exhaust holes was not an issue for the 1-D analyses that follow.

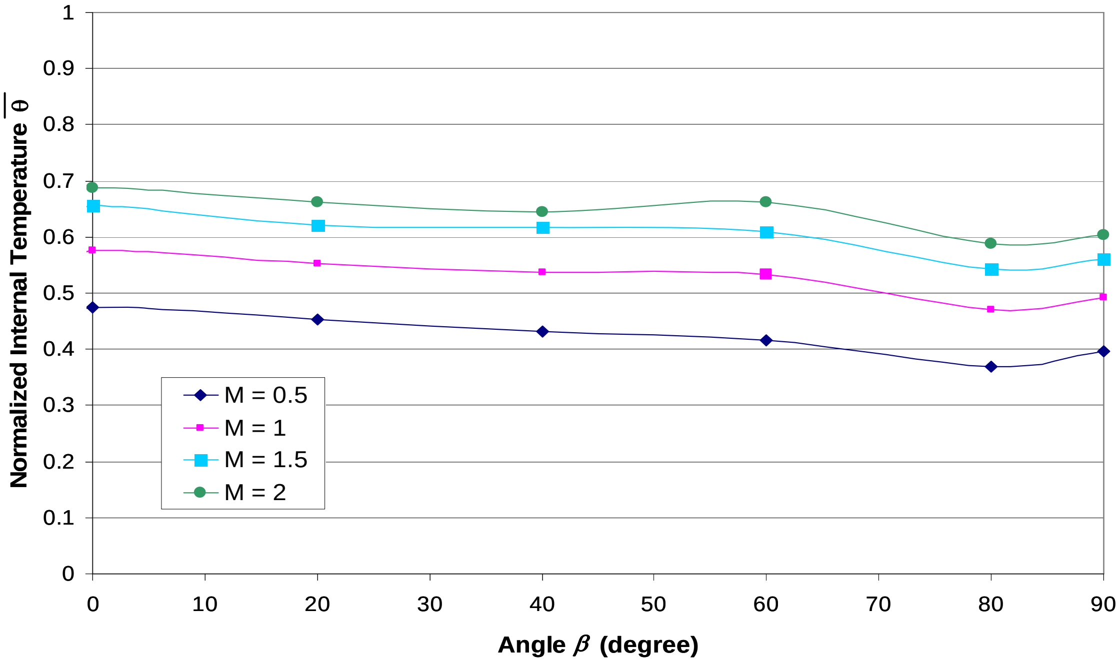

Figure 5.1.10: Profile of the normalized internal temperature with varying *M* at *Tu* = 6%

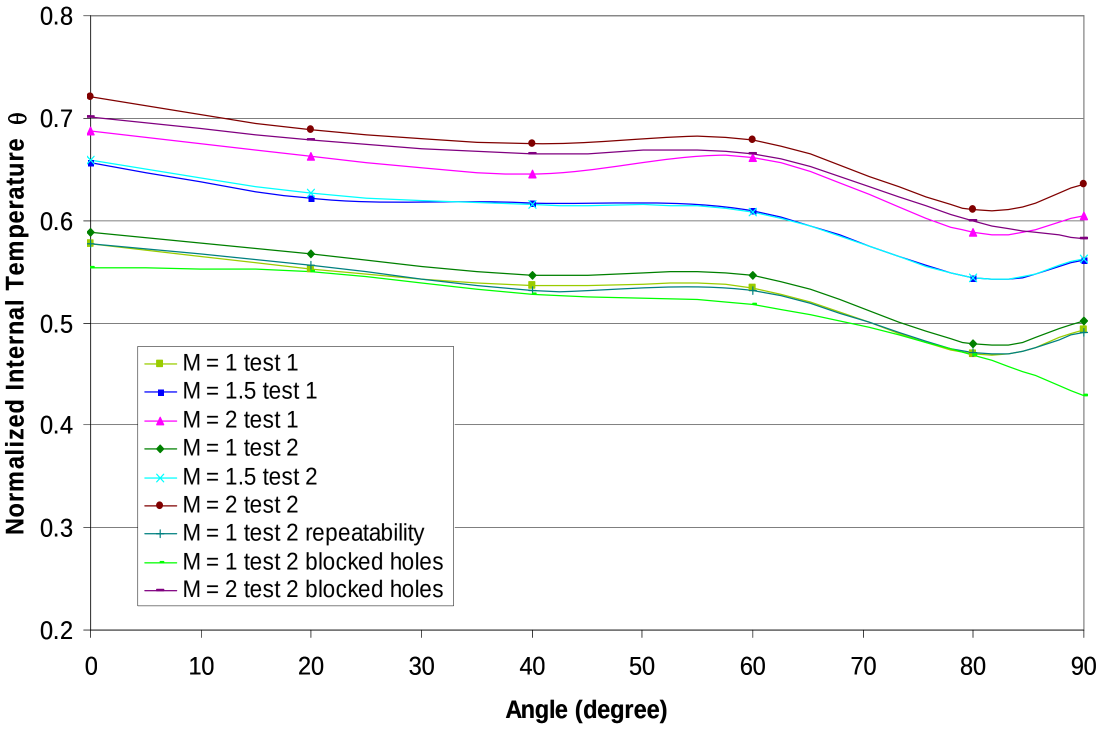

Figure 5.1.11: Profile of the internal normalized temperature with varying *M* at *Tu* = 6% for all tests, including the no holes test.

5.2 HEAT TRANSFER COEFFICIENT MEASUREMENTS

The external heat transfer coefficient was calculated using two different methods. The first one derived from a 1-D heat transfer analysis on the cylindrical leading edge, while the second used heat transfer measurements from the heat flux gauges.

For the first method, a 1-D heat conduction inside the solid was assumed. Since the leading edge was cylindrical, the equation for the heat flux transferred from the external to the internal surfaces is:

$$q''_{ext} = \frac{k\Delta T}{R_{ext} \ln(\frac{R_{ext}}{R_{in}})} \qquad (5.2.1)$$

where R_{ext} and R_{int} are respectively the exterior and interior radius. The 1-D analysis was done using the corrected exterior ϕ values when the exhaust holes were blocked. The ϕ values were roughly constant around the leading edge. Equation 5.2.1 is not valid where the flat part of the leading edge starts. At 90º, the surface is neither a flat plate, nor a cylinder. To face this issue, the heat flux was calculated using an averaged value from the equations for a round part and a flat part. The value found at the 90º position was about 20% lower than the *q"* predicted by Equation 5.2.1.

this equation gives a *q",* 39% lower than for a flat wall at the 90º position. This position was found using an averaged value from q" found using Equation 5.2.1 and the equation for a flat wall. The external heat transfer coefficient was defined by equation 5.2.2:

$$h_{ext} = \frac{q''_{ext}}{T_\infty - T_{w,ext}} \qquad (5.2.2)$$

The freestream temperature, T_∞, the wall temperature $T_{w,ext}$ and the heat flux q''_{ext} were known from the experimental condition and the equation 5.2.1. The heat transfer coefficients are presented in Figure 5.2.1, in terms of the Frossling number; $Fr = \frac{Nu}{\sqrt{Re}}$. The air properties were defined for *Re* and *Nu* at the film temperature, an average temperature of the mainstream and the external surface. The freestream temperature was also used as a reference temperature for *Re* and *Nu* and gave the same results as when the film temperature was used.

It can be noticed that the four blowing ratios followed the same trend. The Frossling number decayed as β increased, with the highest value observed at the stagnation line. The values of the Frossling number were compared with the experimental data of Mouzon (2005), obtained for Tu = 7%. It should be recalled that Mouzon (2005) conducted experiments using a constant heat flux. First, the careful examination of the Frossling number plot, presented in Figure 5.2.1 raises an interesting point. The four blowing ratios showed distinct curves, whereas previous literature papers have proved that *Fr* did not depend on the blowing ratio. The uncertainty analysis was not sufficient to explain the disparity between the four blowing ratios. One explanation for the distinct curves could be the stronger blockage due to the jet exiting the surface at higher blowing ratios. The coolant flow exited the holes perpendicularly to the external surface, causing a blockage to the mainstream flow. The radius of the exhaust holes were *1d*, two times smaller than the impingement jet holes. The impingement plate and the no-film cooled leading edge presented the same number of holes. As a result, the coolant flow exited the exhaust holes with a velocity, twice as high as the one for the impingement plate. As *M* increased, the effect of the blockage should be stronger. Therefore, the flow approaching the leading edge model would see a cylinder with a higher effective diameter at elevated *M*. The boundary layer at any given point would then be thicker than the real diameter, which could cause a drop in the external heat transfer coefficient. However, further investigation need to be done to clearly establish the cause of this discrepancy. Further downstream, the four blowing ratios merged to one value given the uncertainty of 8-9% in *Fr*. Disregarding the difference between the blowing ratios along the stagnation line, these experimental results were in the range of Mouzon's data. Mouzon (2005) measured *Fr* = 1.25 at the stagnation line, which was similar to the current experimental value found at *M* = 1.0. The disparity when using *M* = 0.5 was 6% and rose to 12% when using *M* = 2.0.

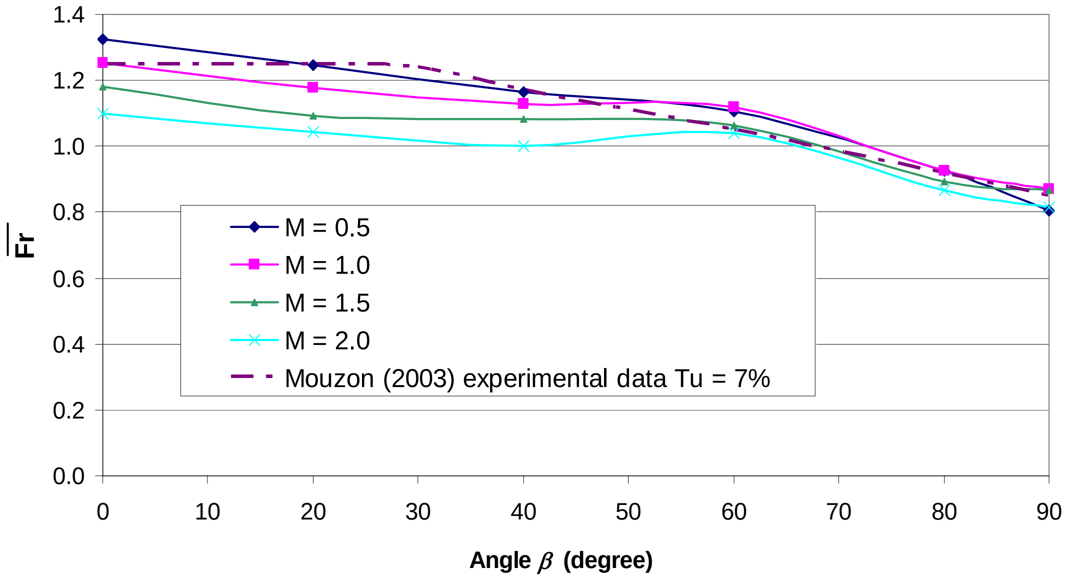

Figure 5.2.1: Determination of the Frossling number with varying *M* at *Tu* = 6%

The external heat transfer coefficient was also analyzed based on the data collected by the heat flux gauges. Keep in mind that the uncertainty of the heat flux gauges was in the 20% range. Despite of this high uncertainty, the use of the heat flux gauges was still found judicious to confirm the heat transfer data obtained from the 1-D analysis.

The heat transfer was measured externally on the stagnation line and at $\beta = 90^{\circ}$ between two exhaust holes. On Figure 5.2.2, the heat flux is plotted as a function of the blowing ratio. The heat flux gauge at $\beta = 90^{\circ}$ gave values slightly larger than the heat flux along the stagnation line, but the two measurements are within the uncertainty for these gauges. The heat transfer slightly increased on the stagnation line from $q'' = 2{,}000$ W/m^2 at $M = 0.5$ to $q'' = 2{,}800$ W/m^2 at $M = 2.0$. At higher blowing ratio, the external heat flux was expected to increase since the internal heat flux was expected to increase with higher velocity impingement jets. It is worth noticing that the heat flux gauges were also able to capture the right trend even though they had high uncertainty.

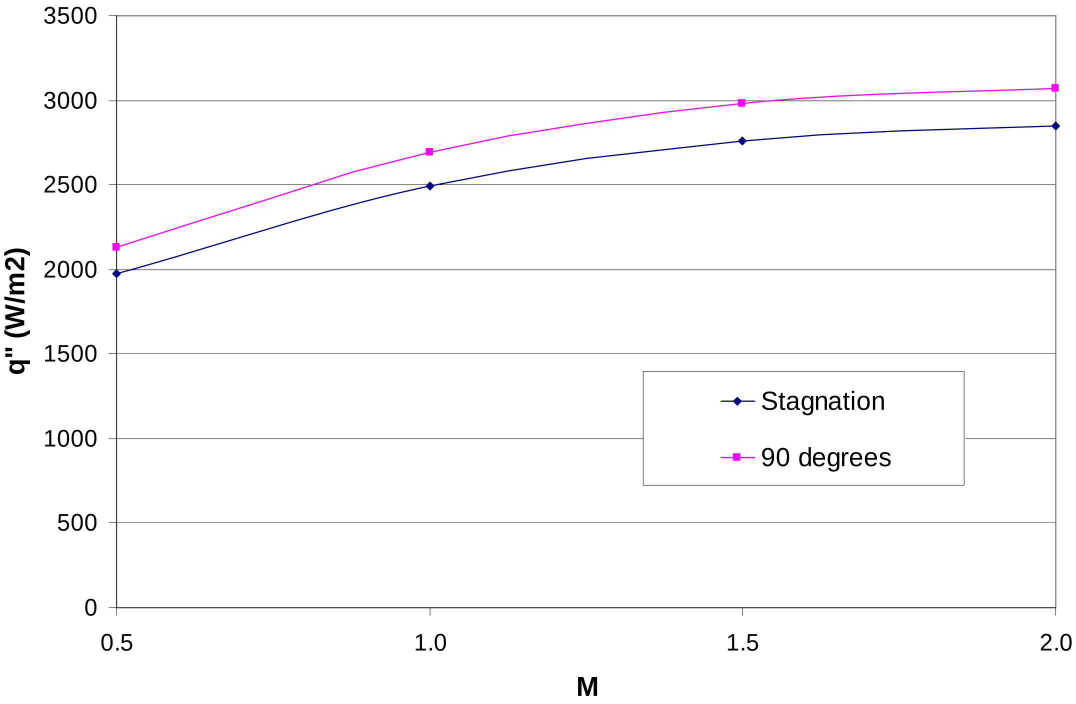

Figure 5.2.2: Heat Flux read by the heat flux gauges along the stagnation line and at 90 degrees for varying *M* at *Tu* = 6

The Frossling number was also calculated using the heat flux measured with the heat flux gauges, and these results are presented in Figure 5.2.3. The distribution of *Fr* was similar to results obtained using a 1-D analysis to estimate heat flux. The heat flux gauges also showed values above but closer to Mouzon's (2005) experimental data.

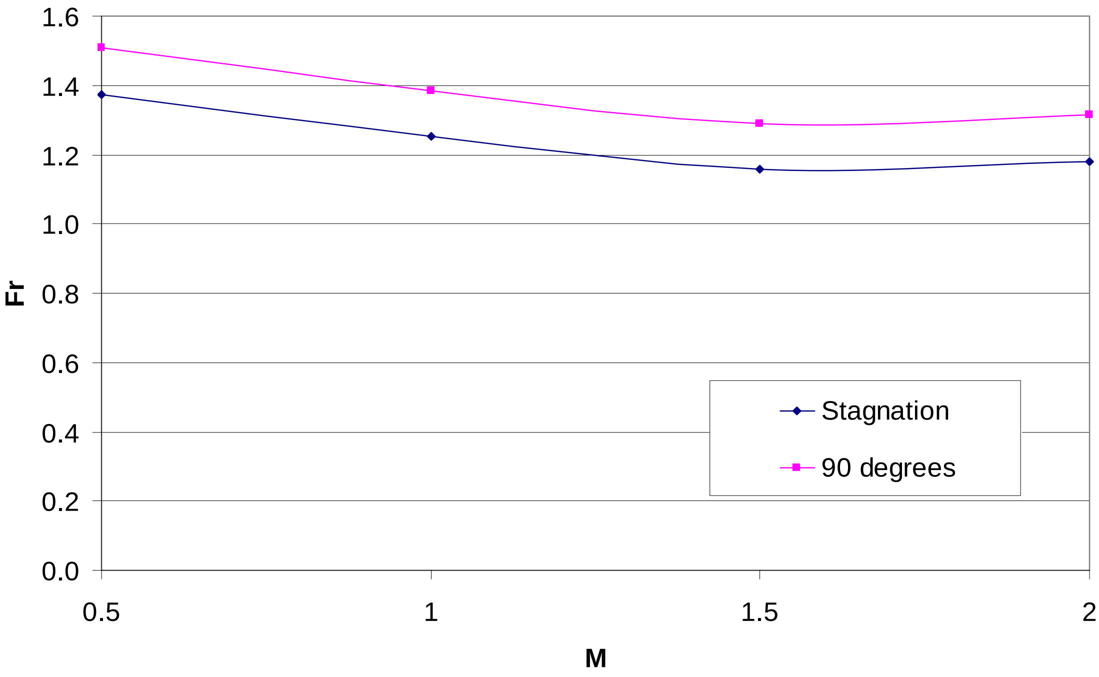

Figure 5.2.3: Calculation of the Frossling number along the stagnation line and at 90 degrees for varying *M* at *Tu* = 6%

Results, based on the heat flux gauge measurements and the 1-D analysis, were compared along the stagnation line to check the consistency of these values. The results are presented in Figure 5.2.4. Mouzon's (2005) experimental data were also included in Figure 5.2.4. The comparison could not be done at $\beta = 90^{o}$ due to convection issues. Either the 1-D analysis did not hold close to the exhaust holes, or the convection effect could not be isolated in the heat flux gauges measurements contrary to the first method. Given the uncertainty on the heat transfer with the heat flux gauges and on the thermal conductivity, both methods gave consistent results. These results were close to Mouzon's experimental values. He claimed an uncertainty in *Fr* of 4%. Figure 5.2.4 shows that *M* = 1.0 was in good agreement with Mouzon's data (2005). Also, both analyses showed a decrease in *Fr* with higher *M*, whereas Mouzon's (2005) data were not a function of *M*, as it was stressed earlier.

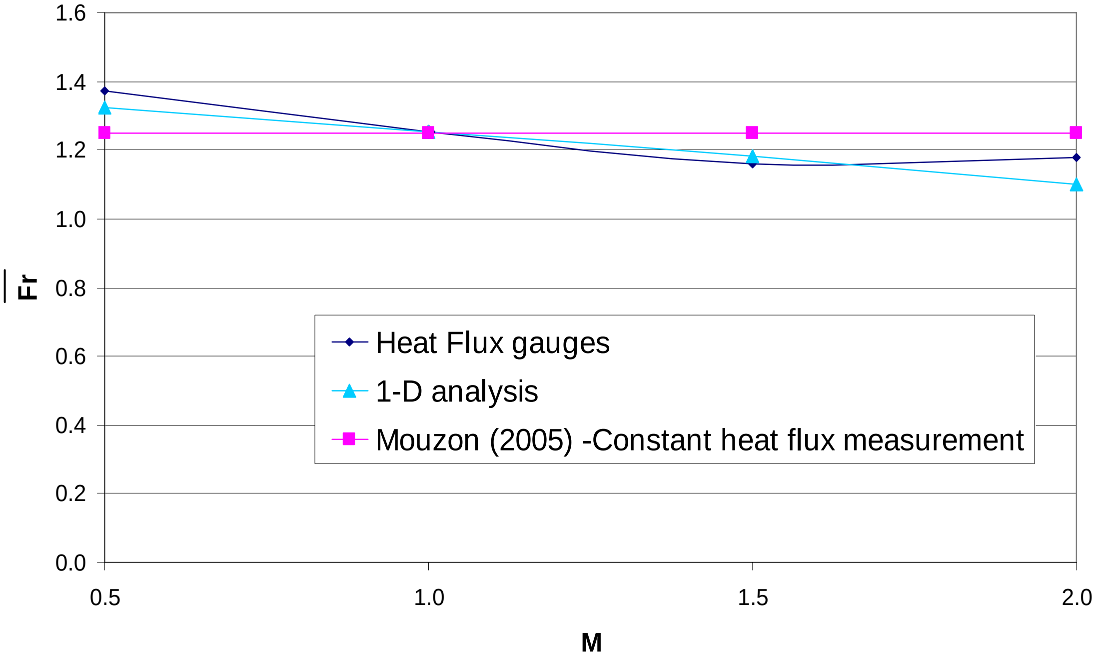

Figure 5.2.4: Comparison of the Frossling number along the stagnation line at *Tu* = 6% for the 1-D analysis and the heat flux gauges measurement

A critical value for the convection through the internal wall was the internal heat transfer coefficient. The internal heat flux at the internal wall for the cylinder part of the leading edge was found from the following equation:

$$q''_{ext} = \frac{k\Delta T}{R_{ext}\ln\left(\frac{R_{ext}}{R_{\text{int}}}\right)} \qquad (5.2.3)$$

Then, the internal heat transfer coefficient was obtained from using *q”* from Equation 5.2.3, the coolant temperature and the measured internal surface temperature, as follows:

$$h_{\text{int}} = \frac{q''_{\text{int}}}{T_{w,\text{int}} - T_c} \qquad (5.2.4)$$

where T_c is the coolant temperature and $T_{w,int}$ is the internal wall temperature. The internal heat transfer coefficient, h_{int}, is examined at different blowing ratios, as shown in Figure 5.2.5. As expected, a higher mass flow rate generated higher *h* values, which better cooled down the external surface.

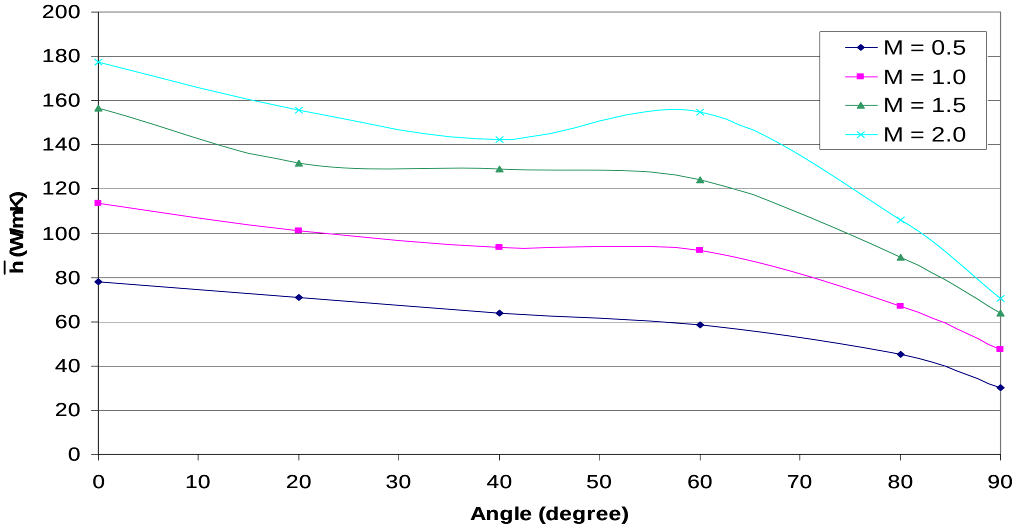

Figure 5.2.5: Comparison of the Frossling number along the stagnation line at *Tu* = 6% for the 1-D analysis and the heat flux gauges measurement

5.3 INFLUENCE OF THE TURBULENCE INTENSITY

Two sets of experiments were run, one at *Tu* = 0.5% and another one at *Tu* = 6%. The experiments were run at the two blowing ratios of *M* = 0.95 and *M* = 1.9. The influence of the turbulence intensity on the laterally averaged overall effectiveness is shown in Figure 5.3.1. As expected, higher turbulence intensity led to lower overall effectiveness since the external heat transfer was increased where as the internal cooling remained identical, as it will be shown later on.

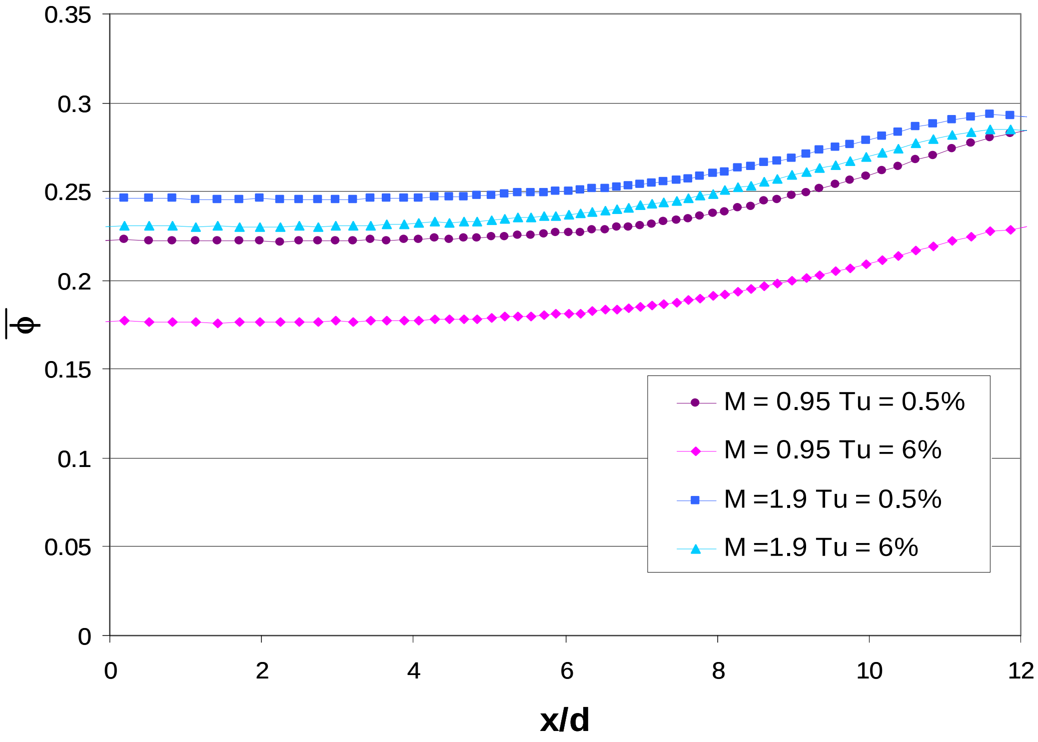

Figure 5.3.1: Comparison of the laterally averaged overall effectiveness with varying turbulence intensity level at *M* = 1.0 and *M* = 2.0

The turbulence intensity had a greater influence on the lower blowing ratio. At *M* = 0.95, the higher *Tu* made $\overline{\phi}$ drop by 20% whereas *M* = 1.9 showed a 7% drop. As expected, the internal heat transfer coefficient remained the same regardless of the external turbulence intensity level, as seen in Figure 5.3.2.

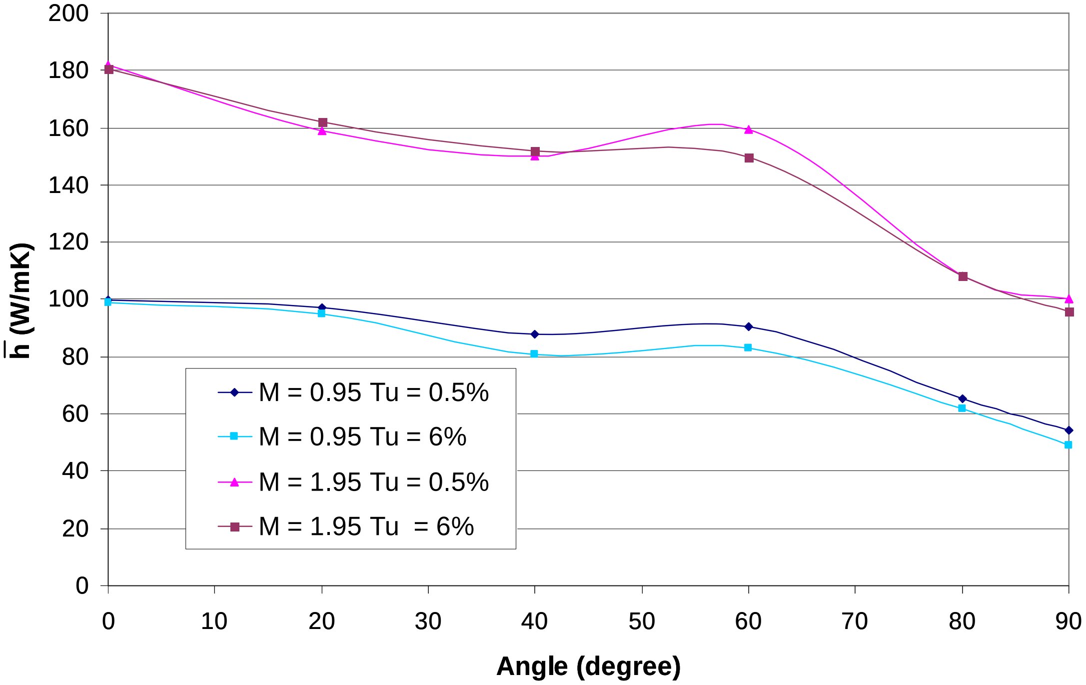

Figure 5.3.2: Comparison of the internal heat transfer coefficient with varying turbulence intensity level at *M* = 0.95 and *M* = 1.95

Analysis of the effects of mainstream turbulence on heat transfer coefficients provided more understanding of these effects. Figure 5.3.3 presents the Frossling number, *Fr,* at both turbulence intensities. The general trend of the Frossling number for a no blowing model was comparable to Mouzon's (2005) trend. The discrepancy between Figures 5.2.1 and 5.3.2 resulted from the blocked holes. Surprisingly, the blocked holes caused a decrease in external heat flux, q''_{ext}, resulting in lower *Fr*. The reason of this decrease is unclear and needs to be solved in the future. For both cases, $Tu = 0.5\%$ and $Tu = 6\%$, two exhaust holes were blocked.

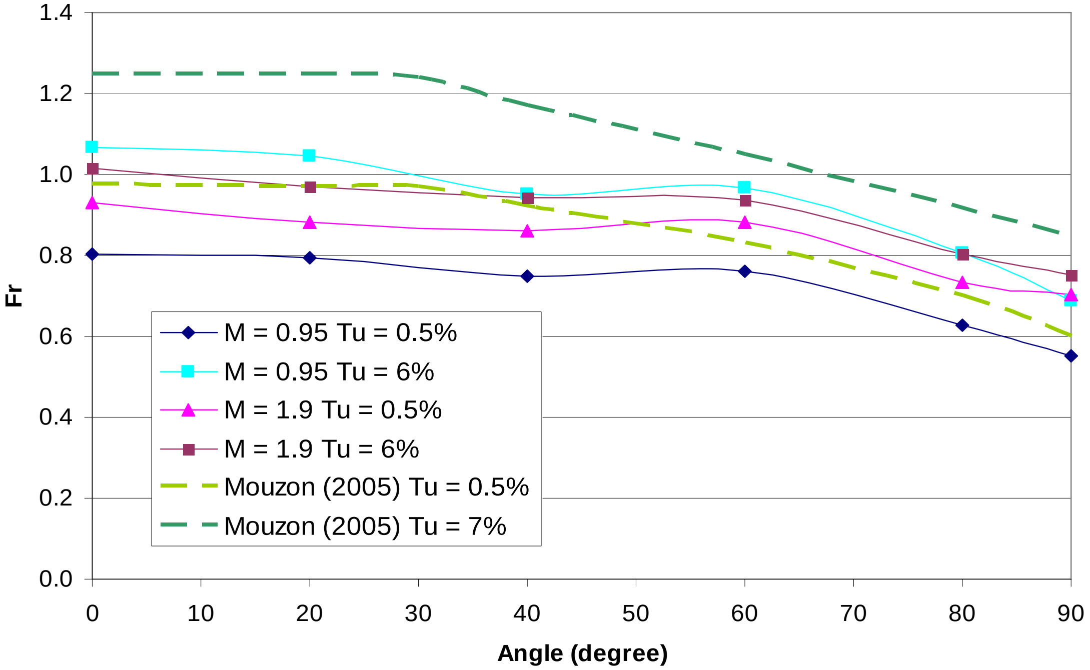

Figure 5.3.3: Comparison of the Frossling number with varying turbulence intensity level at *M* = 0.95 and *M* = 1.9

The disparity among blowing ratio was still observed at $Tu = 0.5\%$. As expected, the elevated mainstream turbulence intensity caused higher heat transfer coefficients, which explains the lower overall effectiveness at $Tu = 6\%$, compared to $Tu = 0.5\%$. There was a 25% increase on *Fr* for both blowing ratios. This 25% increase agreed well with Mouzon's experimental data. He observed the same 25% increase in *Fr* when he increased the turbulence intensity from *Tu* = 0.5% to *Tu* = 7%.

5.4 COMPARISON WITH THE FILM COOLED LEADING EDGE

The current study was undertaken to quantify the internal cooling effect in the film cooled leading edge model. Since the effective blowing ratio was matched, comparison could be done between the no blowing model and the three row leading edge model. Figures 5.4.1 and 5.4.2, at respectively *M* = 1.0 and *M* = 2.0, show the laterally averaged overall effectiveness for the film cooled model compared with the no blowing case. For reference, also shown in Figures 5.4.1 and 5.4.2 are the $\bar{\eta}$ distributions.

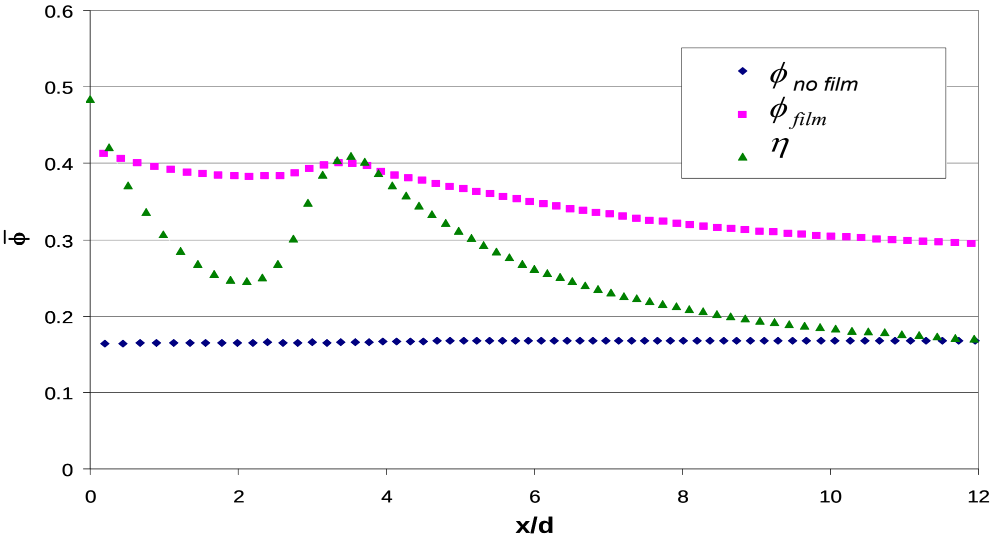

Figure 5.4.1 Comparison of the laterally averaged overall effectiveness for *M* = 1.0 and *Tu* = 6% for the film cooled leading edge (Maikell, 2008) and the no blowing model with the laterally averaged film effectiveness (Davidson and Dyson, 2009)

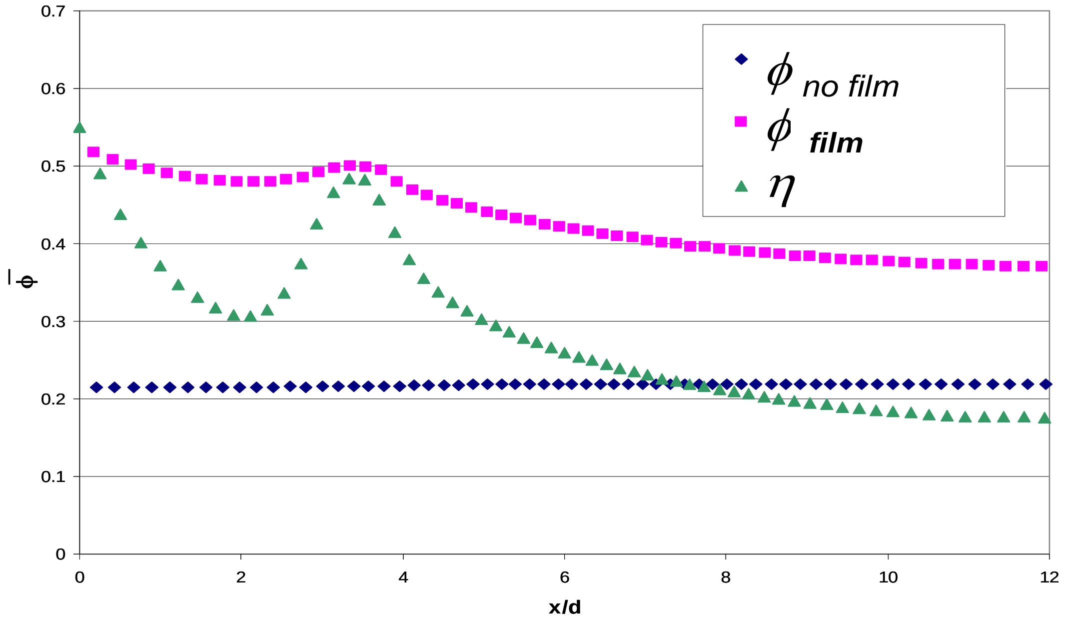

Figure 5.4.2 Comparison of the laterally averaged overall effectiveness for *M* = 2.0 and *Tu* = 6% for the film cooled leading edge (Maikell, 2008) and the no blowing model with the laterally averaged film effectiveness (Davidson and Dyson, 2009)

It is clear that the film cooling design provided a large increase in the overall effectiveness compared to the no-film cooled leading edge. On the stagnation line, a 120% and 150% increase in $\bar{\phi}$ was observed for $M = 1.0$ and 2.0, respectively. Of course, this was expected due to the convective cooling within the coolant holes and the decreased driving temperature (T_{aw} was much colder than T_∞). However, the higher h that occurs with cooling would have a counter acting effect. Interestingly, Figures 5.4.1 and 5.4.2 show that the magnitudes of the $\bar{\eta}$ peaks at the holes location were much higher than the one for $\bar{\phi}$ for the film cooled leading edge. Furthermore, the $\overline{\phi_{film}}$ and $\bar{\eta}$

magnitudes were very similar, which implies that the external heat transfer was very small at these locations. This highlights the effect of convective cooling through the coolant holes and the internal wall at the holes location.

The plots of normalized internal temperature on Figures 5.4.3 and 5.4.4 revealed that, from $\beta = 0$ º to $\beta = 50$ º, the film cooled leading edge experienced a colder internal temperature than the no blowing model. This would be expected due to the additional cooling by the convection effect in the three rows of holes. Recall the numerical simulations, discussed in Chapter 3, showed the convective cooling in the holes provided 63% and 57% of the total cooling for $M = 1.0$ and 2.0, respectively. This could explain the 25% and 45% increase in normalized internal temperature at respectively $M = 1.0$ and $M = 2.0$ from the stagnation line to $\beta = 50$ º. After $\beta = 50$ º, the normalized internal temperature was similar, which might be expected away from the holes.

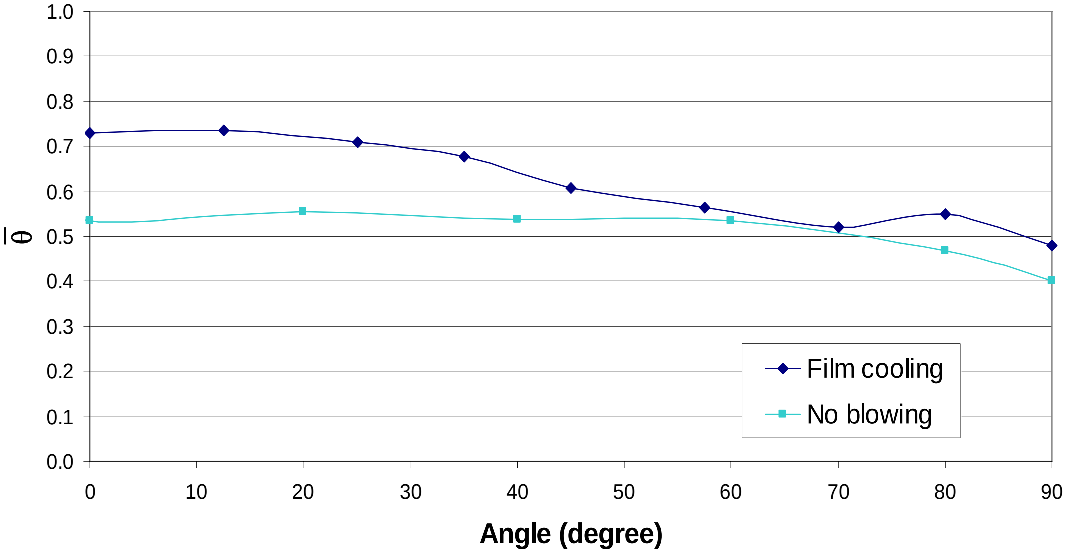

Figure 5.4.3 Comparison of the internal normalized temperature at *M* = 1 and *Tu* = 6% for the film cooled leading edge and the no blowing model

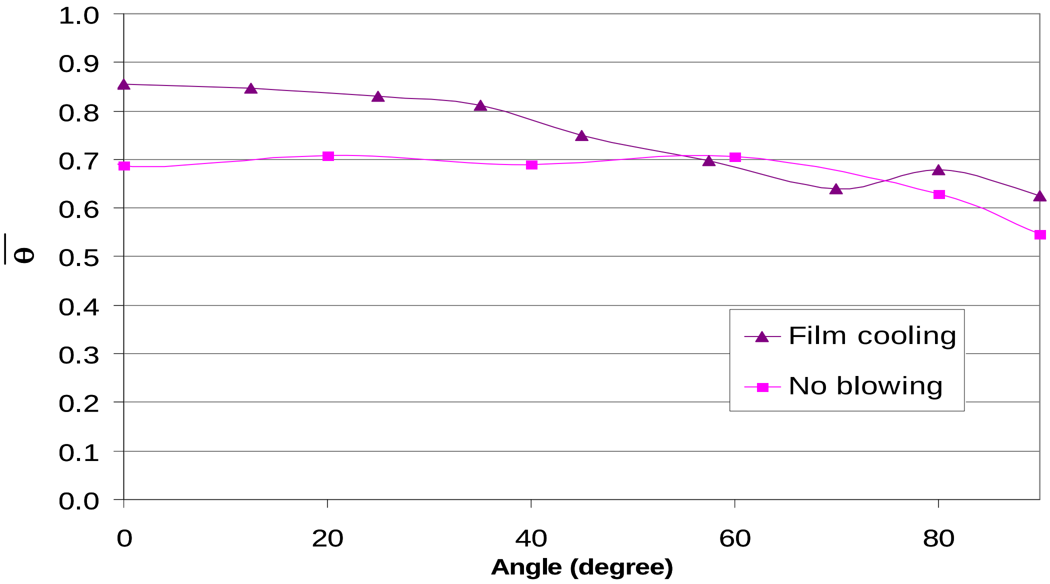

Figure 5.4.4 Comparison of the internal normalized temperature at *M* = 2 and *Tu* = 6% for the film cooled leading edge and the no blowing model

Chapter 6: Conclusions

This chapter summarizes the key results found in this thesis and presents conclusions based on these results. Also, recommendations for future work are presented.

6.1 SUMMARY OF THE RESULTS AND CONCLUSION

This study focused on a conjugate heat transfer analysis to predict the “metal” temperature of a simulated turbine blade leading edge. The leading edge model, that was simulated, was experimentally tested in the TTCRL laboratory by Maikell (2008). The wind tunnel model was designed such that the Biot number for the model matched that for a typical turbine blade at engine conditions. Two film cooling configurations were simulated; the first had three rows of cooling holes, with one row on the stagnation line and two additional rows at ± 25º. The second configuration consisted of a single row along the stagnation line to isolate the stagnation row contribution on the cooling performance. An adiabatic model was also studied to gain insight on the film cooling. For the numerical simulation, internal impingement cooling was artificially simulated with the prescription of internal wall temperatures that were obtained from the experiments. Simulations were done using blowing ratios of $M = 1.0$ and 2.0. The simulations were run using the realizable k-ε turbulence model with the enhanced wall treatment to ensure the most accurate prediction of the external heat transfer coefficients. Special attention was paid to match the experimental boundary conditions of Maikell's (2008) experimental data.

The CFD predictions of adiabatic effectiveness were in very good agreement with experimental measurements when compared in terms of laterally averaged values. But, predicted local values of adiabatic effectiveness near the holes and along the path of the coolant jets were distinctly higher than measured values for both blowing ratios. The discrepancies between the simulated and experimental adiabatic effectiveness results were attributed to the inability of the numerical simulations to correctly predict jet separation. The numerical simulations clearly showed no separation for $M = 1.0$ and slight separation for the stagnation hole for $M = 2.0$, whereas experimental measurements of $\eta < 0.8$ suggest separation for the stagnation and off-stagnation holes for both blowing ratios.

For the conducting model, computational predictions of overall effectiveness followed trends similar to the experimental measurements, but in the stagnation region the predicted overall effectiveness values averaged $\Delta\phi \approx 0.05$ higher than experimental measurements. These discrepancies appear to be associated with errors in η. At the downstream part of the leading edge, predicted overall effectiveness levels were less than experimentally measured levels. This disparity may be explained by the conduction to the impingement plate, which was not simulated in the computations and acted like a heat sink for the experiments.

Even though increased adiabatic effectiveness in the numerical simulations accounted for the increased overall effectiveness, a full explanation of the disparity between computations and experiment required the examination of other parameters. To investigate this discrepancy, convective cooling within the coolant holes was checked to determine whether the levels were higher than experimental measurements. However, the predicted convective cooling within the holes was found to be equal to or less than experimental measurements. A check of the predicted heat transfer coefficient over the external surface in the stagnation region compared to experimental measurements showed slightly lower values predicted. However, the predicted heat transfer coefficient was in the range of the experimental data and was not an explanation of the disparity between computations and experiments.

Computational simulations of a single row of holes along the stagnation line were compared to experimental measurements and to the three row configuration. Comparisons to experiments showed prediction of overall effectiveness in the stagnation region higher than measured values, similar to the results for the three row configuration. Comparison of the adiabatic effectiveness predictions for the one row and the three row configurations showed that the adiabatic effectiveness along the stagnation line was independent of the off-stagnation rows of holes.

The sensitivity to different key parameters was also studied in this thesis. The Biot number sensitivity was one of these studies since the metal airfoils may have different thermal conductivities. Simulations of leading edge with a factor of four increase in the thermal conductivity, i.e. a factor of four decrease in Biot number, showed higher levels of overall effectiveness and a decrease in spatial variation. Therefore, a higher thermal conductivity should be chosen for blade leading edge to improve the overall effectiveness. Then, the sensitivity to the impingement plate was analyzed with the prescription of different internal wall temperature, which simulated different impingement plates. The leading edge model showed very small sensitivity to internal wall temperature. A change in internal temperature of $\Delta\theta \approx \pm 0.05$ modified the external wall temperature by less than $\Delta\phi = 0.01$. This was explained by the increase in internal cooling that was compensated by the decrease in convective cooling through the holes. Another numerical simulation was conducted for the no impingement plate case and compared to simulation with the impingement plate. The key result was the small effect on the ϕ values, when the impingement plate was used. Indeed, the strong convective cooling on the internal stagnation region cooled down the surface very effectively and therefore limited the benefit of having high internal coefficients on the stagnation line.

One of the primary results of this thesis was the evaluation of T_{aw} as the driving temperature. Downstream of the off-stagnation holes, T_{aw} gave very good predictions of the actual heat transfer. The main disparity between the q'' predicted, using T_{aw} and h_f/h_0 from a constant heat flux simulation, and the q'' obtained from the conducting wall simulation was between the row of holes, where discrepancies were as much as 30%. Overall, T_{aw} was a good approximation for the driving heat transfer temperature.

More insight about the internal cooling was gained from the experiments run on a conducting non-film cooled leading edge. The no-blowing model did not include cooling holes designs and the flow exited the leading edge through 32 exhaust holes located on the flat part of the leading edge in order to limit the disturbance from the approaching flow. Contours of overall effectiveness showed a roughly constant surface temperature for the four blowing ratios studied. The results of the overall effectiveness were supplemented by heat transfer measurements with heat flux gauges for a greater understanding of the external and internal heat fluxes. Heat transfer measurements were presented in terms of Frossling number. Even though the current Frossling number gave similar values to Mouzon (2005), Fr showed a surprising dependence on the blowing ratio. An explanation presented in this thesis was the blockage due to the jets exhausting the exhaust holes. The approaching flow would see a lower or higher cylinder diameter than the actual leading edge geometry, depending on the blowing ratio used. Internal heat transfer coefficients were also calculated for the four blowing ratios. A 100% increase in blowing ratio (from $M = 2.0$ to $M = 1.0$) resulted in a 55% increase in internal heat transfer coefficient on the stagnation line. This was in agreement with the previous study of Fenot et al. (2008), which observed a 60% increase in h_{int} for a 100% increase in M. The influence of the mainstream turbulence intensity level was investigated for two blowing ratios, $M = 1.0$ and $M = 2.0$. At higher $Tu = 6\%$, a 25% increase in Fr was observed for both blowing ratios compared to $Tu = 0.5\%$, resulting in lower overall effectiveness. This was consistent with past study of Mouson (2005). Finally, a comparison between the internally cooled leading edge and the film cooled leading edge highlights the complexity of the cooling design. The strong interaction between the internal, convective and film cooling prevents a simple study of each cooling design separately. However, useful insight can be gained by isolating each cooling process.

6.2 RECOMMENDATIONS FOR FUTURE WORK

One area of future research in the computational field could be the simulation of the impingement plate. Therefore, the entire thermal effect of the impingement plate would be taken into account, i.e. the flat part of the leading edge would also be cooled down by the impingement plate presence. Moreover, the simulation of the impingement plate does not require the prescription of an internal wall temperature boundary condition anymore. Another improvement could be the simulation of the entire leading edge to ensure no error due to the imposed symmetry condition, as was encountered with the 2-D simulation.

Another area of future research would be to pursue the work done on T_{aw} as the appropriate driving temperature for heat transfer. The thermal profiles of non-dimensional temperature of the fluid above the wall did not confirm the assumption of T_{aw} as a driving temperature. So far, no justification has been found.

Concerning the experimental field, more research could be done on the conducting no-film cooled leading edge. The measurements uncertainty could certainly be reduced. A better understanding of the internal cooling could be gained with heat flux gauges located on the internal surface. A computation of the no-blowing model would also help understanding the phenomena occurring inside the plenum, not accessible with the IR camera. Finally, the fact that blocked holes artificially increased the overall effectiveness needs to be elucidated.

Last, but not least, studies could be done on the impingement plate design so that the impingement jets impact off the stagnation line, since the impingements jets impacting on the stagnation line proved to have limited effect on the internal convective cooling.

Appendix A.1

There are three major turbulence simulation codes: Reynolds-Averaged Navier Stokes (RANS), Large Eddy Simulation and Direct Numerical Simulation (DNS). RANS equations require models for turbulence, often using additional transport equations. In LES, the large scale turbulence is solved using the Navier-Stokes equations, and the small eddies are modeled. LES requires a huge amount of computer capacity and is not yet applicable to most engineering problems. DNS is the most accurate turbulence code by modeling all eddy length scales. No averaging or turbulence modeling is applied. As a drawback, DNS is highly computationally expensive. Unlike RANS, LES and DNS are time dependent and reflect better the reality since turbulence is unsteady and time dependent. However, LES and DNS are not used in industry since they are too computationally expensive.

A.1.1 REALIZABLE K-ε TURBULENCE MODEL

The realizable k-ε turbulence model is a modified version of the standard k-ε turbulence model, which is the simplest k-ε model. The realizable k-ε turbulence model uses the same equation as the standard k-ε model for the turbulent kinetic energy transport and also has an additional transport equation for ε, as for the standard k-ε turbulence model. However, the transport equation for ε for the realizable k-ε model is a modified version of the one for the standard k-ε model. This model is known to better predict jet spreading on curved surfaces, as well as flows involving separating boundary layers (FLUENT manual).

There are two turbulence transport equations for the realizable k-ε model. The equation for the turbulent kinetic energy, *k*, is defined by the following equation:

$$\frac{\partial}{\partial t}(\rho k)+\frac{\partial}{\partial x_i}(\rho k\overline{u_i})=\frac{\partial}{\partial x_j}\left[\left(\mu+\frac{\mu_t}{\sigma_k}\right)\frac{\partial k}{\partial x_j}\right]+G_k+G_b-\rho\varepsilon-Y_M+S_k \qquad \text{(A.1.1.1)}$$

where the turbulent viscosity is given by Equation A.1.1.2:

$$\mu_t=\rho C_\mu\frac{k^2}{\varepsilon} \qquad \text{(A.1.1.2)}$$

In the case of the realizable k-ε model, C_μ is no more a constant, as was the case for the standard k-ε model and is defined as follows:

$$C_\mu=\frac{1}{A_0+A_s\dfrac{kU^*}{\varepsilon}} \qquad \text{(A.1.1.3)}$$

$$U^*=\sqrt{S_{ij}S_{ij}+\Omega_{ij}\Omega_{ij}} \qquad \text{(A.1.1.4)}$$

$$S_{ij}=\frac{1}{2}\left(\frac{\partial\overline{u_i}}{\partial x_j}+\frac{\partial\overline{u_j}}{\partial x_i}\right) \qquad \text{(A.1.1.5)}$$

The second equation used for the realizable k-ε model is the equation for the turbulence dissipation rate, defined as follows, with arrows pointing to the differing terms between the standard and realizable k-ε turbulence models:

$$\frac{\partial}{\partial t}(\rho\varepsilon)+\frac{\partial}{\partial x_i}(\rho\varepsilon\overline{u_i})=\frac{\partial}{\partial x_j}\left[\left(\mu+\frac{\mu_t}{\sigma_\varepsilon}\right)\frac{\partial\varepsilon}{\partial x_j}\right]+\underset{\uparrow}{\rho C_1 S_\varepsilon}-\rho C_2\frac{\varepsilon^2}{\underset{\uparrow}{k+\sqrt{\nu\varepsilon}}}+C_{1\varepsilon}\underset{\uparrow}{\frac{\varepsilon}{k}}C_{3\varepsilon}G_b+S_\varepsilon \qquad \text{(A.1.1.6)}$$

More details on the constant values used in the previous equations (from Equation A.1.1.1 to Equation A.1.1.6) are available on the FLUENT manual.

A.1.2 WALL TREATMENT

Since the realizable k-ε model can only be used for high *Re* regions, wall treatments have been developed to solve the turbulence near the wall, where the viscosity considerably slows down the fluid. There are three wall treatments available with the realizable k-ε model: standard wall function, non equilibrium wall function and the enhanced wall function that was used in these simulations. For wall function, the flow is not solved in the viscous sub-layer. The non-equilibrium wall function is similar to the wall function, except that the log law used for the mean velocity is sensitive to pressure gradients. The enhanced wall function divides the domain in two regions: a fully turbulent region and a viscosity effected region. The enhanced wall function resolves the viscous sub layer, but the mesh has to be fine enough close to the wall, with generally $y+ < 1$. This last wall function is preferred in case of separation, as was the case in this thesis.

Appendix A.2

This appendix details the boundary conditions used for the simulation for the blowing ratio of $M = 2.0$, as plotted in Figures A.2.1 and A.2.2.

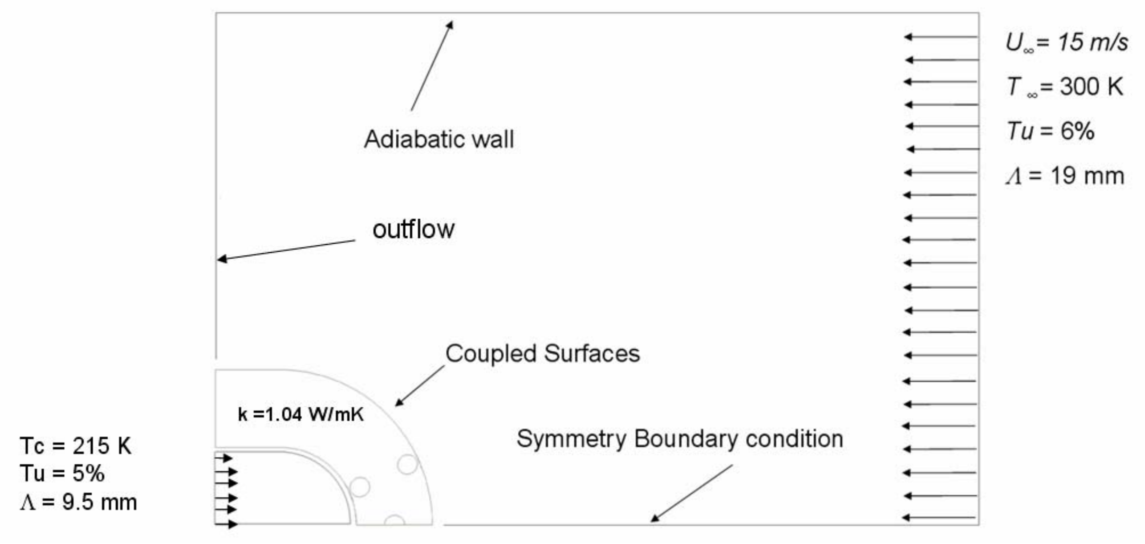

Figure A.2.1 Summary of the boundary conditions used for the simulation for *M* = 2.0

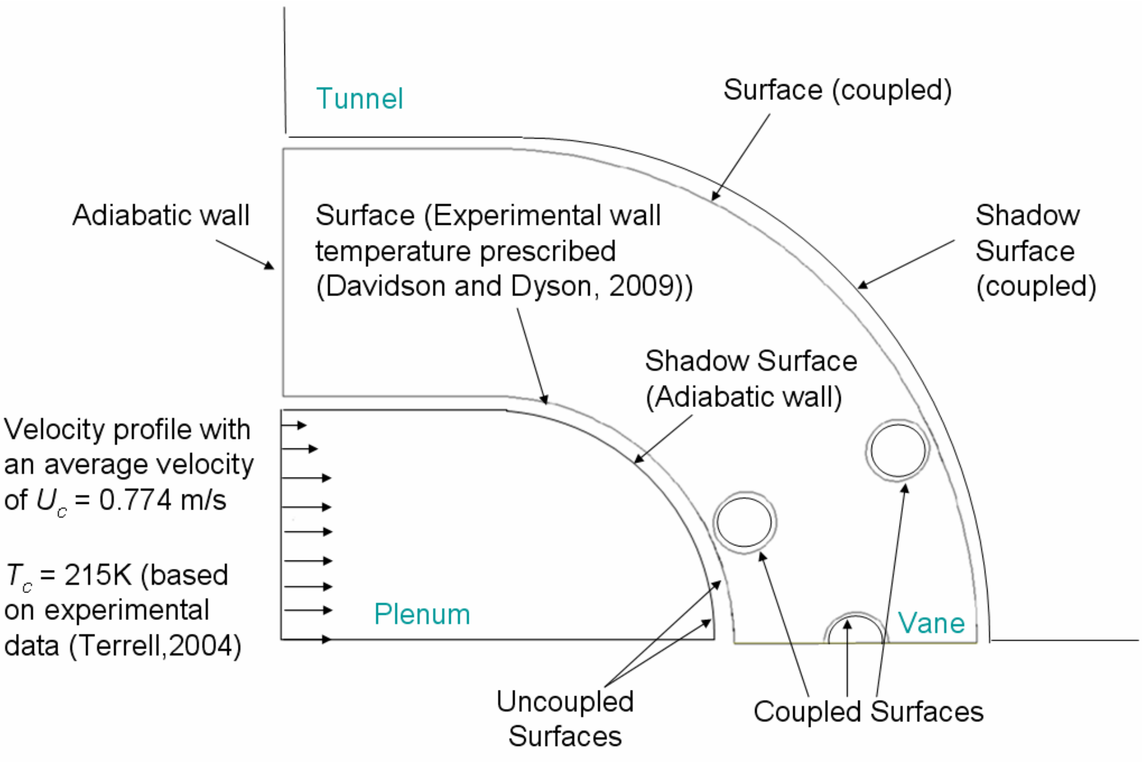

Figure A.2.2 Summary of the boundary conditions used for the simulation for *M* = 2.0 for the leading edge model

References

Bergeles, G., Gosman, A.D. and Launder, B.E., 1978, “The turbulent jet in a cross stream at low injection rates: A three-dimensional numerical treatment”. *Numer. Heat Transfer* Vol. 1, pp. 217–242

Bharti,R.P., Chhabra, R. P., and Eswaran, V., 2007, “A numerical Study of the steady forced convection heat transfer form an unconfined circular cylinder”, Heat Mass Transfer

Chernobrovkin, A. and Lakshminarayana, B., 1998, “Numerical Simulation and Aerothermal Physics of Leading Edge Film Cooling”, ASME Paper No.98-GT-504

Cruse, M.W., 1997, “A Study of Film Cooling Adiabatic Effectiveness for Turbine Blade Leading Edges,” M.S. Thesis, The University of Texas, Austin, Texas.

Ekkad, S.V., Han, J.C., and Du, H., 1997, “Detailed Film Cooling Measurements on a Cylindrical Leading Edge Model: Effect of Free- Stream Turbulence and Coolant Density”, ASME Paper No. 97-GT-181.

Ekkad, S.V. and Han, J.C., 2000, “A transient liquid crystal thermography technique for gas turbine heat transfer measurements”, Meas. Sci. Technol. 11 (2000) pp. 957-968

Fenot, M., Dorignac, E. and Vullierme J.-J., “An experimental study on hot round jets impinging a concave surface”, International Journal of Heat and Fluid flow, 29 (2008) pp. 945-956

Ferguson, J. D., Walters, D. K. and Leylek, J. H., 1998, “Performance of Turbulence Models and Near-Walls Treatments in Discrete Jet Film Cooling Simulations”, ASME Paper No. 98 GT-438

Garg, V.K. and Gaugler, R.E., 1995, “Leading Edge Film Cooling Effects on Turbine Blade Heat Transfer,” ASME Paper No. 95-GT-275.

Hall, E. J., Topp, D. A. and Delaney, R. A., 1994, “Aerodynamic/heat transfer analysis of discrete site film-cooled turbine airfoils”, AIAA 94-3070.

Harrison, K. L., 2006, ”Computational and Experimental Study of Film Cooling Performance Including Shallow Trench Configurations”, M.S. Thesis, University of Texas, Austin, Texas.

Harrison, K. and Bogard, D. G. , 2007, “Use of the Adiabatic Wall Temperature in Film Cooling Research, Part 1: Turbulence Modeling”, ASME Paper GT 2008-51423

Heidmann, J. D., Kassab, A. J., Divo, E. A., Rodriguez, F., and Steinthorsson, E., 2003, “Conjugate Heat Transfer Effects on Realistic Film-Cooled Turbine Vane”, ASME Paper No. GT2003-38553.

Kusterer, K., Hagedorn, T., Bohn, D., Sugimoto, T., and Tanaka, R., 2004, “Conjugate Calculations for a Film-Cooled Blade under Different Operating Conditions”, ASME Paper No. GT2004-53719.

Lakehal, D., Theodoridis, G.S, and Rodi,W. 2001, “Three-dimensional Flow and Heat Transfer Calculations of Film Cooling at the Leading Edge of a Symmetrical Turbine Blade Model”, International Journal of Heat and Fluid Flow Vol. 22 pp. 113-122

Lakehal, D., 2002, “Near-wall Modeling of Turbulent Convective Heat transfer in Film Cooling of Turbine Blades With the Aid of Direct Numerical Simulation Data”, Journal of Turbomachinery, vol. 124.

Laskowski, G. M., Tolpadi, A. K., and Ostrowski, M. C., 2007, “Heat Transfer Predictions of Film Cooled Stationary Turbine Airfoils”, ASME Paper No. GT2007-27497

Laskowski, G. M., Ledezma, G. A., Tolpadi, A. K., and Ostrowski, M. C. (2008) CFD Simulations and Conjugate Heat Transfer Analysis of a High Pressure Turbine Vane Utilizing different Cooling Configurations. ISROMAC12-2008-20065.

Lin, Y.-L., Stephens, M.A., and Shih, T.I-P., 1997, “Computation of Leading-Edge Film Cooling with Injection Through Rows of Compound-Angle Holes”, ASME Paper No. 97-GT-298.

Luo, L., and Razinski E. H. , 2007, Conjugate Heat Transfer Analysis of a Cooled turbine vane using the V2F Turbulence Model. Journal of Turbomachinery, 129:773-781.

Martin, C.A. and Thole, K.A., 1997, “A CFD Benchmark Study: Leading Edge Film-Cooling With Compound Angle Injection,” ASME Paper No. 97-GT-297.

Mazur, Z. Hernandez-Rosette,A., Gracia-Illescas, R. and Luna-Ramirez, A. ,2006, “Analysis of conjugate Heat Transfer of a gas turbine first stage Nozzle”, ASME Paper No. GT2005-68004

Medic G., and Durbin P. A. (2002) Towards improved prediction of heat transfer in turbine blades, Journal of Turbomachinery, Vol. 124 pp.187-192.

Mehendale, A.B. and Han, J.C., 1992, “Influence of High Mainstream Turbulence on Leading Edge Film Cooling Heat Transfer,” ASME Journal of Turbomachinery, Vol. 114, pp. 707-715.

Mills, A. F., 1999, Heat Transfer, second edition, Prentice Hall, Inc.

Momose K., and Kimoto, H., 1999, “Forced Convection Heat Transfer from a Heated Circular Cylinder with Arbitrary Surface Temperature Distributions”, *Trans*. JSME, 63 (613) B, pp 3092-3099

Mouzon, B.D., Terrell, E.J., Albert, J.E., Bogard, D.G., 2005. “Net heat flux reduction and overall effectiveness for a turbine blade leading edge”. ASME Paper No. GT2005-69002.

Nemdili, F., Azzi, A., Theodoridis, G., and Jubran, B., A., 2008, “Reynolds Stress Transport Modeling of Film Cooling at the Leading edge of a Symmetrical Turbine Blade Model, Heat Transfer Engineering, 29:11, pp. 950-960

Ou, S., Rivir, R.B., 2001, “Leading edge film cooling heat transfer with high free stream turbulence using a transient liquid crystal image method”, International Journal of Heat and Fluid Flow (22), 614–623.

Ou, S., Rivir, R.B., 2001,”90 Skew Leading Edge Film Cooling Effectiveness, Heat Transfer, and Discharge Coefficients for Cylindrical Film Holes at High Free Stream Turbulence, RTO AVT Symposium on “Advanced Flow management: part B- Heat Transfer and Cooling in Propulsion and Power Systems”, Loen, Norway, 7-11 May 2001

Papell, S. S., 1981, “Influence of Thermal Boundary Conditions on Heat Transfer From a Cylinder in Crossflow, NASA Technical Paper 1894

Reiss, H. and Bolcs, A., 1999, “Experimental Study of Showerhead Cooling on a Cylinder Comparing Several Configurations Using Cylindrical and Shaped Holes”, ASME Paper No. 99-GT-123.

Rozati, A., Tafti, D.K., 2007. "Large Eddy Simulation of Leading Edge Film Cooling-Part II: Heat Transfer and Effect of Blowing Ratio", ASME Paper No. GT2007-27960

Rozati, A., Tafti, D.K., 2008. "Large-eddy simulations of leading edge film cooling: analysis of flow structures, effectiveness, and heat transfer coefficient'. International Journal of Heat and Fluid Flow 29 (1), 1–17.

Salcudean, M., Gartshore, I., Zhang, K., and McLean, I., 1994, "An Experimental Study of Film Cooling Effectiveness Near the Leading Edge of a Turbine Blade", ASME Journal of Turbomachinery, Vol. 116, pp. 71-79.

Sarkar, S., Das, K. and Basu, D. ,2001, Film cooling on a turbine guide vane: a numerical analysis with a multigrid technique. Proc Instn Mech Engrs, 215(A):39-53.

Starke, C., Janke, E., Hofer, T. and Lengani, D., 2008,"Comparison of a Conventional Thermal Analysis of a Turbine Cascade to a Full Conjugate Heat Transfer Computation", ASME Paper No. GT2008-51151

Scholten, J. W. and Murray, D. B., 1998, "Unsteady heat transfer and velocity of a cylinder in coess flow- I. Low Freestream Turbulence", International Journal of Heat Transfer Vol. 41, pp 1139-1148

Szczepanik, K., Ooi, A., Aye, L., and Rosengarten, G., 2004, "A numerical study of Heat Transfer from a Cylinder in Cross Flow", 15th Australasian Fluid Mechanic Conference, Sydney, Australia, 13-17th December 2004

Tao, Z. , Zhao, Z. , Ding, S. , Xu, T. and Wu, H. , 2009, "Numerical Study of Film-Cooling Performance on a Rotating Model", International Journal of Heat and Mass Transfer, v52 pp 1268-1275

Terrel, E. J, Mouzon, B. D., Bogard, D. G., 2004, "Convective Heat Transfer Through Film Cooling Holes of a Gas Turbine Blade Leading Edge", ASME Paper, No. GT2005-69003

Thakur, S., Wright, J., and Shyy, W., 1997, "Computation of Leading-Edge Film Cooling Flow Over an Experimental Geometry," ASME Paper No. 97-GT-381.

York, W. D. and Leylek, J.H., 2001, "Leading-Edge Film Cooling Physics: Part I-Adiabatic Effectiveness", ASME Paper No. GT-2002-30166

York, W. D. and Leylek, J.H., 2002, “Leading-Edge Film Cooling Physics: Part II- Heat Transfer Coefficient”, ASME Paper No. GT-2002-30167

York, D. W., and Leylek, J. H., 2003, “Three-Dimensional Conjugate Heat Transfer Simulation of an Internally-Cooled Gas Turbine Vane”, ASME Paper No. GT2003-38551.

Yuki, U.M., 1998, “Heat Transfer and Adiabatic Effectiveness Measurements on a Simulated Film-Cooled Turbine Blade Leading Edge”, M.S. Thesis, University of Texas, Austin, Texas.

Zhang, N., Zheng, Z.C., and Eckels, S., 2008, “Study of heat-transfer on the surface of a circular cylinder in flow using an immersed-boundary method”, International Journal of Heat and Fluid Flow Vol. 29, pp.1558-1566

Vita

Laurène D. Dobrowolski was born on September 9, 1984 in Nevers in France, the daugther of Beatrix Thurn and Bruno Dobrowolski. She grew up in Besancon in France. Laurène graduated from Ecole Centrale de Lille in May 2007 with a Bachelors of Science in Mechanical Engineering. During the summer of 2007, Laurène interned at the ONERA (Office National d'Etudes et de Recherches Aerospatiales), the French aerospace lab and worked as a research engineer. In August 2007, she began her Master of Science in Mechanical Engineering at the University of Texas at Austin. Laurène will graduate in August 2009 from both Ecole Centrale de Lille in France and The University of Texas at Austin.

Permanent address: 21, rue des Granges
25,000 Besancon, France

This thesis was typed by the author.